Trinity College Dublin
The University of Dublin

Laser-induced failure modes in plasmonic thin films

---

by

William Maurice Abbott

Trinity College Dublin
Coláiste na Tríonóide, Baile Átha Cliath
The University of Dublin

A thesis submitted in fulfilment of the requirements

for the degree of Doctor of Philosophy

Supervisors: Prof. John F. Donegan

& Prof. David McCloskey

12/04/2019

Declaration

I declare that this thesis has not been submitted as an exercise for a degree at this or any other university and it is entirely my own work.

I agree to deposit this thesis in the University's open access institutional repository or allow the library to do so on my behalf, subject to Irish Copyright Legislation and Trinity College Library conditions of use and acknowledgement.

Signature: _____

Date: _____

Abstract

In order for the areal density of magnetic hard-drives to continue increasing, it is necessary to improve upon current recording technologies. The proposed next-generation magnetic recording process, heat-assisted magnetic recording (HAMR), will potentially allow for areal densities of 4 Tb/in^2 or more, but its implementation is limited by thermal failure of the nanoscale Au plasmonic focusing element that is integral to the recording process. Any attempts at improving the thermal stability of the Au element can only be considered successful if the plasmonic performance of the Au is not negatively affected.

In this thesis, the laser-induced degradation mechanisms on Au thin films are studied, and different stabilization methods are presented. The main source of thermal degradation in the Au was found to be caused by solid-state dewetting. Other degradation mechanisms observed included grain growth and crystalline texturing. The time dynamics of solid-state dewetting were measured using a customized microscope set-up, which allowed for a quantitative comparison between stabilization methods. The stabilization methods studied in this thesis were adhesion layers, alloying and capping layers. While no improvement was observed in the thermal stability of the Au upon alloying, the use of adhesion and capping layers resulted in significant increases in resistance against dewetting, with sub-nanometer adhesion/capping layers resulting in the greatest increase.

In Chapter 1, a brief introduction to the current state of magnetic recording is given, and the motivations behind the work in this thesis are presented. In Chapter 2, the theoretical background behind the main concepts within this thesis are described, including solid-state dewetting, laser-induced heating, and plasmonics. In Chapter 3, the main experimental techniques used within the thesis are described. In Chapter 4, the effects of CW-laser annealing on an Au thin film are discussed, showing the changes in film quality caused by solid-state dewetting, grain growth and crystalline texturing. In Chapter 5, the effect of an adhesion layer on increasing the resistance of the film against solid-state dewetting is discussed, and the optimal thickness for a metallic adhesion layer is found. In Chapter 6, the optical and thermal properties of an AuCu alloy are investigated. In Chapter 7, the effect of dielectric capping layers on the solid-state dewetting characteristics of an Au film is shown, and the optimal adhesion layer/capping layer combination is stated. Finally,

Chapter 8 states the final conclusions that can be taken from the work presented, and gives suggestions for future work are given.

Acknowledgements

Firstly, I would like to thank my supervisors, Prof. John F. Donegan and Prof. David McCloskey. I could not have asked for better supervisors, and I will always be grateful for the advice and support that they gave at all stages of my PhD. I would to thank everyone from the Donegan and McCloskey research groups for their advice, but some specific people are due extra thanks. The first is due to Chris Murray, without whom most of the work presented within this thesis would not have been possible. Thanks to Simon Corbett, for his work on the CCD-TR measurements, and for sharing the lab with me. Thanks to Chuan Zhong, for his work on measuring the plasmonic properties (in conjunction with Chris Smith).

Outside of these groups, there are others in the School of Physics, CRANN, and AMBER who deserve acknowledgement. Thank you to Clive Downing for his work on the TEM studies in Chapter 5, and to Dermot Daly for preparing the lamellae. Thank you to Cormac McGuinness for the XPS measurements. Thank you to Sé at Da Capo Goldsmiths for resizing the Krugerrand coin. Thank you to David O'Regan for some very useful discussions and ideas.

I would like to express my gratitude to those who helped facilitate my research at Argonne National Labratory, in particular my supervisor Prof. Amanda Petford-Long. I would also like to thank Sheng Zhang, for his help with the TEM/SAED studies presented in Chapter 4, as well as the other members of the Petford-Long group for their help and advice. I would also like to express my gratitude to my family in Chicago for rescuing me from the lab at the weekends during my stint in Argonne.

On a personal note, I would like to give a big thank you to my office mates in 4.46, especially Darragh, Emmett, Felim, Lorcan, & Owen: the last 4 years would have been a lot less enjoyable without you. I would like to thank all of my friends for their support, whether it took the form of encouraging words or coffee. Finally, I would like to thank my mother, father, and sister for their constant support, advice, and love.

Publications

- **W.M. Abbott**, C.P. Murray, C. Zhong, C. Smith, C. McGuinness, E. Rezvani, C. Downing, D. Daly, A.K. Petford-Long, F. Bello, D. McCloskey, and J.F. Donegan. “Less is more: improved thermal stability and plasmonic response in Au films via the use of sub-nanometer Ti adhesion layers”. *ACS Applied Materials & Interfaces.* 11 (7), 7607–7614 (2019)

- **W.M. Abbott**, C.P. Murray, C. Zhong, C.M. Smith, C. McGuinness, C. Downing, A.K. Petford-Long, J.F. Donegan, and D. McCloskey. "A Comparison of Ti Adhesion Layers for Thermo-plasmonic Applications". *Photonics Ireland* (Cork, 2018)

- **W.M. Abbott**, C.P. Murray, C. Zhong, C.M. Smith, D. McCloskey, and J.F. Donegan. "Optimizing Ti adhesion layer thickness for plasmonic Au films" in *Gold* (Paris, 2018)
- **W.M. Abbott**, C.P. Murray, C. Zhong, C.M. Smith, D. McCloskey, and J.F. Donegan. "Improved Performance and Thermal Stability in Plasmonic Films with Thinner Adhesion and Capping Layers" in *Conference on Lasers and Electro-Optics (CLEO)* ATu4M.2. (OSA, San Jose, 2018)
- **W.M. Abbott**, S. Corbett, G. Cunningham, A. Petford-Long, S. Zhang, J.F. Donegan, and D. McCloskey. "Solid state dewetting of thin plasmonic films under focused cw-laser irradiation". *Acta Materialia*, 145, 210 (2018)

- **W.M. Abbott**, S. Corbett, G. Cunningham, A. Petford-Long, S. Zhang, J.F. Donegan, and D. McCloskey. "Thermal degradation of thin plasmonic films under focused cw-laser irradiation" in *Photonics Ireland* (Galway, 2017)

List of abbreviations

ALD – Atomic Layer Deposition

AFM – Atomic Force Microscopy

ARXPS – Angle Resolved X-ray Photoelectron Spectroscopy

BPM – Bit Patterned Media

BSE – Back Scattered Electron

CCD – Charge Coupled Device

CCD-TR – CCD-Thermoreflectance

CW – continuous wave

DC – Direct Current

EDX – Energy Dispersive X-ray

EELS – Electron Energy Loss Spectroscopy

FIB – Focused Ion Beam

FWHM – Full Width Half Maximum

HAMR – Heat-assisted Magnetic Recording

IPA – Isopropyl Alcohol

LMR – Longitudinal Magnetic Recording

MBE – Molecular Beam Epitaxy

NFT – Near-Field Transducer

PEELS – Parallel Electron Energy Loss Spectroscopy

PMR – Perpendicular Magnetic Recording

PVD – Physical Vapour Deposition

RF – Radio Frequency

RMS – Root Mean Square

SAED – Select-Area Electron Diffraction

SE – Secondary Electron

SEM – Scanning Electron Microscopy

SERS – Surface Enhanced Raman Spectroscopy

SIL – Solid Immersion Lens

SMR – Shingled Magnetic Recording

SMU – Soft Magnetic Underlayer

SP – Surface Plasmon

SPP – Surface Plasmon Polariton

STEM – Scanning Transmission Electron Microscopy

STM – Scanning Tunnelling Microscopy

TEM – Transmission Electron Microscopy

TFC – Thermal Fly-height Control

UV – Ultra-Violet

XPS – X-ray Photoelectron Spectroscopy

List of Figures

Table of Contents

To the Student Counselling Service in Trinity College Dublin, with gratitude

Ever tried.

Ever failed.

No matter.

Try again.

Fail again.

Fail better.

- Samuel Beckett

Chapter 1: Introduction

1.1 Current issues relating to the future viability of magnetic recording

When one considers the 2 technological pillars of the information age, magnetic storage & integrated circuits, magnetic storage is arguably the least acknowledged in the public consciousness, despite having existed in some form or another since the late 19th century[1]. Moore's law relating to the near-annual halving in size of integrated circuits[2] has captured the public imagination, and is frequently cited in the media as an example of the many ways in which the field of nanotechnology currently impacts our lives[3–5]. The magnetic storage analogue of this law, however, is less known among the public, despite arguably being just as important.

In 2005, Mark Kryder made the observation that, within a 15 year timespan, the areal density of magnetic hard-drives had increased by 3 orders of magnitude[6]. The density increase over this period roughly equates to a 40% increase each year, and this rate, which far outstripped that of Moore, became known as "Kryder's law" [6]. The validity of the observation, however, is unlikely to last. In 2009, Kryder predicted that by 2020, a 2-disk, 2.5 inch 40 Tb hard drive system would cost $40[7]. This target is highly unlikely to be met: at time of writing, one of the largest commercially available magnetic hard-drives is the Seagate *ST8000AS0002*: an 8 Tb 3.5" hard drive[8] fabricated using shingled magnetic recording (SMR)[9] that costs $250[10]. Hence, within the next 2 years, such a drive would need to increase in capacity by 250 %, while at the same time decreasing in price by 625 %, in order to meet Kryder's prediction.

1.1.1 Perpendicular recording

Hard-disk drives that are currently commercially available operate via a process known as perpendicular magnetic recording (PMR). PMR was an improvement on the previous industry standard, longitudinal magnetic recording (LMR), allowing for a greater areal density to be achieved. The fundamentals of both processes are described schematically in

Figure 1.1. In LMR, a ring-like recording head with a narrow (>1 μm) gap is used to create individual magnetic domains: a current is run through the recording head, creating a magnetic dipole at the gap, and the area of the recording layer that passes beneath the gap will become magnetized[11]. The attainable areal density from LMR is limited by its susceptibility to thermal fluctuations, owing to the presence of charged domain walls and relatively low magnetic anisotropies within the recording medium[12].

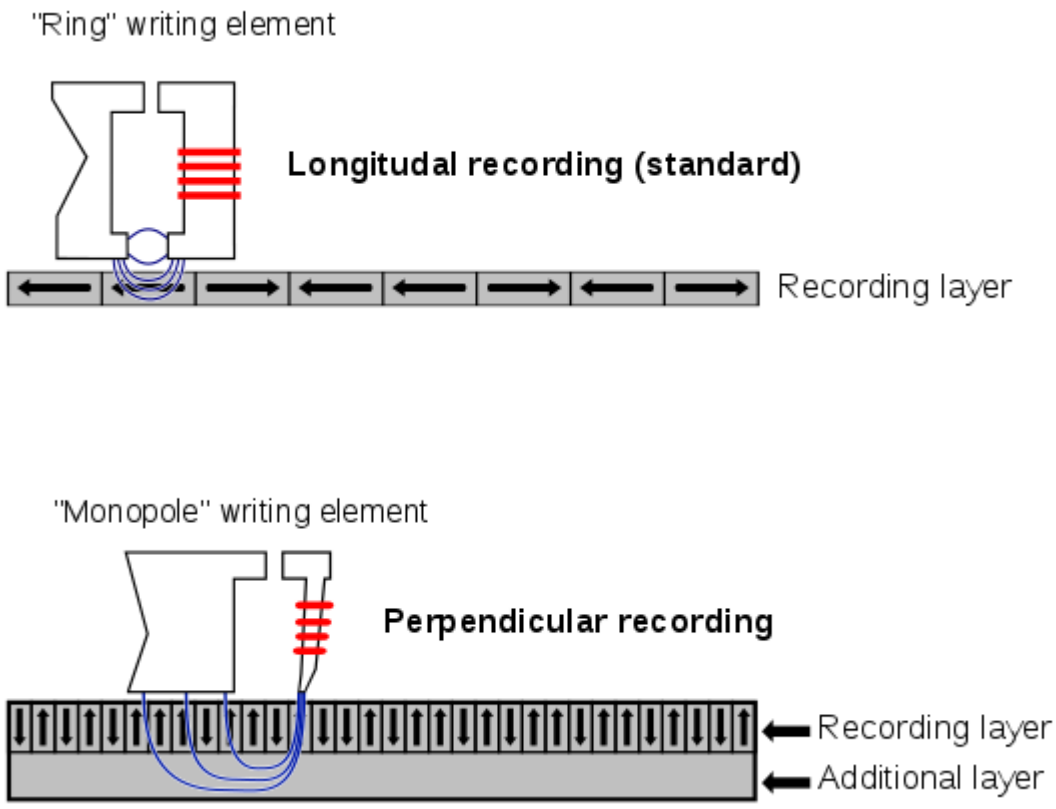

Figure 1.1: ***S****chematic comparison of longitudinal magnetic recording (LMR) and its successor perpendicular magnetic recording (PMR). Public Domain image by Luca Cassioli, via Wikimedia Commons, 2005.*

PMR improves on LMR by having the magnetic domains aligned perpendicularly to the recording layer. It was first conceived in 1976[11] by Shun-ichi Iwasaki, and eventually published in 1977[13] in collaboration with Yoshihisa Nakamura. One key advantage of PMR is that the axis of easy magnetisation for the recording layer is aligned to be almost perfectly perpendicular with the recording layer (as opposed to LMR, where the easy axis is roughly aligned parallel)[14]. This allows narrow, well-defined tracks to be recorded into even relatively thick recording layers[15]. One of the other fundamental differences between PMR and its predecessor are the use of a monopole recording head and the addition of a soft magnetic underlayer (SMU) (i.e. an underlayer that is easy to magnetize and

demagnetize[16]) into the recording medium (see Figure 1.1). The use of the SMU allows for double the possible write field attainable by LMR: this is due to the magnetic pole inducing a magnetic "image" within the SMU, effectively resulting in twice the magnetic field being applied at the gap between the "real" and "virtual" recording heads[15]. This allows for higher magnetic anisotropy materials to be used which in turn will allow for smaller bits[17].

1.1.2 Limiting factors in current recording methods

In order for hard-drive manufacturers to attempt to follow Kryder's law, it has been necessary to continuously replace and improve upon previously used technologies[18]. In Figure 1.2, two different projected roadmaps created in 2015 and 2016[19] respectively for magnetic recording technologies are displayed. Each roadmap shows how magnetic recording techniques have a finite lifetime, and must give way for the next generation.

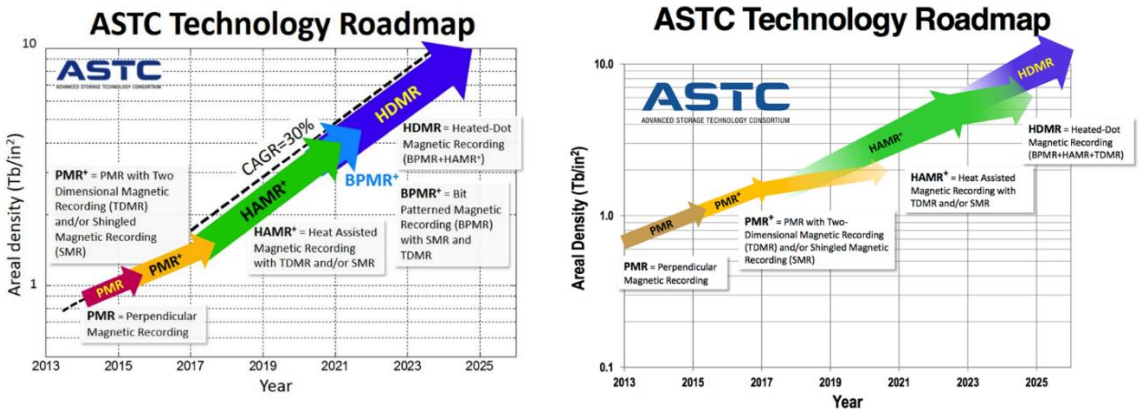

Figure 1.2: ASTC technology roadmaps from 2015 (left) & 2016 (right), showing the predicted timeline for magnetic recording technologies. Note the shift in start point for HAMR and the expanded relevance of PMR in the 2016 roadmap.

As with previous magnetic recording technologies, PMR can only improve the areal density by so much. The limiting factor for PMR is related to the thermal stability of the written bits, which is fundamentally limited by the superparamagnetic effect[20]. The energy (thermal or otherwise) required to completely reverse the direction of a magnetized bit is given by;

$$\Delta E = K_U V \tag{1.1}$$

where K_U is the magnetic anisotropy per unit volume, and V is the volume of the magnetic domain[15]. Hence, in order for a magnetized domain to be stable, ΔE must be significantly larger than the fluctuations in thermal energy (k_BT) that occur under ambient conditions. To ensure a stable domain, it has been recommended that ΔE be at least 40 times greater than k_BT[21], i.e:

$$\frac{K_U V}{k_B T} \geq 40 \tag{1.2}$$

For areal densities to continue increasing, V will need to decrease, and K_U will need to increase in turn so that the magnetic domains will remain thermally stable. While there are many materials with high K_U which would be suitable as a recording layer (such as FePt[22], Co_3Pt[23], and $SmCo_5$[24]) using such materials will introduce problems into the recording process itself. Materials with a higher K_U will require a much higher write-field which, given that there is hard limit on the maximum output field of a recording head (~2.5 T/μ_0)[25], which makes sufficient write-fields unfeasible past a certain point. Based on these considerations, the projected upper limit achievable by PMR in its current form is approximately 1 Tb/in^2 [26].

1.2 Heat-assisted magnetic recording (HAMR)

In order to increase the attainable areal density in magnetic hard-drives, new recording techniques are required. Several different methods have been proposed[27], including using bit-patterned media (BPM)[28] and shingled magnetic recording (SMR)[29]. The most promising candidate to replace current recording methods, however, is heat-assisted magnetic recording (HAMR). This technology is projected to allow areal densities of 4 Tb/in^2 and beyond[30], which can then be further improved through combinations of HAMR, BPM, and SMR[31–35].

1.2.1 Principles of operation

Heat-assisted magnetic recording (HAMR) was devised as a method to circumvent the issues which limit conventional methods such as PMR. HAMR is based on the temperature dependence of magnetic coercivity; higher values of T will result in lower values of K_U. Hence, by heating an area on the magnetic recording medium, a lower write-field will be

required. A schematic diagram illustrating the working principle of HAMR is shown in Figure 1.3. A laser is focused, using a dielectric waveguide[36], onto a device called the near-field transducer (NFT), which focuses the incoming electric field onto the recording layer. This results in a temperature increase in the area which locally decreases the coercivity, thus allowing for a smaller write-field to be used.

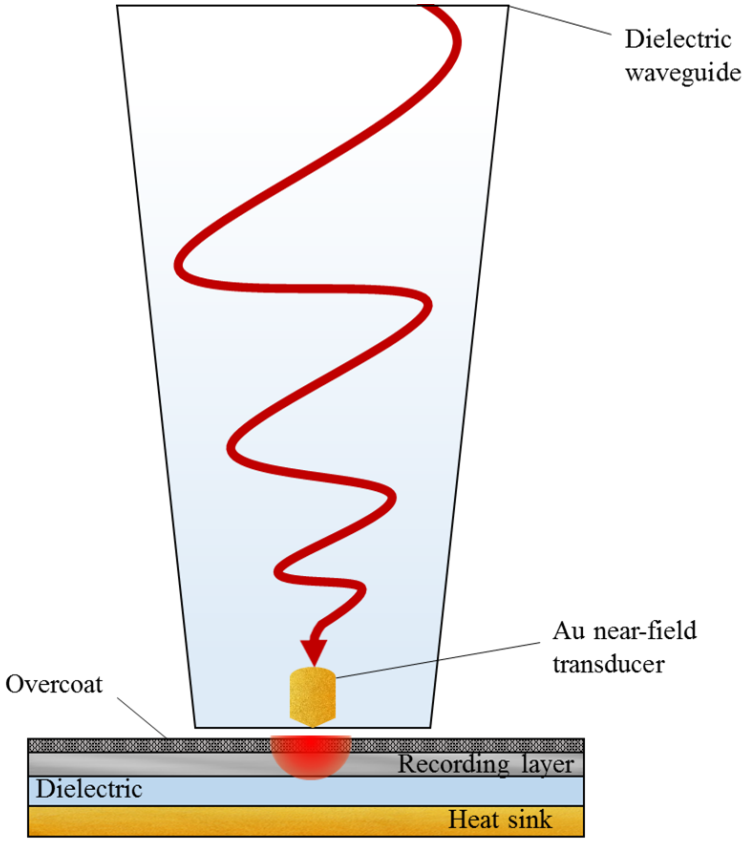

Figure 1.3: Schematic diagram detailing the process of heating the recording medium during the HAMR writing process. The magnetic recording head is not shown.

The ability of HAMR to reduce the written bit size is dependent on the nano-focusing properties of the NFT. In order for areal densities to surpass 1 Tb/in^2, the heated spot size in a HAMR recording process cannot be greater than 50 nm[37]. In most HAMR designs[38–40], the NFT is a plasmonic focusing element, while other designs utilize plasmonics to enhance the near-field intensity from a dielectric focusing element[41]. The coupling of light to the surface plasmons of a metal allows the energy from the light to be focused to spatial dimensions beyond the far-field diffraction limit. [42]. The resolution of a far-field system is given by the following equation:

$$d = \frac{\lambda}{2n\sin\theta} \tag{1.3}$$

where λ is the wavelength of the light, n is the refractive index of the surrounding medium, and θ is the half-angle over which the system can collect light. From the equation, it can be seen that the resolution will depend heavily on n. Solid immersion lenses (SILs) were developed to improve the attainable resolution of systems by containing the entire optical system within a high refractive index material, thus improving the resolution[43]. SILs are not a likely solution for HAMR, however, as a refractive index greater than 4 would be required to achieve the previously mentioned goal of a 50 nm optical spot[37] (by way of reference, one of the highest refractive indices in the visible regime is that of silicon carbide; 2.65)[44]. In order to surpass Abbe's limit, it is necessary to employ modern systems based on plasmonics[45]. Recent work has found plasmonic systems to be capable of beating the diffraction limit for focusing light[46,47]. Further background and the theory on plasmonics will be discussed in Chapter 2.

1.2.2 Current issues in the implementation of HAMR

In the comparison of ASTC roadmaps in Figure 1.2, it can be seen that there is a shift in the predicted start-point for HAMR, due to continuing issues with its development. While the problems that still face HAMR are not considered to be fundamental[48], they are still quite considerable. Such issues include noise reduction and control of the recording media grain characteristics[30]. Possibly the most critical of these issues, however, is the lifetime of the NFT. Budaev and Bogy noted that, when thermally modelling NFTs, several assumptions made when using Maxwell's equations to model the interaction of the laser with the NFT are invalid for nanoscale systems[49]. Fourier's law for thermal transport breaks down at the nanoscale, further complicating attempts at predicting the NFT temperature[50]. Additionally, an accurate model must factor in the existence of a very thin layer at the surface, whose thickness is comparable to the mean free path travelled by conduction electrons in one cycle of light oscillations. It is important to factor in the surface of the NFT, as a surface-based process is what relays the energy to the recording layer. In addition to this, the surface is where electromagnetic radiation is first absorbed, and hence plays a significant role in the failure mode of the NFT[49]. By not factoring these considerations, previous predictions for the lifetimes of NFTs were overly optimistic.

The “lollipop” transducer designed by Challener *et al*, for example, had “lifetimes of up to several tens of track recordings”[38]. This is clearly not a viable method for the mass-production of commercial devices. It has been proposed by several sources[49,51,52] that the high power focused onto the NFT causes a large increase in its temperature, which severely reduces the lifetime. Thermal simulations have shown that the increase in temperature is well below that of the melting point of Au[38]. Significant changes in the geometry of a material, however, can occur at power densities well below those required for melting [53]. Continuing with the example of the lollipop transducer, it was noticed that heating caused a protrusion of the NFT towards the recording layer[38]. Simulations have shown that this is a common effect but, due to the length of the protrusion time, it may be compensated for with a thermal fly-height control (TFC)[54]. Perhaps even more significantly, NFTs undergo significant thermal cycling due to the write process; the temperature response is almost on par with the laser on-off times[54] (see Figure 1.4).

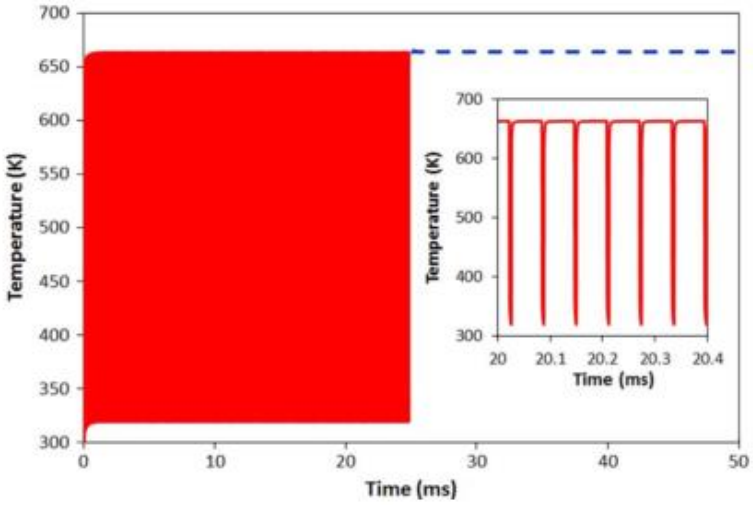

Figure 1.4: Temperature change of the NFT over a time period of 25 ms and (insert) 0.4 ms caused by absorption of laser light during the HAMR process, demonstrating the high degree of thermal cycling occurring. Such thermal cycling will have an effect on the long-term stability of the NFT. Taken from reference[54].

In order to counteract these problems, special care must be put into the design of the transducer. Simulations of a C-aperture NFT (which it is believed can be extrapolated to other NFT designs) have shown that the temperature increase depends on the absorbed power, the size of the NFT, and the spacing between the NFT and the magnetic pole[52]. The relation of absorbed power to temperature increase is somewhat problematic, as the efficiency of the transducer also depends heavily on the absorbed power. This can be

circumvented by choosing transducer materials with a low refractive index *n* and extinction coefficient *k.* Likewise, making the NFT as large as possible helps to disperse the absorbed power better, which leads to a reduction in the temperature increase[52]. While increasing the size of an NFT is relatively simple, the above optical properties may require the development of new, low-loss plasmonic materials, such as metallic alloys, 2-D materials, or semiconductor-based materials[39]. Gold alloys are of particular interest, as they show the best plamonic response and simply require readjusting pre-existing designs. It has been shown that doping Au with Cd can modify its optical properties significantly[55], and other dopants have been demonstrated in NFTs, improving the thermal stability[56].

1.3 Motivation

The motivation behind the work covered in this thesis is to understand the stability of Au nanomaterials under laser irradiation, and to find ways of increasing their stability to aid in the commercialisation of HAMR-written hard-drives. Specifically, thermal issues which occur at relatively low temperatures and over longer timescales are investigated. Laser-induced solid-state dewetting is the main failure mechanism focused on in the thesis, with some additional work on crystalline texturing and grain growth. Au thin films are highly susceptible to solid-state dewetting[57–61] even at low temperatures[62], and any nanoscale device will be even more susceptible to degradation due to the higher surface energy at corners and edges[63]. In addition to solid-state dewetting, Au will also exhibit texturing[57,64] and grain growth[65,66] when annealed, which will have effects on the thermal stability[67] and plasmonic properties[68].

Much of previous work on increasing the thermal stability of NFTs was based on optimizing the NFT design[52,69,70], or by investigating new materials as alternatives to Au[39,71]. This work instead focuses on improving the thermal stability of Au through the use of adhesion and capping layers. There are several advantages to this approach. Firstly, Au demonstrates exceptional resistance to corrosion under normal circumstances[72], making it a more attractive material for industrial applications than Ag[73] (although some of the stabilization methods presented in this thesis could potentially be adapted for Ag or other plasmonic materials). Secondly, the main methods presented here (adhesion and capping layers) simply require 1 or 2 additional material deposition steps, helping to keep the NFT manufacturing process streamlined (a key factor in determining whether an industrial process is cost-effective)[74]. Finally, there is still much to be done on understanding these

stabilization methods. The use of adhesion and capping layers to improve the stability of Au nanomaterials has been previously reported in the literature[75–84]. Only some of this work, however, has focused on optimizing the thickness of these stabilizing layers to ensure either the best stability[81] or optical properties[79,84].

1.4 Thesis overview

In Chapter 2, the theoretical background for the main concepts within the thesis is described. The physical phenomenon of solid-state dewetting is described. Next, optical heating is described, and an equation is derived to evaluate the temperature rise in a thin film irradiated by a continuous wave (CW) laser. Finally, a brief description of noble metal plasmonics is given, and the surface plasmon polariton (SPP) is described.

In Chapter 3, the experimental techniques that are used throughout the subsequent chapters are described. This includes the deposition methods used for sample fabrication, the back-reflected laser signal technique used to quantify the thermal stability of samples, and analytical techniques such as scanning electron microscopy (SEM), atomic force microscopy (AFM), and transmission electron microscopy (TEM).

In Chapter 4, the dynamics of laser-induced solid-state dewetting are studied. The temperature at which solid-state dewetting occurs in Au thin films is elucidated through CCD-thermoreflectance (CCD-TR) measurements, and is compared with the theory outlined in Chapter 2. The time dynamics of solid-state dewetting are studied via the back-reflected laser technique described in Chapter 3, and the effect of film thickness and adhesion on dewetting dynamics is observed. A brief description on the topographical changes in the dewetting films is given. TEM analysis is used to compare the grain growth for Au thin films with and without an adhesion layer. Select-area electron diffraction (SAED) is then used to compare the crystalline texture development for isothermally annealed films and laser-irradiated films. Finally, the development of texture in Au films with an adhesion layer is studied, and the resultant pseudo-biaxial texture is described.

In Chapter 5, the work on adhesion layers in Chapter 4 is built upon, in order to determine the optimal adhesion layer thickness for Au thin films. Au films with varying thickness of Ti adhesion layer are analysed using the back-reflected laser signal technique to determine which thickness results in the highest thermal stability. SEM, X-ray photoelectron spectroscopy (XPS), and TEM analysis are used to determine the physical reason for the

optimal thickness. In addition, the SPP of each film is measured to determine the effect of the adhesion layer on the plasmonic properties. Finally, the above approach is extended to other adhesion layer metals.

In Chapter 6, the optical properties and thermal stability of an AuCu alloy are studied. The specific alloy is introduced, and the reasons for choosing it are outlined. The optical properties of the alloy are measured, and are then used to predict the plasmonic response via the use of 3 different figures of merit. The thermal stability is measured using the back-reflected laser signal technique, and the conditions for material failure are described.

In Chapter 7, the effect of capping layers on laser-induced dewetting is studied. Capping layers of different metal oxides are investigated, and different sputtering-based deposition methods are compared. The thermal stability of each capping layer is studied via the back-reflected laser signal technique, and the irradiated areas are investigated with SEM and AFM. The plasmonic response of each film is compared via the SPP resonance. Finally, the results of Chapters 4, 5, and 7 are compared, and the most stable Au thermo-plasmonic system is proposed.

In Chapter 8, the conclusions from the work presented in this thesis are presented. A summary of the results obtained are given, and ideas for future experiments are outlined.

1.5 Bibliography

(1) Engel, F. K. 1888-1988: A Hundred Years of Magnetic Sound Recording. *J. Audio Eng. Soc.* **1988**, *36* (3), 170–178.

(2) Moore, G. E. Cramming More Components onto Integrated Circuits. *Electronics* **1965**, *38* (8), 114.

(3) Friedman, T. L. Moore's Law Turns 50. *The New York Times*. May 13, 2015, p A27.

(4) Bajarin, T. Moore's Law at 50: What It All Means. *Time*. April 2015.

(5) Sneed, A. Moore's Law Keeps Going, Defying Expectations. *Scientific American*. May 2015.

(6) Walter, C. Kryder's Law. *Sci. Am.* **2005**, *293* (2), 32–33.

(7) Kryder, M. H.; Kim, C. S. After Hard Drives-What Comes Next? In *IEEE Transactions on Magnetics*; 2009; Vol. 45, pp 3406–3413.

(8) ST8000AS0002 Archive v2, 3.5" HDD Flyer - Seagate https://www.seagate.com/www-content/product-content/hdd-fam/seagate-archive-hdd/en-us/docs/archive-hdd-dS1834-3-1411us.pdf (accessed Sep 7, 2018).

(9) StorageReview Enterprise Lab. Seagate Archive HDD Review (8TB) | StorageReview.com - Storage Reviews https://www.storagereview.com/seagate_archive_hdd_review_8tb (accessed Sep 7, 2018).

(10) Will Nicol. The 5 Largest Consumer Hard Drives | Digital Trends https://www.digitaltrends.com/computing/highest-capacity-hard-drives/ (accessed Sep 7, 2018).

(11) Iwasaki, S. Perpendicular Magnetic Recording--Its Development and Realization. *Proc. Jpn. Acad. Ser. B. Phys. Biol. Sci.* **2009**, *85* (2), 37–54.

(12) Victora, R. H.; Khan, M. Micromagnetic Model of Perpendicular Head and Double-Layer Media for 100 Gb/in^2. In *IEEE Transactions on Magnetics*; 2002; Vol. 38, pp 181–185.

(13) Iwasaki, S.; Nakamura, Y. An Analysis for the Magnetization Mode for High Density Magnetic Recording. *IEEE Trans. Magn.* **1977**, *13* (5), 1272–1277.

(14) Varvaro, G.; Casoli, F. *Ultrahigh-Density Magnetic Recording : Storage Materials and Media Designs*.

(15) Khizroev, S.; Litvinov, D. *Perpendicular Magnetic Recording*; Kluwer Academic, 2004.

(16) Fish, G. E. Soft Magnetic Materials. *Proc. IEEE* **1990**, *78* (6), 947–972.

(17) Litvinov, D.; Kryder, M. H.; Khizroev, S. Recording Physics of Perpendicular Media: Soft Underlayers. *J. Magn. Magn. Mater.* **2001**, *232* (1–2), 84–90.

(18) Moser, A.; Takano, K.; Margulies, D. T.; Albrecht, M.; Sonobe, Y.; Ikeda, Y.; Sun, S.; Fullerton, E. E. Magnetic Recording: Advancing into the Future. *J. Phys. D. Appl. Phys.* **2002**, *35* (19), R157–R167.

(19) 2016 ASTC Technology Roadmap | IDEMA http://idema.org/?page_id=5868 (accessed Aug 18, 2018).

(20) Coey, J. M. D. *Magnetism and Magnetic Materials*; Cambridge University Press: Cambridge, 2010.

(21) Challener, W. A.; Gage, E.; Itagi, A.; Peng, C. Optical Transducers for Near Field Recording. *Jpn. J. Appl. Phys.* **2006**, *45* (8B), 6632–6642.

(22) Hu, J. F.; Shi, J. Z.; Zhou, T. J.; Cher, K. M.; Xu, B. X.; Ji, R.; Liu, B. HAMR Medium Structure Design and Its Process for Excellent Thermal Performance. *IEEE Trans. Magn.* **2014**, *50* (3), 96–101.

(23) Yamada, Y.; Suzuki, T.; Kanazawa, H.; Österman, J. C. The Origin of the Large Perpendicular Magnetic Anisotropy in Co_3Pt Alloy Thin Films. *J. Appl. Phys.* **1999**, *85* (8), 5094.

(24) Weller, D.; Moser, A. Thermal Effect Limits in Ultrahigh-Density Magnetic Recording. *IEEE Trans. Magn.* **1999**, *35* (6), 4423–4439.

(25) McDaniel, T. W. Ultimate Limits to Thermally Assisted Magnetic Recording. *J. Phys. Condens. Matter* **2005**, *17* (7), R315–R332.

(26) Wood, R. The Feasibility of Magnetic Recording at 1 Terabit per Square Inch. *IEEE Trans. Magn.* **2000**, *36* (1), 36–42.

(27) Shiroishi, Y.; Fukuda, K.; Tagawa, I.; Iwasaki, H.; Takenoiri, S.; Tanaka, H.; Mutoh, H.; Yoshikawa, N. Future Options for HDD Storage. *IEEE Trans. Magn.* **2009**, *45* (10), 3816–3822.

(28) Richter, H. J.; Dobin, A. Y.; Heinonen, O.; Gao, K. Z.; Veerdonk, R. J. M. V. D.; Lynch, R. T.; Xue, J.; Weller, D.; Asselin, P.; Erden, M. F.; et al. Recording on Bit-Patterned Media at Densities of 1 Tb/In^2 and Beyond. *IEEE Trans. Magn.* **2006**, *42* (10), 2255–2260.

(29) Amer, A.; Holliday, J.; Long, D. D. E.; Miller, E. L.; Pâris, J. F.; Schwarz, T. Data Management and Layout for Shingled Magnetic Recording. In *IEEE Transactions on Magnetics*; 2011; Vol. 47, pp 3691–3697.

(30) Weller, D.; Parker, G.; Mosendz, O.; Champion, E.; Stipe, B.; Wang, X.; Klemmer, T.; Ju, G.; Ajan, A. A HAMR Media Technology Roadmap to an Areal Density of 4 Tb/In^2. *IEEE Trans. Magn.* **2014**, *50* (1), 1–8.

(31) Wang, S.; Wang, Y.; Victora, R. H. Shingled Magnetic Recording on Bit Patterned Media at 10 Tb/In^2. *IEEE Trans. Magn.* **2013**, *49* (7), 3644–3647.

(32) Chen, Y. J.; Leong, S. H.; Xu, B. X.; Yang, H. Z. Challenges and Implementation Approaches of Shingled Heat Assisted Magnetic Recording (HAMR) for 10 Tb/In^2 data Storage. In *MSSC 2014 - Digests of Magnetics Symposium 2014: Celebrating 50 Years of IEEE Magnetics Society*; IEEE, 2014; pp 1–2.

(33) Wang, S.; Ghoreyshi, A.; Victora, R. H. Feasibility of Bit Patterned Media for HAMR at 5 Tb/In^2. *J. Appl. Phys.* **2015**, *117* (17), 17C115.

(34) Vogler, C.; Abert, C.; Bruckner, F.; Suess, D.; Praetorius, D. Heat-Assisted Magnetic Recording of Bit-Patterned Media beyond 10 Tb/In^2. *Appl. Phys. Lett.* **2016**, *108* (10), 102406.

(35) Granz, S.; Zhu, W.; Seng, E. C. S.; Kan, U. H.; Rea, C.; Ju, G.; Thiele, J. U.; Rausch, T.; Gage, E. C. Heat-Assisted Interlaced Magnetic Recording. *IEEE Trans. Magn.* **2018**, *54* (2), 1–4.

(36) Kong, Y.; Chabalko, M.; Black, E. Evanescent Coupling between Dielectric and Plasmonic Waveguides for HAMR Applications. *Magn. IEEE …* **2011**, *47* (10), 2364–2367.

(37) McDaniel, T. W.; Challener, W. A.; Sendur, K. Issues in Heat-Assisted Perpendicular Recording. *IEEE Trans. Magn.* **2003**, *39* (4), 1972–1979.

(38) Challener, W. A.; Peng, C.; Itagi, A. V.; Karns, D.; Peng, W.; Peng, Y.; Yang, X.; Zhu, X.; Gokemeijer, N. J.; Hsia, Y.-T.; et al. Heat-Assisted Magnetic Recording by a near-Field Transducer with Efficient Optical Energy Transfer. *Nat. Photonics* **2009**, *3* (4), 220–224.

(39) Zhou, N.; Xu, X.; Hammack, A. T.; Stipe, B. C.; Gao, K.; Scholz, W.; Gage, E. C. Plasmonic Near-Field Transducer for Heat-Assisted Magnetic Recording. *Nanophotonics* **2014**, *3* (3), 141–155.

(40) Datta, A.; Xu, X. Optical and Thermal Designs of near Field Transducer for Heat Assisted Magnetic Recording. *Jpn. J. Appl. Phys.* **2018**, *57* (9S2), 09TA01.

(41) Kurihara, K.; Nanri, K.; Goto, K. Thermal Simulation for a Two-Dimensional near-Field Optical Recording System Using a Vertical-Cavity Surface-Emitting Laser. *Appl. Phys. Lett.* **2004**, *84* (17), 3415–3417.

(42) Abbe, E. Beiträge Zur Theorie Des Mikroskops Und Der Mikroskopischen Wahrnehmung.

Arch. für Mikroskopische Anat. **1873**, *9* (1), 413–418.

(43) Mansfield, S. M.; Kino, G. S. Solid Immersion Microscope. *Appl. Phys. Lett.* **1990**, *57* (24), 2615–2616.

(44) Shaffer, P. T. B. Refractive Index, Dispersion, and Birefringence of Silicon Carbide Polytypes. *Appl. Opt.* **1971**, *10* (5), 1034.

(45) Li, J.; Yang, C.; Li, J.; Li, Z.; Zu, S.; Song, S.; Zhao, H.; Lin, F.; Zhu, X. Plasmonic Focusing in Nanostructures. *Plasmonics* **2014**, *9* (4), 879–886.

(46) Yang, H.; Li, G.; Su, X.; Cao, G.; Zhao, Z.; Chen, X.; Lu, W. Reflective Metalens with Sub-Diffraction-Limited and Multifunctional Focusing. *Sci. Rep.* **2017**, *7* (1), 12632.

(47) Wang, J.; Zhang, J. Sub-One-Third Wavelength Focusing of Surface Plasmon Polaritons Excited by Linearly Polarized Light. *Opt. Express* **2018**, *26* (11), 14626.

(48) Kryder, M. H.; Gage, E. C.; McDaniel, T. W.; Challener, W. A.; Rottmayer, R. E.; Ju, G.; Hsia, Y.; Erden, M. F. Heat Assisted Magnetic Recording. *Proc. IEEE* **2008**, *96* (11), 1810–1835.

(49) Budaev, B. V.; Bogy, D. B. On the Lifetime of Plasmonic Transducers in Heat Assisted Magnetic Recording. *J. Appl. Phys.* **2012**, *112* (3), 034512.

(50) Bain, J. A.; Malen, J. A.; Jeong, M.; Ganapathy, T. Nanoscale Thermal Transport Aspects of Heat-Assisted Magnetic Recording Devices and Materials. *MRS Bull.* **2018**, *43* (02), 112–118.

(51) Xu, B. X.; Liu, Z. J.; Ji, R.; Toh, Y. T.; Hu, J. F.; Li, J. M.; Zhang, J.; Ye, K. D.; Chia, C. W. Thermal Issues and Their Effects on Heat-Assisted Magnetic Recording System (Invited). *J. Appl. Phys.* **2012**, *111* (7), 07B701.

(52) Xu, B.; Toh, Y. T.; Chia, C. W.; Li, J.; Zhang, J.; Ye, K.; An, C. Relationship Between Near Field Optical Transducer Laser Absorption and Its Efficiency. *IEEE Trans. Magn.* **2012**, *48* (5), 1789–1793.

(53) Inasawa, S.; Sugiyama, M.; Yamaguchi, Y. Laser-Induced Shape Transformation of Gold Nanoparticles below the Melting Point: The Effect of Surface Melting. *J. Phys. Chem. B* **2005**, *109* (8), 3104–3111.

(54) Xu, B.; Li, J.; Toh, Y. T.; Ye, K.; Zhang, J. Dynamic Thermal Responses of Heat-Assisted Magnetic Recording Head in Data Writing Process. *IEEE Trans. Magn.* **2012**, *48* (11), 3280–3283.

(55) Bobb, D. A.; Zhu, G.; Mayy, M.; Gavrilenko, A. V.; Mead, P.; Gavrilenko, V. I.; Noginov,

M. A. Engineering of Low-Loss Metal for Nanoplasmonic and Metamaterials Applications. *Appl. Phys. Lett.* **2009**, *95* (15), 151102.

(56) Zhao, T.; Kautzky, M.; Channeler, W.; Seigler, M. a. HAMR NFT Materials With Improved Thermal Stability, August 25, 2011.

(57) Müller, C. M.; Spolenak, R. Microstructure Evolution during Dewetting in Thin Au Films. *Acta Mater.* **2010**, *58* (18), 6035–6045.

(58) Shaffir, E.; Kauffmann, Y.; Riess, I. Void Formation in Gold Films on Yttrium-Doped Zirconia in the Initial Stage of Dewetting. *Acta Mater.* **2014**, *79*, 59–65.

(59) Seguini, G.; Curi, J. L.; Spiga, S.; Tallarida, G.; Wiemer, C.; Perego, M. Solid-State Dewetting of Ultra-Thin Au Films on SiO_2 and HfO_2. *Nanotechnology* **2014**, *25* (49), 495603.

(60) Lee, S.-H.; Kwak, E.-H.; Jeong, G.-H. Dewetting Behavior of Electron-Beam-Deposited Au Thin Films on Various Substrates: Graphenes, Quartz, and SiO2 Wafers. *Appl. Phys. A* **2015**, *118* (2), 389–396.

(61) Niekiel, F.; Schweizer, P.; Kraschewski, S. M.; Butz, B.; Spiecker, E. The Process of Solid-State Dewetting of Au Thin Films Studied by in Situ Scanning Transmission Electron Microscopy. *Acta Mater.* **2015**, *90*, 118–132.

(62) Abbott, W. M.; Corbett, S.; Cunningham, G.; Petford-Long, A.; Zhang, S.; Donegan, J. F.; McCloskey, D. Solid State Dewetting of Thin Plasmonic Films under Focused Cw-Laser Irradiation. *Acta Mater.* **2018**, *145*, 210–219.

(63) Viarbitskaya, S.; Cuche, A.; Teulle, A.; Sharma, J.; Girard, C.; Arbouet, A.; Dujardin, E. Plasmonic Hot Printing in Gold Nanoprisms. *ACS Photonics* **2015**, *2* (6), 744–751.

(64) Niekiel, F.; Kraschewski, S. M.; Schweizer, P.; Butz, B.; Spiecker, E. Texture Evolution and Microstructural Changes during Solid-State Dewetting: A Correlative Study by Complementary in Situ TEM Techniques. *Acta Mater.* **2016**, *115*, 230–241.

(65) Thompson, C. V. Grain Growth in Thin Films. *Annu. Rev. Mater. Sci.* **1990**, *20* (1), 245–268.

(66) Prószynski, A., Chocyk, D., & Gładyszewski, G. Stress Modification in Gold Metal Thin Films during Thermal Annealing. *Opt. Appl.* **2009**, *39* (4), 705–710.

(67) Marzbanrad, E.; Rivers, G.; Peng, P.; Zhao, B.; Zhou, N. Y. How Morphology and Surface Crystal Texture Affect Thermal Stability of a Metallic Nanoparticle: The Case of Silver Nanobelts and Pentagonal Silver Nanowires. *Phys. Chem. Chem. Phys.* **2015**, *17* (1), 315–324.

(68) Huang, J.-S.; Callegari, V.; Geisler, P.; Brüning, C.; Kern, J.; Prangsma, J. C.; Wu, X.; Feichtner, T.; Ziegler, J.; Weinmann, P.; et al. Atomically Flat Single-Crystalline Gold Nanostructures for Plasmonic Nanocircuitry. *Nat. Commun.* **2010**, *1* (9), 150.

(69) Abadía, N.; Bello, F.; Zhong, C.; Flanigan, P.; McCloskey, D. M.; Wolf, C.; Krichevsky, A.; Wolf, D.; Zong, F.; Samani, A.; et al. Optical and Thermal Analysis of the Light-Heat Conversion Process Employing an Antenna-Based Hybrid Plasmonic Waveguide for HAMR. *Opt. Express* **2018**, *26* (2), 1752–1765.

(70) Zhong, C.; Flanigan, P.; Abadía, N.; Bello, F.; Jennings, B. D.; Atcheson, G.; Li, J.; Zheng, J.-Y.; Wang, J. J.; Hobbs, R.; et al. Effective Heat Dissipation in an Adiabatic Near-Field Transducer for HAMR. *Opt. Express* **2018**, *26* (15), 18842.

(71) Wells, M. P.; Bower, R.; Kilmurray, R.; Zou, B.; Mihai, A. P.; Gobalakrichenane, G.; Alford, N. M.; Oulton, R. F. M.; Cohen, L. F.; Maier, S. A.; et al. Temperature Stability of Thin Film Refractory Plasmonic Materials. *Opt. Express* **2018**, *26* (12), 15726.

(72) Hammer, B.; Norskov, J. K. Why Gold Is the Noblest of All the Metals. *Nature* **1995**, *376* (6537), 238–240.

(73) Frey, T.; Kögel, M. Tarnish Protection of Silver Jewels by Plasmapolymer Coatings. *Surf. Coatings Technol.* **2003**, *174–175*, 902–904.

(74) Liddle, J. A.; Gallatin, G. M. Nanomanufacturing: A Perspective. *ACS Nano*. American Chemical Society March 22, 2016, pp 2995–3014.

(75) Todeschini, M.; Bastos da Silva Fanta, A.; Jensen, F.; Wagner, J. B.; Han, A. Influence of Ti and Cr Adhesion Layers on Ultrathin Au Films. *ACS Appl. Mater. Interfaces* **2017**, *9* (42), acsami.7b10136.

(76) Martinez, W. E.; Gregori, G.; Mates, T. Titanium Diffusion in Gold Thin Films. *Thin Solid Films* **2010**, *518* (10), 2585–2591.

(77) Masahiro, K.; Noboru, S. Effects of Temperature, Thickness and Atmosphere on Mixing in Au-Ti Bilayer Thin Films. *J. Mater. Sci.* **1993**, *28* (18), 5088–5091.

(78) Nagata, H.; Shinriki, T.; Shima, K.; Tamai, M.; Haga, E. M. Improvement of Bonding Strength between Au/Ti and SiO_2 Films by Si Layer Insertion. *J. Vac. Sci. Technol. A Vacuum, Surfaces, Film.* **1999**, *17* (3), 1018.

(79) Habteyes, T. G.; Dhuey, S.; Wood, E.; Gargas, D.; Cabrini, S.; Schuck, P. J.; Alivisatos, A. P.; Leone, S. R. Metallic Adhesion Layer Induced Plasmon Damping and Molecular Linker as a Nondamping Alternative. *ACS Nano* **2012**, *6* (6), 5702–5709.

(80) Cao, P.; Bai, P.; Omrani, A. A.; Xiao, Y.; Meaker, K. L.; Tsai, H. Z.; Yan, A.; Jung, H. S.;

Khajeh, R.; Rodgers, G. F.; et al. Preventing Thin Film Dewetting via Graphene Capping. *Adv. Mater.* **2017**, *29* (36), 1701536.

(81) Albrecht, G.; Kaiser, S.; Giessen, H.; Hentschel, M. Refractory Plasmonics without Refractory Materials. *Nano Lett.* **2017**, *17* (10), 6402–6408.

(82) Kosinova, A.; Wang, D.; Baradács, E.; Parditka, B.; Kups, T.; Klinger, L.; Erdélyi, Z.; Schaaf, P.; Rabkin, E. Tuning the Nanoscale Morphology and Optical Properties of Porous Gold Nanoparticles by Surface Passivation and Annealing. *Acta Mater.* **2017**, *127*, 108–116.

(83) Gao, L.; Chen, L.; Wei, H.; Xu, H. Lithographically Fabricated Gold Nanowire Waveguides for Plasmonic Routers and Logic Gates. *Nanoscale* **2018**.

(84) Debu, D. T.; Ghosh, P. K.; French, D.; Herzog, J. B. Surface Plasmon Damping Effects Due to Ti Adhesion Layer in Individual Gold Nanodisks. *Opt. Mater. Express* **2017**, *7* (1), 73–84.

Chapter 2: Theory of laser-induced heating and solid-state dewetting

In this chapter, the theoretical background for laser-induced heating within a thin metallic film and solid-state dewetting are discussed. The properties of Au, including its optical and mechanical properties, are discussed. A review of solid-state dewetting is then given, detailing its causes, its dependent parameters, and its applications. The equation for the temperature profile on the surface of a thin metallic film under Gaussian illumination with a CW laser is derived. Finally, a brief description of plasmonics, and a theoretical description of a surface plasmon is stated.

2.1 Properties of Gold

Gold (Au) has been a highly prized material since antiquity[1], and it has maintained this enviable status into the modern age, especially in regards to industrial applications. Due to a combination of high electrical conductivity, ease of deposition, and resistance to corrosion[2], Au is a popular candidate for use in a variety of applications.

In order to understand the origin of the macroscopic properties of Au, it is necessary to know its atomic properties. Au has an atomic number of 79 and its only stable isotope has a mass number of 197[3]. The band-structure of Au is quite different from other transition metal elements, and goes some way towards explaining its unique properties (see Figure 2.1). Au has the electronic configuration $[Xe]\ 4f^{14}\ 5d^{10}\ 6s^{1}$. The $6s^1$ electron forms a hybridized sp band, which has a near-parabolic shape, resulting in nearly-free electron behaviour[4]. Due to relativistic effects, the energy of the $6s^1$ orbital in Au is contracted, resulting in it becoming closer in energy to that of the 5d orbitals. Neglecting this effect in calculations will give an incorrect band-structure[5]. This results in the ability of Au to absorb incoming blue light; the remaining wavelengths add up to give Au's distinct lustre. This energetic contraction is also responsible for Au's famous chemical stability; it requires a very strong oxidizing agent to take away the lone $6s^1$ electron (a first ionization potential of 9.225 eV[3]). Interestingly, this is also partly responsible for another famous property of Au: its malleability. Due to the absence of an oxide layer, dislocations are

capable of escaping from the metal as it is being beaten into a thin foil, hence allowing it to be beaten into a thinner foil than other metals[6]. Despite this, Au is a relatively soft metal with a Young's modulus of 79 GPa (compared with a value of 200 GPa for steel)[7].

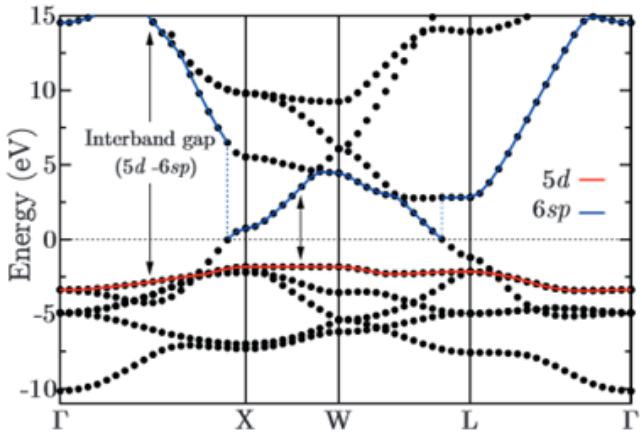

Figure 2.1: bandstructure of Au. Taken from reference [8]

The optical properties of Au in the visible regime (i.e. 400 - 700 nm) cannot be accurately described through the Drude model, as such a model does not account for the interband transitions which play a large role in the optical properties[9]. At least 2 such transitions occur in the near-UV/visible range (at ~330 nm and ~470 nm), and in order to account for these, it is necessary to alter the Drude model as:

$$\varepsilon(\omega) = \varepsilon_{\infty} - \frac{\omega_p^2}{\omega^2 + i\gamma\omega} + G_1(\omega) + G_2(\omega) \qquad (2.1)$$

where G_1 and G_2 represent the interband transitions[9] (a derivation of the general Drude model is given in section 2.4). The n, k, ε_1 and ε_2 values for Au in the visible regime are displayed in Figure 2.2. Due to these unique optical properties, Au is capable of supporting surface plasmons (SPs)[10]. Plasmonics will be discussed further in section 2.4.

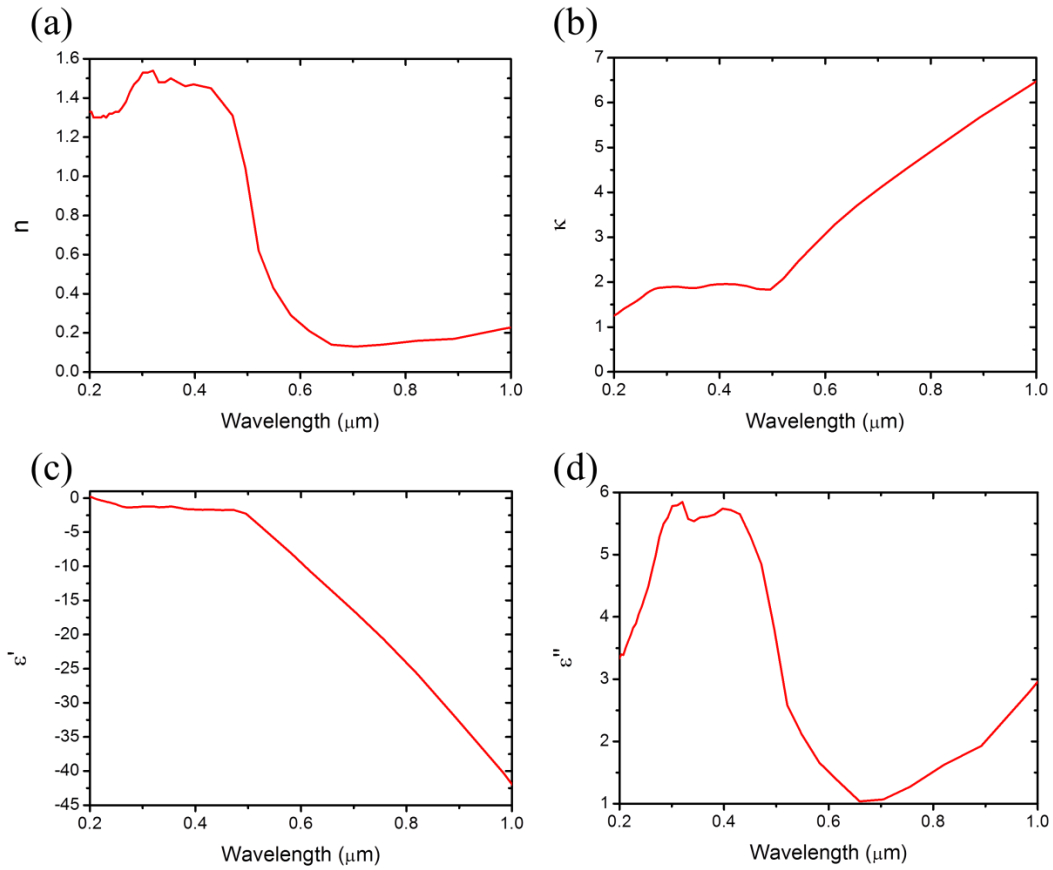

Figure 2.2: optical properties of Au in range 0.2 - 1 μm: (a) n, (b) κ, (c) ε', and (d) ε''. Values taken from reference [11]

2.2 Solid-state dewetting

2.2.1 Energetic considerations of surface wetting

Thin films can be considered meta-stable structures, i.e. the configuration is not the most stable, but is significantly more stable than other configurations. Solid-state dewetting is a process by which a meta-stable thin solid film will begin to agglomerate in order to reduce its surface energy[12].

Much of our current understanding on the wettability of surfaces comes from the work of Thomas Young at the start of the 19th century[13]. The energetics of wetting can be demonstrated by simply considering a single droplet of a liquid on a solid surface within a gaseous/vapour atmosphere. Such a system is displayed in Figure 2.3. There are 3 different types of interface within this system, each with its own associated interfacial energy: the liquid-vapour interface (γ_{LV}), the solid-vapour interface (γ_{SV}), and the solid-liquid interface (γ_{SL}).

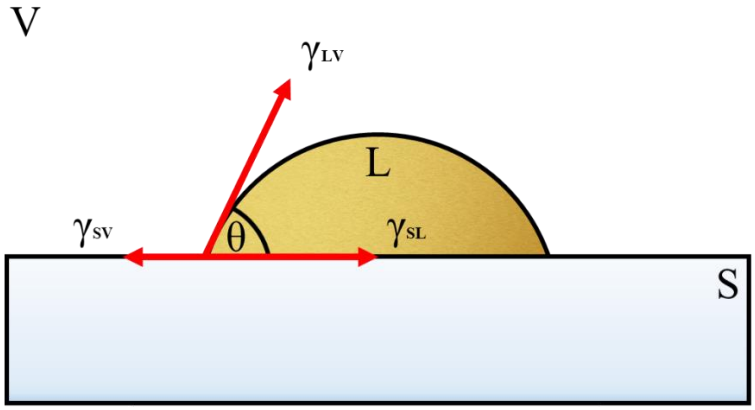

Figure 2.3: demonstration of the energetic considerations of wetting for a liquid drop (L) on a solid surface (S) under vapour (V). The specific case shown is an example of partial wetting (0° < ϑ < 90°). Adapted from reference [14].

Young discovered that the contact angle θ made by the droplet would depend on γ_{LV}, γ_{SV}, and γ_{SL}. At equilibrium, this can be expressed by the equation[14]:

$$\cos\theta = \frac{\gamma_{SV} - \gamma_{SL}}{\gamma_{LV}} \tag{2.2}$$

Generally when discussing the adhesion between 2 materials, the interfacial energy (in this case) is rarely used; instead, the work of adhesion is considered. This is defined as;

$$W_a = (\gamma_{SV} + \gamma_{LV}) - \gamma_{SL} \tag{2.3}$$

By combining equations (2.2) and (2.3), the Young-Dupree equation is obtained;

$$W_a = \gamma_{LV}(1 + \cos\theta) \tag{2.4}$$

As the value for γ_{LV} can be elucidated by other measurements[15], a measurement of θ will give information about the adhesion strength between a film and its substrate. For liquids, θ is normally measured using the sessile drop technique[16]. For the case of measuring W_a between a metal and its substrate, measuring θ may be difficult as thicker films will wet a substrate better. In order to counteract this, it is possible to anneal the sample in order to induce dewetting, and then measure θ[17]. In order to account for the change in value for γ_{LV} from the increase in temperature, the following relation must be used:

$$\gamma_{LV}(T) = \gamma_{LV}(T_0) + (T - T)\left(\frac{\partial \gamma_{LV}}{\partial T}\right)_{T=T_0} \quad (2.5)$$

where $\gamma_{LV}(T)$ and $\gamma_{LV}(T_0)$ are the surface energies of the material at the annealing temperature and the original temperature, respectively[17]. The large (≥ 140°) contact angles of Au on ceramic substrates demonstrate its poor adhesion to such materials[18].

2.2.2 Time dynamics of solid-state dewetting

The above analysis of film adhesion and wettability is only valid for systems in equilibrium: hence additional understanding is required when discussing the process of dewetting as it is occurring. For a polycrystalline film, dewetting will initiate at areas of high surface energy: mainly grain boundaries, triple points (where 3 or more grains meet)[19], or at the film-substrate interface. In Figure 2.4, the occurrence of dewetting at a grain boundary is shown schematically. In order to reduce their surface energy, atoms at the grain boundary will diffuse by capillary action away from the grain boundary. This results in mass transportation to the surface of the film with an increase in the height of the film close to the grain boundary. This phenomenon is known as grain-boundary grooving. The process will continue, eventually resulting in the substrate becoming exposed through a void in the now-discontinuous film. If given enough time, the film will eventually agglomerate into defined individual nanoparticles (as a sphere will have the lowest surface to volume ratio, and hence the lowest surface energy).

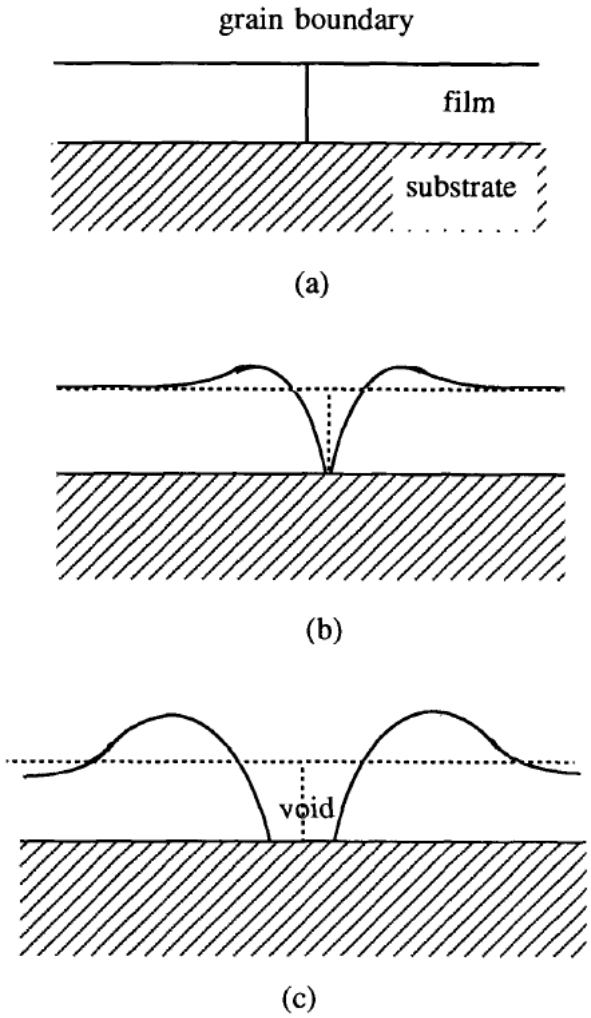

Figure 2.4: schematic diagram detailing the process of solid-state dewetting. (a) film in its initial, continuous state, (b) onset of dewetting, exhibiting grain-boundary grooving, (c) void formation within the film. Taken from reference[19].

In order to mathematically describe the process of grain boundary grooving, the net flux of atoms, j_s, away from the film edge must be considered, as this is the driving force behind the retraction of the crystal grain edge. This is described by the equation[20]:

$$j_s = \frac{-D_s}{kT}\frac{\partial u}{\partial s}v \tag{2.6}$$

where D_s is the surface diffusivity, $\partial\mu/\partial s$ is the change in chemical potential μ over an element of arc length s, and v is the surface concentration of atoms. If the in-plane curvature of the retracting edge r is taken as being larger than the film thickness h, $\partial\mu/\partial s$ can be approximated as[19]:

$$\frac{\partial \mu}{\partial s} \approx \frac{\Delta \mu}{\Delta s} = -\frac{2\Omega \gamma_s}{\pi h^2} \tag{2.7}$$

where Ω is the atomic volume and γ_s is the surface tension. The flux of atoms from the edge will result in a volume transfer V, the rate of which is given by[19]:

$$\frac{dV}{dt} = j_s \ell \Omega = \ell \frac{D_s}{kT} \frac{2\Omega^2 \gamma_s}{\pi h^2} \nu \tag{2.8}$$

where *l* is the total length of the interface. The rate of the edge contraction u can then be described as[19]:

$$u = \frac{dx}{dt} = \frac{1}{h\ell} \frac{dV}{dt} = \frac{D_s}{kT} \frac{2\Omega^2 \gamma_s}{\pi h^3} \nu \tag{2.9}$$

By substituting for D_s the general equation for the diffusion Arrhenius equation[21], the rate of dewetting can be described by the equation[19]:

$$u = \frac{D_0}{kT} \frac{2\nu\Omega^2 \gamma_s \exp(-\frac{Q}{kT})}{\pi h^3} = \frac{\beta \exp(-\frac{Q}{kT})}{kTh^3} \tag{2.10}$$

where where β is the surface diffusion term, and Q is the activation energy for diffusion[22]. β will depend on the diffusion characteristics and the surface energy of the film, whereas Q will depend on the material properties, grain boundaries per unit volume and the surface energy[23]. Hence, the controllable parameters determining at what rate a thin film will dewet are the film thickness and the temperature. Higher temperatures will result in faster rates of dewetting; similarly, thinner films will dewet at a faster rate. The rate of dewetting is generally found by measuring the growth rate of the voids once the dewetting process has started. This is due to the difficultly in separating the onset grain boundary grooving from the surface roughness. The rate can be measured using either *ex-situ* (by measuring the ratio of dewetted to non-dewetted areas in the film at specific annealing steps[24]) or *in-situ* (by measuring the light transmission of the film as a function of time[22]).

2.2.3 Applications of dewetting

Within this thesis, all results pertaining towards solid-state dewetting are based on its prevention. It must be noted, however, that there is a significant amount of work in the

literature where it is utilized in a positive way, mainly for the fabrication of nanoparticle arrays[12,25]. Due to the poor adhesion of plasmonic metals on ceramic substrates[26], annealing can consistently result in nanoparticles for use as plasmonic transducers[27,28] or nanoparticle array films for applications such as surface-enhanced Raman spectroscopy (SERS)[29,30]. The spacing between the nanoparticles, however, will likely be inconsistent due to the semi-random nature of where dewetting will initiate. Work in the literature has focused on solving this issue. One solution involves the use of templates (see Figure 2.5); the dewetting of the deposited film will be constricted by either the substrate[31,32] or the deposited film[33,34], resulting in well-defined particle arrays. In addition to forming elemental particle alloys, solid-state dewetting can also be used in the production of alloyed nanoparticles, by depositing the constituent parts as a multilayer and then annealing[31,35,36].

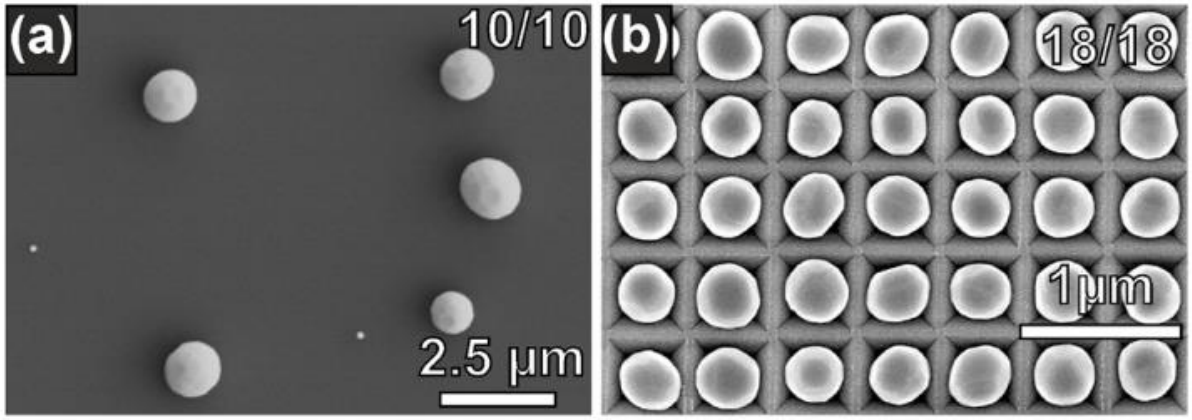

Figure 2.5: comparison of solid-state dewetting on a flat substrate (a) and a patterned substrate (b). Original film was an Au/Ni bilayer. Taken from reference[31].

2.2.4. Solid-state dewetting of Au under isothermal annealing

Au is a popular material for both fundamental and applications-based studies of solid-state dewetting[19,22,24,26,28,30,32–34,37–51] for several reasons. Its high resistance towards corrosion allows the process to be studied without needing to protect the system from oxidation, which is necessary for studies on the dewetting behaviour of Al[52]. Au also adheres poorly with common substrates (such as SiO_2)[26] requiring lower temperatures for experiments: sufficiently thin films (in the case of Au on SiO_2: $\leq$ 15 nm[51]) will dewet spontaneously at room temperature[49] (see Figure 2.6). From the perspective of applications, solid-state dewetting of Au is a simple and effective way of fabricating plasmonic arrays for applications such as SERS or nanofocusing[28,30].

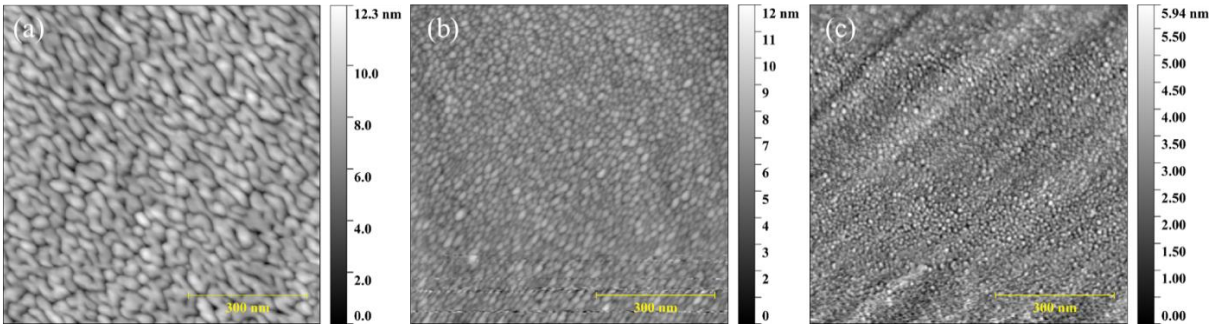

Figure 2.6: As-deposited Au films of initial thickness (a) 5 nm, (b) 2 nm, and (c) 1 nm, all of which have undergone solid-state dewetting to some extent at room temperature.

2.3 Laser heating of a metallic thin film

Within this work, CW-laser heating is regularly used to test the stability of plasmonic thin films against dewetting. Hence, it is crucial to understand the temperature rises expected when using this as a heat source.

As a simple model system, the following system is considered: the steady state temperature rise in the geometry of a thin metal film on a dielectric substrate, heated by a focused Gaussian laser beam (as shown in Figure 2.7).

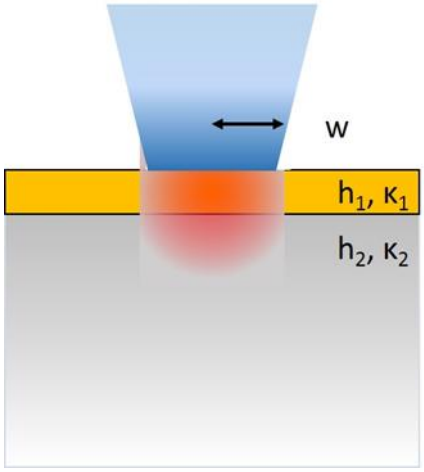

Figure 2.7: schematic diagram of a laser, with beam waist w, heating a thin film (thickness h_1, thermal conductivity κ_1) on a substrate (thickness h_2, thermal conductivity κ_2)

The temperature rise in this case has an analytical form written in terms of an integral which can be found using a Green's function approach[53]. The maximum temperature rise at the surface of the film in the center of the Gaussian illumination is given by:

$$\Delta T_{DC}(0,0) = \frac{P_{abs}}{2\pi\omega_0\kappa_1}\int_0^\infty du\left[\frac{e^{-u^2/4}(\kappa^*-1)e^{-uh_1^*}}{\kappa^*\sinh(uh_1^*)+\cosh(uh_1^*)}\right] \tag{2.11}$$

where P_{abs} is the absorbed optical power, ω_0 the beam waist, κ_1 (κ_2) the thermal conductivity of the thin film (substrate), $\kappa^* = \kappa_{1/}\,\kappa_2$, and *u* is the integration variable. The heating in a simple half space under Gaussian illumination can be written as [53];

$$\Delta T^* = \frac{P_{abs}}{2\kappa_2\omega_0\sqrt{\pi}} \tag{2.12}$$

This simplification treats the thin film as infinitely thin, the substrate as infinitely thick, and doesn't factor in the thermal spreading that will occur in a non-negligible film thickness, as shown in Figure 2.7. By factoring in the film thickness, the following equation is obtained:

$$\Delta T = \frac{\Delta T^*}{\left(1+\frac{2h_1\kappa_1}{\omega_0\kappa_2}\right)} \tag{2.13}$$

which, when combined with equation 2.12, can be written in the form;

$$\Delta T = \frac{P_{abs}}{2\kappa_2\omega_0\sqrt{\pi}}\frac{1}{\left(1+\frac{2h_1\kappa_1}{\omega_0\kappa_2}\right)}$$

$$= \frac{P_{abs}}{2\bar{\kappa}\omega_0\sqrt{\pi}} \tag{2.14}$$

where $\bar{\kappa} = \kappa_2 + 2(h_1/\omega_0)\kappa_1$. From this equation, it can be seen that the temperature the film reaches depends heavily on the thermal conductivity of the substrate and the ratio of the film thickness to the beam waist. This is particularly significant for Au thin films, where

SiO_2 (a poor thermal conductor[54]) is commonly used as a substrate[55–57], and the Au thickness is regularly 50 nm and below for plasmonic applications[56,58–61].

2.4 Plasmonics

The field of plasmonics has developed significantly within the last decade[62–64]. The origin of plasmonic study is regularly credited to Gustav Mie, who explained the optical properties of Au nanoparticles in 1908[65]. Once a photon couples with a SP, a surface plasmon polariton (SPP) is generated, which propagates along the surface of the metal until energy is lost via radiation or absorption by the metal. In order to describe this phenomenon, it is necessary to consider separately the electrons on metal surface, and the electromagnetic wave propagating along the metal surface. First, for the electrons on the metal surface, a semi-classical approach is required. In the plasma model, the valence electrons of metals govern their optical properties. These electrons act as a gas with number density n moving against a fixed background of positive ion cores. When an electric field E is applied, the electrons oscillate. Their oscillations are damped via collisions, which occur with frequency;

$$\gamma = \frac{1}{\tau} \tag{2.15}$$

where τ is the relaxation time of the free electron gas. The motion of a single electron in the free electron gas/plasma can then be described by the equation;

$$m\ddot{x} + m\dot{x}\gamma = -eE \tag{2.16}$$

where m is the electron mass, and x is the position of the electron. By assuming a harmonic time dependence of E (i.e. $E(t) = E_0 e^{-i\omega t}$), then $x(t) = x_0 e^{-i\omega t}$ is a solution for equation (2.16). x_0 incorporates any phase shifts between driving field and response, via;

$$x(t) = \frac{e}{m(\omega^2 + i\gamma\omega)} E(t) \tag{2.17}$$

where ω is the frequency. Electrons that have been displaced then contribute to the macroscopic polarisation P (= -nex), hence;

$$P = \frac{-ne^2}{m(\omega^2 + i\gamma\omega)} E \tag{2.18}$$

By substituting equation (2.18) into the formula for dielectric displacement ($D = \varepsilon_0 E + P$);

$$D = \varepsilon_0 (1 - \frac{\omega_p^2}{\omega^2 + i\gamma\omega}) E \tag{2.19}$$

where $\omega_p^2 = ne^2/\varepsilon_0 m$ is the plasma frequency of the electron gas. From this, the dielectric function of the free electron gas is obtained[66];

$$\varepsilon(\omega) = 1 - \frac{\omega_p^2}{\omega^2 + i\gamma\omega} \tag{2.20}$$

Next, the electromagnetic field propagating along the surface of the metal is considered. This can be done classically by considering 2 semi-infinite non-magnetic media with local dielectric functions ε_1 and ε_2 separated at z = 0. The full set of Maxwell's equations (in the absence of external sources) can then be expressed as;

$$\nabla \times H_j = \varepsilon_j \frac{1}{c} \frac{\partial}{\partial t} E_j \tag{2.21}$$

$$\nabla \times E_j = -\frac{1}{c} \frac{\partial}{\partial t} H_j \tag{2.22}$$

$$\nabla \cdot (\varepsilon_j E_j) = 0 \tag{2.23}$$

$$\nabla \cdot H_j = 0 \tag{2.24}$$

Solutions to these equations can be classified as being either s-polarized (E is parallel to the interface) or p-polarized (H is parallel). As it is necessary for a component of E to be normal to the surface so that waves can be formed and propagate along the surface, only p-polarized oscillations occur. Hence, by taking a wave that only propagates in the x-direction, the following wave components are obtained;

$$E_j = (E_{jx}, 0, E_{jz}) e^{-\kappa_j |z|} e^{i(q_j x - \omega t)} \tag{2.25}$$

$$H_j = (0, E_{jy}, 0) e^{-\kappa_j |z|} e^{i(q_j x - \omega t)} \tag{2.26}$$

where q_j represents the wave vector magnitude. By applying Maxwell's equations:

$$i\kappa_1 H_{1y} = \frac{\omega}{c} \varepsilon_1 E_{1x} \tag{2.27}$$

$$i\kappa_2 H_{2y} = -\frac{\omega}{c} \varepsilon_2 E_{2x} \tag{2.28}$$

$$\kappa_j = \sqrt{q_j^2 - \varepsilon_j \frac{\omega^2}{c^2}} \tag{2.29}$$

Due to the boundary conditions, the E and H components parallel to the surface must be continuous. Hence, from equations (2.27) and (2.28);

$$\frac{\kappa_1}{\varepsilon_1} H_{1y} + \frac{\kappa_2}{\varepsilon_2} H_{2y} = 0 \tag{2.30}$$

$$H_{1y} - H_{2y} = 0 \tag{2.31}$$

This only has a solution when the determinant is zero, thus;

$$\frac{\varepsilon_1}{\kappa_1} + \frac{\varepsilon_2}{\kappa_2} = 0 \tag{2.32}$$

Also because of the boundary conditions, q_j must be continuous. Thus, by combining equations (2.29) and (2.32);

$$q(\omega) = \frac{\omega}{c} \sqrt{\frac{\varepsilon_1 \varepsilon_2}{\varepsilon_1 + \varepsilon_2}} \tag{2.33}$$

This is the surface plasmon condition. In order for $q(\omega)$ to be real, ε_2 must be (a) < 0, and (b) $|\varepsilon_2| > 0$. Hence, by combining equations (2.20) and (2.33), the (SP) frequency can be formulated[66]:

$$\omega_{sp} = \frac{\omega_p}{\sqrt{1 + \varepsilon_2}} \tag{2.34}$$

2.5 Conclusions

In this chapter, the theoretical background behind the main concepts in this thesis is discussed. The heating of thin films via a CW-laser heat source is first discussed, and an equation to evaluate the maximum temperature increase is derived. The theory behind solid-state dewetting is discussed, including the energetic considerations of wettability, and the parameters which effect the rate at which dewetting occurs. Finally, the theory behind surface plasmon polaritons is discussed, and the frequency of the surface plasmon is derived.

2.6 Bibliography

(1) Ogden, J. Gold in Antiquity. *Interdiscip. Sci. Rev.* **1992**, *17* (3), 261–270.

(2) Russell, R. F. Gold in Hybrid Microelectronics. *Gold Bull.* **1974**, *7* (2), 30–34.

(3) Schmidbaur, H.; Cronje, S.; Djordjevic, B.; Schuster, O. Understanding Gold Chemistry through Relativity. *Chem. Phys.* **2005**, *311* (1–2), 151–161.

(4) Urban, A. S. Optothermal Manipulation of Phospholipid Membranes with Gold Nanoparticles, Ludwig-Maximilians-Universitat Munchen, 2010.

(5) Christensen, N. E.; Seraphin, B. O. Relativistic Band Calculation and the Optical Properties of Gold. *Phys. Rev. B* **1971**, *4* (10), 3321–3344.

(6) Nutting, J.; Nuttall, J. L. The Malleability of Gold. *Gold Bull.* **1977**, *10* (1), 2–8.

(7) Kelly, P. F. *Properties of Materials*; 2015.

(8) Rangel, T.; Kecik, D.; Trevisanutto, P. E.; Rignanese, G.-M.; Van Swygenhoven, H.; Olevano, V. Band Structure of Gold from Many-Body Perturbation Theory. *Phys. Rev. B* **2012**, *86* (12), 125125.

(9) Etchegoin, P. G.; Le Ru, E. C.; Meyer, M. An Analytic Model for the Optical Properties of Gold. *J. Chem. Phys.* **2006**, *125* (16), 164705.

(10) Stockman, M. I. Nanoplasmonics: Past, Present, and Glimpse into Future. *Opt. Express* **2011**, *19* (22), 22029.

(11) Johnson, P. B.; Christy, R. W. Optical Constants of the Noble Metals. *Phys. Rev. B* **1972**, *6* (12), 4370–4379.

(12) Thompson, C. V. Solid-State Dewetting of Thin Films. *Annu. Rev. Mater. Res.* **2012**, *42* (1), 399–434.

(13) Young, T. An Essay on the Cohesion of Fluids. *Philos. Trans. R. Soc. London* **1805**, *95* (0), 65–87.

(14) Kaplan, W. D.; Chatain, D.; Wynblatt, P.; Carter, W. C. A Review of Wetting versus Adsorption, Complexions, and Related Phenomena: The Rosetta Stone of Wetting. *J. Mater. Sci.* **2013**, *48* (17), 5681–5717.

(15) De Gennes, P. G. Wetting: Statics and Dynamics. *Rev. Mod. Phys.* **1985**, *57* (3), 827–863.

(16) Lin, S.; Chang, H.; Lin, L.; Huang, P. Measurement of Dynamic/Advancing/Receding Contact Angle by Video-enhanced Sessile Drop Tensiometry. *Rev. Sci. Instrum.* **1996**, *67* (8), 2852–2858.

(17) Gadre, K. S.; Alford, T. L. Contact Angle Measurements for Adhesion Energy Evaluation of Silver and Copper Films on Parylene-n and SiO_2 Substrates. *J. Appl. Phys.* **2003**, *93*, 919–923.

(18) Ricci, E.; Novakovic, R. Wetting and Surface Tension Measurements on Gold Alloys. *Gold Bull.* **2001**, *34* (2), 41–49.

(19) Jiran, E.; Thompson, C. V. Capillary Instabilities in Thin Films. *J. Electron. Mater.* **1990**, *19* (11), 1153–1160.

(20) Mullins, W. W. Theory of Thermal Grooving. *J. Appl. Phys.* **1957**, *28* (3), 333–339.

(21) R. Welty, J.; E. Wicks, C.; E. Wilson, R.; Rorrer, G. *Fundamentals of Momentum, Heat and Mass Transfer*; 1970; Vol. 13.

(22) Jiran, E.; Thompson, C. V. Capillary Instabilities in Thin, Continuous Films. *Thin Solid Films* **1992**, *208* (1), 23–28.

(23) Manuela Müller, C.; Spolenak, R. Dewetting of Au and AuPt Alloy Films: A Dewetting Zone Model. *J. Appl. Phys.* **2013**, *113* (9), 094301.

(24) Niekiel, F.; Schweizer, P.; Kraschewski, S. M.; Butz, B.; Spiecker, E. The Process of Solid-State Dewetting of Au Thin Films Studied by in Situ Scanning Transmission Electron Microscopy. *Acta Mater.* **2015**, *90*, 118–132.

(25) Kracker, M.; Wisniewski, W.; Rüssel, C. Textures of Au, Pt and Pd/PdO Nanoparticles Thermally Dewetted from Thin Metal Layers on Fused Silica. *RSC Adv.* **2014**, *4* (89), 48135–48143.

(26) Lee, S.-H. H.; Kwak, E.-H. H.; Jeong, G.-H. H. Dewetting Behavior of Electron-Beam-Deposited Au Thin Films on Various Substrates: Graphenes, Quartz, and SiO_2 Wafers. *Appl. Phys. A* **2015**, *118* (2), 389–396.

(27) Karakouz, T.; Tesler, A. B.; Bendikov, T. A.; Vaskevich, A.; Rubinstein, I. Highly Stable Localized Plasmon Transducers Obtained by Thermal Embedding of Gold Island Films on Glass. *Adv. Mater.* **2008**, *20* (20), 3893–3899.

(28) Tesler, A. B.; Chuntonov, L.; Karakouz, T.; Bendikov, T. A.; Haran, G.; Vaskevich, A.; Rubinstein, I. Tunable Localized Plasmon Transducers Prepared by Thermal Dewetting of Percolated Evaporated Gold Films. *J. Phys. Chem. C* **2011**, *115* (50), 24642–24652.

(29) Merlen, A.; Gadenne, V.; Romann, J.; Chevallier, V.; Patrone, L.; Valmalette, J. C. Surface Enhanced Raman Spectroscopy of Organic Molecules Deposited on Gold Sputtered Substrates. *Nanotechnology* **2009**, *20* (21), 215705.

(30) Liu, G. Q.; Liu, Z. Q.; Chen, Y. H.; Huang, K.; Li, L.; Tang, F. L.; Gong, L. X.; Hu, Y.; Zhang, X. N. Surface-Enhanced Raman Scattering Effect of Gold Nanoparticle Arrays: The Influence of Annealing Temperature, Excitation Power and Array Thickness. *Opt. - Int. J. Light Electron Opt.* **2013**, *124* (21), 5124–5126.

(31) Herz, A.; Wang, D.; Schaaf, P. Dewetting of Au/Ni Bilayer Films on Prepatterned Substrates and the Formation of Arrays of Supersaturated Au-Ni Nanoparticles. *J. Vac. Sci. Technol. B Microelectron. Nanom. Struct.* **2014**, *32* (2), 021802.

(32) Wang, Y. M.; Lu, L.; Srinivasan, B. M.; Asbahi, M.; Zhang, Y. W.; Yang, J. K. W. High Aspect Ratio 10-Nm-Scale Nanoaperture Arrays with Template-Guided Metal Dewetting. *Sci. Rep.* **2015**, *5*, 9654.

(33) Kim, D.; Giermann, A. L.; Thompson, C. V. Solid-State Dewetting of Patterned Thin Films. *Appl. Phys. Lett.* **2009**, *95* (25), 2009–2011.

(34) Namsani, S.; Singh, J. K. Dewetting Dynamics of a Gold Film on Graphene: Implications for Nanoparticle Formation. *Faraday Discuss.* **2016**, *186* (0), 153–170.

(35) Kracker, M.; Worsch, C.; Bocker, C.; Rüssel, C. Optical Properties of Dewetted Thin Silver/Gold Multilayer Films on Glass Substrates. *Thin Solid Films* **2013**, *539*, 47–54.

(36) Herz, A.; Wang, D.; Kups, T.; Schaaf, P. Solid-State Dewetting of Au/Ni Bilayers: The Effect of Alloying on Morphology Evolution. *J. Appl. Phys.* **2014**, *116* (4), 044307.

(37) Niekiel, F.; Kraschewski, S. M.; Schweizer, P.; Butz, B.; Spiecker, E. Texture Evolution and Microstructural Changes during Solid-State Dewetting: A Correlative Study by Complementary in Situ TEM Techniques. *Acta Mater.* **2016**, *115*, 230–241.

(38) Nsimama, P. D.; Herz, A.; Wang, D.; Schaaf, P. Influence of the Substrate on the Morphological Evolution of Gold Thin Films during Solid-State Dewetting. *Appl. Surf. Sci.* **2016**, *388*, 475–482.

(39) Magnozzi, M.; Bisio, F.; Canepa, M. Solid-State Dewetting of Thin Au Films Studied with Real-Time, in Situ Spectroscopic Ellipsometry. *Appl. Surf. Sci.* **2017**, *421*, 651–655.

(40) Sudheer; Mondal, P.; Rai, V. N.; Srivastava, A. K. A Study of Growth and Thermal Dewetting Behavior of Ultra-Thin Gold Films Using Transmission Electron Microscopy. *AIP Adv.* **2017**, *7* (7), 075303.

(41) Bischof, J.; Scherer, D.; Herminghaus, S.; Leiderer, P. Dewetting Modes of Thin Metallic Films: Nucleation of Holes and Spinodal Dewetting. *Phys. Rev. Lett.* **1996**, *77* (8), 1536–1539.

(42) Gadkari, P. R.; Warren, A. P.; Todi, R. M.; Petrova, R. V.; Coffey, K. R. Comparison of the

Agglomeration Behavior of Thin Metallic Films on SiO_2. *J. Vac. Sci. Technol. A Vacuum, Surfaces, Film.* **2005**, *23* (4), 1152.

(43) Müller, C. M.; Spolenak, R. Microstructure Evolution during Dewetting in Thin Au Films. *Acta Mater.* **2010**, *58* (18), 6035–6045.

(44) Amram, D.; Klinger, L.; Rabkin, E. Anisotropic Hole Growth during Solid-State Dewetting of Single-Crystal Au–Fe Thin Films. *Acta Mater.* **2012**, *60* (6), 3047–3056.

(45) Farzinpour, P.; Sundar, A.; Gilroy, K. D.; Eskin, Z. E.; Hughes, R. A.; Neretina, S. Altering the Dewetting Characteristics of Ultrathin Gold and Silver Films Using a Sacrificial Antimony Layer. *Nanotechnology* **2012**, *23* (49), 495604.

(46) Wang, D.; Schaaf, P. Nanoporous Gold Nanoparticles. *J. Mater. Chem.* **2012**, *22* (12), 5344.

(47) Schaefer, B. T.; Cheung, J.; Ihlefeld, J. F.; Jones, J. L.; Nagarajan, V. Stability and Dewetting Kinetics of Thin Gold Films on Ti, TiOx and ZnO Adhesion Layers. *Acta Mater.* **2013**, *61* (20), 7841–7848.

(48) Kosinova, A.; Klinger, L.; Kovalenko, O.; Rabkin, E. The Role of Grain Boundary Sliding in Solid-State Dewetting of Thin Polycrystalline Films. *Scr. Mater.* **2014**, *82*, 33–36.

(49) Seguini, G.; Curi, J. L.; Spiga, S.; Tallarida, G.; Wiemer, C.; Perego, M. Solid-State Dewetting of Ultra-Thin Au Films on SiO_2 and HfO_2. *Nanotechnology* **2014**, *25* (49), 495603.

(50) Shaffir, E.; Kauffmann, Y.; Riess, I. Void Formation in Gold Films on Yttrium-Doped Zirconia in the Initial Stage of Dewetting. *Acta Mater.* **2014**, *79*, 59–65.

(51) Tesler, A. B.; Maoz, B. M.; Feldman, Y.; Vaskevich, A.; Rubinstein, I. Solid-State Thermal Dewetting of Just-Percolated Gold Films Evaporated on Glass: Development of the Morphology and Optical Properties. *J. Phys. Chem. C* **2013**, *117* (21), 11337–11346.

(52) Hieke, S. W.; Breitbach, B.; Dehm, G.; Scheu, C. Microstructural Evolution and Solid State Dewetting of Epitaxial Al Thin Films on Sapphire (α-Al_2O_3). *Acta Mater.* **2017**, *133*, 356–366.

(53) Bäuerle, D. *Laser Processing and Chemistry*; Springer Berlin Heidelberg: Berlin, Heidelberg, 2011.

(54) Andersson, S.; Dzhavadov, L. Thermal Conductivity and Heat Capacity of Amorphous SiO_2: Pressure and Volume Dependence. *J. Phys. Condens. Matter* **1992**, *4* (29), 6209–6216.

(55) Okumura, M.; Nakamura, S.; Tsubota, S.; Nakamura, T.; Azuma, M.; Haruta, M. Chemical

Vapor Deposition of Gold on Al_2O_3, SiO_2, and TiO_2 for the Oxidation of CO and of H_2. *Catal. Letters* **1998**, *51* (1/2), 53–58.

(56) Malureanu, R.; Lavrinenko, A. Ultra-Thin Films for Plasmonics: A Technology Overview. *Nanotechnology Reviews*. 2015, pp 259–275.

(57) Kosinova, A.; Wang, D.; Baradács, E.; Parditka, B.; Kups, T.; Klinger, L.; Erdélyi, Z.; Schaaf, P.; Rabkin, E. Tuning the Nanoscale Morphology and Optical Properties of Porous Gold Nanoparticles by Surface Passivation and Annealing. *Acta Mater.* **2017**, *127*, 108–116.

(58) Challener, W. A.; Peng, C.; Itagi, A. V.; Karns, D.; Peng, W.; Peng, Y.; Yang, X.; Zhu, X.; Gokemeijer, N. J.; Hsia, Y.-T.; et al. Heat-Assisted Magnetic Recording by a near-Field Transducer with Efficient Optical Energy Transfer. *Nat. Photonics* **2009**, *3* (4), 220–224.

(59) Qin, H. L.; Wang, D.; Huang, Z. L.; Wu, D. M.; Zeng, Z. C.; Ren, B.; Xu, K.; Jin, J. Thickness-Controlled Synthesis of Ultrathin Au Sheets and Surface Plasmonic Property. *J. Am. Chem. Soc.* **2013**, *135* (34), 12544–12547.

(60) Abadía, N.; Bello, F.; Zhong, C.; Flanigan, P.; McCloskey, D. M.; Wolf, C.; Krichevsky, A.; Wolf, D.; Zong, F.; Samani, A.; et al. Optical and Thermal Analysis of the Light-Heat Conversion Process Employing an Antenna-Based Hybrid Plasmonic Waveguide for HAMR. *Opt. Express* **2018**, *26* (2), 1752–1765.

(61) Zhong, C.; Flanigan, P.; Abadía, N.; Bello, F.; Jennings, B. D.; Atcheson, G.; Li, J.; Zheng, J.-Y.; Wang, J. J.; Hobbs, R.; et al. Effective Heat Dissipation in an Adiabatic Near-Field Transducer for HAMR. *Opt. Express* **2018**, *26* (15), 18842.

(62) Lee, B.; Lee, I.-M.; Kim, S.; Oh, D.-H.; Hesselink, L. Review on Subwavelength Confinement of Light with Plasmonics. *J. Mod. Opt.* **2010**, *57* (16), 1479–1497.

(63) Atwater, H. A.; Polman, A. Plasmonics for Improved Photovoltaic Devices. *Nat. Mater.* **2010**, *9* (3), 205–213.

(64) Link, S.; Masiello, D. J. Introduction: Plasmonics in Chemistry. *Chem. Rev.* **2018**, *118* (6), 2863–2864.

(65) Mie, G. Beiträge Zur Optik Trüber Medien, Speziell Kolloidaler Metallösungen. *Ann. Phys.* **1908**, *330* (3), 377–445.

(66) Maier, S. A. *Plasmonics : Fundamentals and Applications*; Springer, 2007.

Chapter 3: Experimental methods

3.1 Introduction

In this chapter, a general overview of the different experimental techniques used throughout the thesis will be given. The methods used to fabricate, analyse, and measure samples will be discussed in terms of their theoretical background and operation, while discussion on their specific uses in relation to the research will be regulated to the relevant subsequent chapters in this thesis.

The sample preparation methods used in this work include solvent cleaning, and oxygen plasma cleaning. The fabrication methods used include e^--beam evaporation thin film deposition, and sputtering thin film deposition. Finally, the analysis techniques include absorption spectroscopy, scanning electron microscopy, transmission electron microscopy, atomic force microscopy, and back-reflected laser-signal collection.

3.2 Sample preparation

When fabricating samples in the form of a thin film, it is of the utmost importance that the substrate has been sufficiently cleaned. Any organic residue still remaining can significantly compromise the adhesion strength of the film to the substrate[1]. For a cleaning method to be appropriate, it must (a) remove any remaining organic material, and (b) not damage or chemically alter the substrate[2]. Additionally**,** different types of deposition methods will result in different adhesion behaviour: sputtered films have been shown to have a better adhesion with their substrate than evaporated films, due to the bombardment of energetic atoms removing adsorbates from the substrate[3].

3.2.1 Solvent cleaning

One approach for the removal of organic contaminants from a substrate is solvent cleaning. By washing the substrate in a suitable solvent, the organic contaminants will dissolve in the solvent and will be washed away with it[4]. Acetone (chemical formula:

$(CH_3)_2CO$) is one of the most widely used chemical cleaning agents for a variety of reasons. Firstly, it is an excellent solvent, and many organic materials are soluble within it[5]. Secondly, for the case of SiO_2 substrates, acetone will not react with the substrate. Acetone molecules will however weakly adsorb to the SiO_2, but this can be mitigated by heating the substrate above 100°C[6].

In this thesis, samples were rinsed in acetone, followed by isopropyl alcohol (IPA), prior to deposition. Acetone and IPA were sourced from Sigma Aldrich, with purities of > 99.9% and > 99.7%, respectively. During the cleaning process, samples were placed in an ultrasonic bath for 5 minutes in order to aid the cleaning process.

3.2.2 Oxygen plasma cleaning

Plasma cleaning is based on the idea of oxidizing organic residues that are on the surface of the substrate, which can then be removed via the vacuum pump of the plasma chamber (see Figure 3.1). Several different gases can be used for this process, including oxygen, hydrogen, and chlorine[4]. In the case of oxygen plasma, organic residues are oxidized to form chemicals such as CO_2, CO, and H_2O, which are all sufficiently volatile to be removed by vacuum pumping[7]. It has been previously shown that plasma cleaning is more effective than solvent cleaning[8], as fewer residues are left once the cleaning process has been completed.

In this thesis, an Electronic Diener Pico oxygen plasma system was used to clean samples prior to sputtering deposition.

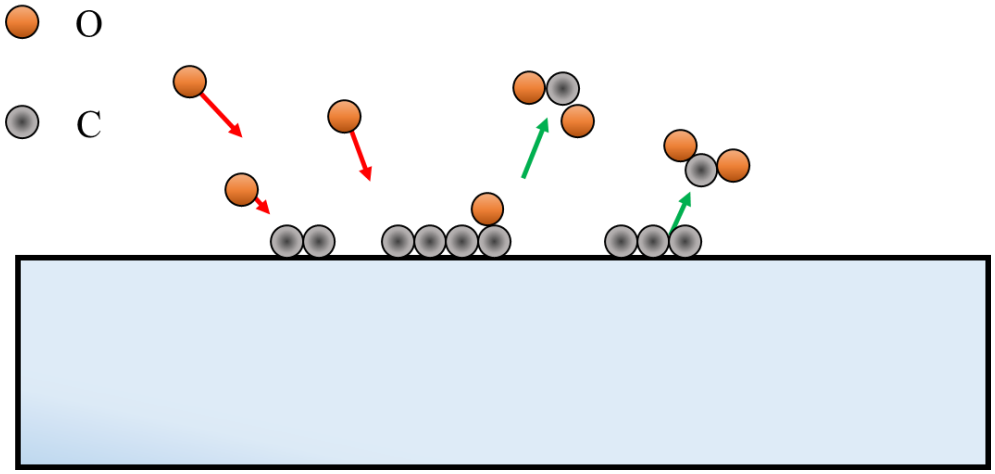

Figure 3.1: Schematic diagram illustrating the removal of carbon contaminants from a substrate by oxygen plasma cleaning

3.3 Deposition techniques

3.3.1 Electron-beam evaporation

Electron-beam (e^--beam) evaporation is a physical vapour deposition (PVD) technique used in the production of thin films. The basic technique is shown in Figure 3.2. The material to be deposited is held in a crucible made of a refractory material, such as tungsten, or ceramic such as alumina. At the start of the deposition process, the target material is irradiated with a high-kinetic energy electron beam. The energy transfer from the electrons will cause the target material to melt or sublimate, and eventually vaporize, coating the inside of the vacuum chamber (and the substrate)[9].

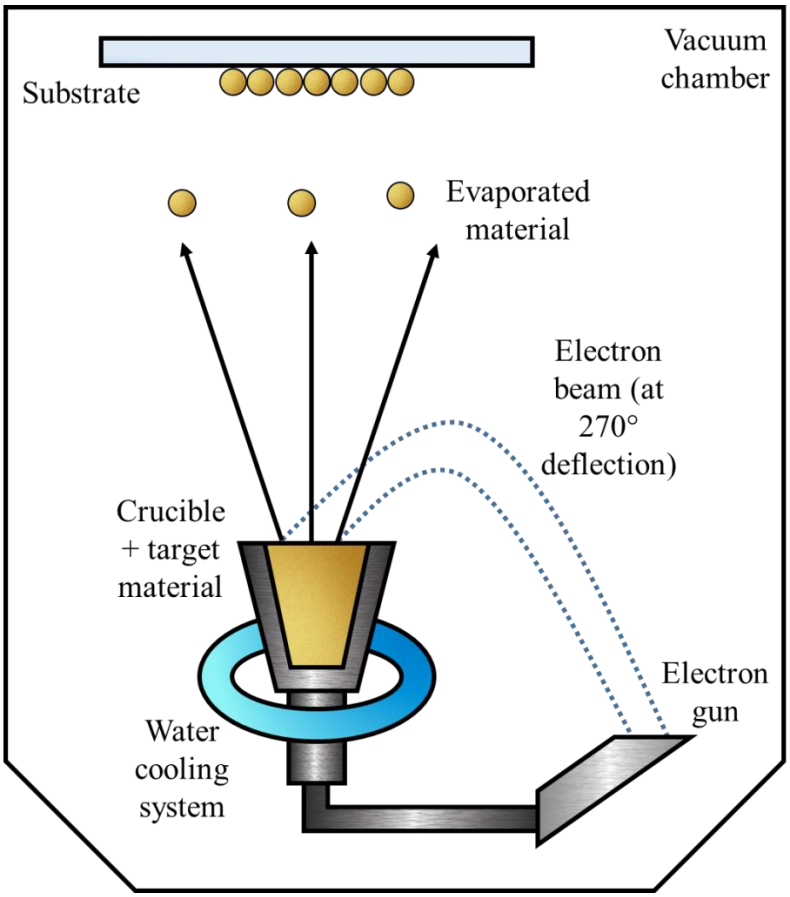

Figure 3.2: Schematic diagram detailing the electron-beam evaporation deposition process.

In this thesis, a Temescal FC-2000 electron-beam evaporator was used for the fabrication of Au, Ti/Au, and Cr/Au films. Target materials were supplied by Kurt J. Lesker, with purities of > 99.99%. Deposition rates ranged from 1 - 2 Å s^{-1}.

3.3.2 Sputtering

Sputtering deposition is a PVD technique which is based on the idea of using an energetic plasma to eject atoms from a target material. A basic schematic for a sputtering deposition system is shown in Figure 3.3. The substrate and the target material are connected to a voltage source, forming the anode and cathode respectively. At the start of the deposition process, the bombarding gas (usually an inert gas, such as Ar) is pumped into the deposition chamber. Given a sufficient gas pressure and voltage across the anode and cathode, the gas will be converted into a plasma. Ions from the plasma will be accelerated towards the cathode, where they will collide with the sputtering target, causing the ejection of target material atoms towards the substrate. The voltage source across the electrodes can either be direct-current (DC) or radio-frequency (Rf). Rf sputtering has several advantages over the DC equivalent; electrically reversing the cathode and anode helps negate charge build-up in the system (crucial for the deposition of dielectrics), and the additional electron movement caused by the switching polarity increases the chances of further ionization, resulting in a denser plasma[10]. One further way of increasing the plasma density (and hence the sputtering rate) is through the use of magnetron sputtering[11]. The magnetron uses a closed magnetic field to trap electrons near the cathode. This process results in denser plasmas generated at lower pressures, increased deposition rates, and uniform coatings[12].

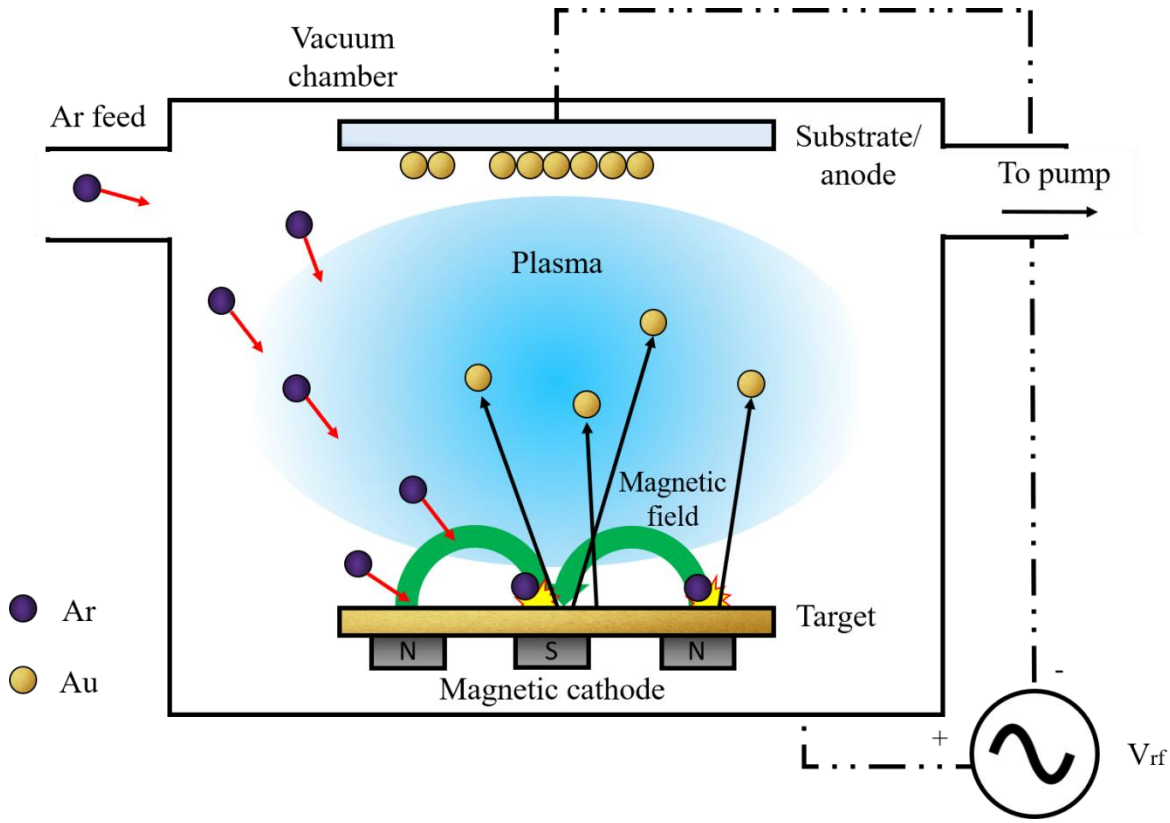

Figure 3.3: Schematic diagram detailing the RF magnetron sputtering deposition process, where Ar^+ is the bombarding ion and Au is the sputtering material.

Both metallic and dielectric films can be fabricated using Rf magnetron sputtering, but when using dielectric targets (as opposed to reactive sputtering[13]), Rf sputtering will be required[3]. The rate of deposition in the sputtering process is related to the energy of the plasma ions, and, perhaps more crucially, the material in question being sputtered. For a given ion energy, each material will have a specific sputter yield *Y*, i.e. the ratio of emitted (sputtered) particles to that of incident particles (note that *Y* can be a greater or less than 1). Sputter yields for the materials investigated in this thesis are shown in Table 3.1, for an Ar ion energy of 500 eV.

Table 3.1: sputtering yields for elemental materials investigated in this thesis. Adapted from reference [10]

Material	Sputtering yield
Al	0.9
Au	1.7
Cr	1.1
Ta	0.5
Ti	0.5
W	0.5

In this thesis, a SHAMROCK 19608 DC/RF sputtering system was used to produce Au thin films with a variety of ultra-thin adhesion layers. Sputtering targets were supplied by Lesker, Millron, and Testbourne, with material purities of ≥ 99.99%. The base pressure of the system was $5x10^{-7}$ Torr. Films were deposited at ambient temperature in mTorr Ar partial pressures producing stable deposition rates ranging from 0.08-0.36 Å s^{-1}. This allowed for timed depositions of adhesion layers to a nominal accuracy of +/- 0.1 Å. The target thicknesses in this work are based on deposition rates calculated for thicker films, not actual measurements, and hence should only be regarded as nominal. The system used has previously shown an ability to deposit sub-nanometer layers for magnetic tunnel junction devices[14], and given the high dependence on accurate thicknesses for such devices, the nominal thicknesses for the adhesion layers were considered acceptable.

3.4 Analysis techniques

3.4.1 Absorption spectroscopy

From the description of thin film optical heating given in Chapter 2, an estimate of the temperature increase can only be known if the amount of power absorbed by the film is known. Absorption spectroscopy is an analytical method which will give information about the how the optical absorption of a given material (measured in percent) will vary over a set series of wavelengths. When light is incident on a material, the light will either be reflected by the material, transmitted through the material, or be absorbed by the material.

In this thesis, a Perkins Elmer UV-Vis absorption spectrophotometer was used to obtain optical absorption data. The transmission of each sample under investigation was

measured, followed by its reflectivity. The percentage absorption was then calculated using the relation:

$$A = 100 - T - R \tag{3.1}$$

An integrating sphere was use to sure any diffuse transmission or reflection was also measured to ensure a truly accurate measure of absorption.

3.4.2 Scanning electron microscopy (SEM)

Scanning electron microscopy (SEM) is an electron microscopy technique utilized for materials analysis. A schematic for a typical SEM set-up is displayed in Figure 3.4. The electron beam is focused onto the sample using a magnetic lens. The scanning coil uses a magnetic field to raster the beam along the area of interest, in order to produce an image. When the electron beam hits the surface of the sample, different types of electrons are emitted, including low energy (< 50 eV) secondary electrons and back-scattered electrons[15]. Each type of electron will provide different information about the sample. For example, secondary electrons originate from inelastic collisions of the beam electrons with the sample, resulting in the emission of weakly bound electrons from the surface of the sample. Collecting this type of electron will give information about the topography of the sample, as well as a certain amount of information about the elemental composition[16]. In contrast, back-scattered electrons (BSEs) originate from elastic collisions of the beam electrons with atoms in the sample. They are more sensitive to the atomic number of the emitting material than secondary electrons, which hence gives more information about the elemental composition of the sample[17].

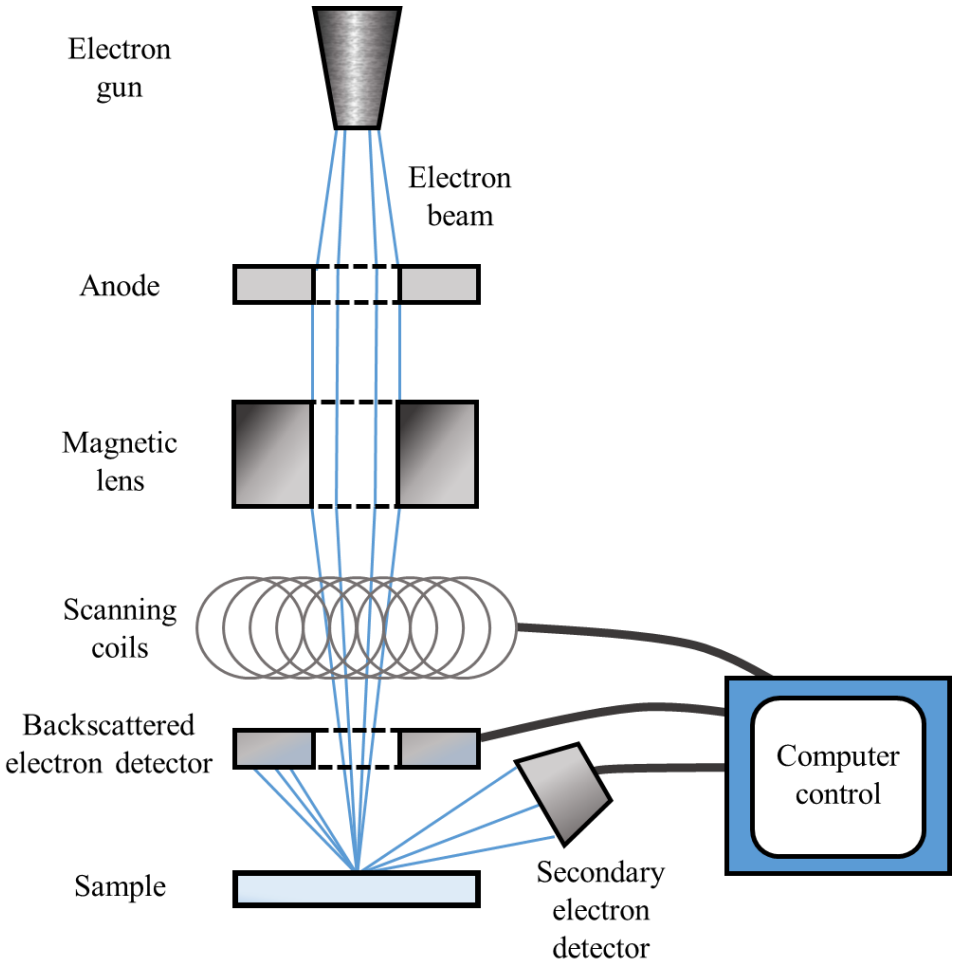

Figure 3.4: schematic diagram of a scanning electron microscope, with detectors for backscattered and secondary electrons.

While SEM does not have the sample resolution capabilities of the transmission electron microscopy (TEM) (5 nm resolution[18] versus 0.05 nm resolution in state of the art systems[19]), it does has the advantage over the TEM of being capable of imaging bulk samples[20].

In this thesis, SEM imaging was carried out in order to provide information on the micro- and nanoscale changes occurring in the dewetting films. A Zeiss ULTRA scanning electron microscopy was used. The beam voltage was operated at a range of 5 – 6 kV. In order to increase the conductivity of the samples (and hence reduce charge build-up), conductive Ag paint (RS Components) was applied to the edges of each sample and to the SEM sample holder, thus grounding the sample. Unless otherwise specified, all SEM images were taken using the secondary electron (SE2) detector.

3.4.3 Transmission electron microscopy (TEM)

Transmission electron microscopy (TEM) is an electron microscopy technique which allows very high resolution images to be taken of nanoscale materials. The basic operation of the instrument is superficially similar to that of an optical microscope, with the main difference being in the use of electrons as an illumination source, which allows for a much larger resolution. The highest resolution possible in a microscope will be determined by the Abbe limit[21], i.e.

$$d = \frac{\lambda}{2n\sin\theta} \tag{3.2}$$

As the wavelength of an electron will depend on its momentum, it can be changed within a TEM through the accelerating voltage of the beam:

$$\lambda = \frac{h}{\left[2m_0 eV\left(1+\frac{eV}{2m_0c^2}\right)\right]^{1/2}} \tag{3.3}$$

Hence, the resolution of the TEM can be increased by using higher accelerating voltages[22]. A basic TEM set-up is displayed in Figure 3.5.

While TEM is has many advantages over other forms of microscopy, it does have some significant drawbacks. The resolution of a TEM is theoretically only limited by the acceleration of the electron beam, but in practice the system is limited by its lenses which can be subject to several defects, including different types of aberrations and astigmatism[22]. Additionally, as the technique is based on the transmission of electrons through a sample, the sample in question must be electron transparent. This requires samples to either be pre-made on specially designed TEM substrates, for the sample to be back-etched until an appropriate thickness (e.g. 50 nm) is reached[23], or for a lamellae to be cross-sectioned from the sample using a focused-ion beam (FIB)[24]. Finally, a TEM is a very costly technique to run, with each eV of accelerating energy costing upwards of $5[22].

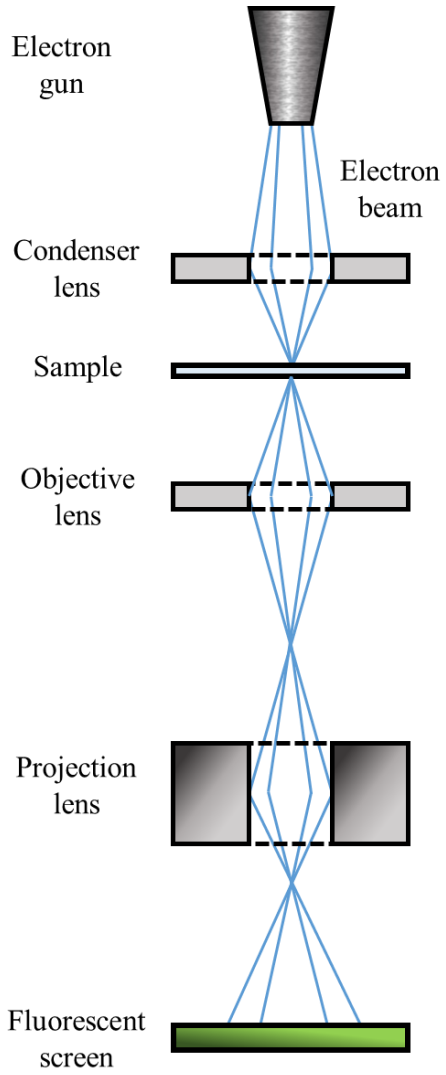

Figure 3.5: schematic diagram of a transmission electron microscope, operating in bright-field imaging mode.

In this thesis, TEM imaging was carried out in order to analyze films of the lowest thicknesses studied. 2 different TEM systems were used. For the crystallographic analysis in Chapter 4, a JEOL 2100F with a spherical aberration corrector was used. The beam was operated with a beam voltage of 200 kV in all instances of use. For the cross-sectional analysis in Chapter 5, a FEI Titan 80 – 300kV FEG S/TEM scanning/transmission electron microscope was used. The S/TEM was equipped with an EDAX energy dispersive X-ray (EDX) detector and a Gatan Tridiem spectrometer for electron energy loss spectroscopy (EELS) analysis.

3.4.4 Electron energy-loss spectroscopy (EELS)

Electron energy-loss spectroscopy (EELS) is a technique which allows information on atomic composition and chemical bonding to be obtained during TEM. EELS is based on the principle of inelastic scattering of electrons (see Figure 3.6). When an electron interacts with a material, there is a chance that it will be scattered elastically (with no subsequent loss of energy) or inelastically (with a subsequent loss of energy). The elastic scattering can be caused by phonons, plasmons, outer- or inner-shell electrons, and/or inter- and intra-band transitions, among other processes. The energy loss from the process will be unique to the material in question, and allows definitive fingerprinting of the material composition and its chemical properties[25].

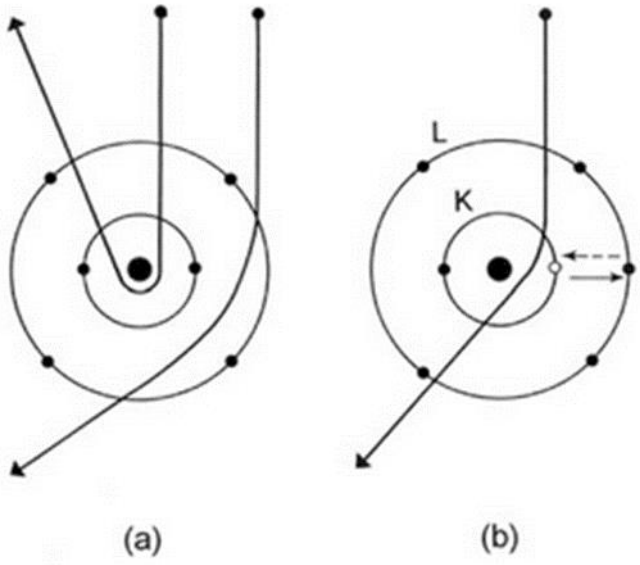

Figure 3.6: electron scattering by atoms, the principle of operation for EELS. (a) elastic scattering, (b) inelastic scattering

In this thesis, EELS measurements were used to identify diffused species during TEM investigations. EELS measurements were performed using a FEI Titan field emission transmission electron microscope (TEM) with accelerating voltages between 80 kV and 300 kV. Sample cross-sections were prepared using a Zeiss Auriga focused ion beam (FIB) system.

3.4.5 X-ray photoelectron spectroscopy (XPS)

X-ray photoelectron spectroscopy (XPS) is a surface analysis technique, which gives information on chemical composition. The basic principle for XPS is detailed in Figure 5.3. When an X-ray photon is absorbed by a core-shell electron, it may lead to the ejection of the electron from the atom (the core-shell hole may then be filled by an electron of a higher energy level, leading to either X-ray fluorescence or non-radiative Auger emission). The electron is then collected by the XPS detector, and its kinetic energy (E_k) is measured. The E_k of this electron is given by;

$$E_k = h\nu - E_B - E_R - \phi - \delta E \tag{5.1}$$

where hν is the energy of the absorbed X-ray photon, E_B is the binding energy of the electron, E_R is the recoil energy, ϕ is the work function, and δE is a term which takes electrostatic charging of the sample into consideration[26]. As hν and ϕ are known quantities for the given measurement, E_R is negligible, and δE can be corrected for, measuring E_k via XPS allows E_B to be measured. The resultant XPS spectra will show peaks at all detected E_B values, and when these are referenced against a database[27], will give information on elements present and their chemical composition. As XPS has a low sampling depth (around 10 nm[26], but the exact depth will depend on the sample in question), it is an invaluable technique for analysing surfaces.

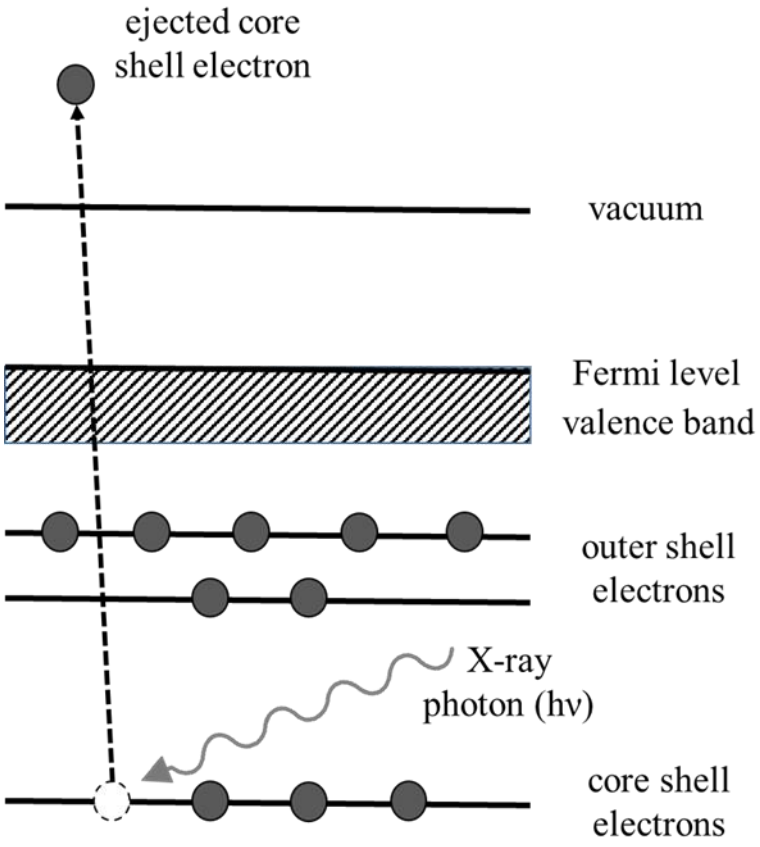

Figure 3.7: schematic demonstrating the ejection of a core-shell electron after absorbing an X-ray: the basic principle behind X-ray photoelectron spectroscopy. Recreation of schematic shown in [26]

In this thesis, XPS measurements were performed in order to detect the presence of diffused elements at the surface of thin films. XPS measurements were carried out in ultra-high vacuum (< 2×10^{-10} mbar) using monochromated Al K_α x-rays from an Omicron XM1000 MkII x-ray source measured with a multichannel Omicron EA125 energy analyzer. The binding energy scale was referenced to the Au 4f level at 84.0 eV. Ti 2p core-level spectra were fitted with Voigt line-shapes using CasaXPS software.

3.4.6 Atomic force microscopy (AFM)

In 1986, Gerd Binning (co-inventor of the scanning tunnelling microscope (STM[28]), Calvin Quate and Christopher Gerber, developed the atomic force microscope (AFM)[29]. A typical AFM set-up (pictured in Figure 3.8) consists of a probe attached to a cantilever (a lever fixed at one end), onto which there is a laser positioned. The laser reflects from the cantilever into a detector, which gives the position of the cantilever. As the probe moves

across the sample, the change in cantilever position will be inputted into a computer, generating an image[30].

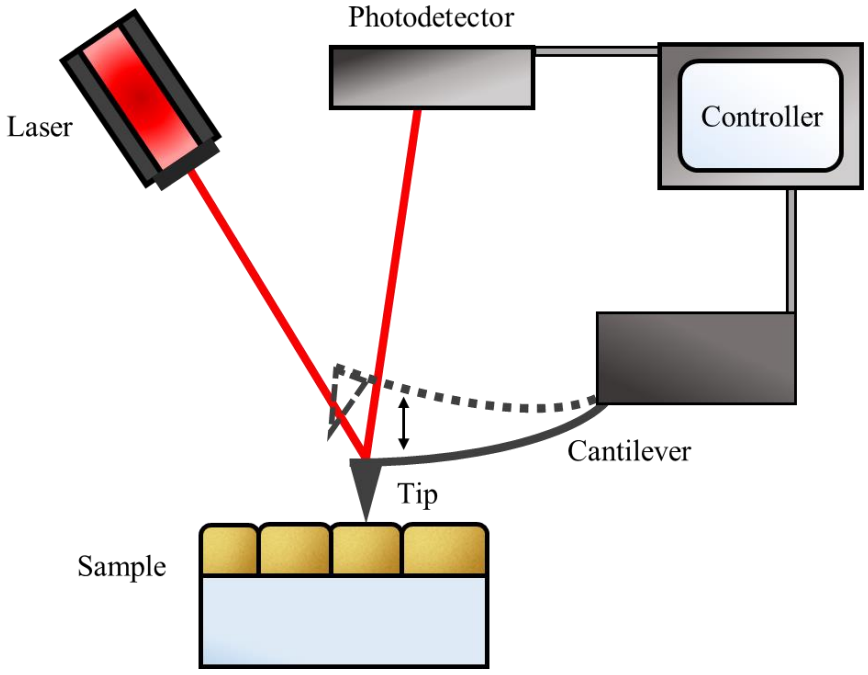

Figure 3.8: schematic diagram of an atomic force microscope, operating in tapping mode.

AFM is very versatile, in that images can be obtained using different techniques, or modes. Three of the most commonly used are; contact mode, non-contact mode, and intermittent contact, or "tapping", mode. Intermittent contact, or "tapping", mode is, in a way, a combination of the previous two modes. In this mode, the tip oscillated at large amplitudes, moving from the attractive force region to the repulsive region. There are several advantages to this approach. The lateral forces experienced in contact mode are eliminated, and the tip passes through any contaminants, unlike non-contact mode. Also, the tip-sample contact allows investigation into the sample properties. While the tip does come into contact with the sample, the cantilever is usually set to oscillated at such a high frequency that damaged is minimalized. This, coupled with the lack of lateral forces, makes tapping mode a popular method for investigating easily damaged samples[30].

In this thesis, AFM measurements were used to investigate changes in surface roughness of heat-treated films, as an additional method of quantifying their thermal stability. AFM measurements were performed using an Asylum MFP-3D. AFM was used in tapping mode with BudgetSensors Tap300Al-G silicon AFM probes.

3.4.7 Back-reflected laser measurement

Measurement of the time dynamics of solid-state dewetting generally takes one of two forms: *in-situ* measurement that monitors the change in an affected parameter as dewetting proceeds[31], or *ex-situ* measurement that analyses the extent of dewetting at fixed time points[32]. Both methods are disadvantaged in that each sample can only be used for one single measurement, hence requiring a large number of samples to be made. Ideally, a measurement of the dewetting characteristics of a film could be performed multiple times on the same sample, improving the statistics and minimizing sample count.

In order to fulfil these criteria, a novel method of analysing the dewetting characteristics of thin films was devised. The technique is based on the change in reflectivity which occurs in a thin film as it dewets. While it is known that heating a metal will also cause a change in its reflectivity due to the thermoreflectance effect[33], this change is negligible compared to the changes occurring during dewetting: at the laser wavelength of 488 nm, the thermoreflectance coefficient is close to zero[34]. The magnitude of the change in reflectivity from a change in temperature due to the thermoreflectance effect is determined by the thermoreflectance coefficient. Hence, when the coefficient is close to zero, there will be a negligible change in reflectivity on increasing the temperature, and any changes in reflectivity occurring in the film are purely the result of solid-state dewetting. To take an example of a temperature increase of 200 K for an Au film of arbitrary thickness, the reflectivity would decrease by 0.25% at the wavelength of 488 nm[34].

A cw-laser heat source is used to induce solid-state dewetting in a thin film: as this occurs, the back-reflected laser is collected by a photodiode (see Figure 3.9). As the film dewets, the reflectivity will decrease, and hence the back-reflected laser signal will decrease. This gives real-time information about the progress of dewetting as it occurs. The measurement is superficially similar to that demonstrated by Jiran and Thompson[31], but there are several key differences; a laser is used as a heat-source and is also used as the probe, and multiple measurements on a single sample are possible, which hence allows for a greater statistical significance to be obtained.

In order to know the power incident on the samples (and hence the absorbed power), it is necessary to measure the reflection and/or transmission of the microscope objective. A 50/50 beamsplitter was placed at the back of the microscope objective. The laser was then passed through this beamsplitter and focused by the objective onto a test film of known

reflectivity. The beam was then reflected back through the objective after which it was split by the beamsplitter. The power measured at the beamsplitter is given by the equation;

$$P_{out} = T_{MO}^2 T_{SP} R_S R_{SP} P_{in} \tag{3.4}$$

where P_{in} is the input power, T_{MO} is the transmission through the microscope objective, T_{SP} and R_{SP} are the transmission and reflectivity of the splitter, and R_S is the reflectivity of the sample. This equation can be rearranged, giving the transmission through the microscope objective, assuming all other quantities are known;

$$T_{MO} = \sqrt{\frac{P_{out}}{P_{in} T_{SP} R_S R_{SP}}} \tag{3.5}$$

Hence, the actual power that is transmitted onto the sample can be found by multiplying the power measured at the back of the objective (after the beamsplitter) by T_{MO}. The absorbed power can be known by multiplying the incident power P_{in} by T_{MO} and the absorption percentage of the material in question, A (which can be measured using absorption spectrometry), i.e:

$$P_{abs} = P_{in} T_{MO} A \tag{3.6}$$

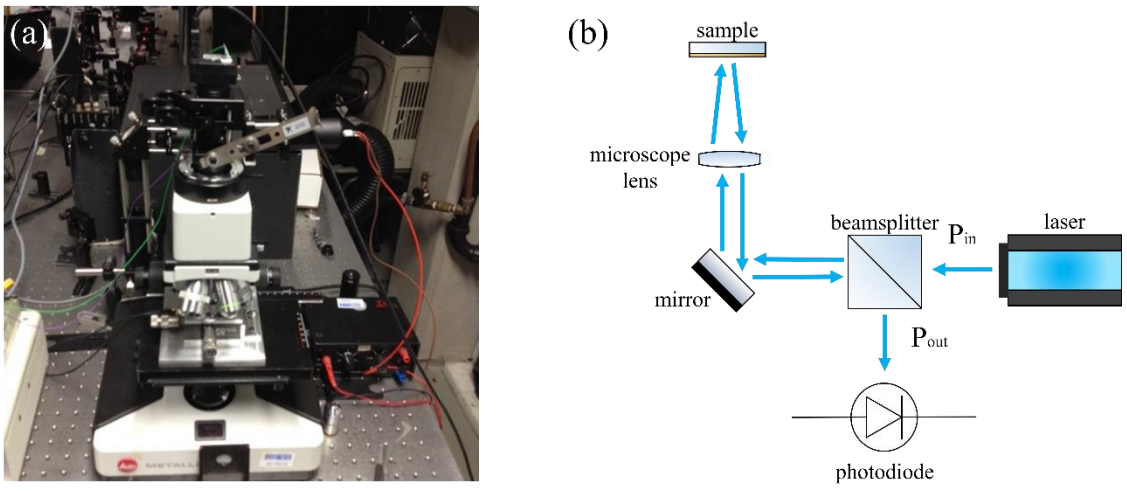

Figure 3.9: (a) photograph of the customized microscope set-up used for the back-reflected laser technique; (b) schematic diagram detailing the basic set-up of the back-reflected laser signal technique, used to measure the time dynamics of solid-state dewetting.

In order to increase the accuracy of the results, it is necessary to take multiple measurements on each sample and an average be taken. This will increase the signal-to-noise ratio and improve the statistics on each result. An example of this can be seen in Figure 3.10. Figure 3.10a shows the normalized raw data for the 2 nm Cr/10 nm Au sample irradiated at 5 mW with a 1.8 μm beam, and Figure 3.10b shows the degradation curve for the above sample after averaging for 5 iterations. The averaging process helps to increase the signal-to-noise ratio significantly. Further averaging will result in better statistics.

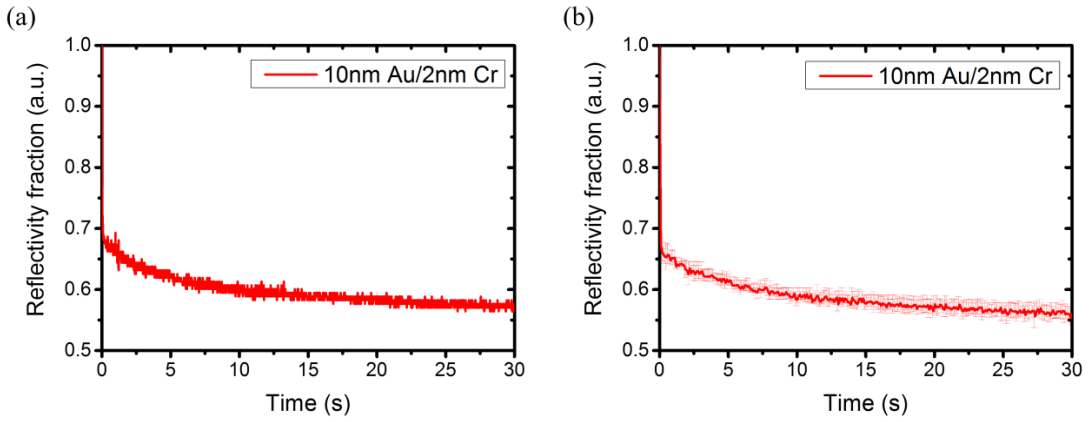

Figure 3.10: demonstration of the effect of averaging the signal in the back-reflected laser signal technique. (a) raw data for 2 nm Cr/10 nm Au film, (b) average of 5 iterations of the measurement

In order to obtain a way of quantitatively comparing the dewetting behavior of different films, a half-life ($T_{1/2}$) is extracted from each reflectivity curve. This is done by finding the time at which the reflectivity of the film has decreased by half of its total decrease. This method is necessary, as attempts at fitting the reflectivity data proved unsuccessful. In Figure 3.11, attempts at fitting an exponential decay and a double exponential to the reflectivity curves for 2 different films (2 nm Cr/10 nm Au and 2 nm Cr/50 nm Au) irradiated at 5 mW with a beam waist of 2.95 μm are shown. Both films exhibit what can be considered the "extremes" of the reflectivity curves: a rapid decay (Figure 3.11a) and a slower, gradual decay (Figure 3.11b). The exponential decay fit does not fit either curve well, while the double exponential only fits the 2 nm Cr/50 nm Au. Hence necessitating a manual measurement of $T_{1/2}$.

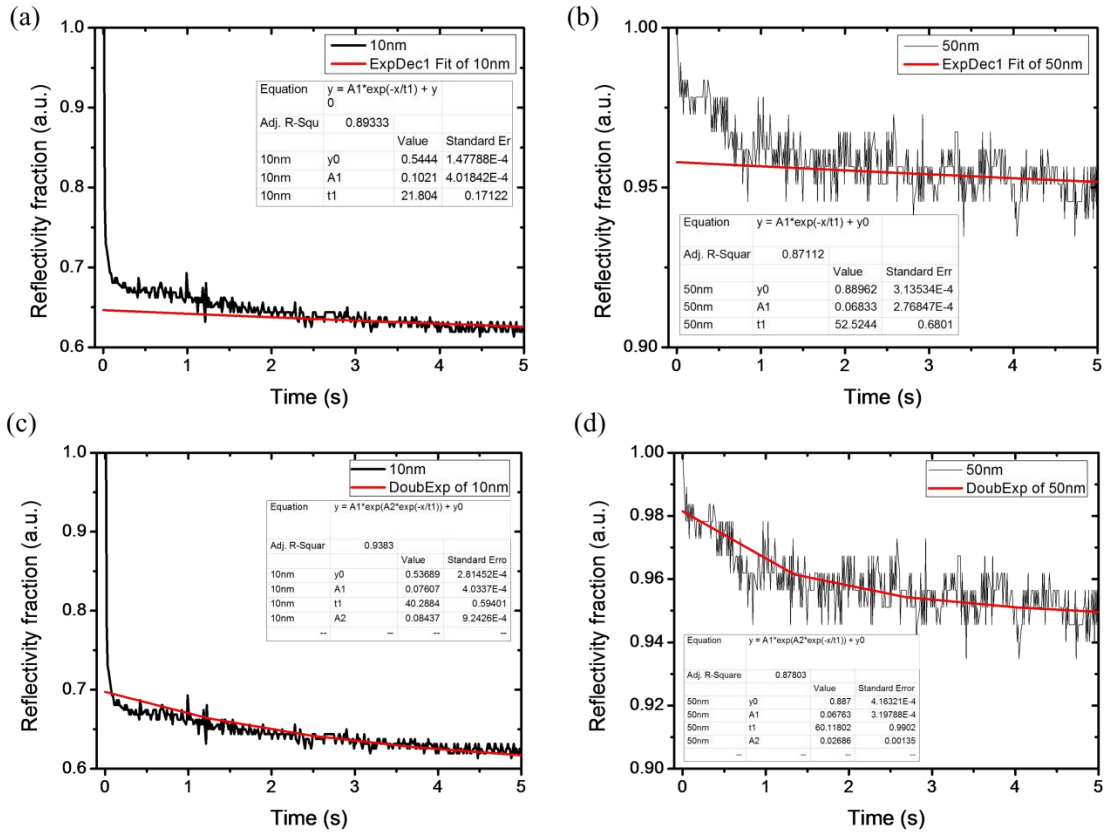

Figure 3.11: Attempts at fitting exponential decay curves to reflectivity data for (a) 2 nm Cr/10 nm Au film, and (b) 2 nm Cr/50 nm Au, irradiated at 5 mW with a beam waist of 2.95 μm. Fitting was attempted using OriginLab software.

3.5 Conclusions

In this chapter, the main experimental methods used throughout this thesis are described. The cleaning methods used for preparing the quartz substrate are shown, and the deposition techniques of electron-beam evaporation and sputtering are detailed. Conventional analysis techniques such as absorption spectroscopy, scanning electron microscopy, transmission electron microscopy, and atomic force microscopy are outlined. Finally, the back-reflected laser signal technique used to measure the dewetting resistance of Au films is detailed in full.

3.6 Bibliography

(1) Koski, K.; Hölsä, J.; Ernoult, J.; Rouzaud, A. The Connection between Sputter Cleaning and Adhesion of Thin Solid Films. *Surf. Coatings Technol.* **1996**, *80* (1–2), 195–199.

(2) Turner-Walker, G. The Nature of Cleaning: Physical and Chemical Aspects of Removing Dirt, Stains and Corrosion. In *International Symposium on Cultural Heritage Conservation*; 2012.

(3) Vossen, J. L.; Kern, W. *Thin Film Processes II*; Academic Press, 1991.

(4) Martin, P. M. *Handbook of Deposition Technologies for Films and Coatings : Science, Applications and Technology*; Elsevier, 2010.

(5) Remler, R. F. The Solvent Properties of Acetone. *Ind. Eng. Chem.* **1923**, *15* (7), 717–720.

(6) Zaki, M. I.; M. A. Hasan; Al-Sagheer, F. A.; Pasupulety, L. Surface Chemistry of Acetone on Metal Oxides: IR Observation of Acetone Adsorption and Consequent Surface Reactions on Silica−Alumina versus Silica and Alumina. **1999**.

(7) Petasch, W.; Kegel, B.; Schmid, H.; Lendenmann, K.; Keller, H. . Low-Pressure Plasma Cleaning: A Process for Precision Cleaning Applications. *Surf. Coatings Technol.* **1997**, *97* (1–3), 176–181.

(8) O'Kane, D. F.; Mittal, K. L. Plasma Cleaning of Metal Surfaces. *J. Vac. Sci. Technol.* **1974**, *11* (3), 567–569.

(9) *Advanced Nano Deposition Methods*; Lin, Y., Chen, X., Eds.; Wiley-VCH Verlag GmbH & Co. KGaA: Weinheim, Germany, 2016.

(10) Seshan, K. *Handbook of Thin-Film Deposition Processes and Techniques : Principles, Methods, Equipment and Applications*; Noyes Publications/William Andrew Pub, 2002.

(11) Kelly, P. J.; Arnell, R. D. Magnetron Sputtering: A Review of Recent Developments and Applications. *Vacuum* **2000**, *56* (3), 159–172.

(12) Bräuer, G.; Szyszka, B.; Vergöhl, M.; Bandorf, R. Magnetron Sputtering – Milestones of 30 Years. *Vacuum* **2010**, *84* (12), 1354–1359.

(13) Musil, J.; Baroch, P.; Vlček, J.; Nam, K. H.; Han, J. G. Reactive Magnetron Sputtering of Thin Films: Present Status and Trends. *Thin Solid Films* **2005**, *475* (1–2), 208–218.

(14) Feng, G.; Van Dijken, S.; Feng, J. F.; Coey, J. M. D.; Leo, T.; Smith, D. J. Annealing of CoFeB/MgO Based Single and Double Barrier Magnetic Tunnel Junctions: Tunnel Magnetoresistance, Bias Dependence, and Output Voltage. *J. Appl. Phys.* **2009**, *105* (3), 033916.

(15) *Scanning Electron Microscopy for the Life Sciences*; Schatten, H., Ed.; Cambridge University Press: Cambridge, 2012.

(16) Sakai, Y.; Yamada, T.; Suzuki, T.; Ichinokawa, T. Contrast Mechanisms of Secondary Electron Images in Scanning Electron and Ion Microscopy. *Appl. Surf. Sci.* **1999**, *144–145*, 96–100.

(17) Goldstein, J.; Newbury, D. E.; Michael, J. R.; Ritchie, N. W. M.; Scott, J. H. J.; Joy, D. C. *Scanning Electron Microscopy and X-Ray Microanalysis*.

(18) Lawes, G. *Scanning Electron Microscopy and X-Ray Microanalysis*; Published on behalf of ACOL, Thames Polytecnic, London, by Wiley, 2003.

(19) Kisielowski, C.; Freitag, B.; Bischoff, M.; van Lin, H.; Lazar, S.; Knippels, G.; Tiemeijer, P.; van der Stam, M.; von Harrach, S.; Stekelenburg, M.; et al. Detection of Single Atoms and Buried Defects in Three Dimensions by Aberration-Corrected Electron Microscope with 0.5-Å Information Limit. *Microsc. Microanal.* **2008**, *14* (05), 469–477.

(20) Reimer, L. *Scanning Electron Microscopy : Physics of Image Formation and Microanalysis*; Springer.

(21) Abbe, E. Beiträge Zur Theorie Des Mikroskops Und Der Mikroskopischen Wahrnehmung. *Arch. für Mikroskopische Anat.* **1873**, *9* (1), 413–418.

(22) Williams, D. B. (David B.; Carter, C. B. *Transmission Electron Microscopy : A Textbook for Materials Science*; Springer, 2009.

(23) Yao, B.; Coffey, K. R. Back-Etch Method for Plan View Transmission Electron Microscopy Sample Preparation of Optically Opaque Films. *J. Electron Microsc. (Tokyo).* **2008**, *57* (2), 47–52.

(24) Mayer, J.; Giannuzzi, L. A.; Kamino, T.; Michael, J. TEM Sample Preparation and FIB-Induced Damage. *MRS Bull.* **2007**, *32* (05), 400–407.

(25) Egerton, R. F. *Electron Energy-Loss Spectroscopy in the Electron Microscope*; Springer US: Boston, MA, 1996.

(26) Walls, J. M.; Smith, R. *Surface Science Techniques.*; Elsevier Science, 1994.

(27) Crist, B. V. *Handbook of Monochromatic XPS Spectra*; Wiley, 2000.

(28) Binnig, G.; Rohrer, H. Scanning Tunneling Microscopy. *IBM J. Res. Dev.* **1986**, *30* (4), 355–69.

(29) Binnig, G.; Quate, C. F.; Gerber, C. Atomic Force Microscope. *Phys. Rev. Lett.* **1986**, *56* (9), 930–933.

(30) Eaton, P.; West, P. *Atomic Force Microscopy*; Oxford University Press, 2010; Vol. 9780199570.

(31) Jiran, E.; Thompson, C. V. Capillary Instabilities in Thin, Continuous Films. *Thin Solid Films* **1992**, *208* (1), 23–28.

(32) Niekiel, F.; Schweizer, P.; Kraschewski, S. M.; Butz, B.; Spiecker, E. The Process of Solid-State Dewetting of Au Thin Films Studied by in Situ Scanning Transmission Electron Microscopy. *Acta Mater.* **2015**, *90*, 118–132.

(33) Farzaneh, M.; Maize, K.; Lüerßen, D.; Summers, J. A.; Mayer, P. M.; Raad, P. E.; Pipe, K. P.; Shakouri, A.; Ram, R. J.; Hudgings, J. A. CCD-Based Thermoreflectance Microscopy: Principles and Applications. *J. Phys. D. Appl. Phys.* **2009**, *42* (14), 143001.

(34) Abad, B.; Borca-Tasciuc, D.-A.; Martin-Gonzalez, M. S. Non-Contact Methods for Thermal Properties Measurement. *Renew. Sustain. Energy Rev.* **2017**, *76*, 1348–1370.

Chapter 4 - Laser-induced dewetting of Au thin films

4.1 Introduction

In Chapter 2, a review of the literature concerning solid-state dewetting of thin films was given. While there is a great deal of work in the literature on dewetting under isothermal annealing, there have been few studies on laser-induced dewetting[1–6], and fewer still on CW-laser induced dewetting[7,8]. Laser induced dewetting experiments tend to use pulsed laser systems. There are 2 main reasons for this. First, for work that focuses on analysing the processes involved, the rapid rates of dewetting that will occur from using high-intensity pulsed-laser sources will minimize the effect of the substrate on the film dewetting process, i.e chemical reactions between the film and the substrate, or film atoms diffusing into the substrate[1]. Secondly, most recent work on dewetting has been focused on its utility for synthesizing nanoparticle arrays (see Figure 4.1), and pulsed-laser systems allow for rapid array formation[2,3,5]. From a superficial level, the processes occurring in laser-induced dewetting appear similar to those that occur during isothermal dewetting[9]: agglomeration of film material into particles at high powers (Figure 4.1), and formation of voids at lower powers (Figure 4.2). The two processes cannot be directly compared, however, as using the laser as a heat source will result in an inherent thermal gradient in the film, as opposed to the isothermal case. Such a thermal gradient will result in solid-state dewetting occurring mainly at the beam focus, as opposed to the isothermal case, where the dewetting process will occur throughout the film. Regardless, it is vital that a full understanding of the failure mechanisms at lower laser power intensities and longer timescales is obtained if the long term thermal stability of Au plasmonic elements is to be improved.

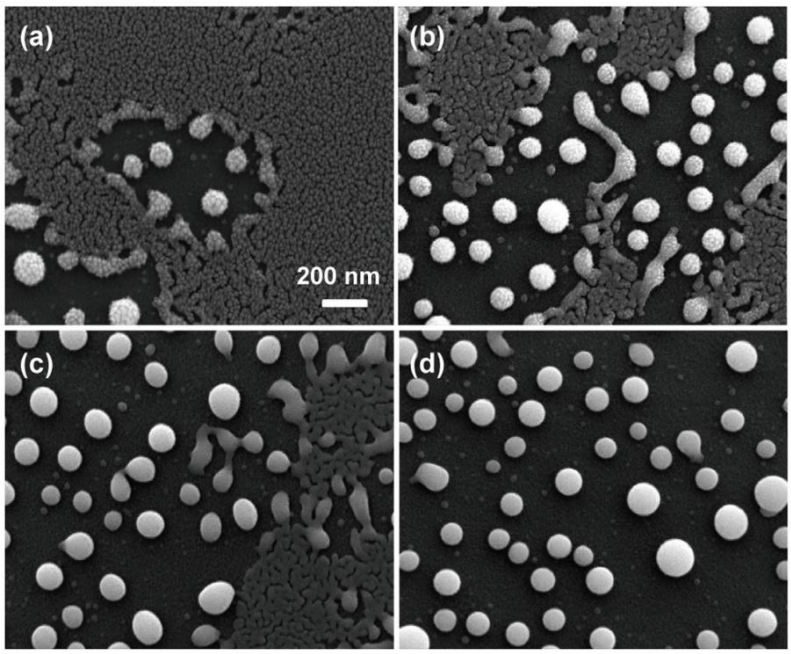

Figure 4.1: pulsed laser-induced dewetting of 15 nm Ag film on glass, with (a) 1 pulse, (b) 10 pulses, (c) 100 pulses, and (d) 1000 pulses. The pulse energy was 25 mJ in all cases. Taken from reference [6]

During the process of solid-state dewetting, the crystalline texture of the film will be affected[10,11]. Crystalline texture refers to how the individual crystallites are collectively orientated. In crystalline materials, each crystallographic facet will have a specific surface energy, depending on the arrangement of the atoms on the surface. In the case of Au, a metal with an fcc structure, the (111) facet will have the lowest energy due to it having the highest packing density, followed by the (100) and (110) facets, respectively[12]. The development of crystalline texture in thin films will occur during all stages of film growth, and during post-processing of the film[13].

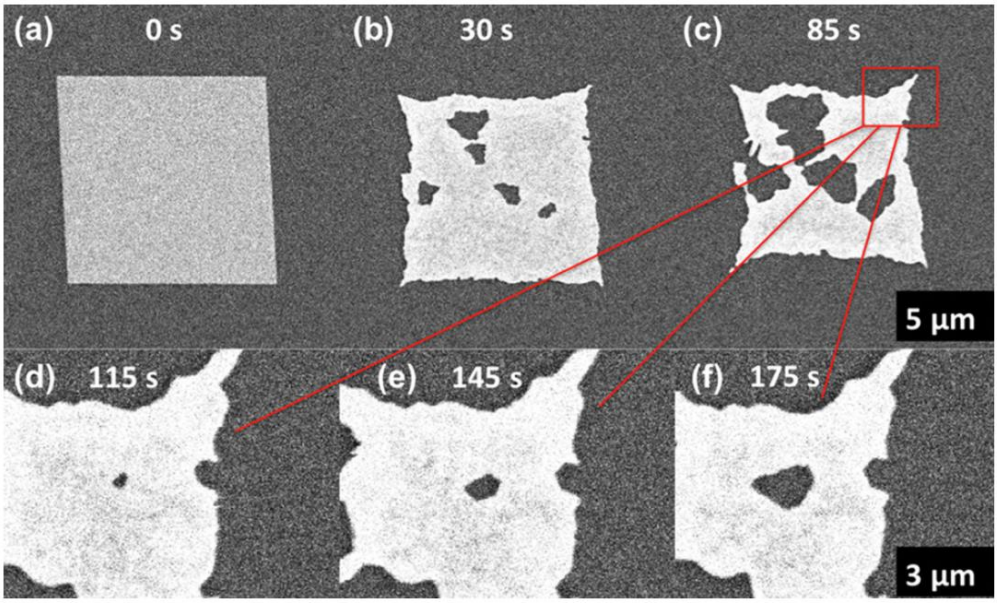

Figure 4.2: pulsed laser-induced dewetting of 10 nm Au film on SiO_x substrate, irradiated with 51 kW/cm^2 in 100 ms pulse widths at a 20% duty cycle. Note the formation and growth of voids as dewetting develops. Taken from reference [4]

In this chapter, the laser-induced dewetting dynamics of Au thin films are studied. Films are irradiated with a 488 nm CW-laser, with varying beam waists. The effect of the absorbed power is studied, as is the effect of film thickness. The effect of standard 2 nm Ti and Cr adhesion layers on the dewetting dynamics is also studied by way of comparison. Laser-induced crystallographic changes in Au thin films are also studied. Work is first done comparing the laser-induced grain growth of Au films with and without adhesion layers, via transmission electron microscope (TEM) analysis. The development of crystalline textures by isothermal annealing is then discussed, and is then compared with the textures that develop during laser-annealing. Finally, the effect of adhesion layers on the development of crystallographic texture is studied.

4.2 Experimental details

Au films with thicknesses in the range of 10 - 50nm were deposited on SiO_2 substrates via electron-beam evaporation. The cleaning of the SiO_2 substrates and the electron-beam evaporation process are discussed in detail in sections 3.2.1 and 3.3.1 respectively. It was predicted that the SiO_2 substrate would result in addition substrate effects on the dewetting process: SiO_2 does not chemically react with Au[14], and diffusion of Au into SiO_2 is negligible at temperatures below 600^oC[15].

The dewetting dynamics of Au films were measured using the back-reflected laser technique described in Chapter 3. The films were irradiated with absorbed powers in the range of 1 – 11 mW. In order to ensure consistency for the absorbed powers across each sample, optical absorption spectra were taken for each film so that the input laser power could be adjusted accordingly using the laser control panel. Across the different Au thicknesses, there was a non-negligible change in absorption at 488 nm (the irradiating wavelength). Hence, the incident power on each sample changed using the laser control panel to ensure that the absorbed power would remain constant across the samples being measured. The spectra for the 10, 25, and 50 nm Au films are displayed in Figure 4.3.

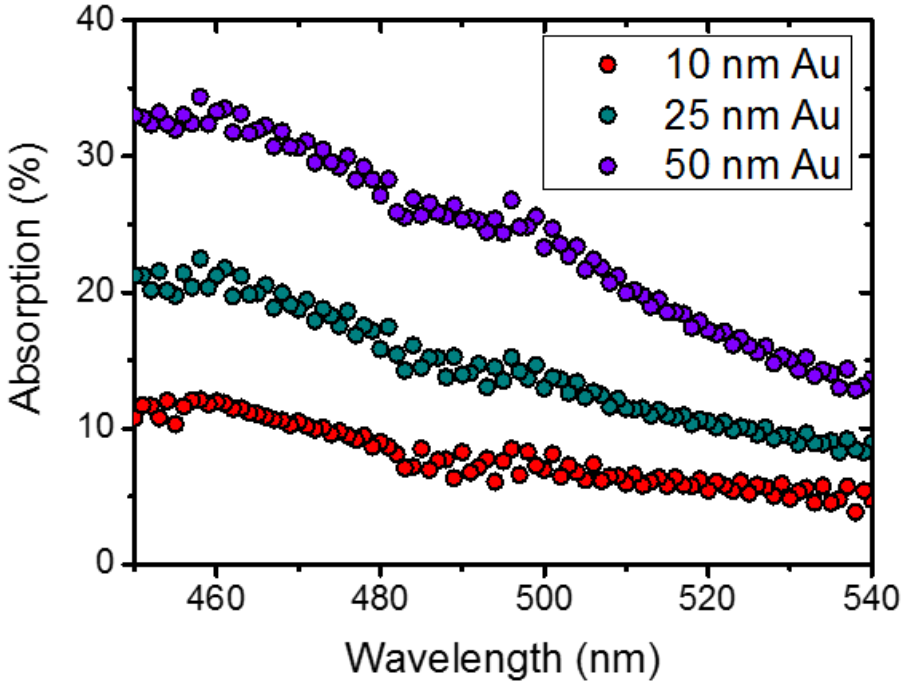

Figure 4.3: absorption spectra for 10 nm, 25 nm, and 50 nm Au films, in the range from 450 nm to 540 nm.

SEM images were obtained using a Zeiss ULTRA scanning electron microscope. All images were obtained with an accelerating voltage of 5 keV, and using the SE2 detector. As all films were deposited on SiO_2 substrates, Ag conductive paint (RS Components) was used to ground the samples during imaging in order to negate charging effects.

TEM images and SAED patterns were obtained using a JEOL 2100F transmission electron microscope, with a spherical aberration corrector. The beam was operated at 200 kV in all

instances of use. For these studies, Au films of thickness 10 nm, 25 nm, and 50 nm were deposited on Hummingbird TEM grids with a 50 nm SiO_x membrane.

4.2.1 CCD-thermoreflectance (CCD-TR)

CCD-thermoreflectance (CCD-TR) is a technique which allows diffraction limited measurement of the local temperature rise by monitoring small changes in the light reflected from the sample. As the refractive index of a material will be dependent on its temperature, the reflectivity will vary depending on the temperature of the material[16]. The reflectivity of Au is strongly temperature dependent in the visible spectrum (see Figure 4.4), with a value of -2.2×10^{-4} K^{-1} at the monitoring wavelength of 515 nm [17].

Each CCD-TR measurement is an average of 1000 temperature cycles at 4 Hz resulting in a temperature resolution of 0.7 K. 1000 temperature cycles are required so that the results converge to the "true" value, as at lower cycles there will be a statistical bias[18]. The peak temperature rise was monitored and plotted for a range of absorbed powers. As in the case of the back-reflected laser measurements, the total absorbed power in each case was calculated by taking into account losses of the microscope system and the transmission and reflection of the thin films.

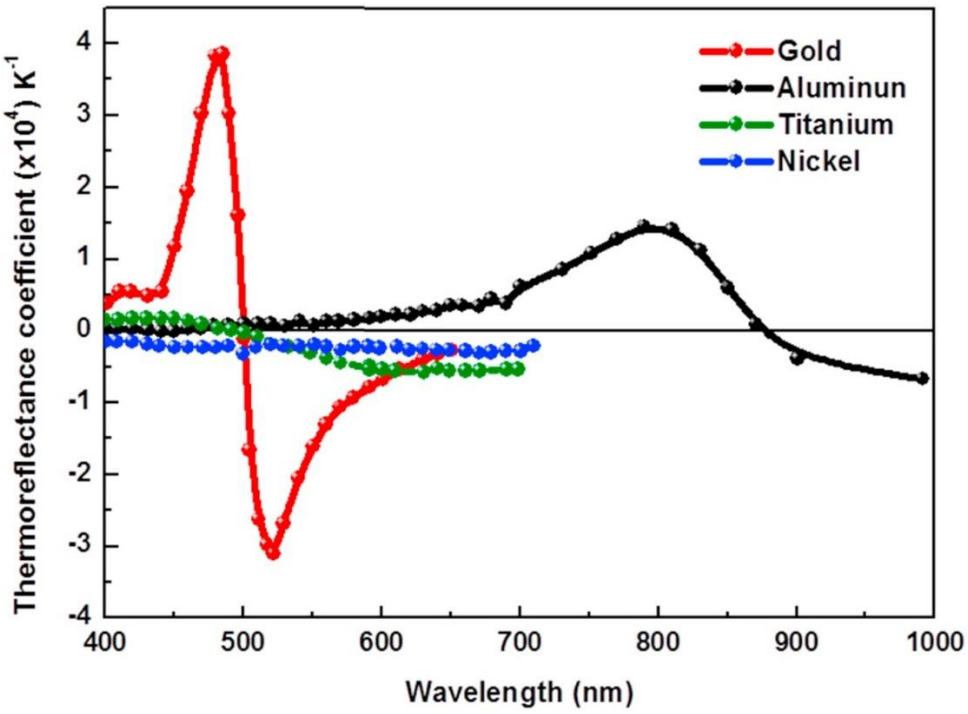

Figure 4.4: thermoreflectance coefficients of different metals as a function of wavelength. Note the highly negative value for Au close to 515 nm, which was the chosen monitoring wavelength for this set of experiments. Taken from reference [19]

4.2.2. Select-area electron diffraction (SAED)

There are several methods for determining the crystalline texture of a film, with the most commonly used techniques involving electron beam microscopy. Select-area electron diffraction (SAED) is one such method. This technique utilizes electron diffraction within a TEM to obtain a diffraction pattern (generally a ring pattern due to the large number of crystallites involved), and the texture can be found by analysing the relative intensity of the diffraction rings. Ignoring dynamic effects, the intensity of a particular diffraction ring for a given crystalline texture can be calculated via the following equation;

$$I_{hkl} = I_0 \lambda^2 \left(\frac{\Phi_{hkl}}{\Omega} \right) \Delta V \frac{d_{hkl}^2 p}{4\pi L \lambda} \tag{4.1}$$

where I_0 is the intensity of the incident electron beam, λ is the wavelength of the beam, Φ is the structure amplitude, Ω is the volume of the unit cell, ΔV is the volume of the crystal, p is the multiplicity factor for hkl planes, & L is the distance between the specimen and the

film[20]. As this equation does not factor in dynamic effects, however, its applicability is not valid for thicker films.

SAED has several advantages in regards to obtaining the texture; it is standard issue in most commercial TEMs, and it can obtain textures for films with very small (> 50 nm) crystal grains. Its disadvantages are that films must be sufficiently thin so that they are electron transparent, and information about individual grains can only be obtained one at a time (assuming that the TEM resolution is sufficiently able to focus on individual grains within the sample).

Crystallographic textures were obtained via SAED patterns generated through electron diffraction in a TEM. So that the samples investigated would be electron transparent, 25 nm Au films were investigated; 1 sample without an adhesion layer, 1 sample with a 2 nm Ti adhesion layer, and 1 sample with a 2nm Cr adhesion layer. The materials were deposited onto a Hummingbird 50 nm SiO_2 grid membrane. The TEM used was a JEOL 2100F, which was equipped with a spherical-aberration corrector. A 200 kV beam voltage was used in all instances of use. The resulting SAED patterns were analysed using Gatan software so that peaks could be obtained. The operation of the TEM tool in obtaining SAED patterns is discussed in detail in chapter 3. No X-Ray diffraction (XRD) measurements were taken for this study.

4.3 Results & Discussion

4.3.1 Measurement of the onset temperature for laser-induced dewetting

In order to determine the onset temperature for laser-induced dewetting, a CCD-TR map was taken of the samples during the laser-annealing process. An example map is shown in Figure 4.5a, for an absorbed power of 2.5 mW and a beam waist of 22.7 μm. The irradiating laser produces a localized temperature rise with a Gaussian profile. To confirm this, a 2D profile was taken of the CCD-TR map, and was fitted with a Gaussian line shape (Figure 4.5b). The fitting parameters calculated a beam waist of 22.0 ± 0.2 μm, which is close to the measured beam waist of 22.7 μm.

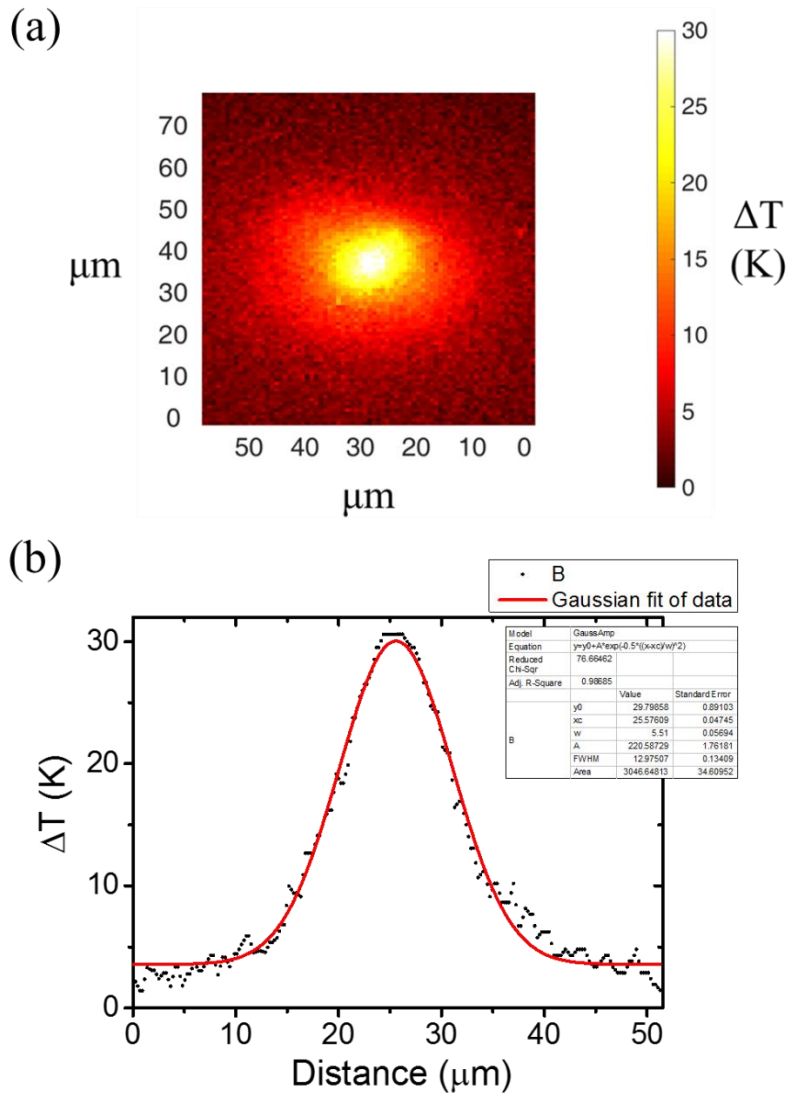

Figure 4.5: (a) CCD-TR image of laser-irradiated area, below the dewetting threshold. (b) Gaussian fit of CCD-TR heat-map

By extracting the maximum temperature rise for a given input power from the CCD-TR images, the validity of Equation 2.14 can be elucidated. Based on Equation 2.14, a linear dependence is expected for the relationship between the peak temperature and absorbed power, and an inverse dependence for the temperature rise and beam waist. These linear dependences are validated for low powers (< 4 mW) for three beam waists of 22.7 μm, 11.4 μm, and 1.8 μm (Figure 4.6). Tighter focusing results in a higher temperature rise as expected, however this is partially compensated by the increase in effective thermal conductivity for smaller beam waists. This increase in effective thermal conductivity is due to the smaller ratio of beam area (the source of heat within the film) to beam circumference (the boundary from which the heat will conduct into the rest of the film): the lateral heat flux within the thin film will become more effective as there is effectively more conduction

pathways for the heated area to conduct to. By fitting the data with Equation 2.14, the thermal conductivity of the film can be extracted. Values of 266 ± 7 W/m/K, 261 ± 2 W/m/K, and 259 ± 6 W/m/K were measured for beam waists of 1.8 μm, 11.4 μm, and 22.7 μm, respectively. In order to confirm the validity of the measurements, the thin film electrical conductivity was measured using a four-point probe technique. For the case of metals where heat is transferred predominantly by free electrons, the Wiedemann-Franz-law relates the electrical and thermal conductivity via

$$\kappa = L\sigma T \tag{4.2}$$

where the Lorentz number L = 2.44x10^{-8} W/m/K^2 is an empirical constant, and T is the absolute temperature. Using this approach, an electrical resistivity of 1.59 × 10^{-8} Ωm was measured for the 50 nm Au film. Using Equation 4.2, a value of κ = 261 W/m/K was calculated. This agreement confirms that the temperature rise at the surface of the Au film is being accurately measured. The Au thin film thermal conductivity has been reduced from the bulk value of 314 W/m/K due to electron scattering from the surface interface and the grain boundaries, and compares well with other reduced values reported in the literature[21].

When the absorbed power is > 4 mW, there is a noticeable decrease in the slope for the plotted data. This is the result of solid-state dewetting occurring in the Au film, which causes a permanent change in the reflectivity of the film (see Figure 4.7). Due to this, the temperature of the film cannot be measured, as the reflectivity change from the dewetting cannot be decoupled from that caused by the thermoreflectance effect. In order to know the temperature, it is necessary to use equation 2.14, whose validity was confirmed for absorbed powers ≤ 4 mW and is assumed to be valid for greater temperatures. As the thermo-reflectance effect is so small, it can be taken that it does not alter the validity of equation 2.14. It is expected, however, that solid-state dewetting will occur at powers ≤ 4 mW and given enough irradiation time. Due to the inherent non-constant heat source used in CCD-TR, however, it is not expected that solid-state dewetting will occur during the measurements at theses lower powers.

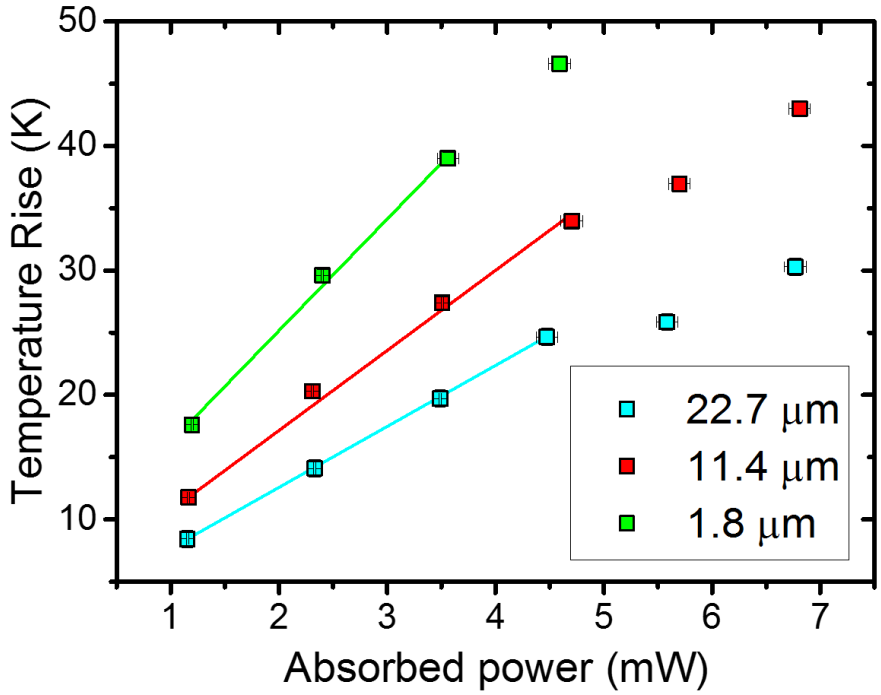

Figure 4.6: plot of induced film temperature increase as a function of absorbed laser power for different beam waists. The linear relationship breaks down once the film begins to undergo solid-state dewetting.

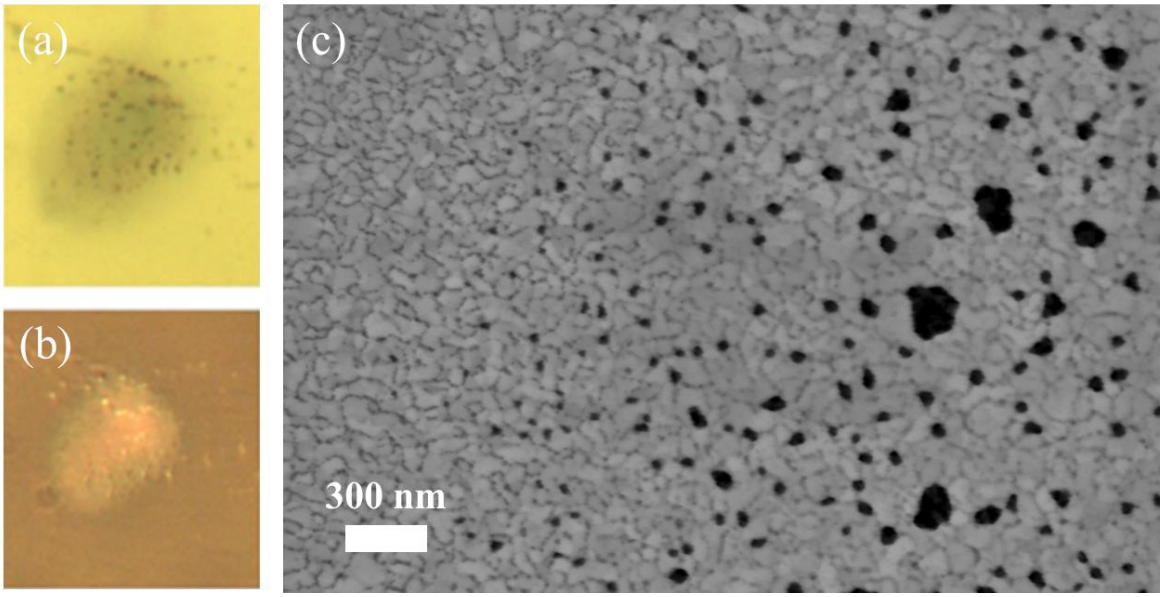

Figure 4.7: change in macroscopic optical properties for a dewetted film, irradiated with 5 mW absorbed power with a beam waist of 22.7 μm. (a) induced reflectivity decrease, (b) induced transmission increase, (c) SEM of area shown in (a) and (b).

4.3.2 Laser-induced dewetting

SEM imaging was used to investigate the effect of laser-irradiation on the heat-affected area of the 50 nm Au film. The film was irradiated with 1 mW absorbed power with a beam waist of w_0 = 1.8 μm, for 120 s. This measurement was performed separately to the CCD-TR measurements, to ensure a continuous irradiation. Figure 4.8 shows the extent of the dewetting that occurred. Despite a relatively low absorbed power, dewetting can still be clearly observed. This demonstrates how susceptible Au films are to laser-induced degradation. It must be noted that, as the absorbed power is only causing an induced maximum temperature increase of ~ 10 K, the dewetted area is still smaller than the beam waist. Aside from the main dewetted area, other changes in the film quality can be observed. By comparing the enlarged areas in the Figure 4.8b and Figure 4.8c, a noticeable increase in the grain size can be seen in the area close to the irradiation centre. There are a significant number of voids close to the heat-affected zone, mainly at grain boundaries and triple points, where the film has already begun to dewet. The contrast between the different grains has also increased, due to the grain boundary grooving that occurs at the onset of dewetting[22]. Additionally, some hillocks can be observed near the edge of the heat affected zone, which will be discussed later in the chapter.

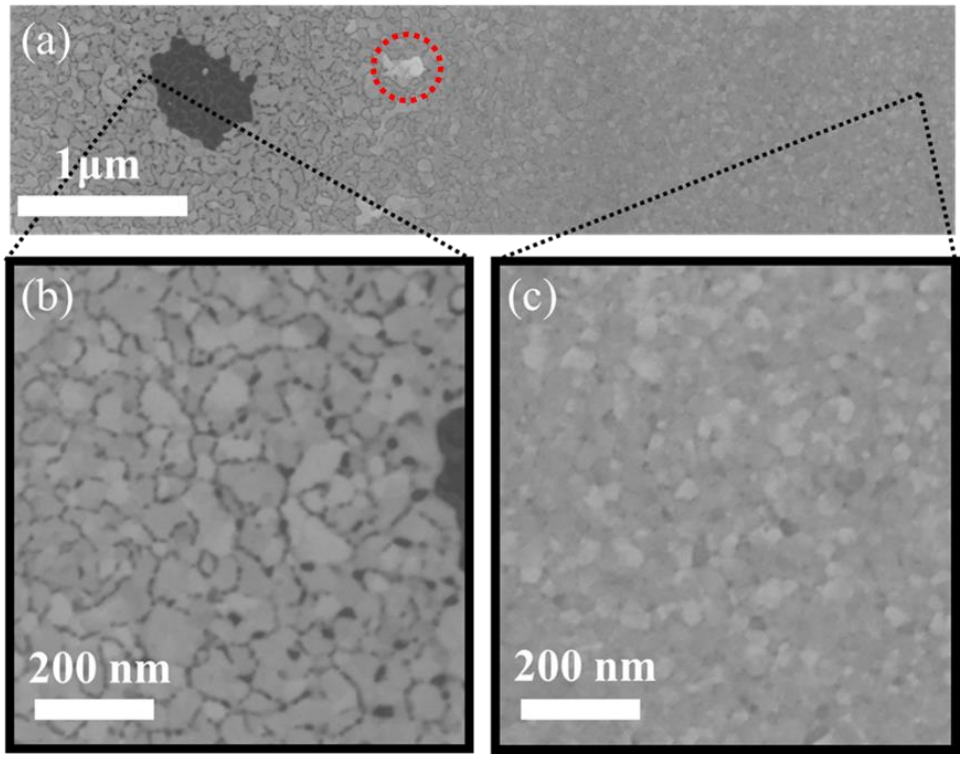

Figure 4.8: (a) Stitched-together SEM images of dewetted film after prolonged laser irradiation at 1 mW absorbed power, (b) close-up of area near irradiation point, and (c) close-up of pristine area outside of heat-affected zone. Red dashed circle highlights a hillock present near the laser-irradiated area.

In Figure 4.9, the reflectivity curves for the 50 nm Au film at different absorbed powers are shown. For all experiments, the beam waist was 2.95 μm. As the magnitude of the absorbed power increases, the rate of dewetting increases. This is fully expected, as larger absorbed powers will result in higher temperatures (as shown by equation 2.14), and higher temperatures result in faster rates of dewetting (as shown by equation 2.10). Due to the inherent noise in the measurements, it is necessary to take multiple measurements and obtain an average.

From the averaged reflectivity curves, the dewetting half-life ($T_{½}$) was extracted by measuring the time at which the normalized reflectivity had reached half the difference between its original and final value. Due to the complex nature of the dewetting process, we found that the curve did not follow a simple exponential or bi-exponential decay. The value of $T_{1/2}$ does however provide a metric for comparison of the films stability. The values are plotted as a function of absorbed laser power in Figure 4.10. By way of comparison, $T_{1/2}$ values for 2 nm Ti/50 nm Au and 2 nm Cr/50 nm Au films are included. As can be clearly seen, the adhesion layers make the Au much more stable against dewetting, with the 2 nm Ti/50 nm Au film by far the most stable film. The characteristic time varies by close to 3 orders of magnitude between the 50 nm Au film and the 2 nm Ti/50 nm Au film at higher absorbed powers. The 2 nm Cr/50 nm Au film film, while less stable than the Au:Ti film by approximately 1 order of magnitude, is also much more stable than the unadhered Au film (by 1 order of magnitude).

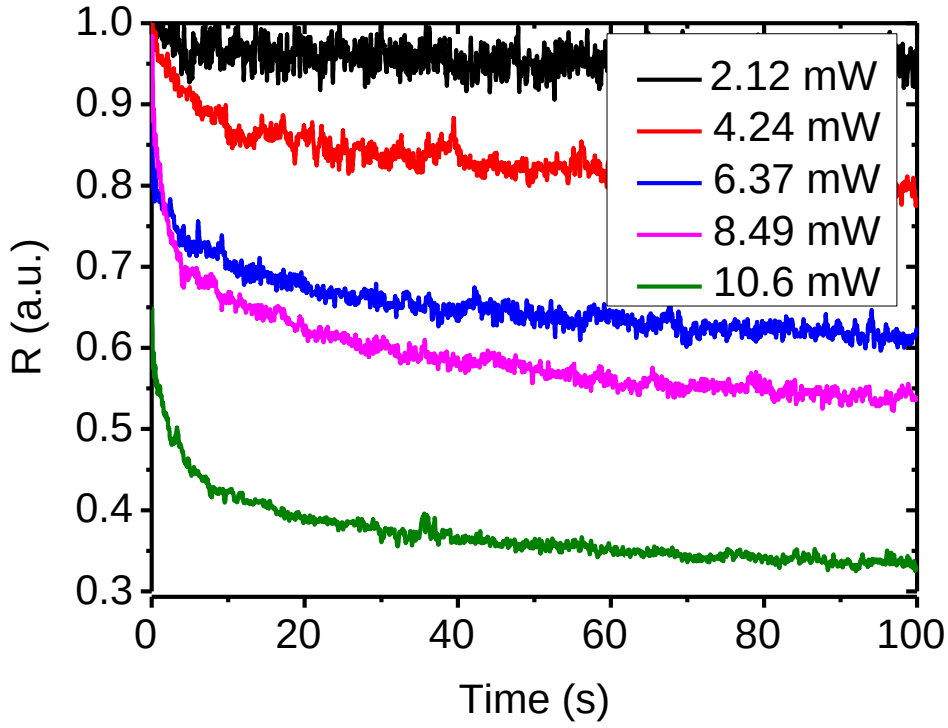

Figure 4.9: change in reflectivity for 50 nm Au film during laser irradiation at different absorbed powers.

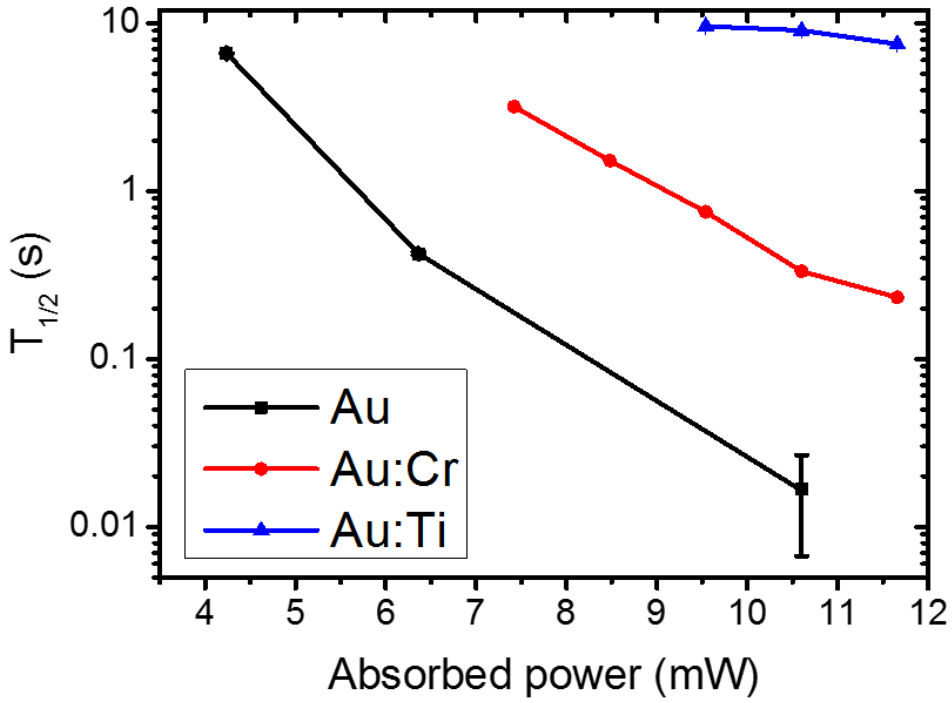

Figure 4.10: $T_{1/2}$ values measured for 50 nm Au, 2 nm Cr/50 nm Au, and 2 nm Ti/50 nm Au films for different absorbed powers. Beam waist was 2.95 μm for all measurements. Error bars for $t_{1/2}$ values greater than 0.1 are smaller than symbols. Lines are added to guide the eye.

The characteristic dewetting time is also expected to be strongly dependent on the film thickness as per Equation 2.10. In Figure 4.11, the reflectivity curves for Au films of thickness 10 nm, 25 nm and 50 nm are shown. The reflectivity of Au decreases upon decreasing thickness, hence the original reflectivities were normalized to 1. The absorbed power for each film was 5 mW, with a beam waist of 2.95 μm. The 50 nm film dewetted at the slowest rate of the films investigated, with the 10 nm film dewetting at the quickest rate. The rate of dewetting for the 10 nm film was so rapid, that the reflectivity dropped to its minimum value within 2×10^{-3} s.

As before, the half-life $T_{1/2}$ was extracted from each reflectivity curve, so that a quantitative comparison between the film stabilities could be made. $T_{1/2}$ values were measured for 10 nm, 25 nm, and 50 nm Au films with and without a 2 nm adhesion layer of either Cr or Ti. The $T_{1/2}$ values are plotted in Figure 4.12. $T_{1/2}$ was first plotted as a function of $1/h^3$ (Figure 4.12a), as would be suggested by Equation 2.10. The thermal conductivity (and hence the temperature) of the laser-irradiated film will change as dewetting occurs, hence it is not appropriate, so the data was then plotted as a function of thickness (Figure 4.12b). As was shown in Figure 4.10, the use of adhesion layers significantly improves the stability of Au films against dewetting. In particular, the 2 nm Ti/50 nm Au film was so stable that a characteristic degradation time could not be obtained at powers less than 5 mW. As the films become thinner, however, the benefit of the improved adhesion begins to become outweighed by the decrease in film thickness. Based on the data shown, the stability of the films drops drastically when the film thickness is less than 25 nm. As before, the Ti/Au films are the most stable, followed by Cr/Au, and then Au. The adhesion layer has a much more pronounced effect for the 10 nm films, due to their greater tendency towards dewetting.

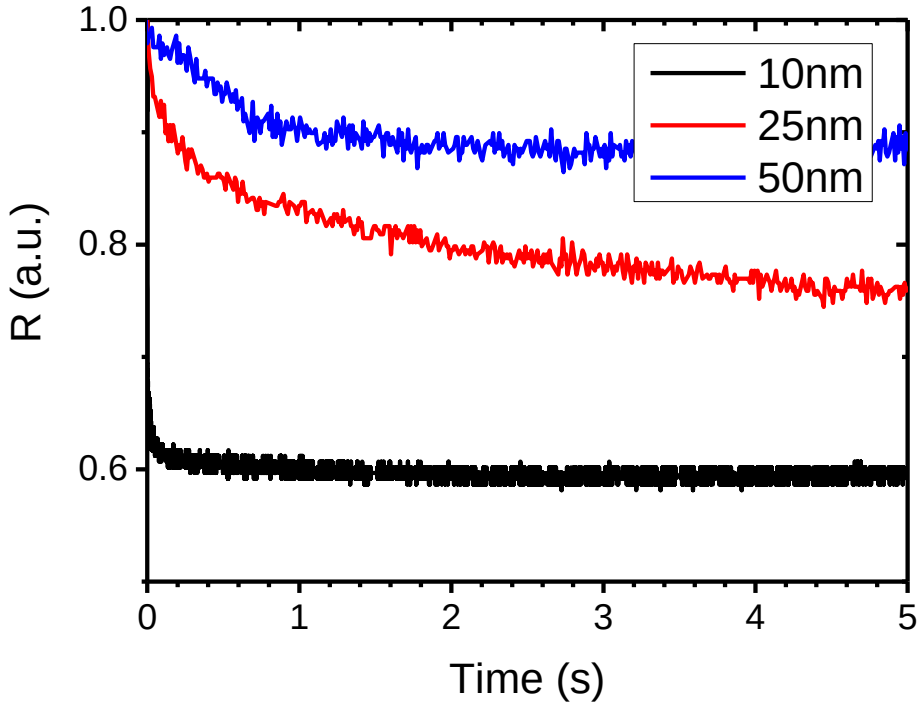

Figure 4.11: change in reflectivity for Au films of different thicknesses during laser irradiation

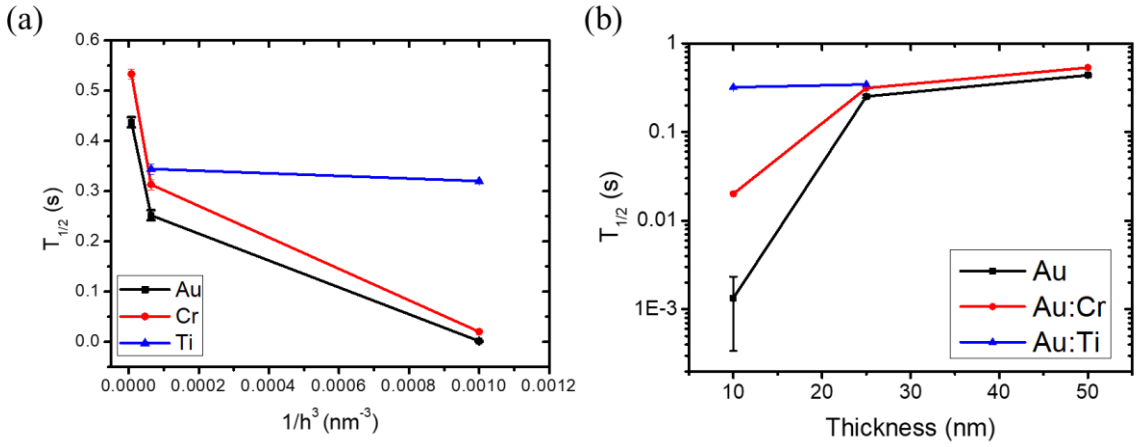

Figure 4.12: $T_{1/2}$ values measured for Au, Cr/Au, and Ti/Au films with varying thickness of Au, plotted as (a) $1/h^3$, and (b) h. The absorbed power for each film was maintained as 5 mW for each sample, with a beam waist of 2.95 μm. Error bars for $t_{1/2}$ values greater than 0.01 are smaller than symbols. Dashed lines are added to guide the eye.

A qualitative analysis of the effectiveness of the adhesion layers was performed via imaging the irradiated films after a fixed irradiation time. Figure 4.13 shows a comparison of TEM images from each film after irradiation with an incident power of 10 mW (hence with different absorbed powers) with a beam waist of 2.95 μm for 5 s. It must be noted that the scale bars are different for different images, so that the laser-affected areas for each film can be seen clearly. The bright central regions are areas where the film has completely dewetted from the substrate. The surrounding regions show speckled contrast in which the dark spots indicate the position of voids that have formed during irradiation. Films with large areas of bright contrast indicate films that have undergone significant amounts of solid-state dewetting. The images are in agreement with data in Fig. 4.12, in that they clearly demonstrate the stabilizing effect of both adhesion and film thickness leading to a decrease in size of the dewetted and damaged regions. The most stable system, the 2 nm Ti/50 nm Au film, showed little significant degradation, which is entirely consistent with the inability to obtain a value for $T_{1/2}$, as shown by Fig. 4.12. By contrast, the least stable system, the 10 nm Au film, shows a complete removal of material from the central irradiated region, and the formation of spherical nanoparticles up to 10 μm away from the irradiated region. By analyzing the images using ImageJ, it was found that the particles had an average radius of 54 (± 2) nm, which equates to a mass of 1.01×10^{-17} kg per particle. This is equivalent of the mass in a square area of side 228 nm in the original film prior to the occurrence of solid-state dewetting.

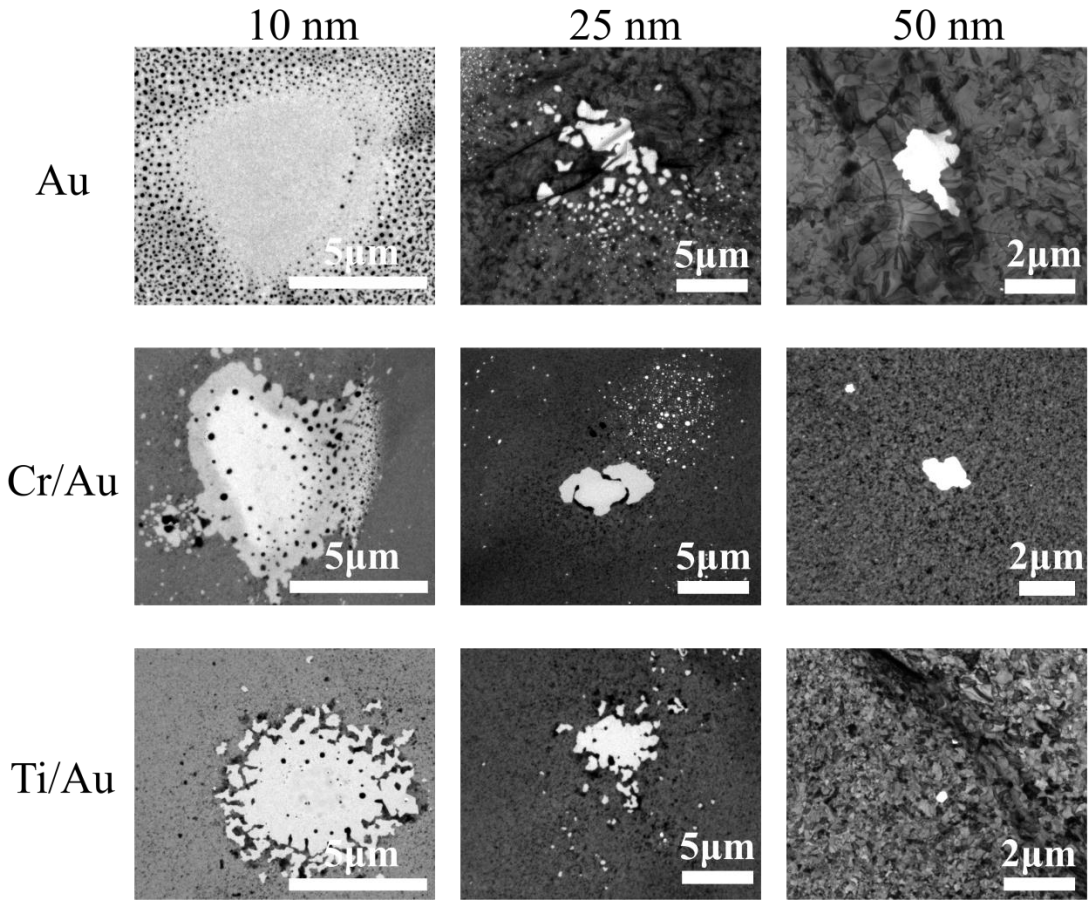

Figure 4.13: TEM images of dewetting as a function of film thickness for differ-ent adhesion layers. The incident laser power and spot size were fixed at 18.25 mW and 2.95 µm respectively. Note the different scale bars for different images.

A change in the film topography was also observed between films with and without an adhesion layers (Figure 4.14). For the 50 nm Au film, there is an increase in the height of the retracting edge, due to material diffusing into it as the voids grow and the film agglomerates[23]. Due to the relatively large irradiating power (20 mW absorbed) and irradiation time (300 s), the agglomeration of the Au results in large particles. By contrast, for the 2 nm Ti/50 nm Au film, the height increases are solely due to material agglomeration in localized areas, as opposed to being evenly distributed along the film edge (the film edges being those areas of the film beside the exposed SiO_2 substrate, itself distinguished by the areas of darker contrast on SEM). These localized areas are known as hillocks[24,25], and can be observed in samples with and without adhesion layers (see Figure 4.15). It has been previously demonstrated that hillocks are formed in thin films during annealing as a way of relieving compressive stress[24]. The formation of hillocks is a further example of thermal instability in an Au film, as such effects would be highly undesirable in the HAMR process, as any changes in the shape of the NFT will likely affect its plasmonic

properties. As their very presence is an indicator of the poor thermal stability of the films, using AFM to measure specific topographic changes was considered unnecessary.

Where this stress originates differs depending on the film in question. In the case of the 50 nm Au film, this stress originates in the deposition of the film. Au thin films deposited on SiO_2 substrates will grow by Volmer-Weber growth[26] (i.e. the Au will form islands or clusters that will eventually coalesce into a continuous film). The initial stress within the film is compressive, but becomes tensile as soon as the clusters begin to coalesce. Once the film becomes continuous, the tensile stress reduces, eventually returning to a compressive state[27–29]. There was initially a certain degree of debate as to the source of this compressive stress, until it was found to be due to capillary effects that occur during the precoalescence stage of the film growth[29]. The origin of the compressive stress in Ti/Au films will be discussed in greater detail in Chapter 5.

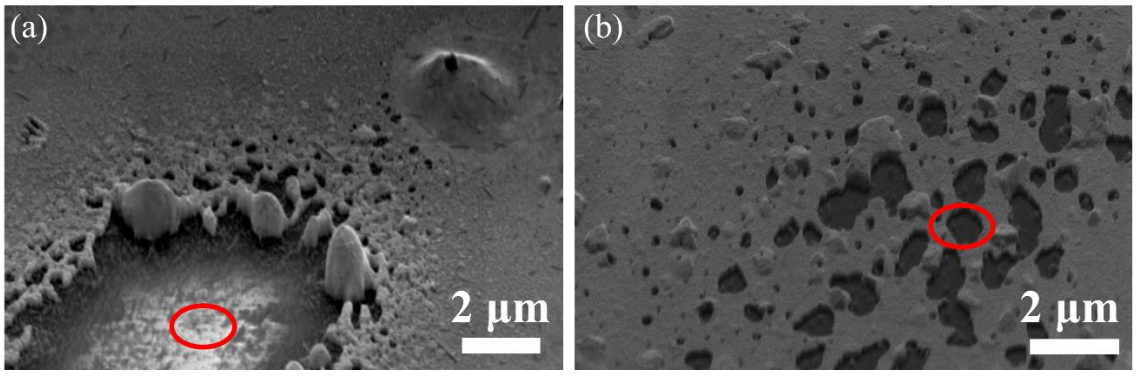

Figure 4.14: Angled (70°) SEM images showing topography changes in (a) 50 nm Au film, and (b) 2nm Ti/50 nm Au film after laser irradiation. Films were irradiated with 20 mW of absorbed power, with a beam waist of 22.7 µm. Centre of the irradiated area in each image is marked in red.

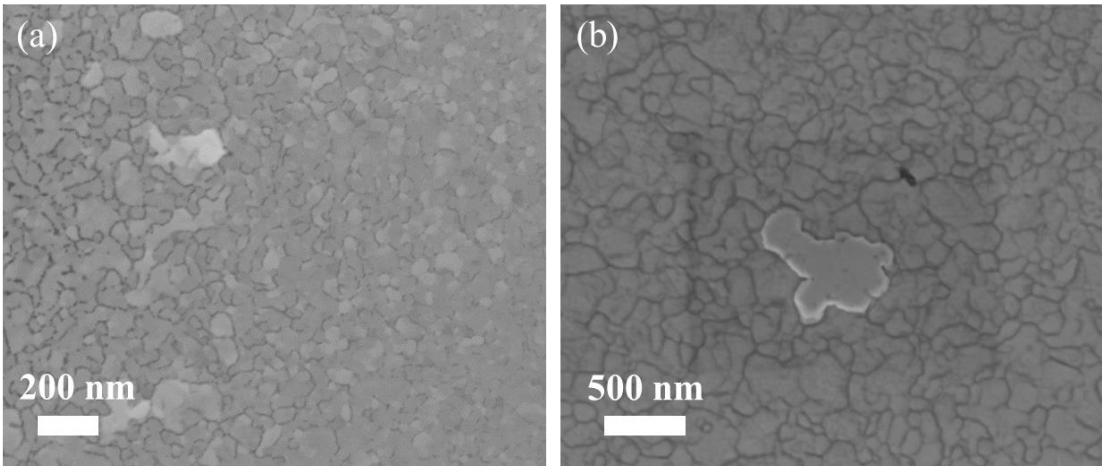

Figure 4.15: SEM images comparing hillocks formed in (a) 50 nm Au film, and (b) 2 nm Ti/50 nm Au film

4.3.3. Laser-induced grain growth in Au thin films

A comparison of the grain growth behaviour for 25 nm Au films with and without adhesion layers can be seen in Figure 4.16. The grain size was measured by measuring the size of individual grains using ImageJ image processing software by measuring the length of the grain along its longest axis, and averaging the results using OriginLab software. Prior to irradiation, the films each had an average grain size of 25.4 ± 0.6 nm. Previous studies on the effect of adhesion layers on grain development have shown that adhesion layers will result in a more homogenous distribution of grain sizes (averaging at 40 nm and 36 nm for Ti/Au and Cr/Au films, respectively)[30]. This was not the case for the films fabricated for these experiments. For the Au film without an adhesion layer, this average increased to 200 ± 10 nm at a distance of 7 μm away from the irradiation centre, i.e. close to an eightfold increase. This distance away from the irradiation centre was chosen for analysis as it was the closest point to the irradiation centre that had not experienced significant solid-state dewetting. By comparison, the grain size increase at this distance for films with a Ti or Cr adhesion layer are 30.8 ± 0.6 nm and 26.1 ± 0.5 nm, respectively. From this result, it can be seen that the grain growth is highly dependent on the adhesion of the Au film to its substrate.

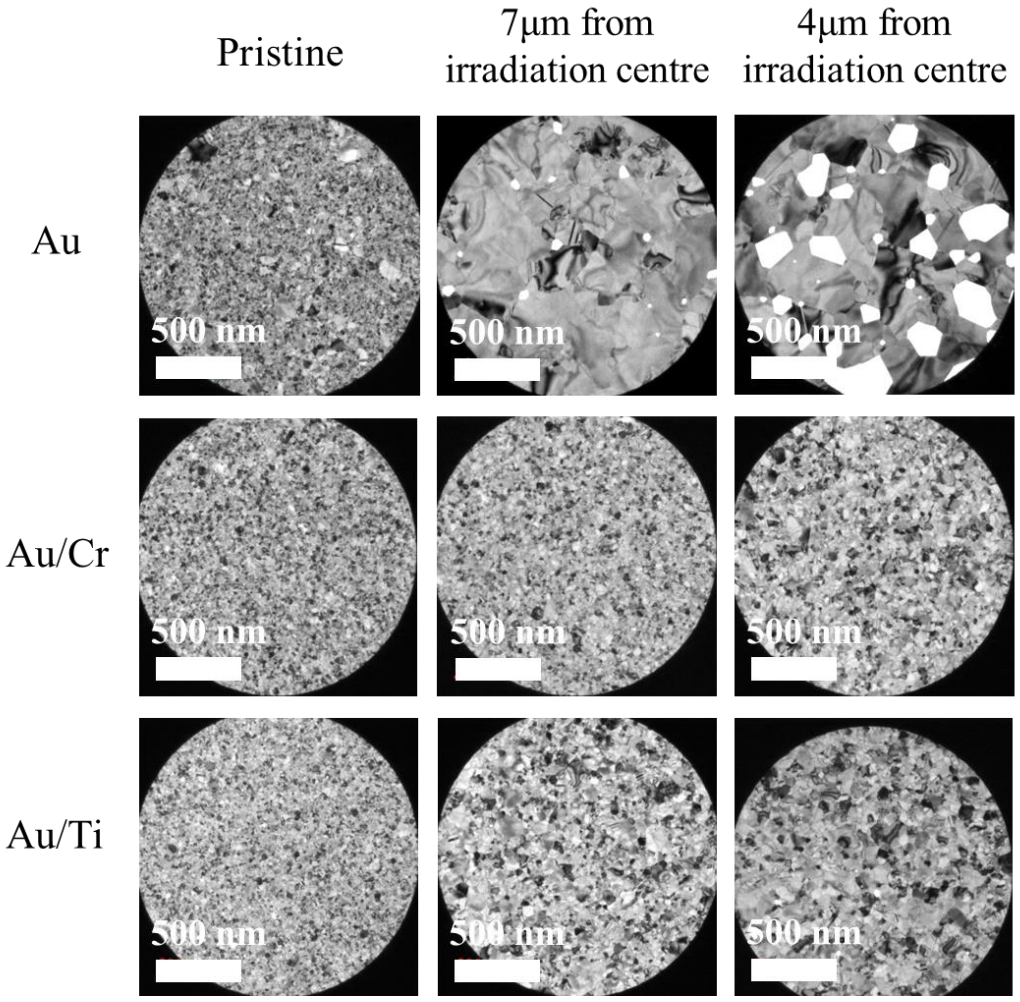

Figure 4.16: chart demonstrating laser-induced grain growth in Au thin films, with and without adhesion layers.

4.3.4. Laser-induced texturing in Au thin films

For the as-deposited films, the diffraction pattern can be observed in Figure 4.17a. The intensity ratios of the peaks are indicative of a randomly-oriented texture. As the films were deposited at room temperature, this result is not an anomaly; the crystallites did not have sufficient energy to reorient themselves into a more energetically favourable orientation. When the film is isothermally annealed, the diffraction pattern changes significantly (Figure 4.17b). The (220) peak now has the highest intensity by a significant margin. The peaks that occur in a polycrystalline sample with a preferred out-of-plane orientation will mainly occur from lattice planes whose normal is perpendicular to the out-of-plane orientation[11]. Hence, this result indicates that the film now has a [111] texture. As the (111) facet has the lowest surface energy for FCC metals (such as Au), a [111] texture would result in the lowest surface energy for each crystallite, and for the film as a whole. A

[111] texture regularly forms when Au is deposited above room temperature[11], as there is sufficient thermal energy for the crystallites to reorient themselves.

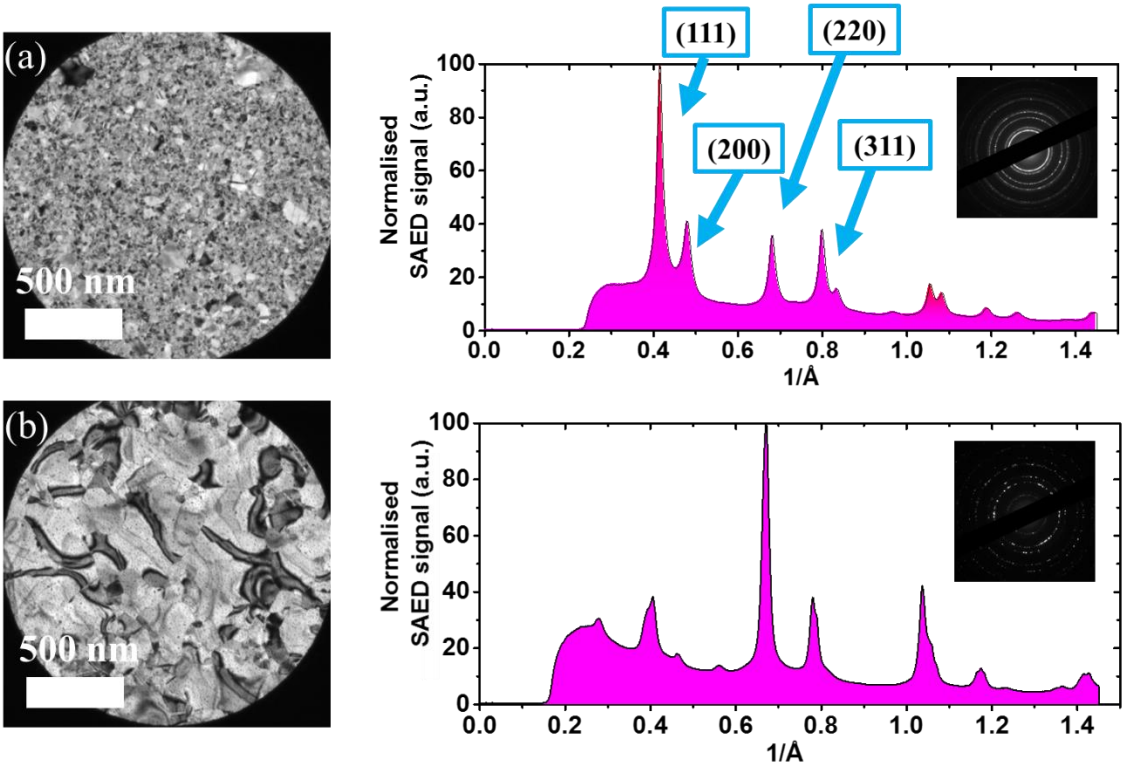

Figure 4.17: diffraction peaks for 25 nm Au film annealed at 500°C; (a) pre-anneal, and (b) post-anneal, with original diffraction patterns as inserts.

In the case of Au films that have been heated via laser irradiation, the texture development differs significantly from that of the isothermally-heated case. The comparison is shown in Figure 4.18. The diffraction peaks from 3 different areas on a laser-irradiated Au film are displayed; the pattern obtained from the irradiation centre, the pattern obtained from an area ~4μm away from the irradiation centre, and a pristine area outside of the heat-affected zone. In the central area, only an amorphous background signal can be seen, demonstrating the dewetting of the film directly under the irradiating laser. Outside of the central area, the Au displays unusual diffraction peaks; a dominant (111) peak, weak (220) & (311) peaks, and a complete disappearance of the (200) peak. These do not correspond exactly with any regularly observed texture (i.e. the peaks associated with the random orientation or the [111] out-of-plane orientation shown in Figure 4.17), but due to the dominance of the (111) peak, it is most similar with that of a [110] texture. The most likely cause for this occurrence is due to high changes in the film caused by dewetting; as the film increases in height and can no longer be considered 2-dimensional, the out-of-plane face is now no longer automatically the largest face of the film as a whole. Hence, it will

become more energetically favourable for lower energy facets (such as (111)) to reorient to directions that are no longer out of plane[31,32] . This unusual Au texture could be seen strongly throughout the heat-affected areas of the film, and could be observed up to a distance of 10 µm away from the irradiation centre (see Figure 4.19).

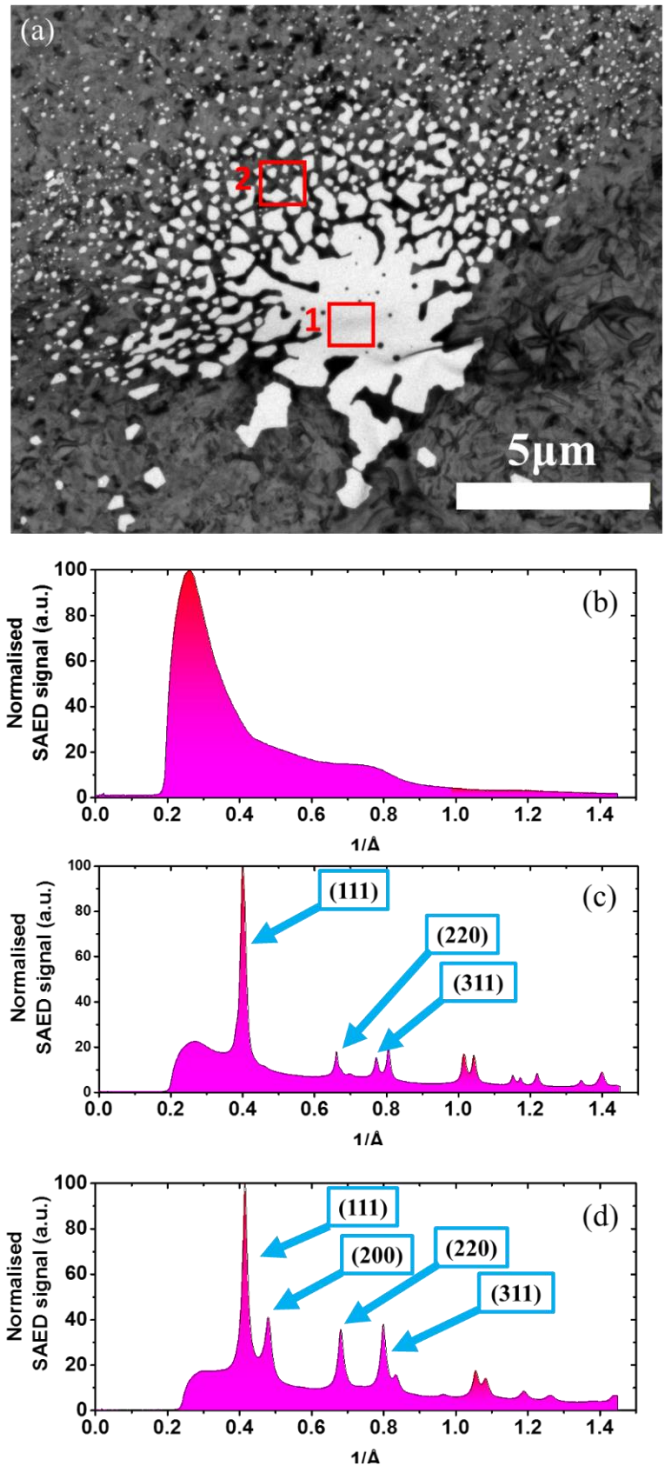

Figure 4.18: laser-induced texturing in 25 nm Au film; (a) TEM image of area under investigation, (b) diffraction peaks for area 1, (c) diffraction peaks for area 2, (d) diffraction peaks for the film pre-laser anneal

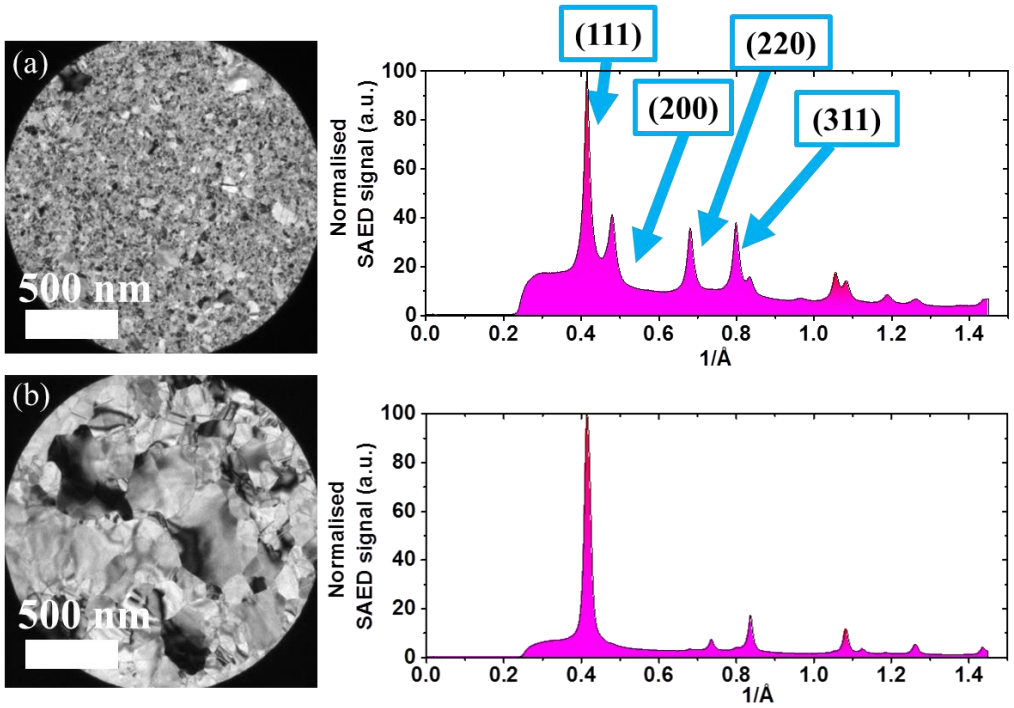

Figure 4.19: diffraction peaks for 25 nm Au film (a) pre-laser anneal, and (b) post-laser anneal, 10 um from irradiation centre.

The use of metallic adhesion layers has previously been shown to significantly increase the thermal stability of Au films (see Figure 4.12), and previous work has shown that using adhesion layers will result in a well-defined [111] out-of-plane texture[30]. A random crystalline texture was observed, however, for as-deposited 2 nm Ti/25 nm Au films (see Figure 4.20). This is potentially due to the small grain sizes observed in the pre-annealed samples, which generally result in randomly orientated textures[13]. Upon isothermal annealing at 500°C, a prominent [111] texture developed, as was the case with the isothermally annealed 25 nm Au film without an adhesion layer.

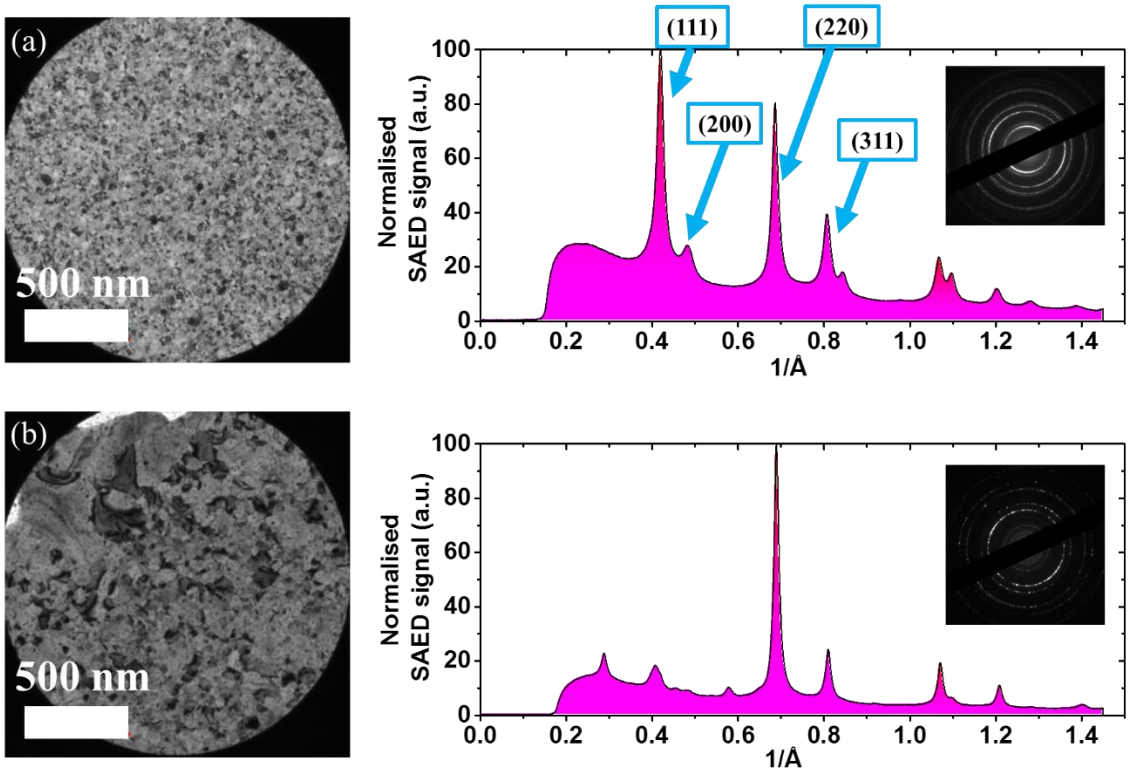

Figure 4.20: diffraction peaks for 2 nm Ti/25 nm Au film annealed at 500°C; (a) pre-anneal, and (b) post-anneal, with original diffraction patterns as inserts

For the case of laser-irradiated Au films with an adhesion layer, the resulting crystalline texture is again different. The diffraction ring patterns for 25 nm Au films with 2nm Cr and Ti adhesion layers can be seen in Figure 4.21. Initially, the patterns look as typical diffraction rings, but on closer inspection strong arcs can be seen within the (111) and (220) rings, which appear perpendicular to each other. This is in strong contrast with the pre-anneal diffraction patterns, where continuous rings can be seen (see Figure 4.20a). When referenced against standard fcc diffraction patterns[33], it was found that the (111) and (220) reflections were only perpendicular with each other when $[11\bar{2}]$ was the out-of-plane orientation. Hence, these arcs suggest a preferred $[11\bar{2}]$ out-of-plane orientation, and additionally a certain level of preferred orientation in-plane. The crystallographic texture where there is a preferred in-plane and out-of-plane orientation is known as a "biaxial texture". A schematic detailing this texture is shown in Figure 4.22. In the case of the films detailed here, it is clear that a true biaxial texture is not being observed; if this were the case, then a van-Laue diffraction pattern would be observed. As the pattern produces prominent arcs, it suggests that there is a small spread with the in-plane orientation. Hence,

it can be said that these films display a *pseudo-biaxial texture*[7]. The reason for this in-plane orientation spread is due to the use of a laser as a heat source.

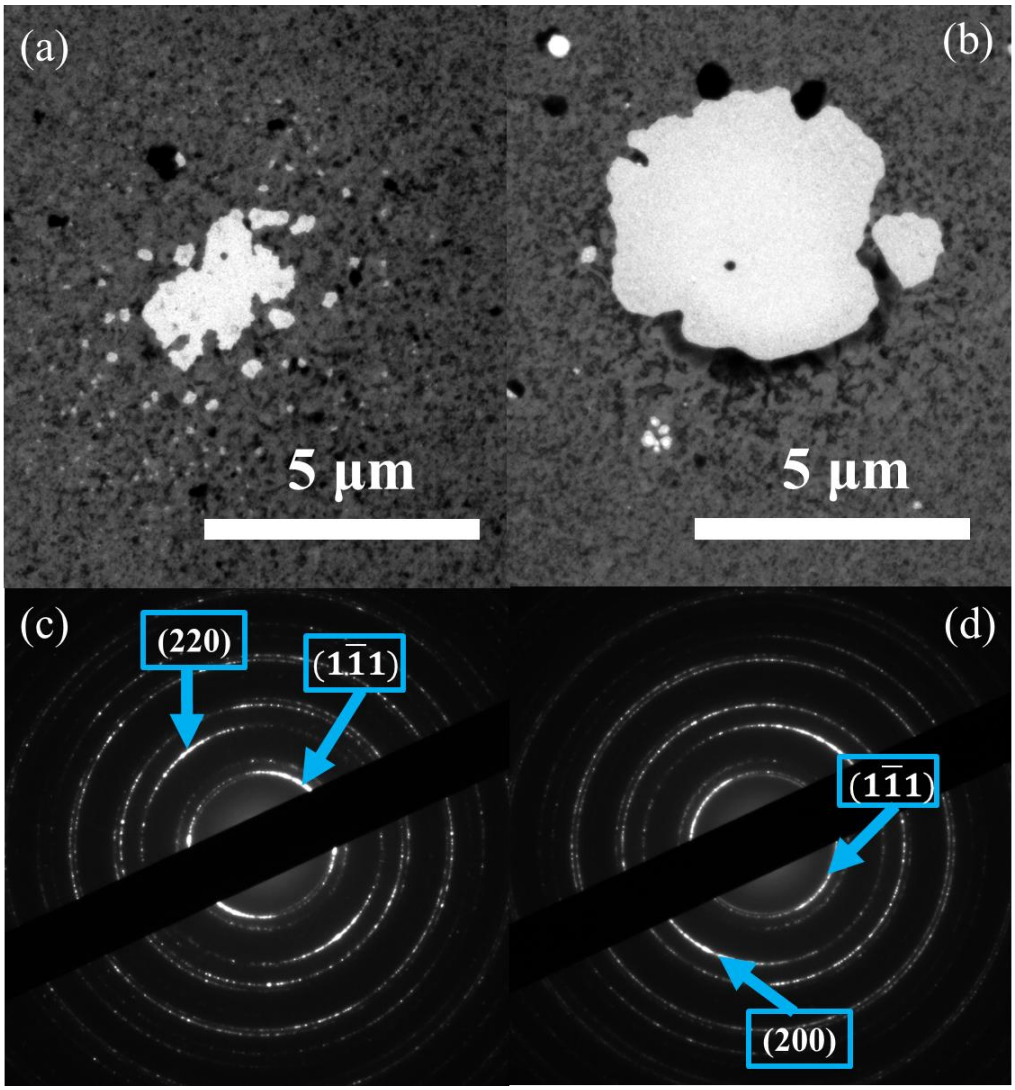

Figure 4.21: demonstration of pseudo-bixial texture in Au films. (a) laser-irradiated area of 2 nm Ti/25 nm Au film, (b) laser-irradiated area of 2 nm Cr/25 nm Au film, (c) diffraction pattern obtained for Ti/Au film, (d) diffraction pattern obtained for Cr/Au film.

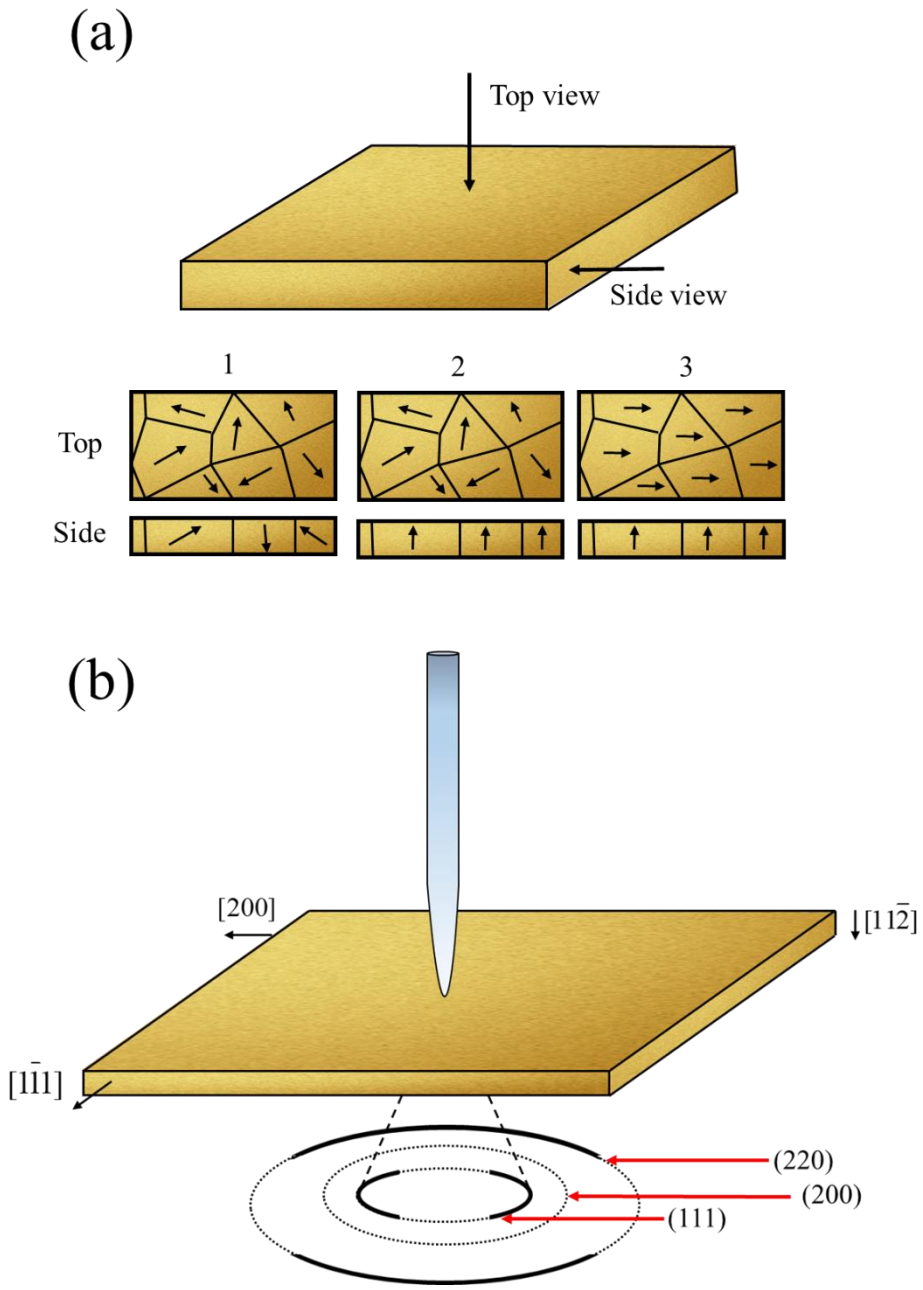

Figure 4.22: (a) types of crystallographic textures in polycrystalline thin films; random (1), uniaxial texture (2), biaxial texture (3). (b) schematic demonstrating electron-diffraction by a pseudo-biaxially textured film.

4.4 Conclusions

In this chapter, the dewetting dynamics of CW-laser-irradiated Au films was studied. CCD-TR was used to evaluate the minimum temperature increase required to induce solid-state dewetting, and it was found that dewetting would occur for a 50 nm Au film at a temperature increase of 50^{o}C. The effect of film thickness, adhesion, and input power was studied. The rate of dewetting is strongly correlated with the input absorbed power, and

films with larger thicknesses are less susceptible to dewetting. Standard 2 nm metal adhesion layers will significantly increase the thermal stability of the Au, with Cr increasing stability by 1 order of magnitude and Ti by 2 orders of magnitude. Hillocks will form in Au films during the dewetting process, with a greater density of hillocks being formed for Ti/Au films.

Additionally, the effect of laser annealing on the crystallographic properties of Au thin films was studied. The growth of Au grains during annealing is inhibited when an adhesion layer is used. A 25 nm Au film will develop a [110] out-of-plane texture when laser annealed: as the film dewets, it can no longer be considered 2-dimensional system and the largest surface area is no longer necessarily facing out-of-plane. In the case of 25 nm Au films with 2 nm Cr/Ti adhesion layers, a pseudo-biaxial texture will develop, with the $[11\bar{2}]$ in-plane orientation directed outwards from the laser-annealed area.

4.5 Bibliography

(1) Trice, J.; Thomas, D.; Favazza, C.; Sureshkumar, R.; Kalyanaraman, R. Pulsed-Laser-Induced Dewetting in Nanoscopic Metal Films: Theory and Experiments. *Phys. Rev. B - Condens. Matter Mater. Phys.* **2007**, *75* (23), 235439.

(2) Rack, P. D.; Guan, Y.; Fowlkes, J. D.; Melechko, A. V.; Simpson, M. L. Pulsed Laser Dewetting of Patterned Thin Metal Films: A Means of Directed Assembly. *Appl. Phys. Lett.* **2008**, *92* (22), 223108.

(3) Fowlkes, J. D.; Wu, Y.; Rack, P. D. Directed Assembly of Bimetallic Nanoparticles by Pulsed-Laser-Induced Dewetting: A Unique Time and Length Scale Regime. *ACS Appl. Mater. Interfaces* **2010**, *2* (7), 2153–2161.

(4) Roberts, N. A.; Magel, G. A.; Hartfield, C. D.; Moore, T. M.; Fowlkes, J. D.; Rack, P. D. In Situ Laser Processing in a Scanning Electron Microscope. *J. Vac. Sci. Technol. A Vacuum, Surfaces, Film.* **2012**, *30* (4), 041404.

(5) Nikov, R. G.; Nedyalkov, N. N.; Atanasov, P. A.; Hirsch, D.; Rauschenbach, B.; Grochowska, K.; Sliwinski, G. Characterization of Ag Nanostructures Fabricated by Laser-Induced Dewetting of Thin Films. *Appl. Surf. Sci.* **2015**.

(6) Oh, Y.; Lee, M. Single-Pulse Transformation of Ag Thin Film into Nanoparticles via Laser-Induced Dewetting. *Appl. Surf. Sci.* **2017**, *399*, 555–564.

(7) Abbott, W. M.; Corbett, S.; Cunningham, G.; Petford-Long, A.; Zhang, S.; Donegan, J. F.; McCloskey, D. Solid State Dewetting of Thin Plasmonic Films under Focused Cw-Laser Irradiation. *Acta Mater.* **2018**, *145*, 210–219.

(8) Douaud, A.; Messaddeq, S. H.; Boily, O.; Messaddeq, Y. Laser-Induced Dewetting of Silver-Doped Chalcogenide Glasses. *Appl. Surf. Sci.* **2018**, *445*, 1–7.

(9) Thompson, C. V. Solid-State Dewetting of Thin Films. *Annu. Rev. Mater. Res.* **2012**, *42* (1), 399–434.

(10) Müller, C. M.; Spolenak, R. Microstructure Evolution during Dewetting in Thin Au Films. *Acta Mater.* **2010**, *58* (18), 6035–6045.

(11) Niekiel, F.; Kraschewski, S. M.; Schweizer, P.; Butz, B.; Spiecker, E. Texture Evolution and Microstructural Changes during Solid-State Dewetting: A Correlative Study by Complementary in Situ TEM Techniques. *Acta Mater.* **2016**, *115*, 230–241.

(12) Wang, S. G.; Tian, E. K.; Lung, C. W. Surface Energy of Arbitrary Crystal Plane of Bcc and Fcc Metals. *J. Phys. Chem. Solids* **2000**, *61* (8), 1295–1300.

(13) Thompson, C. V.; Carel, R. Texture Development in Polycrystalline Thin Films. *Mater. Sci. Eng. B* **1995**, *32* (3), 211–219.

(14) Bauer, R. S.; Bachrach, R. Z.; Brillson, L. J. Au and Al Interface Reactions with SiO2. *Appl. Phys. Lett.* **1980**, *37* (11), 1006–1008.

(15) McBrayer, J. D.; Swanson, R. M.; Sigmon, T. W. Diffusion of Metals in Silicon Dioxide. *J. Electrochem. Soc.* **1986**, *133* (6), 1242.

(16) Farzaneh, M.; Maize, K.; Lüerßen, D.; Summers, J. A.; Mayer, P. M.; Raad, P. E.; Pipe, K. P.; Shakouri, A.; Ram, R. J.; Hudgings, J. A. CCD-Based Thermoreflectance Microscopy: Principles and Applications. *J. Phys. D. Appl. Phys.* **2009**, *42* (14), 143001.

(17) Favaloro, T.; Bahk, J. H.; Shakouri, A. Characterization of the Temperature Dependence of the Thermoreflectance Coefficient for Conductive Thin Films. *Rev. Sci. Instrum.* **2015**, *86* (2), 024903.

(18) Mayer, P. M.; Lüerßen, D.; Ram, R. J.; Hudgings, J. A. Theoretical and Experimental Investigation of the Thermal Resolution and Dynamic Range of CCD-Based Thermoreflectance Imaging. *J. Opt. Soc. Am. A* **2007**, *24* (4), 1156.

(19) Abad, B.; Borca-Tasciuc, D.-A.; Martin-Gonzalez, M. S. Non-Contact Methods for Thermal Properties Measurement. *Renew. Sustain. Energy Rev.* **2017**, *76*, 1348–1370.

(20) Vaĭnshteĭn, B. K. (Boris K. *Structure Analysis by Electron Diffraction*; Pergamon Press, 1964.

(21) Schmidt, A. J.; Cheaito, R.; Chiesa, M. Characterization of Thin Metal Films via Frequency-Domain Thermoreflectance. *J. Appl. Phys.* **2010**, *107* (2), 024908.

(22) Jiran, E.; Thompson, C. V. Capillary Instabilities in Thin, Continuous Films. *Thin Solid Films* **1992**, *208* (1), 23–28.

(23) Jiran, E.; Thompson, C. V. Capillary Instabilities in Thin Films. *J. Electron. Mater.* **1990**, *19* (11), 1153–1160.

(24) Kweon, S. Y.; Yeom, S. J.; Sun, H. J.; Kim, N. K.; Yu, Y. S.; Lee, S. K. Intrinsic Stress Dependence of Pt Hillock Formation and Its Related Electrical Properties of SBT Capacitor. *Integr. Ferroelectr.* **1999**, *25* (1–4), 299–309.

(25) Shaffir, E.; Kauffmann, Y.; Riess, I. Void Formation in Gold Films on Yttrium-Doped Zirconia in the Initial Stage of Dewetting. *Acta Mater.* **2014**, *79*, 59–65.

(26) Lee, S.; Hong, J.; Oh, S. Real-Time Ellipsometry Studies of Gold Thin-Film Growth. *Jpn. J. Appl. Phys.* **1997**, *36* (Part 1, No. 6A), 3662–3668.

(27) Floro, J. A.; Hearne, S. J.; Hunter, J. A.; Kotula, P.; Chason, E.; Seel, S. C.; Thompson, C. V. The Dynamic Competition between Stress Generation and Relaxation Mechanisms during Coalescence of Volmer–Weber Thin Films. *J. Appl. Phys.* **2001**, *89* (9), 4886.

(28) Chason, E.; Sheldon, B. W.; Freund, L. B.; Floro, J. a; Hearne, S. J. Origin of Compressive Residual Stress in Polycrystalline Thin Films. *Phys. Rev. Lett.* **2002**, *88*, 156103.

(29) Koch, R.; Hu, D.; Das, a. K. Compressive Stress in Polycrystalline Volmer-Weber Films. *Phys. Rev. Lett.* **2005**, *94* (14), 1–4.

(30) Todeschini, M.; Bastos da Silva Fanta, A.; Jensen, F.; Wagner, J. B.; Han, A. Influence of Ti and Cr Adhesion Layers on Ultrathin Au Films. *ACS Appl. Mater. Interfaces* **2017**, *9* (42), acsami.7b10136.

(31) Gladkikh, A.; Lereah, Y.; Glickman, E.; Karpovski, M.; Palevski, A.; Schubert, J. Hillock Formation during Electromigration in Cu and Al Thin Films: Three-Dimensional Grain Growth. *Applied Physics Letters*. American Institute of Physics March 6, 1995, p 1214.

(32) Wei, H. L.; Huang, H.; Woo, C. H.; Zheng, R. K.; Wen, G. H.; Zhang, X. X. Development of 〈110〉 Texture in Copper Thin Films. *Appl. Phys. Lett.* **2002**, *80* (13), 2290–2292.

(33) Williams, D. B.; Carter, C. B. *Transmission Electron Microscopy: A Textbook for Materials Science*; Springer, 2009; Vol. 11.

Chapter 5: Effect of adhesion layer thickness on Au thin films

5.1 Introduction

In Chapter 4, the dynamics of laser-induced dewetting of Au thin films was studied. It was found that Au films are highly susceptible to laser-induced dewetting, but this can be mitigated via the use of 2 nm Cr or Ti adhesion layers. While there has been a great deal of work in the literature about the effect of film thickness on dewetting dynamics[1,2], at the time of writing there has been no work on the effect that the adhesion layer thickness has on the stability of Au films.

The use of thin oxidizing metallic adhesion layers are a common industry tactic to improve the bonding of Au thin films to oxide substrates[3], with the microelectronics industry in particular having contributed to our collective understanding of this process[4–6]. The results shown in Chapter 4 demonstrate that adhesion layers can significantly inhibit crystal grain growth and solid-state dewetting of Au[2]. The improved stability, however, comes with its own set of costs; metallic adhesion layers cause the plasmonic response to be damped significantly[7,8]. The thickness of the adhesion layer will determine the extent of the damping, with calculations showing that the level of damping is reduced for sub-nanometer Ti layers[7,9]. This is a highly limiting effect for applications that require both thermal stability and optimized plasmonic properties, and hence has repercussions in the developing field of thermo-plasmonics[10], as well as in the commercialization of plasmonic applications such as heat-assisted magnetic recording (HAMR)[11]. Recent work on organic monolayers, such as (3-mercaptopropyl)trimethoxysilane[7], have shown that it is possible to improve Au/SiO_2 adhesion without sacrificing plasmonic response (see Figure 5.1), but due to the poor thermal stability of such layers (due to a boiling point of 215 °C[12]), they will not be able to solve the issue for high temperature plasmonic applications, including HAMR.

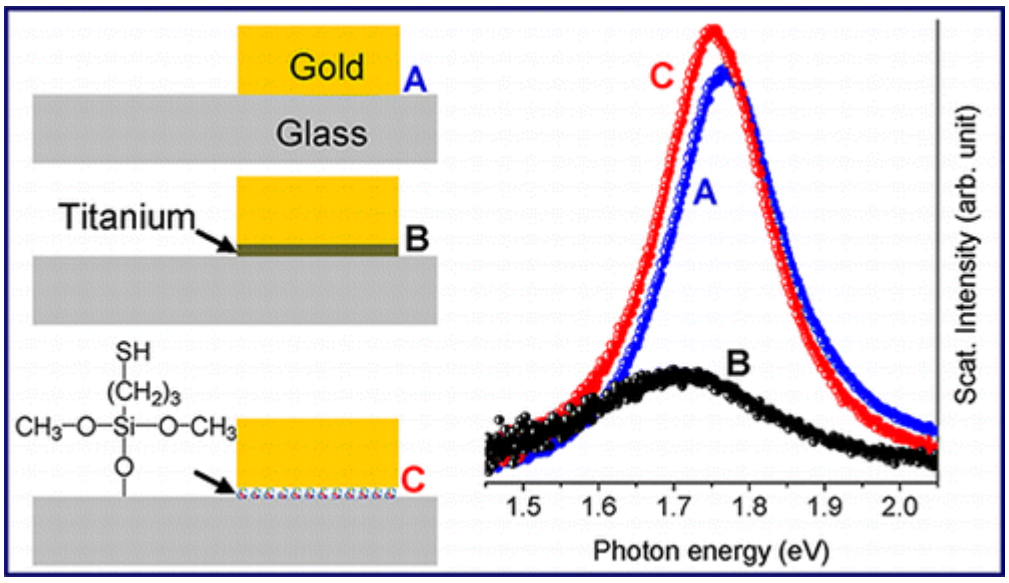

Figure 5.1: comparison of the optical scattering intensity for Au nanodisks without an adhesion layer (A), with a 2 nm Ti adhesion layer (B), and an organic self-assembled monolayer (SAM) (C). Taken from reference [7]

In this chapter, the properties of 50 nm Au films with Ti adhesion layers of varying thickness are studied. The effectiveness of the adhesion layers in preventing dewetting is studied using the back-reflected laser technique described in Chapter 3, as well as measuring the change in resistivity after isothermal annealing. The annealed films are characterized via SEM, TEM, & XPS, and from these studies an explanation for the differences in stability is given. The plasmonic properties of the Ti/Au films are then studied by measuring the SPP response, in order to observe the effect that decreasing the adhesion layer thickness has on the plasmonic damping. Finally, these studies are extended to other metallic adhesion layers, namely Al, Cr, Ta, and W, so that the optimal adhesion layer for thermo-plasmonic applications can be elucidated.

5.2 Experimental details

x nm M/50 nm Au films were deposited onto SiO_2 substrates using an Rf magnetron sputtering system, where x = 0.1, 0.2, 0.5, 1, 2, 5, and M = Ti, Ta, W, Cr, Al. The cleaning of the SiO_2 substrates and the magnetron sputtering process are discussed in detail in sections 3.2.1 and 3.3.2 respectively. The dewetting dynamics of the films were measured using the back-reflected laser technique described in Chapter 3. Films were irradiated with absorbed powers of 20, 25, and 30 mW. The focal spot $1/e^2$ radius was 1.8 μm for all measurements taken. In order to ensure consistency for the absorbed powers across each

sample, optical absorption spectra were taken for each film so that the input power could be adjusted via the laser control panel accordingly, to within a tolerance of 0.03 mW . It was found that the absorption at 488 nm did not vary significantly for the samples investigated. Regardless, the incident power was adjusted for each sample so that the absorbed powers would remain consistent for each measurement. Example absorption spectra for Ti/Au films are given in Figure 5.2.

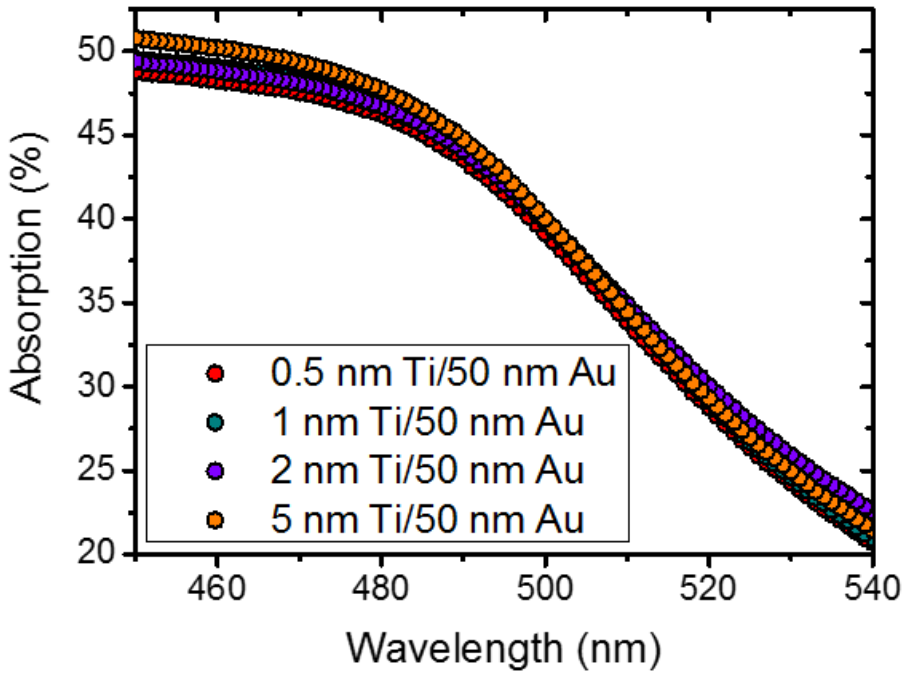

Figure 5.2: absorption spectra for Ti/Au films, from 450 nm to 540 nm. At 488 nm (the irradiating wavelength), there is not a significant difference in the absorption across the different Ti thicknesses.

SEM measurements were performed using a Zeiss ULTRA scanning electron microscope. The beam voltage was maintained at 5 kV and the SE2 detector was used for all images obtained.

Resistivity measurements were performed using an Alessi Industries 4-point probe stage with a Keithley 2401 Sourcemeter.

AFM measurements were performed using an Asylum MFP-3D. AFM was used in tapping mode with Nanosensors SuperSharpSilicon probe type SSS-NCH-10.

TEM analysis was performed using a FEI Titan field emission TEM with an accelerating voltages of 300 kV. Sample cross-sections were prepared using a Zeiss Auriga focused ion beam (FIB) system. Further details on the operation of the instrument are given in Chapter 3.

Surface plasmon polariton measurements were obtained using SOPRA GESP 5 variable angle spectroscopic ellipsometer, set to a Kretschmann configuration. The SPPs were excited with a wavelength of 633 nm.

Additional techniques will now be introduced that provide important information about the stability mechanisms of Ti adhesion layers.

5.3 Results & Discussion

5.3.1 Effect of Ti adhesion layer thickness on Au dewetting dynamics

In Figure 5.3, degradation curves for 50 nm Au films with varying thickness of Ti adhesion layer are shown. The films were irradiated with 25 mW of absorbed power from a 488 nm laser. Unexpectedly, films with the standard 2 nm and 5 nm thick Ti adhesion layers were not the most stable systems; on the contrary, these adhesion layers resulted in a faster rate of dewetting. The slowest rate of dewetting was from the 0.5 nm Ti adhesion layer, followed by 0.2 nm and 1 nm.

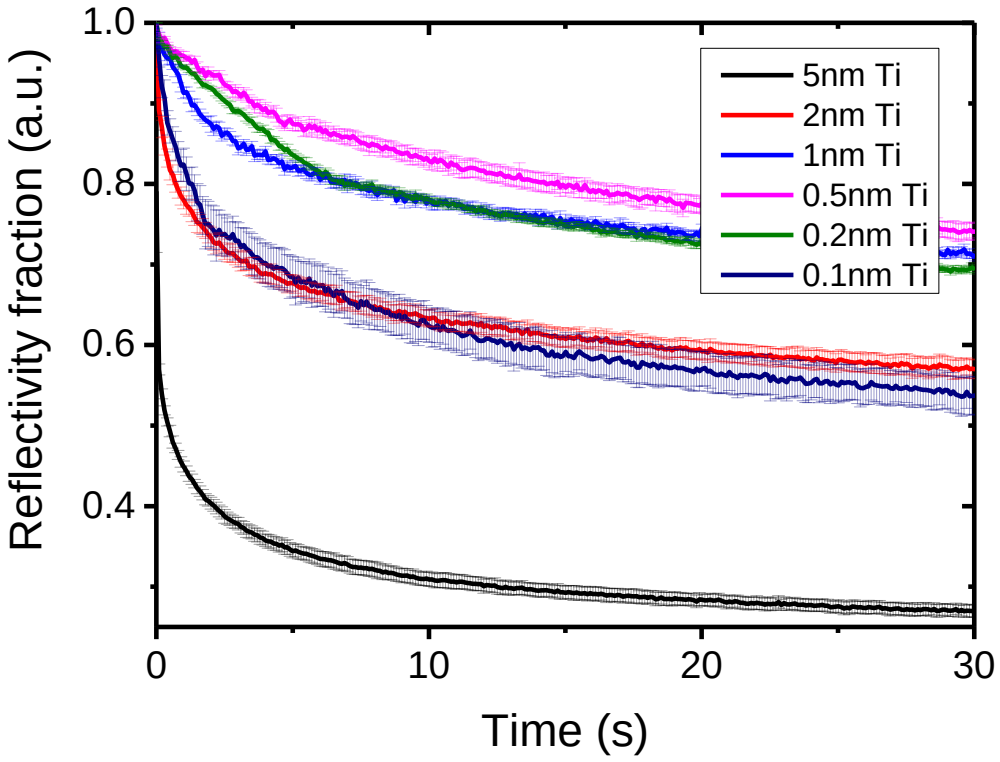

Figure 5.3: dewetting curves obtained from the back-reflected laser signal irradiating 50 nm Au films with varying thicknesses of Ti adhesion layers.

By extracting the half-life ($T_{1/2}$) from the degradation curves, a quantitative comparison could be made between the induced thermal stabilities of the Ti adhesion layers. Figure 5.4 displays the $T_{1/2}$ values obtained from absorbed powers of 20 mW, 25 mW, and 30 mW, for each Ti adhesion layer investigated. Using equation (2.14), the maximum temperature increase at the beam focus for each absorbed power was calculated to be 195 K, 244 K, and 292 K, respectively. The $T_{1/2}$ values give the following order of stability for Ti adhesion layers; 0.5 nm > 0.2 nm > 1 nm > 0.1 nm > 2 nm > 5 nm. This result is highly counterintuitive, as many Au thin film applications use 2 - 5 nm Ti adhesion layers (and occasionally even thicker adhesion layers[16]). These results suggest that the standard approaches to Ti adhesion layers are far from optimal, and that using excessively thick adhesion layers actually harms the long-term thermal stability of the Au. For adhesion layers with a thickness of < 0.5 nm, it is unlikely that a continuous film of Ti has been deposited, hence the drop in stability observed at these thicknesses. This is best demonstrated by the optical images of the 0.1 nm Ti/50 nm Au film, where several blisters can be observed in the film prior to laser annealing (Figure 5.5). Blistering is a specific form of delamination, and occurs regularly in Au films without an adhesion layer. Due to

the extent of the blistering in the 0.1 nm Ti/50 nm Au film, it is reasonable to assume that there is very poor coverage of Ti at these thicknesses.

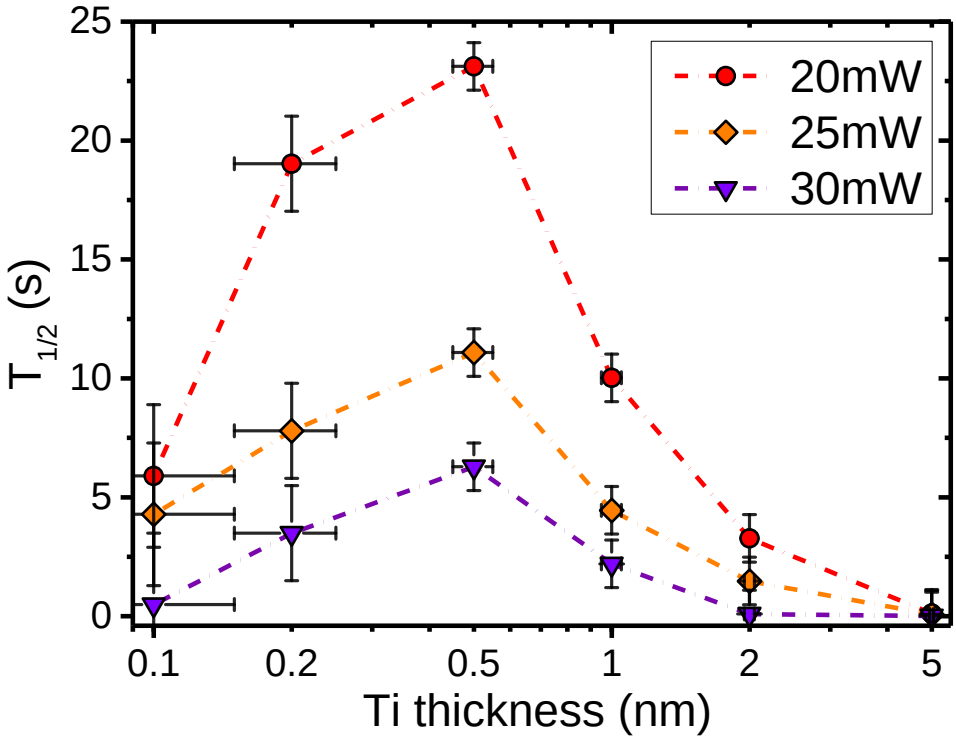

Figure 5.4: plot of dewetting half-life ($T_{1/2}$) against Ti adhesion layer thickness for Ti/Au films at different absorbed powers. Dashed lines are added to guide the eye.

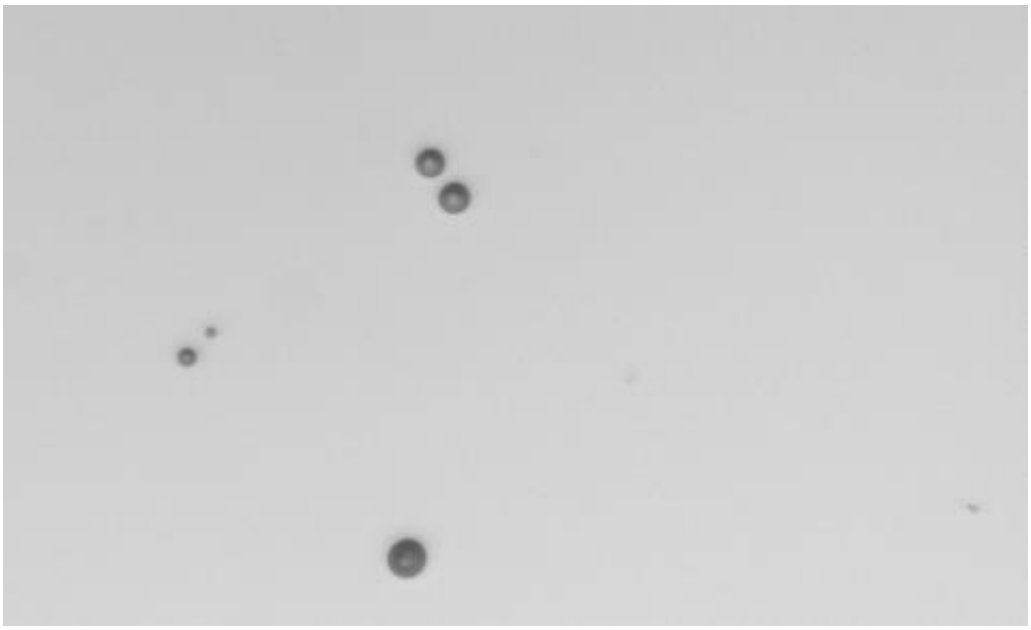

Figure 5.5: optical image of 0.1 nm Ti/50 nm Au film, showing blistering prior to any heat-treatment

In Figure 5.6, SEM images of the irradiated areas of the Ti/Au films are shown. The top row of SEM images shows the films as deposited, before being irradiated by the laser. Each film is continuous with no pinholes, and the grain size for each film is qualitatively comparable. This is important for comparing the effectiveness of the Ti adhesion layers, as any differences in grain size will have an additional effect on the dewetting dynamics[17]. For an absorbed power of 20 mW, a considerable difference can be seen in the conferred stability of the different adhesion layers. The $T_{1/2}$ measurements in Figure 5.4 showed that 0.5 nm is the optimal thickness for a Ti adhesion layer, and this is emphatically confirmed with the SEM images, where the 0.5 nm Ti/50 nm Au film is the only film not to have exhibited solid-state dewetting at the absorbed power of 20 mW. For the other adhesion layers investigated at this power (1 nm, 2 nm, and 5 nm), the area of the central dewetted area (the areas with darker contrast indicating the exposed SiO_2 substrate) increases as the adhesion layer thickness increases. In addition to the central dewetted area, other changes in film quality can be seen for Au films with thicker adhesion layers. The contrast between the grain boundaries increases for films with non-optimal adhesion layers, indicative of grain boundary grooving which occurs at the onset on solid-state dewetting[18]. Additionally, each Au film exhibits the presence of hillocks[19] post-irradiation, with a higher density of hillocks observed for films with thicker adhesion layers. It must be noted that hillocks are formed in films as a way of relieving compressive stress, suggesting that using thicker adhesion layers compressively stresses a thin film once it is annealed.

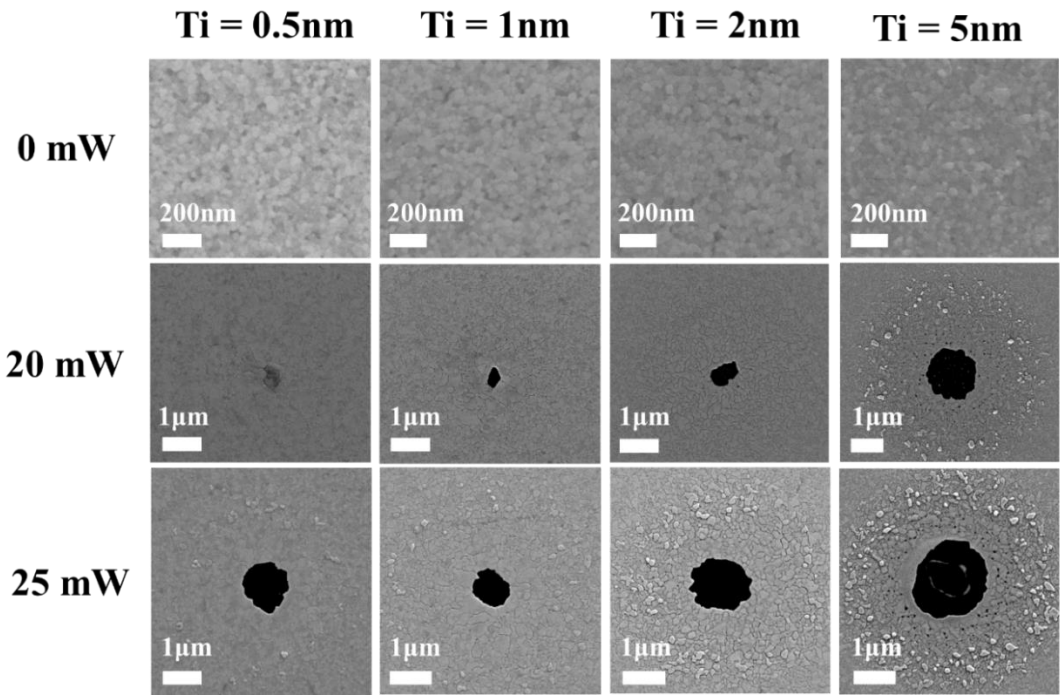

Figure 5.6: chart of SEM images comparing the pristine and laser irradiated areas of Ti/Au films. Dark area indicates exposed SiO_2 substrate due to dewetting at the location of the laser spot.

Due to the large thermal gradient induced during the laser dewetting analysis, it cannot be assumed that the films will behave similarly when subject to an isothermal anneal. Hence, it is necessary to investigate the effect of a constant temperature on the Ti/Au films. The films chosen for analysis were those with the best (0.5 nm Ti/50 nm Au) and worst (5 nm Ti/50 nm Au) resistance to dewetting from the results in Figure 5.6. In Figure 5.7, the effect of a 10 hr 250^{o}C isothermal anneal on Ti/Au films is shown. The temperature of 250^{o}C was chosen as the annealing temperature in the hope that it would be sufficient to see a distinct stability difference between the 5 nm Ti/50 nm Au and 0.5 nm Ti/50 nm Au samples. It was based on the results found by Martinez *et al* where they showed that significant amounts of Ti could be found to have diffused into a polycrystalline Au film at this temperature. In the case of the 0.5 nm Ti/50 nm Au film, there is little change in the resistivity over 10 hrs, implying a highly stable system. In contrast, the 5 nm Ti/50 nm Au film shows a marked increase in resistivity, with a 40% increase observed after 10 hrs. This increase is attributable to dewetting in the film.

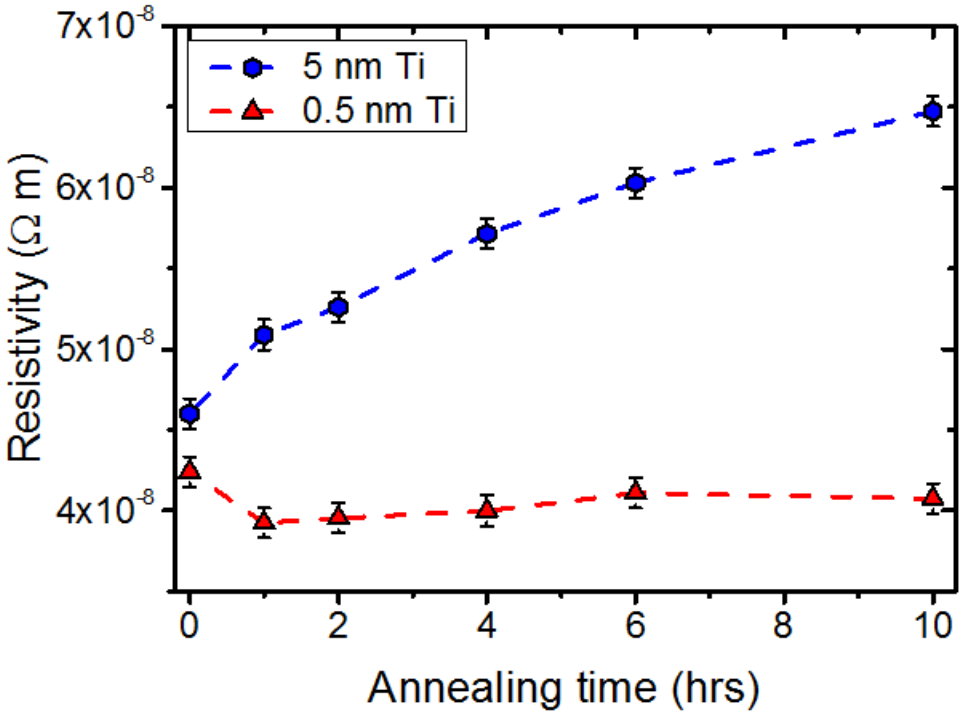

Figure 5.7: resistivity measurements for Ti/Au films during 250°C anneal. Dashed lines are added to guide the eye.

In Figure 5.8, atomic force microscope (AFM) topographical images of the Ti/Au films after the 10 hr 250°C anneal are shown. The 0.5 nm Ti/50 nm Au film (Figure 5.8a) shows some pinhole defects, but in general remains in good condition, with a RMS surface roughness of 0.51 nm. The 5 nm Ti/50 nm Au film (Figure 5.8b) is qualitatively in a more advanced state of degradation, with a greater grain boundary contrast, and a RMS surface roughness of 1.10 nm: over twice that of the 0.5 nm Ti/50 nm Au film. The pure white areas in each image are surface contaminants, which may have landed on the samples during annealing. These have been excluded from surface roughness calculations.

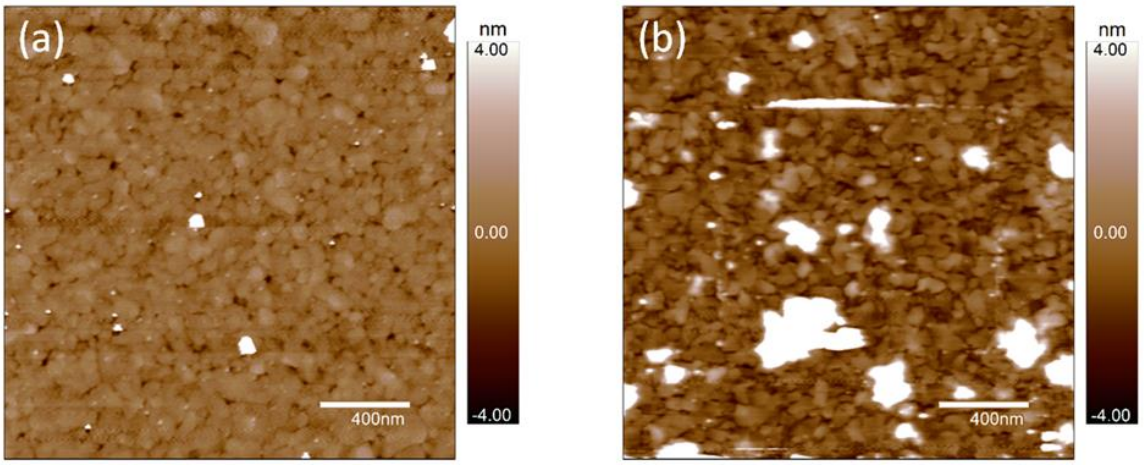

Figure 5.8: AFM measurements of (a) 0.5 nm Ti/50 nm Au and (b) 5 nm Ti/50 nm Au films, after annealing at 250°C for 10 hrs. The white areas in each image are contamination materials from the heating furnace, and they have been excluded from the calculations of surface roughness.

Based on the results shown in Figures 5.7 and 5.8, it is clear that the stabilizing effect of sub-nanometer adhesion layers is not unique to the laser-annealing case, and can in fact be generalized to solid-state dewetting in general. This is a key result, as it proves that the stabilizing effects are entirely dependent on the thickness of the adhesion layer, and are not affected by the heat source. Hence, all subsequent studies in this chapter will focus exclusively on the isothermally annealed case, due to the relative ease in preparing samples for study under the material analysis techniques to be used: namely TEM, XPS, and ellipsometry.

5.3.2 Investigation into the increased stability for sub-nanometre adhesion layers

In order to investigate the reason behind the improved stability conferred by sub-nanometer adhesion layers, cross-sections of annealed Ti/Au films were studied under TEM. 50 nm Au films with Ti adhesion layers of 0.5 nm and 5 nm were studied; these films exhibited the best and worst dewetting resistance, respectively, hence it was hoped that a larger structural contrast could be seen between them post-anneal. The films were annealed for 10 hrs at 250°C in air. In Figure 5.9, high-resolution TEM images of the 0.5 nm Ti/50 nm Au and 5 nm Ti/50 nm Au films can be seen. In each image, the areas where Ti and Au would be expected to be found prior to annealing (based on the order of deposition) are labelled accordingly. The areas of darker contrast are Au due to its high atomic number; conversely, the relatively low atomic numbers of Si and Ti result in similar (but not identical) areas of brighter contrast. For the Ti 0.5 nm/Au 50 nm system, it can be

seen that after 10 hrs of annealing, there are no signs of dewetting or changes in film quality. In the case of the 5 nm Ti/50 nm Au, however, the morphology of the Au layer has changed drastically, particularly at the Ti interface. Most notable at the interface is the "sharkfin" protrusion into the Au film. The TEM contrast is the same as that of the Ti adhesion layer area, suggesting that Ti has diffused through the Au grain boundaries.

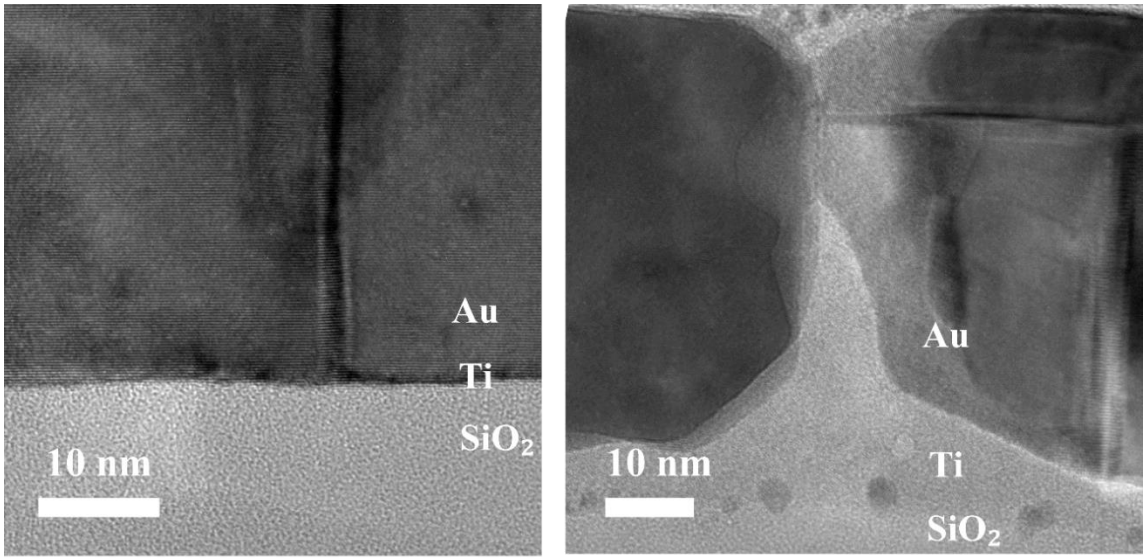

Figure 5.9: high-resolution TEM images of 0.5 nm Ti/50 nm Au film (left), and 5 nm Ti/50 nm Au film (right), after 10 hr 250°C anneal. The Au, Ti, and SiO_2 labels indicate where the respective materials would be expected to be found prior to annealing, based on the deposition order.

EELS mapping was used to determine whether Ti had diffused through either Au film, and the resultant maps can be seen in Figure 5.10. In the case of the 0.5 nm Ti/50 nm Au film, the Ti adhesion layer remains confined to within a 2 nm area, suggesting that very little Ti has moved from its original area of deposition. In a stark contrast, a strong Ti signal can be observed within the Au grain boundaries for the 5 nm Ti/50 nm Au film. This is strong evidence that, upon annealing, Ti has diffused from the adhesion layer through the grain boundaries. A similar effect is not observed in the case of the 0.5 nm Ti/50 nm Au film, likely due to there being 10x less Ti available. For the 0.5 nm Ti/50 nm Au case, there is almost certainly at least one grain boundary in view due to the relatively large field of view: however the contrast from the HAADF-STEM image means that they cannot be clearly seen

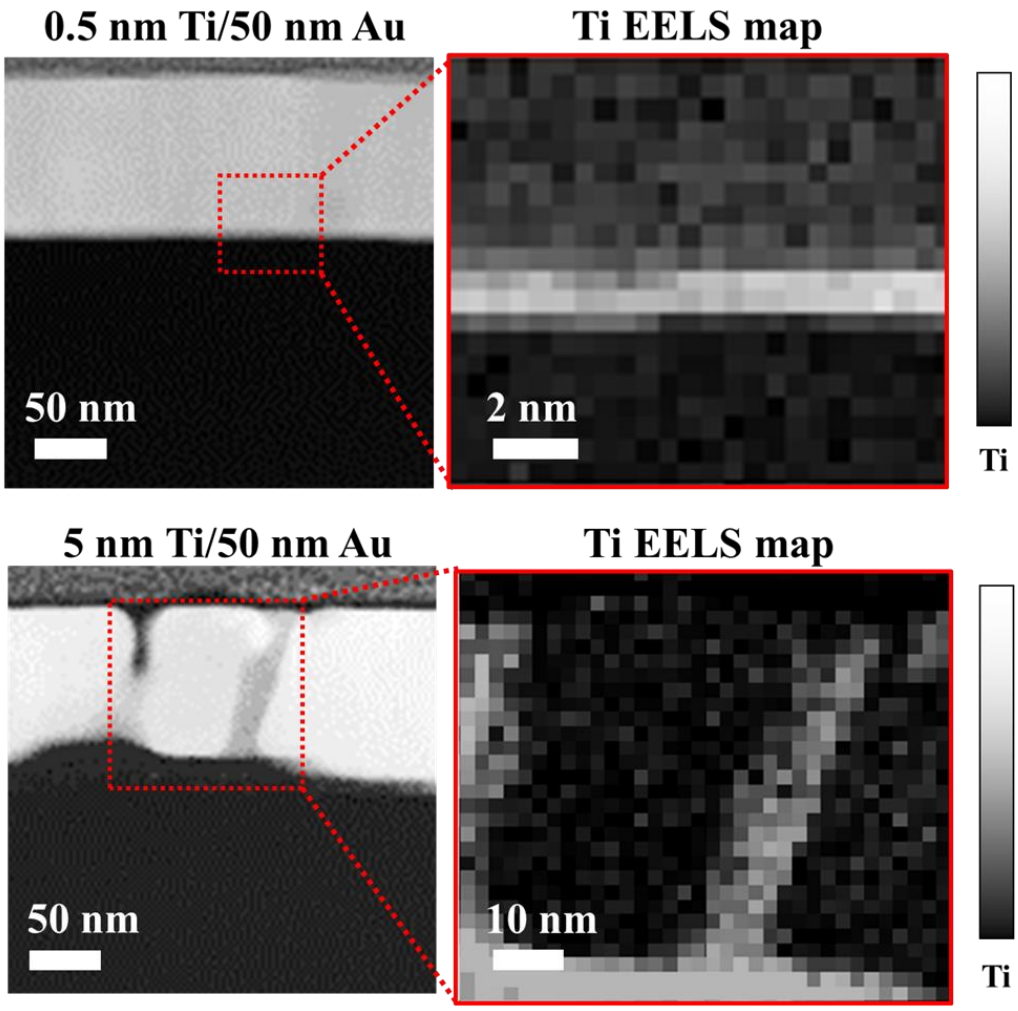

Figure 5.10: EELS mapping of Ti signal within Ti/Au films. (a) HAADF-STEM image of 0.5 nm Ti/50 nm Au film, (b) Ti EELS map of area in (a). (c) HAADF-STEM image of 5 nm Ti/50 nm Au film, (b) Ti EELS map of area in (c).

In Figure 5.9, small particles can be observed in the Ti adhesion layer. By using parallel electron energy-loss spectroscopy (PEELS) on a particle (and a non-particle areas, for comparison), it was found that the particles are metallic Ti surrounded by TiO_2 (Figure 5.11). This suggests that, after the Ti has diffused to the surface of the Au film, the oxidized Ti does not act as a protective barrier to the Ti within the original area of the adhesion layer, allowing it in turn to become oxidized. The particles are remnant metallic Ti.

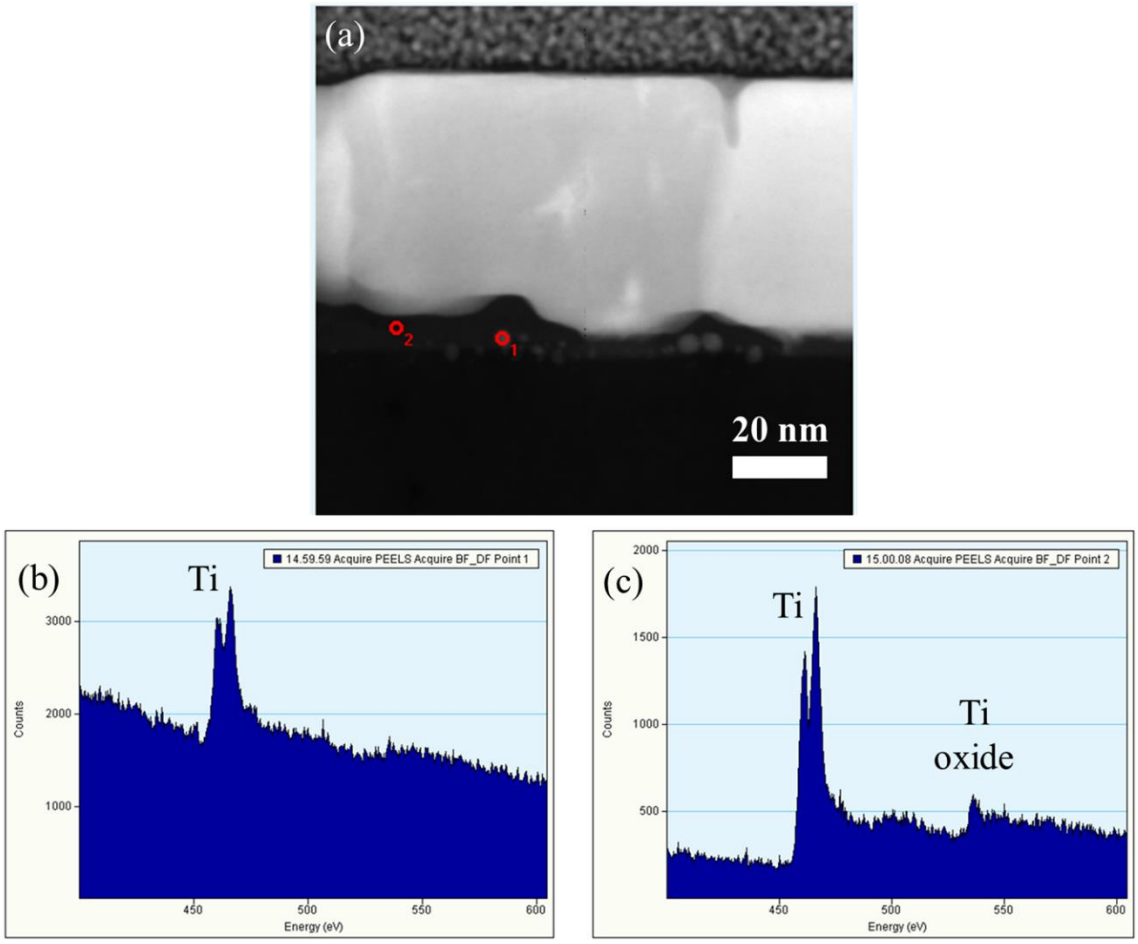

Figure 5.11: Parallel energy-loss electron spectroscopy (PEELS) of 5 nm Ti adhesion layer. (a) HAADF-STEM image of 5 nm Ti/50 nm Au film; (b) PEELS of remnant metallic Ti particle; (c) PEELS of oxidized area of Ti adhesion layer.

In order to determine whether the Ti diffused to the surface of the Au film, XPS analysis was performed of the 0.5 nm Ti/50 nm Au and 5 nm Ti/50 nm Au films. In Figure 5.12, XPS spectra for Au films annealed at 250°C with different Ti adhesion layer thicknesses are shown. The Ti 5 nm/Au 50 nm film shows a Ti $2p_{3/2}$ peak at 458.9 eV, which conversely, is not observable for the Ti 0.5 nm/Au 50 nm film. Fitting the Ti $2p_{3/2}/2p_{1/2}$ core levels with Voigt line-shapes (Figure 5.13) gives a value for the Ti $2p_{3/2}$ binding energy of 458.9±0.1 eV, with a spin-orbit splitting of 5.64 eV consistent with Ti(IV)O_2[20].

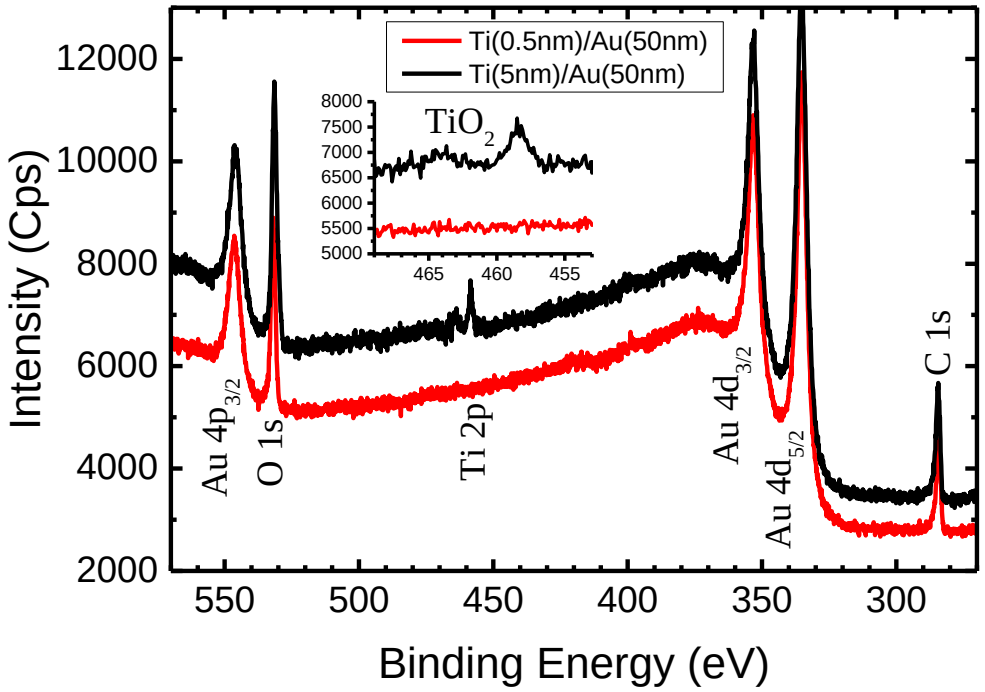

Figure 5.12:XPS spectra for 0.5 nm Ti/50 nm Au film (red) and 5 nm Ti/50 nm Au film (black), after 10 hr 250°C anneal.

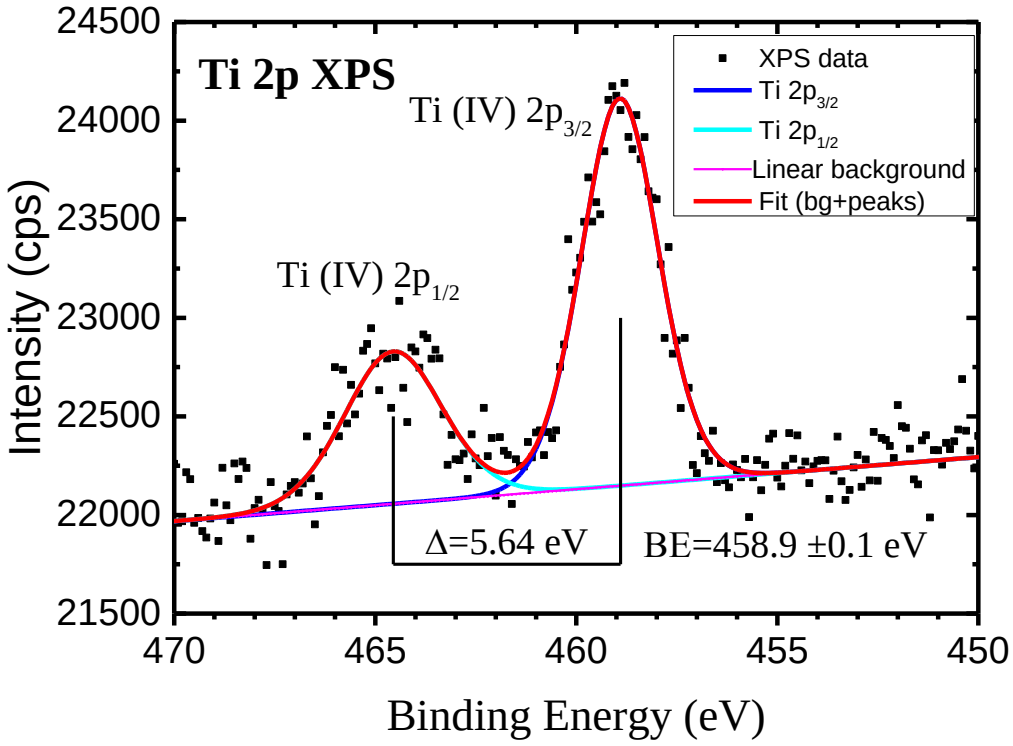

Figure 5.13: Gaussian-Lorentzian fitting of Ti 2p XPS peaks.

In order to confirm that the Ti 2p signal obtained in Figure 5.13 is due to Ti at the surface of the Au, as opposed to Ti at the Au/SiO_2 interface that has been exposed by the film dewetting, angle-resolved XPS measurements were performed. Figure 5.14 shows the angle-resolved XPS (ARXPS) measurements for the Ti 5nm/Au 50nm sample. Notably, the 2p Ti peak does not decrease as the take-off angle increases (where ARXPS becomes more surface sensitive), again indicating that Ti has diffused to the surface of the Au film. Unlike the cross-sectional TEM analysis shown in Figure 5.11, no metallic Ti 2p signal is observable in the XPS, either at normal incidence or at any other angle as in the ARXPS. Plots of the relative intensities of Ti, O, and Au peaks as a function of take-off angle (Figure 5.15), show that at the lowest take-off angles, the areal intensities of the Ti 2p and TiO_2 O 1s peaks increase while consistently exhibiting a 1:2 Ti:O stoichiometry, conclusively demonstrating the presence of TiO_2 at the film surface.

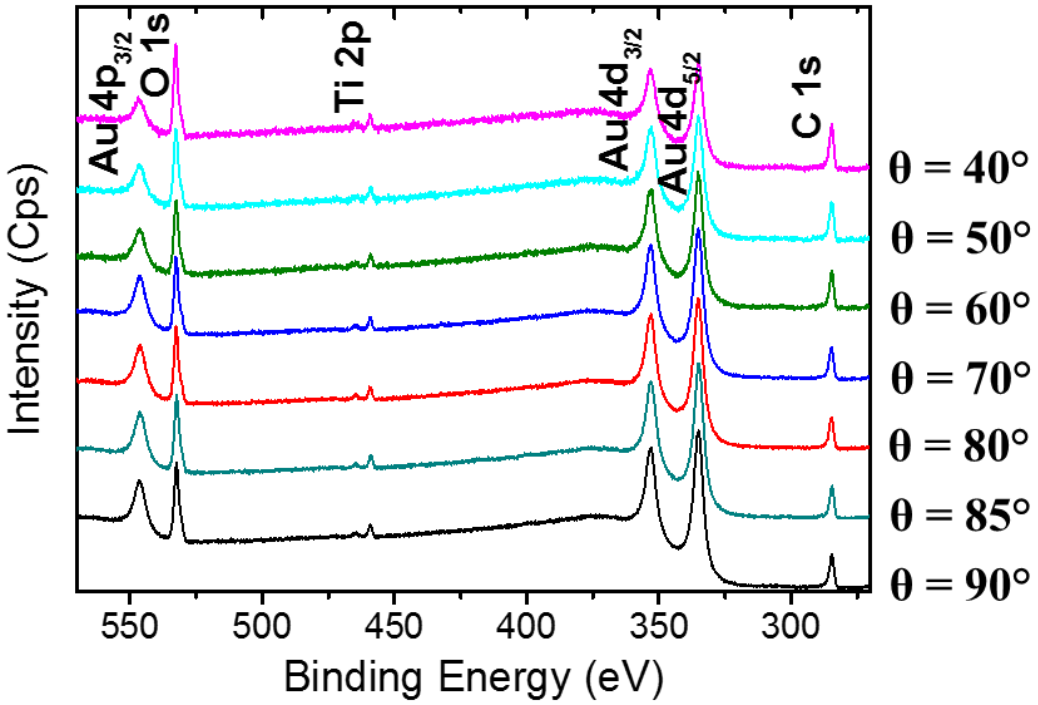

Figure 5.14: Angle-resolved XPS spectra for 5 nm Ti/50 nm Au film after 10 hr 250°C anneal.

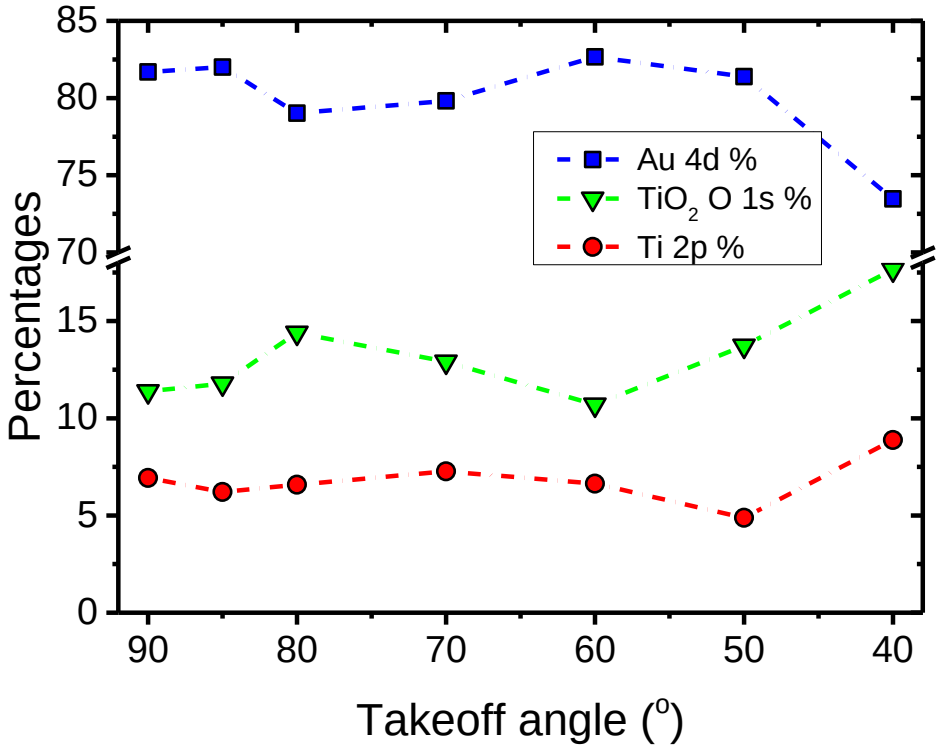

Figure 5.15: plot of the relative intensities for Au 4d, TiO_2 O 1s, and Ti 2p XPS peaks as a function of takeoff angle. Dashed lines are added to guide the eye. Error bars are smaller than symbols.

Based on these results, a mechanism for the increased stability of the sub-nanomater adhesion layers can be outlined. The increased stability conferred by using sub-nanometer adhesion layers is due to there being less (if any) excess Ti available to diffuse through the Au grain boundaries. A schematic for this process is shown in Figure 5.16. At temperatures above 175°C, Ti will diffuse into Au thin films[5], mainly through Au grain boundaries[4] due to the activation energy for diffusion into grain boundaries being lower than that for volume diffusion[21]. Eventually this Ti will reach the surface and oxidize to form TiO_2. It is proposed that the diffusion of the Ti through the Au grain boundaries causes compressive stress within the film[22], which decreases the stability of the film against dewetting. Stresses within thin films have previously been shown to induce dewetting without any additional temperature increase[23]. The high density of hillocks observed in the annealed 5 nm Ti/50 nm Au film (Figure 5.6) confirms the presence of compressive stress due to Ti diffusion within the film[24].

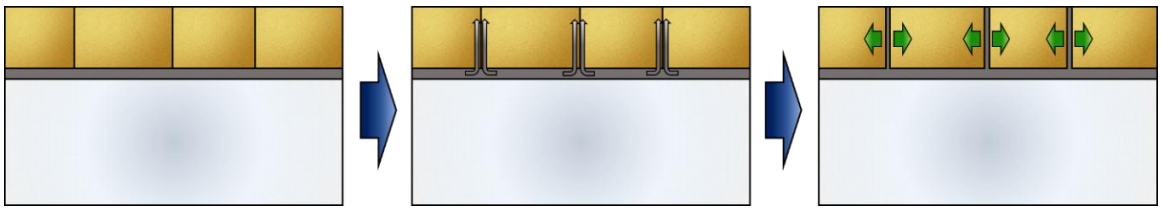

Figure 5.16: schematic detailing the process of Ti diffusion through Au grain boundaries, leading to compressive stress within the Au film.

5.3.3 Dependency of Au plasmonic damping on Ti adhesion layer thickness

For any attempt at improving the thermal stability of a plasmonic film to be considered successful, it is necessary that the plasmonic response does not deteriorate. In order to determine the dependence of plasmonic damping on adhesion layer thickness, the surface-plasmon polaritons (SPPs) for each Ti/Au system were measured. The reflectance data for each film is given in Figure 5.17. As the adhesion layer becomes thinner, the resultant SPP resonance becomes both stronger and spectrally sharper, indicating less damping. The best performing system is the 0.5 nm Ti/50 nm Au film, which has the deepest resonance and narrowest full-width half-maximum (FWHM). This result is consistent with previous studies on the effect of sub-nanometre adhesion layers on plasmonic properties[7,9].

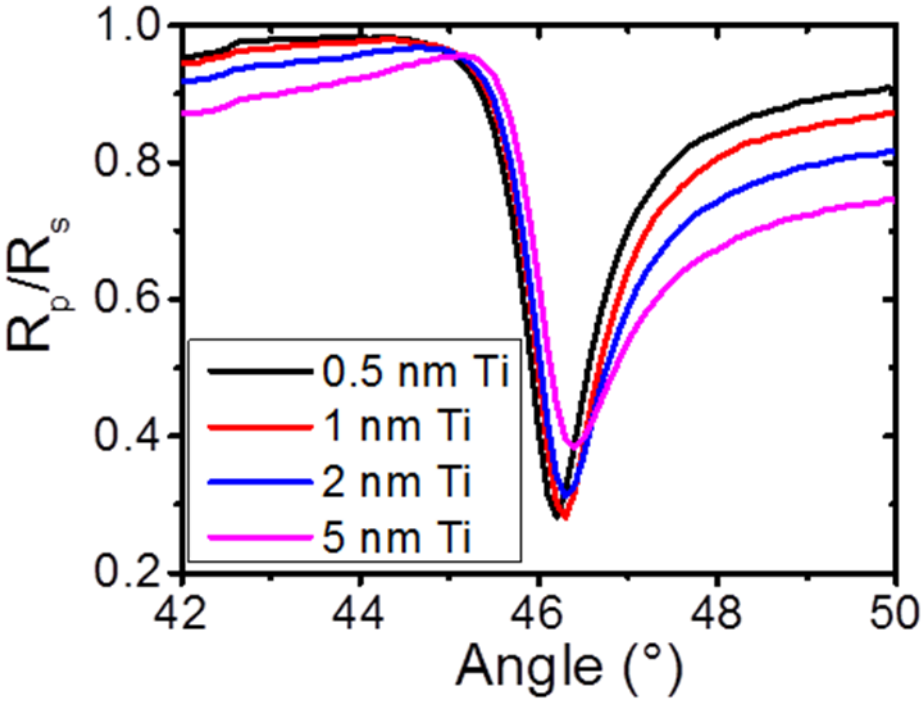

Figure 5.17: surface plasmon polariton (SPP) measurements of 50 nm Au films with varying thickness of Ti adhesion layer.

In order to investigate the thermal stability of the above plasmonic responses, the SPPs of the 0.5 nm Ti and 5 nm Ti adhesion layer samples were measured before and after a 10 hr 250°C anneal. The reflectance data is shown in Figure 5.18. Once the films have been annealed at 250°C, the stability enhancement of the 0.5 nm adhesion layer becomes more apparent. The reflectivity dip depth decreases significantly for the Ti 5 nm/Au 50 nm, whereas it increases slightly for the Ti 0.5 nm/Au 50 nm film. This improved plasmonic performance after annealing for the 0.5 nm Ti adhesion layer is likely due to grain growth in the Au, which will reduce the number of scattering points within the film[25].

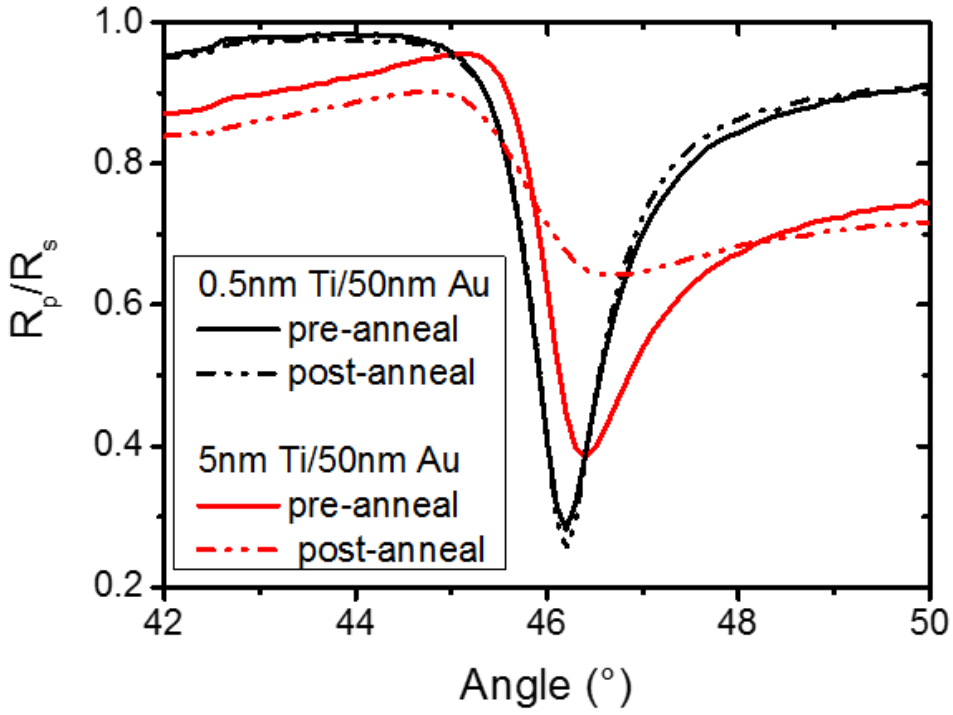

Figure 5.18: surface plasmon polariton measurements for Ti/Au films pre- and post-anneal at 250°C for 10 hrs.

5.3.4 Comparison of Au dewetting behaviour for different metal adhesion layers

In order to achieve a full optimization of metallic adhesion layers for Au thin films, it is necessary to compare different metals. As per Todeshini *et al*, different metals will have different overall effects on the properties of the Au film[3], and hence different metals suit certain applications better than others. In the case of stabilising Au for thermo-plasmonic applications, a successful metal adhesion layer will need to increase the adhesion strength between Au and SiO_2, be stable at high temperatures, and have a minimal effect on the plasmonic response. Cr and Ti are standard adhesion layer metals used in a variety of

applications[3]. Both Cr and Ti, however, will diffuse into the Au film at sufficiently high temperatures[4,26]. While Ti will primarily diffuse through the Au grain boundaries[4] (discussed in greater detail in section 5.3.2), Cr will diffuse into the Au crystallites[26]. Al may have some promise as an adhesion layer, as due to its own plasmonic properties[27] a plasmonic bilayer could be formed[28], allowing for an improvement in the Au adhesion without degrading the plasmonic properties. Ta and W also show some promise, as simulations have shown that their adhesion energies with Au are significantly larger than that of Cr[29].

In order to compare the thermal stability of 50 nm Au films with different metal adhesion layers, the back-reflected laser signal measurement (see Chapter 3) was used to probe their tendency towards dewetting. The films were irradiated with 20 mW of absorbed power with a 1.8 μm beam spot size. From the resultant dewetting curves, $T_{1/2}$ values were extracted and plotted against the thickness of the adhesion layer, as seen in Figure 5.19. From this graph, it can be seen that in general the metal adhesion layers show the same increase in stability on decreasing thickness as exhibited by Ti adhesion layers in section 5.3.1. Only W deviates from this trend; while thinner W adhesion layers do result in more stable systems, the relative increase in stability for decreasing thickness is markedly less that that observed for other metals. In addition, the 5 nm W adhesion layer is the best of all 5 nm adhesion layers studied, by a significant margin (the next best performing 5 nm adhesion layer, Ta, results in a system 4.8 times less stable). It has been previously shown that W does not readily diffuse into Au when annealed at 300°C[30], which goes some way towards explaining this anomalous result.

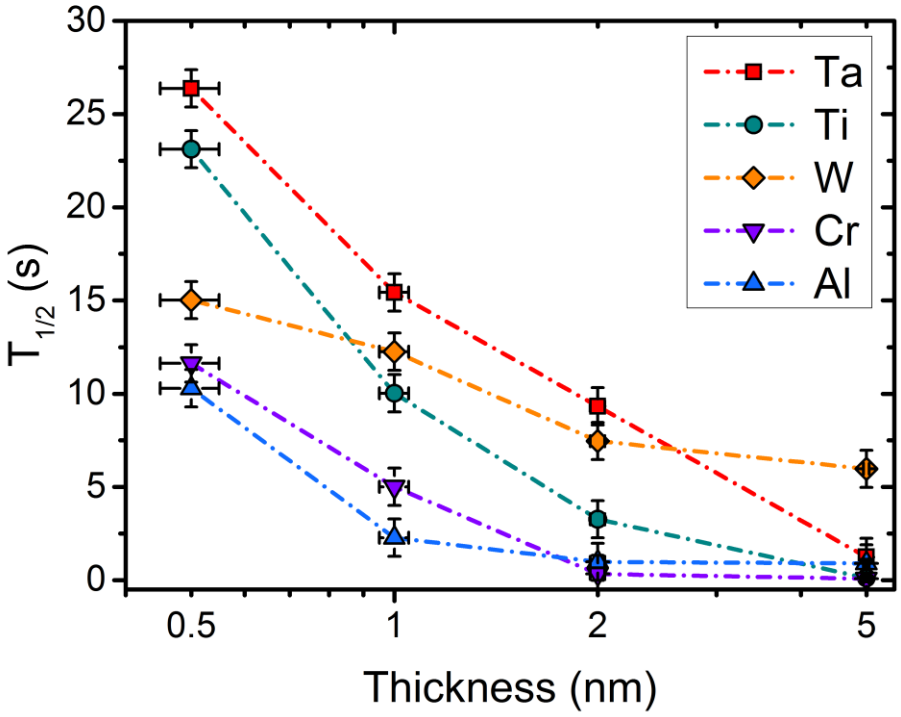

Figure 5.19: $T_{1/2}$ values for 50 nm Au films with different adhesion layers as a function ofadhesion layer thickness. Samples were irradiated with 20 mW of absorbed power with a beam waist of 1.8 μm. Dashed lines are added to guide the eye.

The SPPs of the Au films with different adhesion layer metals were then compared, in order to determine which metal was most suitable as an adhesion layer for plasmonic applications. In Figure 5.20, the FWHM of SPP measurements for 50 nm Au films with Ta and Ti adhesion layers were compared. A lower FWHM indicates a spectrally sharper resonance, and hence will result in better focusing of the SPP. For both adhesion layers, the FWHM decreases upon decreasing the thickness of the adhesion layer. In the case of the Ta adhesion layer, the FWHM decreases by larger amount than the equivalent thickness of Ti. Such a result implies that for plasmonic applications, Ta is a better adhesion layer than Ti.

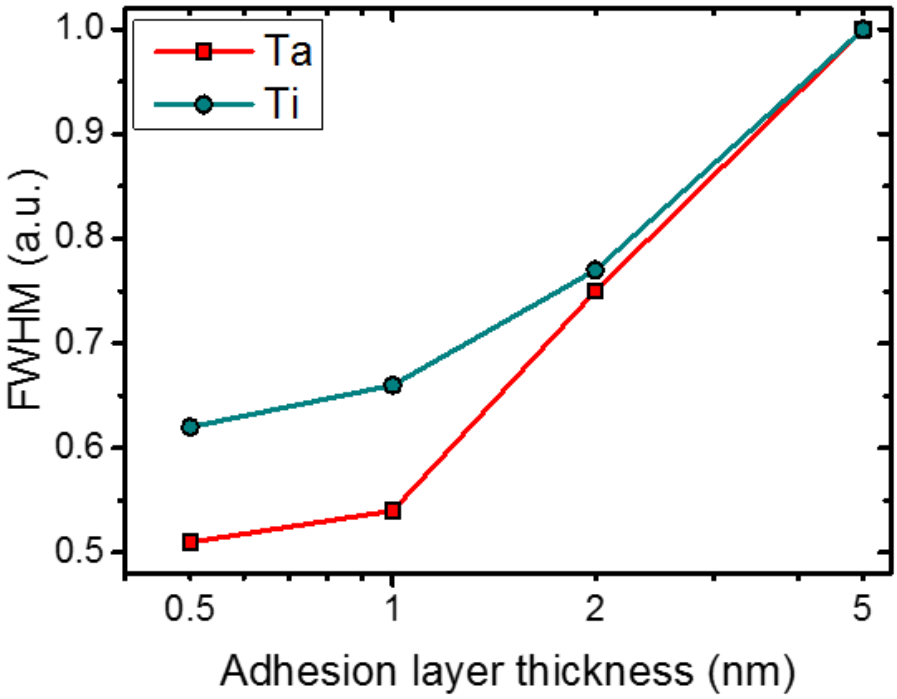

Figure 5.20: comparison of the SPP full-width half-maxima (FWHM) for 50 nm Au films with different thicknesses of Ti and Ta adhesion layers. Lines are added to guide the eye.

From these results, it can be concluded that the optimal adhesion layer for thermo-plasmonic applications of Au is 0.5 nm Ta. When compared with the standard adhesion layers of 2 nm Ti and 2 nm Cr, 0.5 nm Ta increases the stability against dewetting by factors of 8 and 80, respectively. Just as important is the effect of the Ta on the plasmonic response: the FWHM of the SPP resonance is reduced by 34% when using a 0.5 nm Ta adhesion layer as opposed to a standard 2 nm Ti adhesion layer.

5.4 Conclusions

In this chapter, work was to done to optimize metal adhesion layers for Au used in thermo-plasmonic applications, such as HAMR. First, the optimal thickness of Ti adhesion layer was investigated by testing the conferred stability against solid-state dewetting, and by measuring the SPP response. Counterintuitively, it was found that standard thicknesses of Ti adhesion layer (2 – 5 nm) result in a system that is considerably less stable than one using sub-nanometer adhesion layers. It was found that 0.5 nm is the optimal thickness,

with thinner layers unable to form a continuous film. Through a combination of TEM and XPS analysis, it was found that Ti from 5 nm adhesion layers will diffuse through the Au grain boundaries and oxidize upon annealing, causing compressive stress within the Au film. This is the reason for the increased thermal stability from using sub-nanometer adhesion layers, as there is less Ti available to diffuse through the Au grain boundaries, while still being sufficient to ensure that Au adheres well to the substrate.

Finally, different metal adhesion layers were compared using the above methods. From the results, the following order on the stabilisation against solid-state dewetting for the adhesion layer metals could be elucidated, based on the $T_{1/2}$ value obtained for 0.5 nm thick adhesion layer; Ta > Ti > W > Cr > Al. When all adhesion layer thicknesses are considered, Ta outperformed all other metals except for W at 5 nm. By comparing the FWHM of the SPP, it was found that Ta damps the plasmonic resonance less than Ti. From this, it can be concluded that 0.5 nm Ta is the optimal adhesion layer to use for applications that require consistent optical performance at high temperatures. This work has implications beyond HAMR and thermos-plasmonics, and is relevant for any application that requires Au thin films to remain stable at high temperatures.

5.5 Bibliography

(1) Seguini, G.; Curi, J. L.; Spiga, S.; Tallarida, G.; Wiemer, C.; Perego, M. Solid-State Dewetting of Ultra-Thin Au Films on SiO_2 and HfO_2. *Nanotechnology* **2014**, *25* (49), 495603.

(2) Abbott, W. M.; Corbett, S.; Cunningham, G.; Petford-Long, A.; Zhang, S.; Donegan, J. F.; McCloskey, D. Solid State Dewetting of Thin Plasmonic Films under Focused Cw-Laser Irradiation. *Acta Mater.* **2018**, *145*, 210–219.

(3) Todeschini, M.; Bastos da Silva Fanta, A.; Jensen, F.; Wagner, J. B.; Han, A. Influence of Ti and Cr Adhesion Layers on Ultrathin Au Films. *ACS Appl. Mater. Interfaces* **2017**, *9* (42), acsami.7b10136.

(4) Martinez, W. E.; Gregori, G.; Mates, T. Titanium Diffusion in Gold Thin Films. *Thin Solid Films* **2010**, *518* (10), 2585–2591.

(5) Masahiro, K.; Noboru, S. Effects of Temperature, Thickness and Atmosphere on Mixing in Au-Ti Bilayer Thin Films. *J. Mater. Sci.* **1993**, *28* (18), 5088–5091.

(6) Nagata, H.; Shinriki, T.; Shima, K.; Tamai, M.; Haga, E. M. Improvement of Bonding Strength between Au/Ti and SiO_2 Films by Si Layer Insertion. *J. Vac. Sci. Technol. A Vacuum, Surfaces, Film.* **1999**, *17* (3), 1018.

(7) Habteyes, T. G.; Dhuey, S.; Wood, E.; Gargas, D.; Cabrini, S.; Schuck, P. J.; Alivisatos, A. P.; Leone, S. R. Metallic Adhesion Layer Induced Plasmon Damping and Molecular Linker as a Nondamping Alternative. *ACS Nano* **2012**, *6* (6), 5702–5709.

(8) Madsen, S. J.; Esfandyarpour, M.; Brongersma, M. L.; Sinclair, R. Observing Plasmon Damping Due to Adhesion Layers in Gold Nanostructures Using Electron Energy Loss Spectroscopy. *ACS Photonics* **2017**, *4* (2), 268–274.

(9) Debu, D. T.; Ghosh, P. K.; French, D.; Herzog, J. B. Surface Plasmon Damping Effects Due to Ti Adhesion Layer in Individual Gold Nanodisks. *Opt. Mater. Express* **2017**, *7* (1), 73–84.

(10) Baffou, G.; Quidant, R. Thermo-Plasmonics: Using Metallic Nanostructures as Nano-Sources of Heat. *Laser Photon. Rev.* **2013**, *7* (2), 171–187.

(11) Budaev, B. V.; Bogy, D. B. On the Lifetime of Plasmonic Transducers in Heat Assisted Magnetic Recording. *J. Appl. Phys.* **2012**, *112* (3), 034512.

(12) The PCR Research Chemicals Catalog 1990-1991. *PCR Inc, Gainsville, FL*; 1990.

(13) Walls, J. M.; Smith, R. *Surface Science Techniques.*; Elsevier Science, 1994.

(14) Crist, B. V. *Handbook of Monochromatic XPS Spectra*; Wiley, 2000.

(15) Egerton, R. F. *Electron Energy-Loss Spectroscopy in the Electron Microscope*; Springer US: Boston, MA, 1996.

(16) Bolshakova, I.; Shurygin, F.; Moroz, A.; Kost, Y.; Mykhashchuk, Y.; Radishevskiy, M.; Vasyliev, O.; Kuech, T. Temperature Effect on Electrophysical Properties of As-Deposited Gold Nanofilms for Use in Electronics Devices and Sensor Technology. In *Advanced Trends in Radioelecrtronics, Telecommunications and Computer Engineering (TCSET)*; IEEE, 2018; pp 471–474.

(17) Thompson, C. V. Solid-State Dewetting of Thin Films. *Annu. Rev. Mater. Res.* **2012**, *42* (1), 399–434.

(18) Jiran, E.; Thompson, C. V. Capillary Instabilities in Thin, Continuous Films. *Thin Solid Films* **1992**, *208* (1), 23–28.

(19) Shaffir, E.; Kauffmann, Y.; Riess, I. Void Formation in Gold Films on Yttrium-Doped Zirconia in the Initial Stage of Dewetting. *Acta Mater.* **2014**, *79*, 59–65.

(20) Bennett, R. A.; Mulley, J. S.; Newton, M. A.; Surman, M. Spectroscopy of Ultrathin Epitaxial Rutile TiO_2 (110) Films Grown on W(100). *J. Chem. Phys.* **2007**, *127* (8), 084707.

(21) Manuela Müller, C.; Spolenak, R. Dewetting of Au and AuPt Alloy Films: A Dewetting Zone Model. *J. Appl. Phys.* **2013**, *113* (9), 094301.

(22) Ostrovsky, A. S.; Bokstein, B. S. Grain Boundary Diffusion in Thin Films under Stress Fields. *Appl. Surf. Sci.* **2001**, *175–176*, 312–318.

(23) Coll, M.; Gázquez, J.; Pomar, A.; Puig, T.; Sandiumenge, F.; Obradors, X. Stress-Induced Spontaneous Dewetting of Heteroepitaxial $YBa_2Cu_3O_7$ Thin Films. *Phys. Rev. B* **2006**, *73* (7), 075420.

(24) Soon, Y. K.; Si, K. C.; Seung, J. Y.; Jae, S. R. Platinum Hillocks in Pt/Ti Film Stacks Deposited on Thermally Oxidized Si Substrate. *Japanese J. Appl. Physics, Part 1 Regul. Pap. Short Notes Rev. Pap.* **2001**, *40* (10), 5850–5855.

(25) McPeak, K. M.; Jayanti, S. V.; Kress, S. J. P.; Meyer, S.; Iotti, S.; Rossinelli, A.; Norris, D. J. Plasmonic Films Can Easily Be Better: Rules and Recipes. *ACS Photonics* **2015**, *2* (3), 326–333.

(26) Moody, N. R.; Adams, D. P.; Volinsky, A. A.; Kriese, M. D.; Gerberich, W. W. Annealing Effects on Interfacial Fracture of Gold-Chromium Films in Hybrid Microcircuits. *MRS Proc.* **1999**, *586*, 407–419.

(27) Knight, M. W.; King, N. S.; Liu, L.; Everitt, H. O.; Nordlander, P.; Halas, N. J. Aluminum for Plasmonics. *ACS Nano* **2014**, *8* (1), 834–840.

(28) Zhong, C.; Ballantine, K. E.; Kervick, C.; Smith, C. M.; Mullarkey, D.; Shvets, I. V.; Donegan, J. F.; McCloskey, D. Mapping of Surface Plasmon Dispersion in Thin Ag–Au Layered Composite Films. *J. Opt. Soc. Am. B* **2016**, *33* (4), 566.

(29) Zotti, L. A.; Sanvito, S.; O'Regan, D. D. A Simple Descriptor for Energetics at Fcc-Bcc Metal Interfaces. *Mater. Des.* **2018**, *142*, 158–165.

(30) Nowicki, R. S. Diffusion Barriers between Gold and Semiconductors. *Gold Bull.* **1982**, *15* (1), 21–24.

Chapter 6: Thermo-plasmonic properties of an AuCu alloy

6.1 Introduction

As research has progressed on the optimization of plasmonic devices, it has become necessary for researchers to turn their attention to new materials which may aid in the development of devices which are both more efficient[1], and possess a greater thermal stability[2]. Metal alloys have been a natural choice for such investigations. Throughout history[3], alloying metals has allowed for the development of materials with better properties than their constituent parts, with Japanese Damascus steel being one of the most cited historical examples[4]. One example of alloying in the case of gold can be found in the development of crown gold (Figure 6.1). The 22 kt alloy, consisting of 22 parts gold and 2 parts copper, was first introduced into the British financial system by King Henry VIII. Formerly, a 23 kt alloy was used for gold coinage: this alloy was much softer due to the higher concentration of Au, which invited scammers to file-off parts of the coin. In addition, the coins were prone to deformations and wear due to the high malleability[5].

Figure 6.1: examples of gold crown coinage, introduced by Henry VIII in 1526. These particular coins were minted between 1526 and 1529. "Henry_VIII_Crown_756826.jpg" by CNG is licensed under Creative Commons BY-SA 2.5.

For plasmonic applications, there are several potential benefits to be gained from alloying. AuCu alloys are well understood in the literature, and are considered an "ideal model" of bimetallics[6]. Au and Cu form a substitutional solid solution, i.e. under most circumstances the addition of an atom of one element to a structure of the other replaces atoms of the latter at random. This is possible due to the atomic radii of Au (0.144 pm) and Cu (0.128 pm) being within 15 % of each other[7]. This is highly beneficial for plasmonic applications: as both Au and Cu exhibit a plasmonic resonance in the visible spectrum, the plasmon resonance can be fine-tuned through alloying[8]. Cu has a higher electrical conductivity than Au, which can help prolong the lifetime of the SPP, as Joule heating will negatively affect SPP propagation[9].

There remain, however, several issues related with alloying which prevents their wider use in plasmonic applications. Care must be taken with the specific amounts of alloying material used, as there is a strong possibility that the alloyed material will perform worse than the pure metals alone[10]. For example, Figure 6.2 shows the measured bulk plasma frequency and damping times for a range of AuCu and AuAg alloys. In all cases measured, the damping time is lower than that of the pure constituent metals, suggesting that the additional components in the metal matrix are resulting in a higher likelihood of scattering.

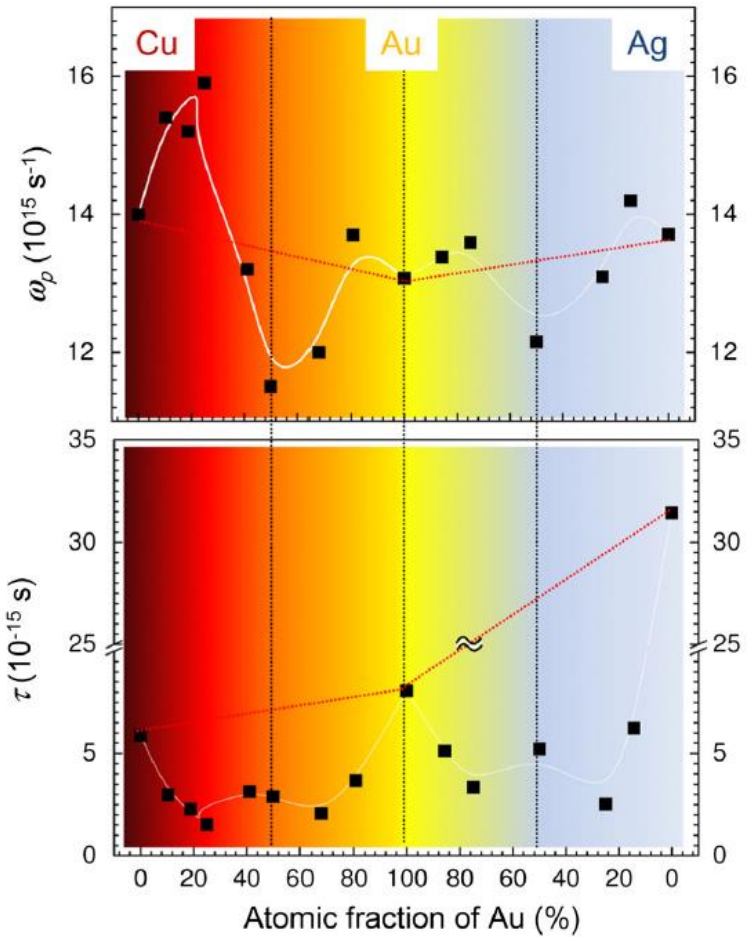

Figure 6.2: measurements of bulk plasma frequency ω_p and damping times τ for AuAg and AuCu alloys. Note that none of the alloys tested have a higher τ value that observed in its constituent parts. Taken from reference [10]

The above issues, however, could potentially be outweighed by any stability improvements conferred onto the plasmonic devices being utilized for high-temperature applications. There is some considerable promise in using alloys to stabilize films against dewetting; previous work has shown how AuPt thin films are significantly more resistant to dewetting that pure Au. The reason given for this increase in stability is due to a change in diffusion parameters: Au & Pt atoms require more energy to be able to diffuse through the altered matrix[11]. A similar increase in stability against dewetting has also been seen in AgTi alloyed films. In this case, however, the increase in stability is attributed to the diffusion of Ti to the surface, which oxidizes and forms a protective layer[12]. In addition to dewetting, other stability benefits can be obtained through alloying. In the case of the AuCu system, Au helps to stabilize Cu against oxidization, by inhibiting the growth of CuO_2 islands on the film surface[13].

In this chapter, the thermal stability of an AuCu alloy is studied. The back-reflected laser dewetting measurement is used to compare the stability with standard Au films. The optical characteristics of the film are measured, so that their plasmonic properties may be evaluated and compared with values for pure Au and Cu films.

6.2 Experimental details

SEM images were obtained using a Zeiss ULTRA SEM. The beam voltage was 5 kV and the SE2 detector was used for all images obtained.

Optical absorption measurements were obtained using a Perkin Elmer UV-Vis Spectrophotometer.

n & κ values were obtained using a SOPRA GESP 5 variable angle spectroscopic ellipsometer.

AFM analysis was undertaken using an Asylum MFP-3D, with BudgetSensors Tap300Al-G silicon AFM probes.

6.2.1 Deposition of the AuCu alloy

The Krugerrand is an investment currency, produced in South Africa[14]. By weight, it consists of 91.67% Au, and 8.33% Cu (the same ratios used in the crown gold alloy mentioned previously); this translates into atomic percentages of 78.02% and 21.98%, respectively (see Figure 6.3). The Au/Cu ratio in the Krugerrand is potentially useful for thermo-plasmonic applications for a number of reasons. In its bulk form, the Krugerrand alloy is mechanically harder than pure Au, hence its utility as coinage throughout history[15]. The Au/Cu ratio is sufficient to inhibit oxidation under ambient conditions[16], making it more practical to use than pure Cu.

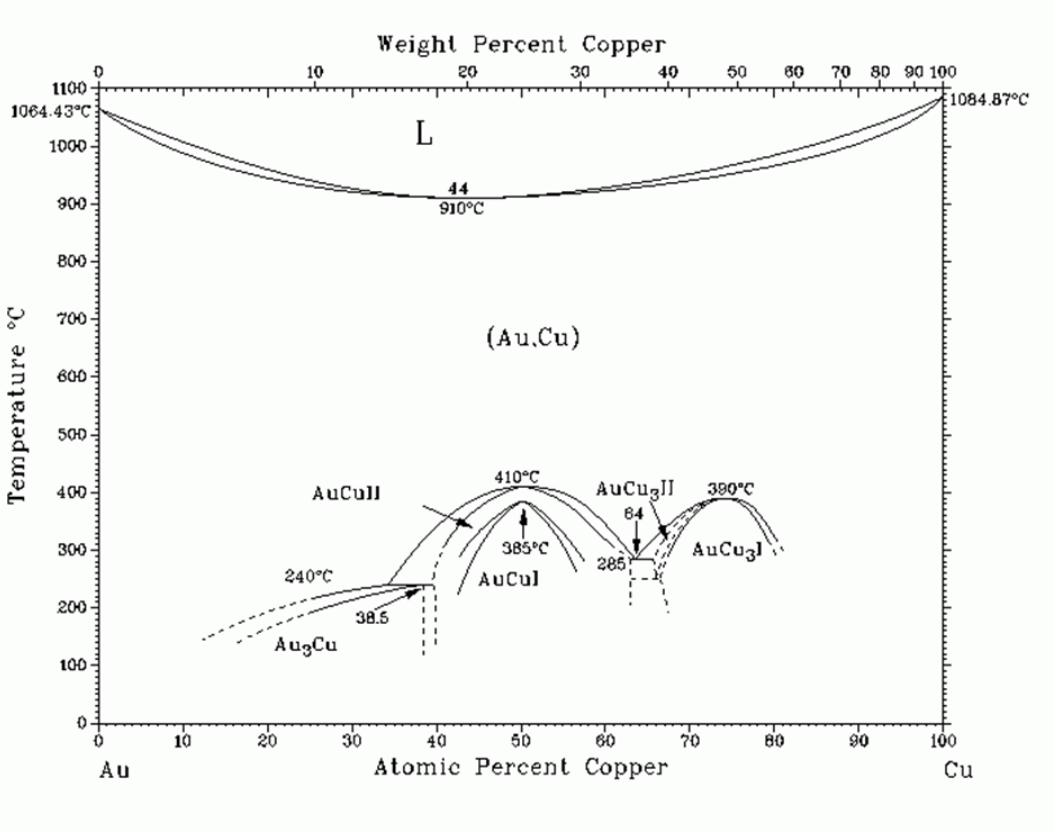

Figure 6.3: AuCu phase diagram from 0°C to 1100°C. Note that below the melting point, the Au-Cu system forms a solid-solution, except for specific intermetallic compounds that can be formed at specific temperatures (indicated by dashed and solid lines).

Films of the Krugerrand alloy were deposited using a GATAN sputtering system, with a Krugerrand coin obtained from Irish Gold Bullion as the sputtering target. The diameter of the coin was reduced through cutting and filing, in order for it to fit flush within the sputtering system (see Figure 6.4). Films of 50 nm and 100 nm thickness were deposited onto SiO_2 substrates, at a rate of 0.36 $Å.s^{-1}$.

Figure 6.4: preparation of Krugerrand coin for film deposition. (a) Krugerrand after reducing the radius to the correct size, (b) the Krugerrand in the sputtering target holder, (c) the Krugerrand in the deposition chamber of the sputtering system.

6.3 Results & Discussion

6.3.1 Optical properties of AuCu alloy

The optical properties of the deposited AuCu alloy were measured so that the plasmonic performance could be elucidated. First, the optical absorption of the AuCu alloy was measured so that the absorbed power could be known during measurements of the thermal stability. The optical transmission, reflectivity, and absorption of a 50 nm AuCu film are shown in Figure 6.5. At 488 nm, the illumination frequency used for the laser-induced dewetting measurements, the AuCu alloy absorbs ~46%, compared to 50 nm Au, which absorbed ~44% (see Chapter 5).

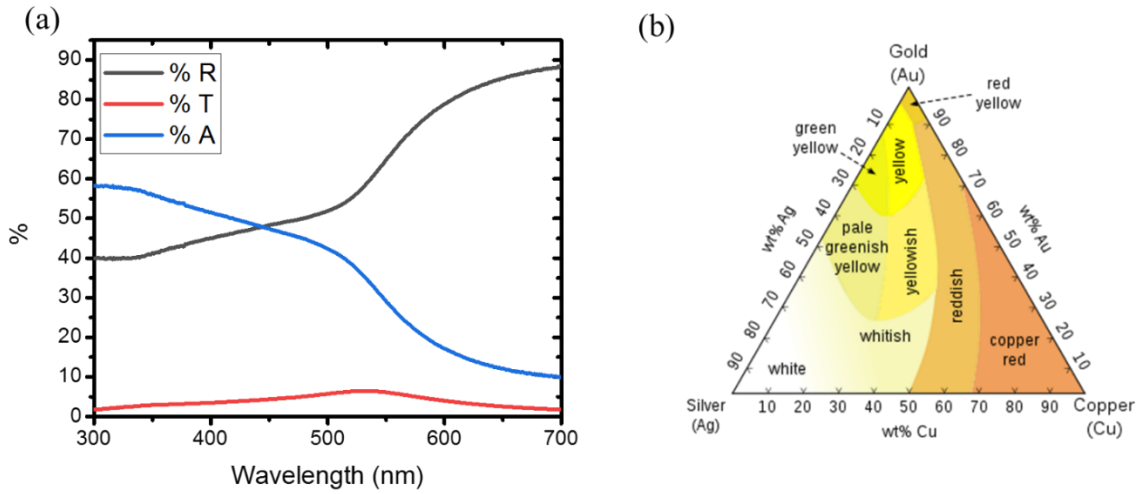

Figure 6.5: optical properties of AuCu alloy. (a) optical absorption spectra for 50 nm AuCu film, and (b) ternary plot of Au-Cu-Ag alloys, showing resultant colour in the bulk. "Ag-Au-Cu-colours-english.svg" by Metallos is licensed under BY-SA 4.0.

The complex refractive index for 50 nm and 100 nm thick AuCu films were measured via ellipsometry. The resultant n and κ values are shown in Figure 6.6, in addition to previously measured values for Au and Cu for comparison[17]. Similarly shaped n and κ curves can be observed for each material, but the specific values differ for each wavelength. In the case of the n values, the AuCu alloy has a larger n value at longer wavelengths.

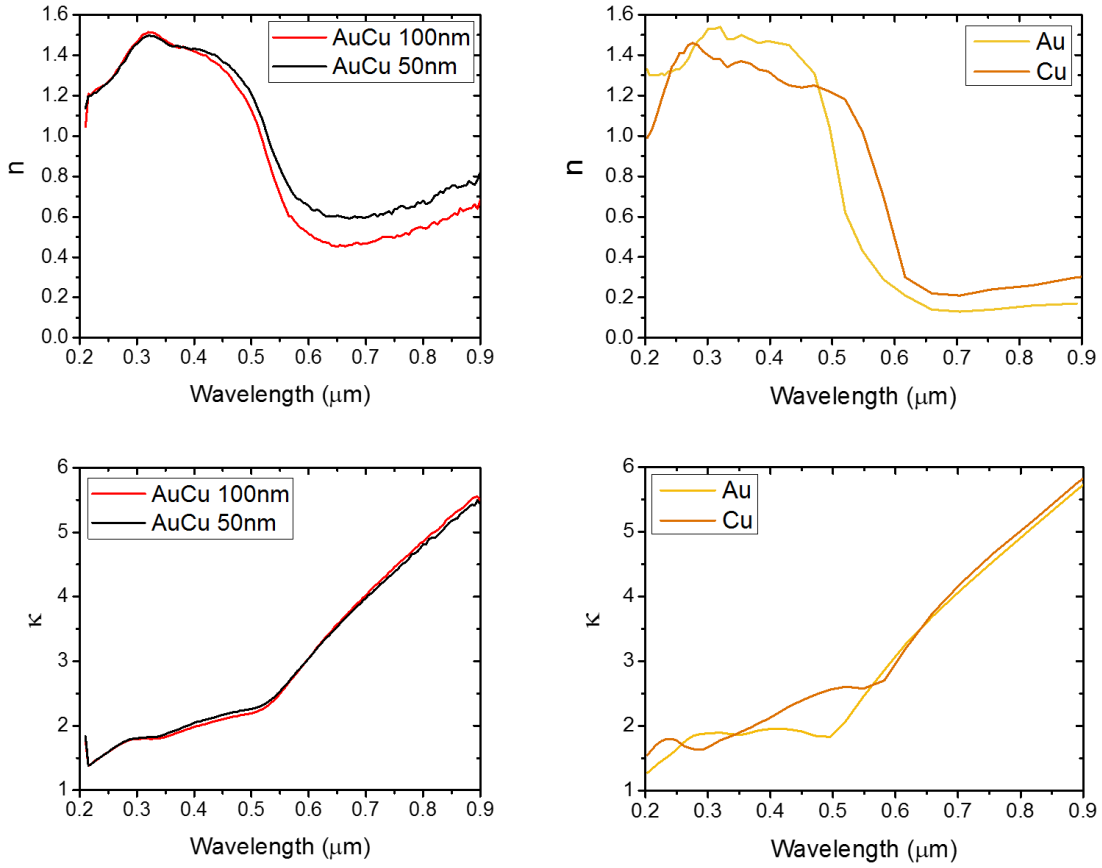

Figure 6.6: measured n and κ values for 50 nm and 100 nm AuCu film, and n and κ values for pure Au and Cu. Plots are separated into 4 different graphs for clarity. n and κ values for Au and Cu taken from reference[17]**.**

The differences in n values for the different thicknesses of the AuCu alloy are likely due to differences in surface roughness[18]. In Figure 6.7, AFM analysis for each AuCu film is shown. From the AFM images, each film appears to be continuous. The root-mean square of the surface roughness, however, shows a much larger surface roughness in the 100 nm AuCu film (1.02 nm) compared with that of the 50 nm AuCu film (0.53 nm). This may suggest that the differences in optical properties are due to the very differing surface roughnesses[19].

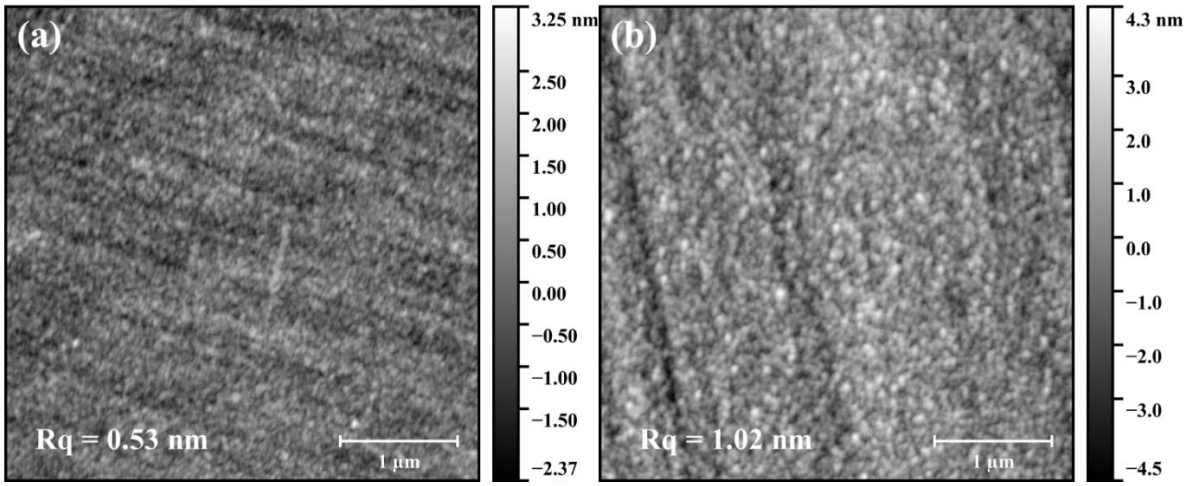

Figure 6.7: AFM images of AuCu alloy thin films, at thicknesses of (a) 50 nm, and (b) 100 nm. Root mean square roughness (Rq) values are shown inset.

From the measured n and κ values, the real and imaginary parts of the relative electric permittivity ε were calculated, using the relations[20];

$$\varepsilon' = n^2 - \kappa^2 \tag{6.1}$$

$$\varepsilon'' = 2n\kappa \tag{6.2}$$

The resultant values for the AuCu alloy are plotted in Figure 6.8, in addition to values for Au and Cu calculated from previously measurements of n and κ taken for film thicknesses between 29.7 nm and 46.5 nm[17].

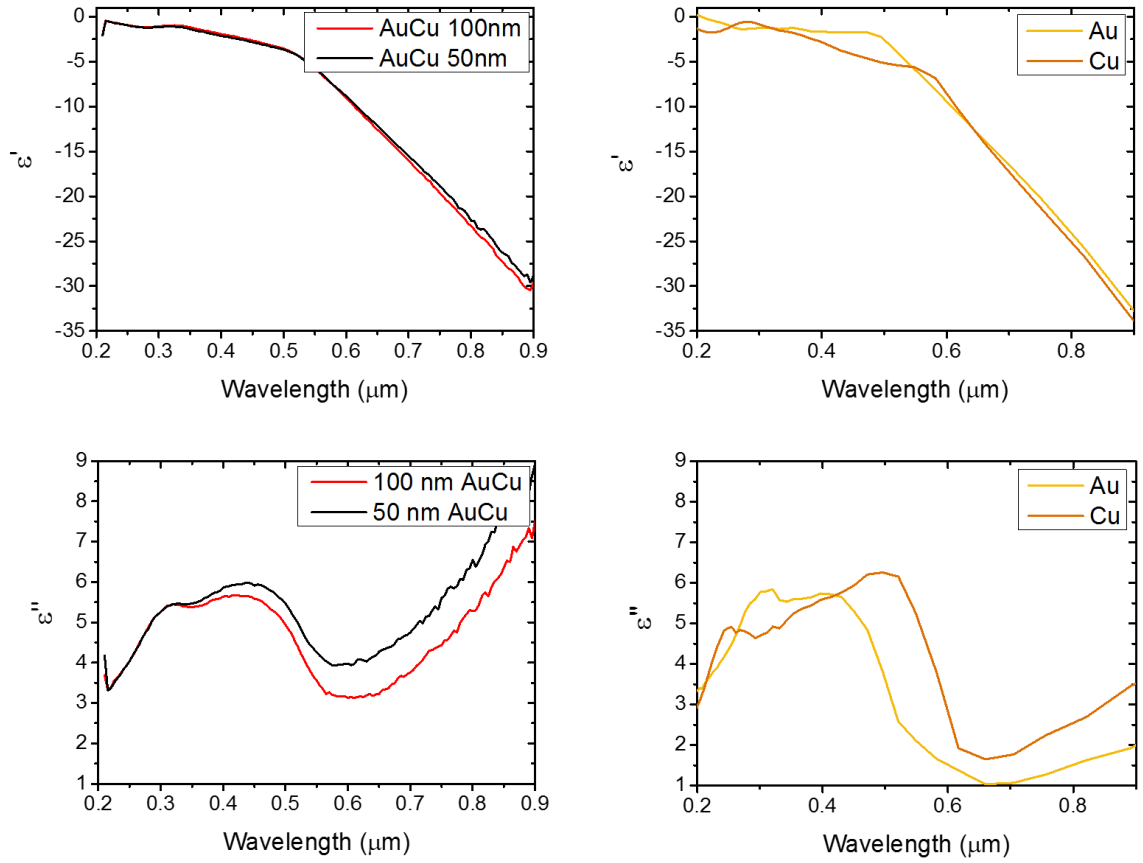

Figure 6.8: ε' and ε'' spectra for Au, Cu, and 50 nm and 100 nm AuCu films, calculated using n and κ values from Figure 6.6. As before, plots are separated into 4 different graphs for clarity. Values for Au and Cu taken from reference[17].

With these values, the potential plasmonic performance of the AuCu alloy could be compared with that of its constituent parts. The existence of a surface plasmon is predicated on the material in question having a negative value for ε', and if the losses within the medium are small, i.e. $\varepsilon'' < |\varepsilon'|$. Hence, a common way of quantifying the performance of a plasmonic material is by calculating the quality factor (Q) as follows[21]:

$$Q = \frac{-\varepsilon'}{\varepsilon''} \tag{6.3}$$

The convenience of the Q-factor as a quantifier is based on it depending only on the optical properties of the material in question, which are either easily available in the literature[17] or can be measured with standard optical characterisation methods. In Figure 6.9, the Q factor for the AuCu alloy as a function of wavelength is plotted. By way of comparison, the Q factors for pure Au and Cu are plotted simultaneously, using the data

obtained by Johnson and Christy[17]. There is some similarity in the data for each of the metals shown: all show a poor Q factor for wavelengths shorter than 500 nm, and at longer wavelengths the Q factor begins to increase and roughly plateaus at ~650 nm. The metals are easily distinguished, however, in the magnitude of Q. Au shows the best performance, followed by Cu, and then AuCu. This is to be expected, as the alloying in likely causing an increase in scattering points for the surface plasmons. The Q-factor at an excitation wavelength of 633 nm gives values of 9.84 (Au), 6.53 (Cu), 3.55 (100 nm AuCu), and 2.71 (50 nm AuCu), demonstrating the expected loss in plasmonic capabilities upon alloying.

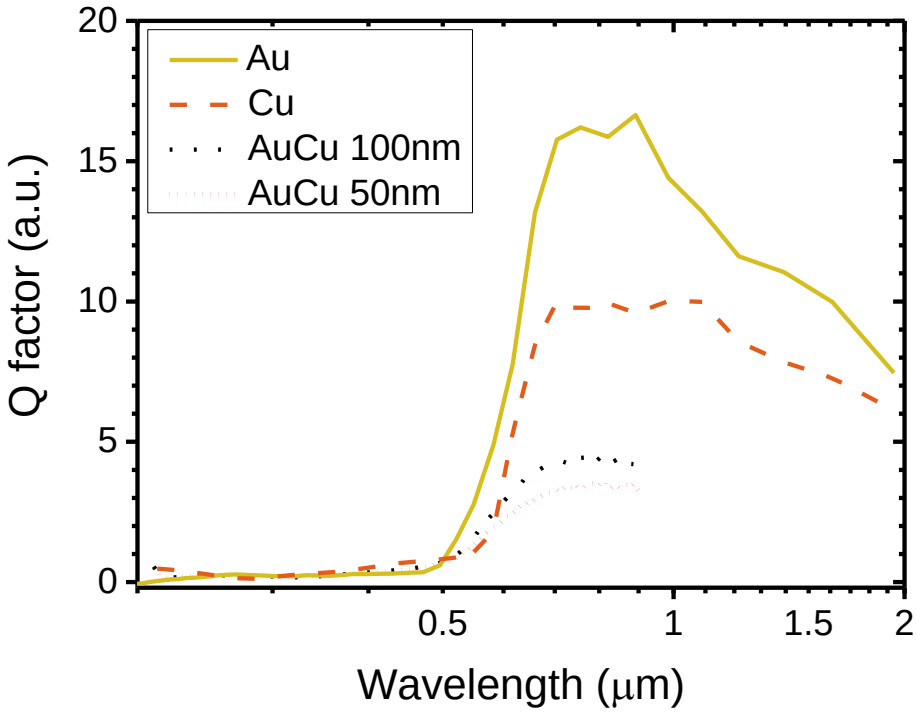

Figure 6.9: plasmonic Q-factor as a function of wavelength for Au, Cu, and AuCu alloy at different thicknesses.

The use of equation (6.3) as a measure of thermo-plasmonic performance is not entirely appropriate, as it does not contain any dependence on the surrounding medium, or does not distinguish between different possible plasmonic functionalities. Such functionalities would include near-field enhancement and heat-generation. In order to circumvent this issue, Lalisse *et al* formulated 2 figures of merit for quantifying different aspects of thermo-plasmonic performance[1]. The Faraday (Fa) number quantifies the ability of a material to enhance the optical near-field. It can be defined as:

$$Fa = 9\left|\frac{\varepsilon' + \varepsilon''}{\varepsilon' + \varepsilon'' + 2\varepsilon_s}\right|^2 \tag{6.4}$$

where ε_s is the relative permittivity of the surrounding medium. The Fa number is highly relevant as a figure of merit for HAMR materials, as the ability of the NFT to enhance the near-field will give a good measure of its success[22]. Figure 6.10 displays the Fa numbers as a function of wavelength for the AuCu alloy, in addition to the Fa numbers for pure Au and Cu. Air (ε_r = 1.00059) was chosen as the surrounding medium. In contrast to the calculated Q-factors displayed in Figure 6.9, the order of Fa was found to be Au > AuCu > Cu. Upon alloying, the resonance redshifts from the original Au peak (λ_{res} = 520.9 nm) towards the Cu peak (λ_{res} = 582.1 nm), ultimately resulting in a resonance peak at 555 nm. This result is in agreement with previous work on fine-tuning the plasmonic resonance through alloying[8].

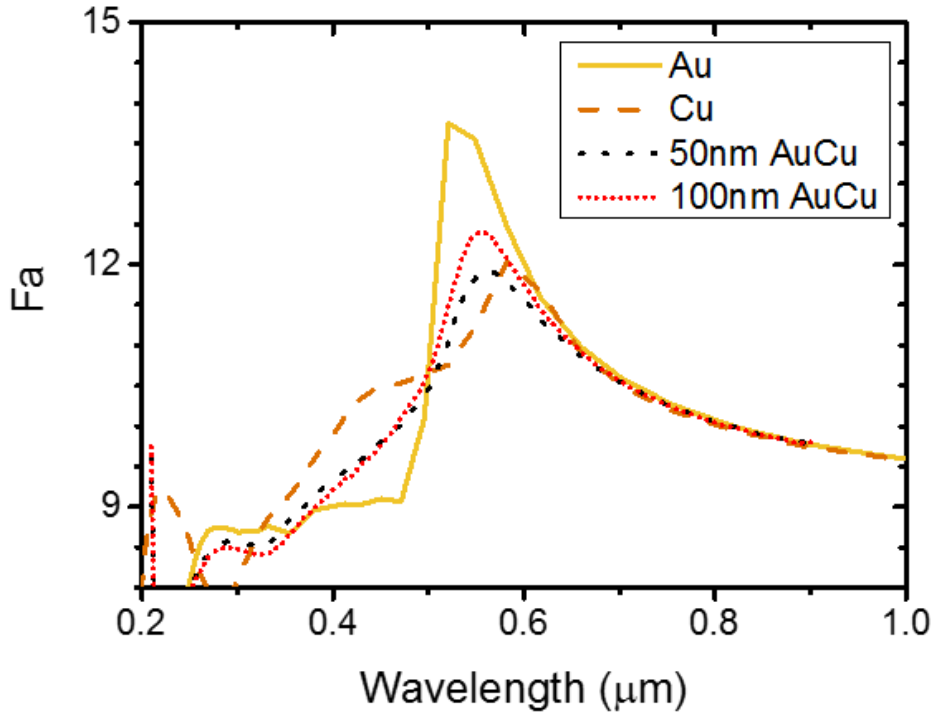

Figure 6.10: Faraday (Fa) numbers as a function of wavelength for Au, Cu, and AuCu alloy.

In order to measure the efficiency of a material as a plasmonic heater, the dimensionless Joule (Jo) number is used. It can be defined as:

$$Jo = \frac{9e\varepsilon''}{n_s}\left|\frac{\varepsilon_s}{\varepsilon' + \varepsilon'' + 2\varepsilon_s}\right|^2 \tag{6.5}$$

where e is a dimensionless measure of the photon energy, defined as $e = \lambda_{ref}/\lambda$, where $\lambda_{ref} \approx$ 1240 nm. The Jo numbers as a function of wavelength for the AuCu alloy are plotted in Figure 6.11. Calculated Jo numbers for Au and Cu are again shown for comparison. Each material exhibits a Jo resonance peak at the same location as the Fa resonance.

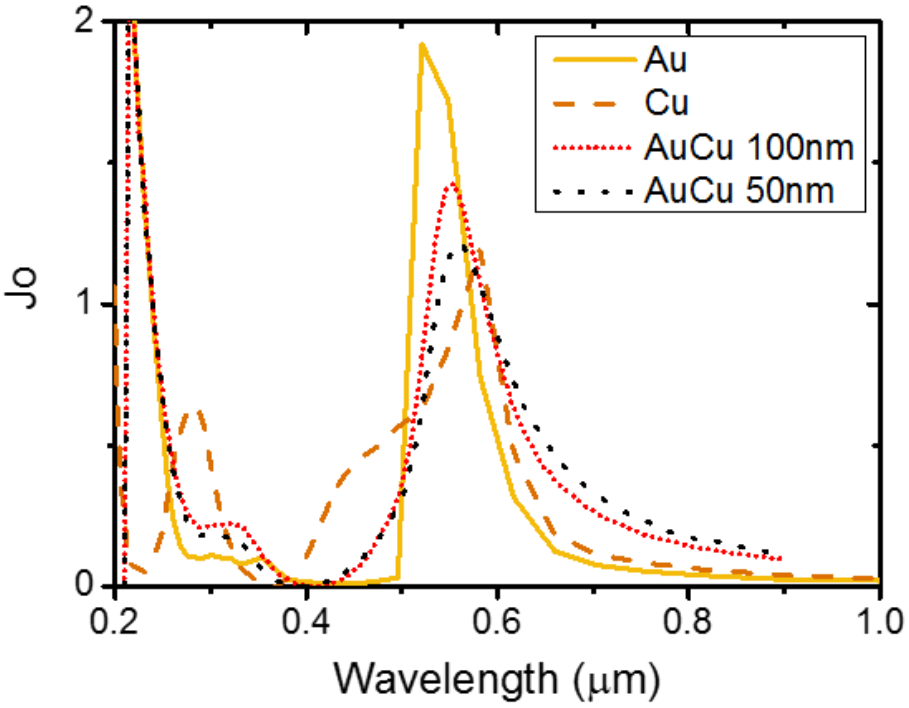

Figure 6.11: Joule (Jo) numbers as a function of wavelength for Au, Cu, and AuCu alloy.

7.3.2 Thermal stability of AuCu alloy

The thermal stability of the AuCu film was measured using the back-reflected laser-signal technique described in Chapter 3. It must be noted that no adhesion layer was utilized in these experiments. The absorbed power was varied from 5 – 15 mW, and the beam waist was fixed at 1.8 μm for all measurements. The resultant degradation curves are shown in Figure 6.12. The AuCu film shows a poor thermal stability, even worse than that of a 50 nm Au film without any adhesion layer (see Chapter 4). The rapid drop in reflectivity suggests that there are processes occurring at the radiation centre other than dewetting, such as oxidation.

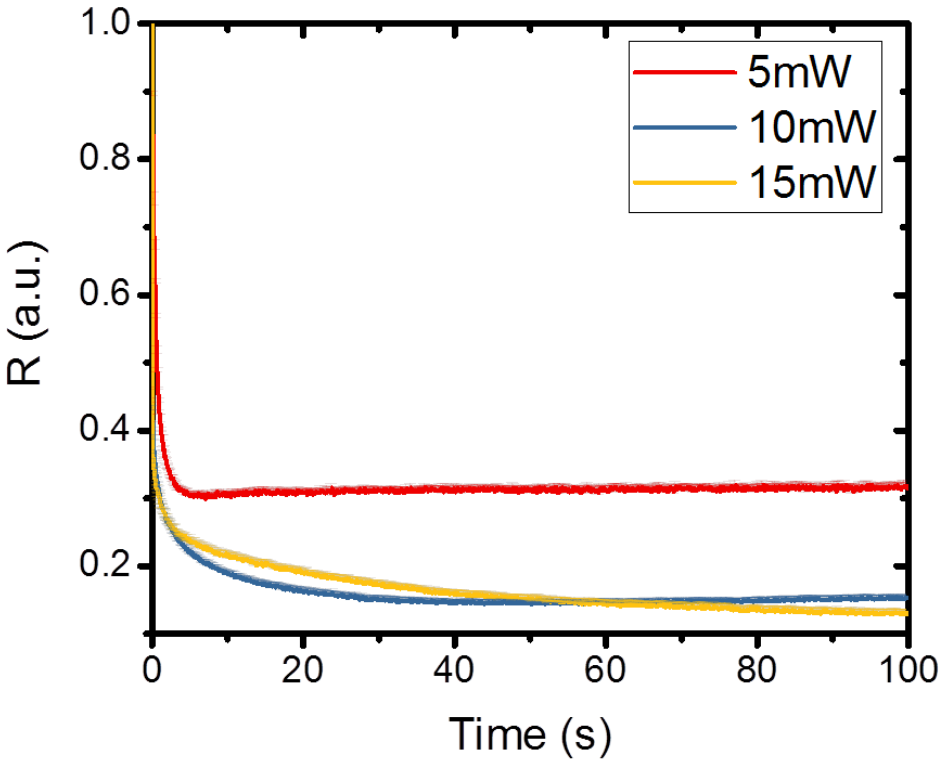

Figure 6.12: degradation curves for 50 nm AuCu film at different absorbed powers. The beam waist was 1.8μm for all measurements.

SEM images of the irradiated areas are shown in Figure 6.13, with a non-irradiated area for comparison. Even at low absorbed powers, the film has dewetted significantly and shown major changes at the point of irradiation. Irradiated areas appear to have an increased surface roughness, with the edge of the dewetted area breaking down into particles.

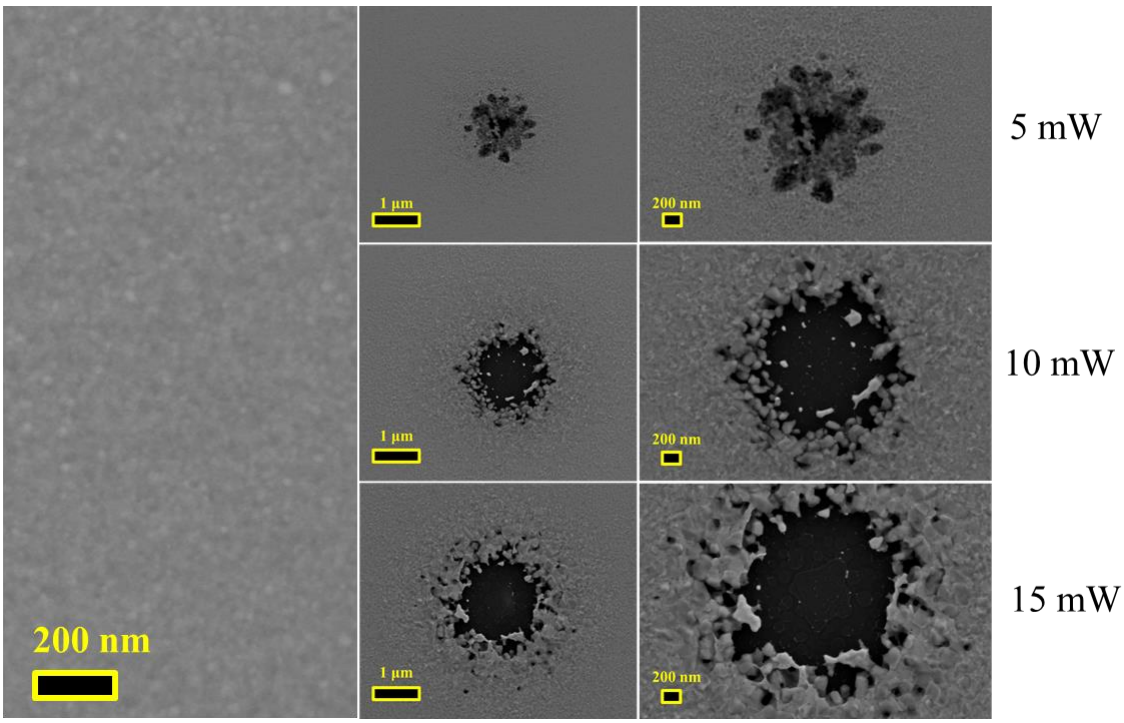

Figure 6.13: SEM images of 50 nm AuCu film, pre-irradiation (left) and post-irradiation at different absorbed powers (right).

The reason for the poor thermal stability is due to segregation and oxidation of the Cu within the alloyed film. It has been shown previously that, while alloying Au with Cu will improve the stability under ambient conditions, sufficient heating will cause the Cu to segregate and oxidize[13]. This can be seen clearly in Figure 6.14. In Figure 6.14a, a laser-annealed area of a 100 nm Cu film is shown. As the film is irradiated, the surface oxidizes, forming a flaky surface component. Raman spectroscopy measurements determined this to be CuO. A similar surface component can be seen in Figure 6.14b, in the laser-annealed area of the 50 nm AuCu film, albeit in much smaller quantities.

These results suggest that alloying Au with plasmonic metals capable of oxidation, such as Ag, Al, or Cu, will not help to improve the thermal stability of the film. Calculations of the Fa and Jo numbers show a decrease in the plasmonic efficiency upon alloying when compared to pure Au, and when there is no resultant increase in thermal stability, their use cannot be justified. Hence, no further experiments were carried out on the AuCu films.

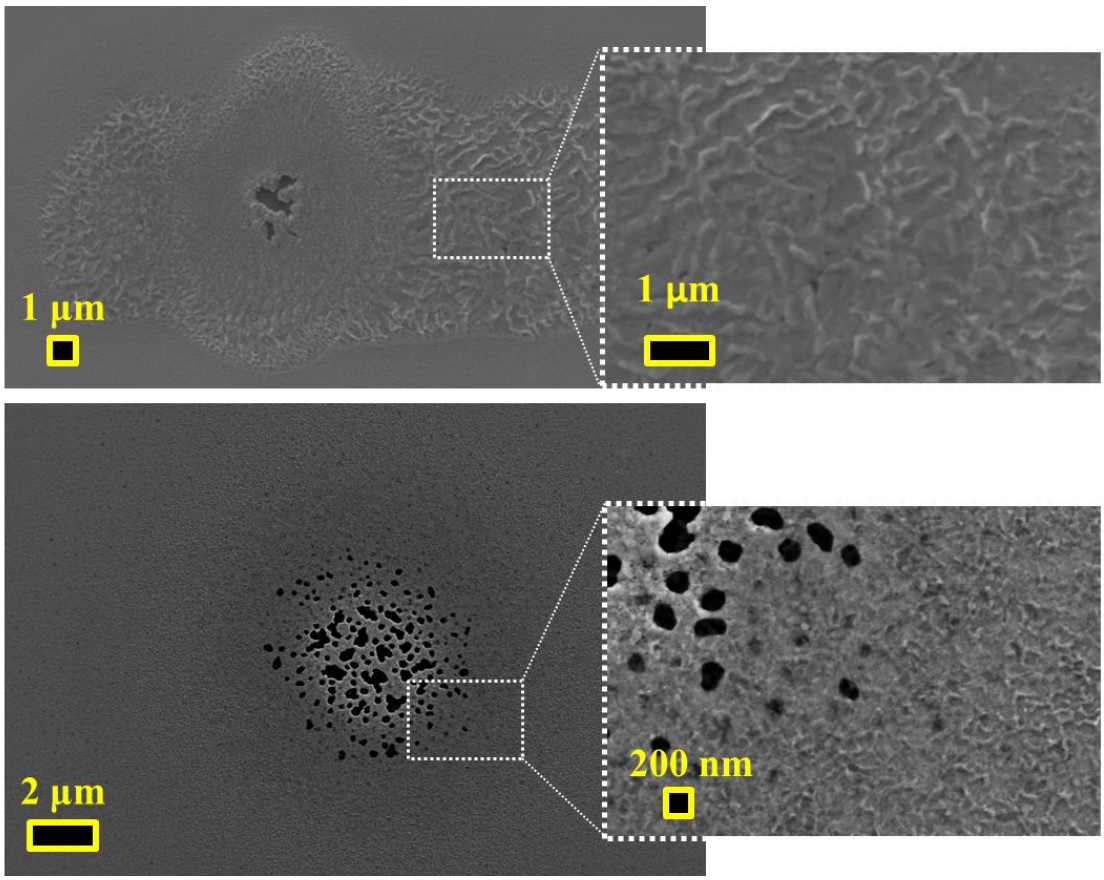

Figure 6.14: SEM images of laser-irradiated areas on a 100 nm Cu film (top) and a 50 nm AuCu film (bottom). Similar material growth can be seen on both films, suggesting oxidation of Cu.

6.4 Conclusions

In this chapter, work is done to analyse the optical properties and thermal stability of AuCu alloys, specifically that of the South African Krugerrand investment currency (91.67% Au, and 8.33% Cu by weight). Calculations of the plasmonic quality factor based on the measured optical properties showed a poorer performance when compared with pure metals, but the thermo-plasmonic effectiveness was found to be between that of Au and Cu. Differences in optical and plasmonic properties for different thicknesses of the AuCu alloy were determined to be due to differences in surface roughness. When measuring the thermal stability of the films, it was found that the AuCu would still dewet at relatively low absorbed powers, which resulted in a large reduction in the film quality. The reduction in thermal stability compared to a pure Au film is due to oxidation of the Cu: upon heating, the Cu segregates to the film surface and oxidizes. These results suggest that alloying with oxidizing species is not a feasible solution towards improving the stability of Au for thermo-plasmonic applications. Further work on the stability of this alloy could involve the

use of both adhesion and capping layers. The use of an adhesion layer will potentially help prevent dewetting, and a capping layer will potentially help prevent oxidation of the Cu. In the case of the capping layer, it will be necessary to use a material that is oxygen impermeable: in Chapter 7, capping layers of alumina are investigated for the stabilization of Au. The thicknesses of capping layer investigated (≤ 5 nm), however, may not be suitable for the prevention of Cu oxidation due to alumina only becoming oxygen impermeable at thicknesses greater than 4 nm[23]. The stabilization effects of capping layers on Au will be discussed in Chapter 7.

6.5 Bibliography

(1) Lalisse, A.; Tessier, G.; Plain, J.; Baffou, G. Quantifying the Efficiency of Plasmonic Materials for Near-Field Enhancement and Photothermal Conversion. *J. Phys. Chem. C* **2015**, *119* (45), 25518–25528.

(2) Wells, M. P.; Bower, R.; Kilmurray, R.; Zou, B.; Mihai, A. P.; Gobalakrichenane, G.; Alford, N. M.; Oulton, R. F. M.; Cohen, L. F.; Maier, S. A.; et al. Temperature Stability of Thin Film Refractory Plasmonic Materials. *Opt. Express* **2018**, *26* (12), 15726.

(3) Smith, C. S. *A History of Metallography : The Development of Ideas on the Structure of Metals before 1890*; MIT Press, 1988.

(4) Reibold, M.; Paufler, P.; Levin, A. A.; Kochmann, W.; Pätzke, N.; Meyer, D. C. Carbon Nanotubes in an Ancient Damascus Sabre. *Nature* **2006**, *444* (7117), 286–286.

(5) Craig, J. *The Mint: A History of the London Mint from A.D. 287 to 1948*; Cambridge University Press, 1953.

(6) Wang, G.; Xiao, L.; Huang, B.; Ren, Z.; Tang, X.; Zhuang, L.; Lu, J. AuCu Intermetallic Nanoparticles: Surfactant-Free Synthesis and Novel Electrochemistry. *J. Mater. Chem.* **2012**, *22* (31), 15769–15774.

(7) Ladd, M. *Crystal Structures - Lattices and Solids in Stereoview*; Horwood, 2002.

(8) Motl, N. E.; Ewusi-Annan, E.; Sines, I. T.; Jensen, L.; Schaak, R. E. Au-Cu Alloy Nanoparticles with Tunable Compositions and Plasmonic Properties: Experimental Determination of Composition and Correlation with Theory. *J. Phys. Chem. C* **2010**, *114* (45), 19263–19269.

(9) Sun, Q.-C.; Ding, Y.; Goodman, S. M.; H. Funke, H.; Nagpal, P.; Lindquist, N. C.; Nagpal, P.; McPeak, K. M.; Norris, D. J.; Oh, S.-H.; et al. Copper Plasmonics and Catalysis: Role of Electron–phonon Interactions in Dephasing Localized Surface Plasmons. *Nanoscale* **2014**, *6* (21), 12450–12457.

(10) Nishijima, Y.; Hashimoto, Y.; Seniutinas, G.; Rosa, L.; Juodkazis, S. Engineering Gold Alloys for Plasmonics. *Appl. Phys. A* **2014**, *117* (2), 641–645.

(11) Manuela Müller, C.; Spolenak, R. Dewetting of Au and AuPt Alloy Films: A Dewetting Zone Model. *J. Appl. Phys.* **2013**, *113* (9), 094301.

(12) Kawamura, M.; Zhang, Z.; Kiyono, R.; Abe, Y. Thermal Stability and Electrical Properties of Ag–Ti Films and Ti/Ag/Ti Films Prepared by Sputtering. *Vacuum* **2013**, *87*, 222–226.

(13) Wang, L.; Yang, J. C. Enhanced Nucleation and Decreased Growth Rates of Cu_2O in

$Cu_{0.5}Au_{0.5}$ (001) Thin Films During in Situ Oxidation. *J. Mater. Res.* **2011**, *20* (07), 1902–1909.

(14) Glynn, C.; Conley, R. The Industrial Use of Gold. *Gold Bull.* **1979**, *12* (4), 134–139.

(15) Asher, H. H. Hardness Study of Transformations in Gold-Copper Alloys. *J. Dent. Res.* **1934**, *14* (5), 349–358.

(16) Okada, M.; Tsuda, Y.; Oka, K.; Kojima, K.; Diño, W. A.; Yoshigoe, A.; Kasai, H. Experimental and Theoretical Studies on Oxidation of Cu-Au Alloy Surfaces: Effect of Bulk Au Concentration. *Sci. Rep.* **2016**, *6* (1), 31101.

(17) Johnson, P. B.; Christy, R. W. Optical Constants of the Noble Metals. *Phys. Rev. B* **1972**, *6* (12), 4370–4379.

(18) Shen, P.-T.; Sivan, Y.; Lin, C.-W.; Liu, H.-L.; Chang, C.-W.; Chu, S.-W. Temperature- and Roughness- Dependent Permittivity of Annealed/Unannealed Gold Films. *Opt. Express* **2016**, *24* (17), 19254.

(19) Fenstermaker, C. A.; McCrackin, F. L. Errors Arising from Surface Roughness in Ellipsometric Measurement of the Refractive Index of a Surface. *Surf. Sci.* **1969**, *16*, 85–96.

(20) Fox, M. Optical Properties of Solids; Oxford University Press, 2001.

(21) Stockman, M. I. Nanoplasmonics: Past, Present, and Glimpse into Future. *Opt. Express* **2011**, *19* (22), 22029.

(22) Challener, W. A.; Peng, C.; Itagi, A. V.; Karns, D.; Peng, W.; Peng, Y.; Yang, X.; Zhu, X.; Gokemeijer, N. J.; Hsia, Y.-T.; et al. Heat-Assisted Magnetic Recording by a near-Field Transducer with Efficient Optical Energy Transfer. *Nat. Photonics* **2009**, *3* (4), 220–224.

(23) Campbell, T.; Kalia, R. K.; Nakano, A.; Vashishta, P.; Ogata, S.; Rodgers, S. Dynamics of Oxidation of Aluminum Nanoclusters Using Variable Charge Molecular-Dynamics Simulations on Parallel Computers. *Phys. Rev. Lett.* **1999**, *82* (24), 4866–4869.

Chapter 7 - Effect of capping layers on the dewetting dynamics of Au plasmonic films

7.1 Introduction

In Chapter 5, it was demonstrated that, via the use of sub-nanometer adhesion layers, significant improvements could be made in the thermal stability of Au thin films. As the stability enhancement maximizes at an adhesion layer thickness of 0.5 nm, it is necessary to explore other stabilisation processes so that higher temperatures may be withstood.

The process of solid-state dewetting will nucleate at areas of high surface energy in the film, such as grain boundaries, triple points, the film/substrate interface, and at the film/air interface. Previous studies have shown that the activation energy for surface diffusion can be significantly smaller than that of grain boundary diffusion[1]; hence, the dewetting behaviour of a thin film can be controlled by modifying the surface energy. The simplest way of doing this is via the use of capping layers, as demonstrated in Figure 7.1. Capping layers have previously been shown to help stabilize polymer thin films from dewetting[2,3], and recent work has extended this to help stabilize Au thin films[3] and nanostructures[4–6]. Calculations have shown that the effectiveness of a capping layer will depend strongly on its stiffness[3]; capping layers with a Young's Modulus of 1 TPa (equivalent to a monolayer of graphene[7]) will result in a much higher stability than a layer with a Young's Modulus of 0.01 GPa (comparable with that of a ripe banana[8]). The reason for this is, as there are changes in the film topography as the film agglomerates during the dewetting process[9], a mechanically stiff capping layer will be able to suppress this behaviour[3].

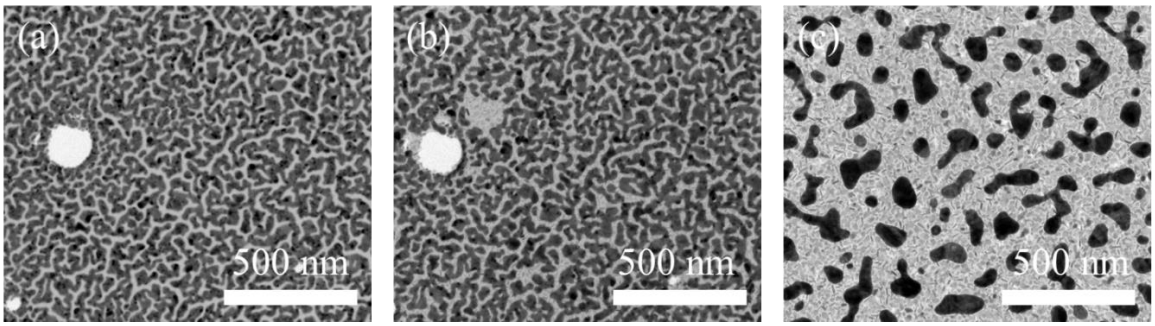

Figure 7.1: stabilization effect of altering the surface properties for a 10 nm Au film on 50 nm SiO_2 membrane; (a) TEM image prior to annealing; (b) area in (a) after 500°C anneal while coated with C deposits; (c) uncoated area after 500°C anneal.

Al_2O_3 has emerged as a promising capping material candidate for plasmonic applications[4,6] for a variety of reasons. Firstly, it has been shown that when in the α-phase (a.k.a. sapphire), Al_2O_3 does not dissolve into the Au during bonding, thus forming a well-defined interface between the materials[10]. Secondly, Al_2O_3 is a commonly used substrate for optical applications; hence it is already well-known how Au/Al_2O_3 systems will behave optically[11]. Additionally, Al_2O_3 has good mechanical properties, with the α-phase[12] in particular having a superior Young's Modulus compared with that of the amorphous phase[13], which helps fulfil the criterion of a large Young's Modulus put forward by Cao *et al* for a functional capping layer[3]. Finally, and perhaps most importantly, Al_2O_3 possesses a very high thermal stability, which has seen it used as a refractory coating material[14]. As is the case with the mechanical properties, crystalline phases of Al_2O_3 were found to perform better as refractory materials than the amorphous phase[15].

In addition to Al_2O_3, there are other metal oxides that can be investigated as capping layers. Based on the utility of Ti and Ta as adhesion layers (see Chapter 5), their oxides were considered as alternate capping layer materials. Both titanium dioxide (TiO_2) and tantalum pentoxide (Ta_2O_5) have been used as passivation layers for Si-based solar cells[16,17]. The Young's Modulus of TiO_2 will depend on its deposition method, but in general is poorer than that of alpha-Al_2O_3[18]. TiO_2 has been shown, however, to damp the plasmonic response of Au much less than metallic Ti when used as an adhesion layer[19].

There are several outstanding issues with using metal oxides as a capping layer. Previous works on Al_2O_3 capping layers have used either molecular-beam epitaxy (MBE) or atomic layer deposition (ALD) as a deposition method, both slow and costly processes[20,21]. Recent work has found that when capping discontinuous Au films, Au "whiskers" can grow and disrupt the capping layer[22]. Additionally, it has generally been found in previous studies

that thicker capping layers result in a higher stability than thinner layers[4,6] (see Figure 7.2), which may result in increased plasmonic damping.

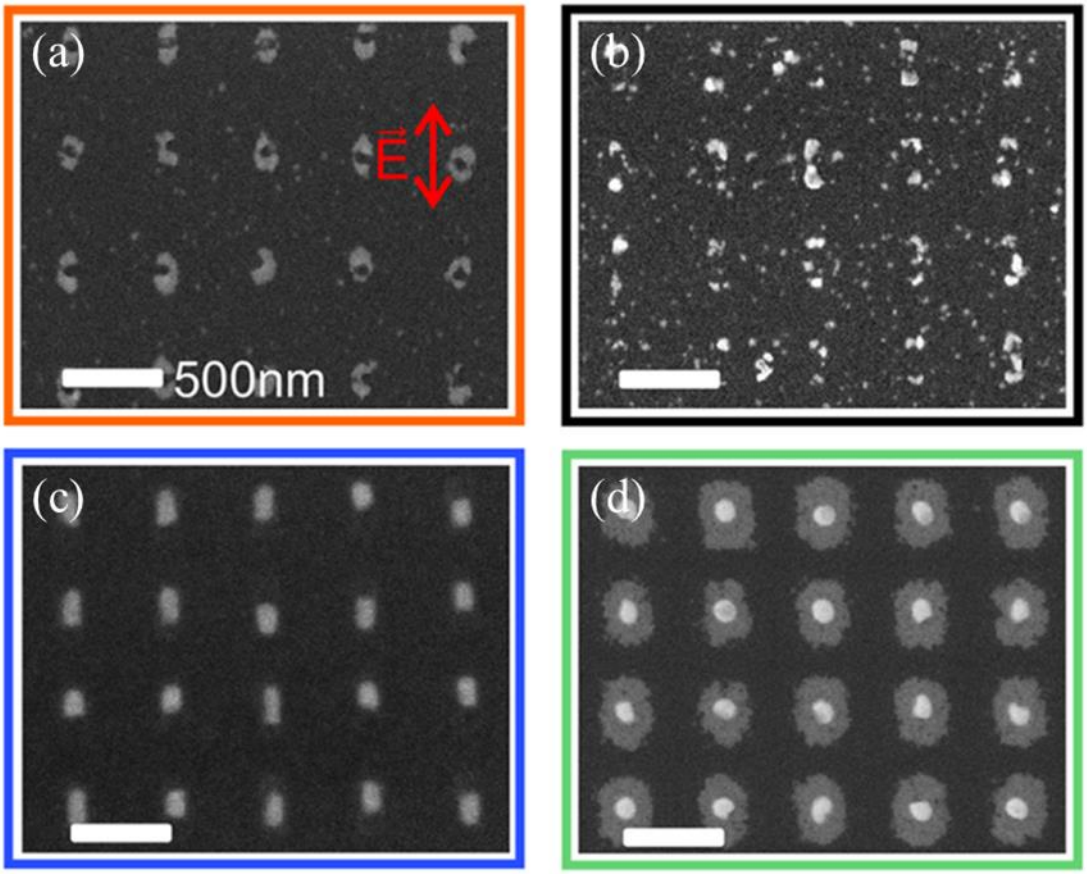

Figure 7.2: SEM images of Au nanorods after annealing at 1100°C with (a) no capping layer, (b) 4 nm Al_2O_3 capping layer, (c) 40 nm Al_2O_3 capping layer, (d) 150 nm IC1-200 capping layer. Taken from reference[4].

In this chapter, the effects of metal oxide capping layers on the dewetting characteristics of 50 nm Au films are studied. Three of the metal oxide layers are manufactured by first depositing a thin layer of the metal, and then allowing it to oxidize in air. A capping layer deposited using a metal oxide (AlOx) sputtering target is also studied by way of comparison. The thickness dependence on the stability is measured using the back-reflected laser signal technique described in Chapter 3. The plasmonic properties of the capped films are studied via measurement the SPP. Finally, based on the work in this chapter and that in Chapters 4 and 5, the optimal configuration for thermally stabilizing an Au plasmonic film will be given.

7.2 Experimental details

The films investigated were 0.5 nm Ti/50 nm Au films with varying thickness of metal oxide capping layers (see Figure 7.3). The samples were prepared using the Rf magnetron sputtering method discussed in section 3.3.2. In the case of aluminium oxide capping layers, 2 different methods were used in their production. In the first case, the capping layer was deposited directly using an AlO_x sputtering target. For the second case, Al was deposited directly onto the Au surface, and was allowed to oxidize in air. Al will oxidize readily under ambient conditions, and will general form amorphous Al_2O_3 up to a thickness of 4 nm[23,24]. The same approach was taken when fabricating samples with capping layers of TiO_2 and Ta_2O_5[25].

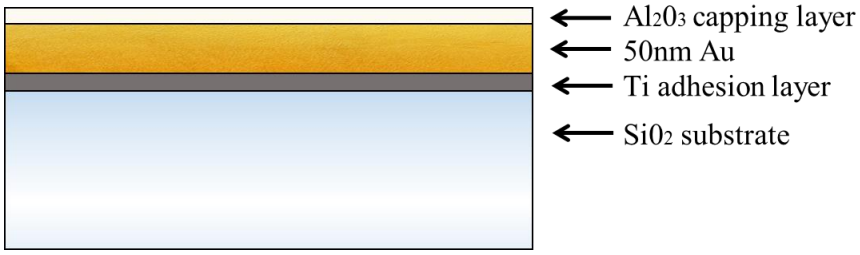

Figure 7.3: schematic diagram of capping layer samples fabricated.

The dewetting characteristics of the samples were studied using the back-reflected laser technique described in Chapter 3. The absorbed powers were maintained at 30 mW with a laser beam waist of 1.8 μm, so that a direct comparison could be made with the adhesion layer results in Chapter 5. To accommodate this, sample measurements were run for 600 s as opposed to 100 s, as the capped samples would be expected to exhibit a higher stability than their uncapped counterparts. An optical absorption spectrum of each sample was taken so that the absorbed power across all samples was consistent. Absorption spectra were taken using a Perkins Elmer UV-Vis Spectrophotometer.

Irradiated areas were investigated using SEM, as described in Chapter 3. The beam voltage was set to 6 kV as opposed to 5 kV, in order to offset the loss in resolution caused by the dielectric capping layer.

Surface plasmon polariton measurements were obtained using SOPRA GESP 5 variable angle spectroscopic ellipsometer, set to a Kretschmann configuration. The SPPs were excited with a wavelength of 633 nm.

7.3 Results & Discussion

7.3.1 Solid-state dewetting of capped Au films

Prior to measuring the solid-state dewetting characteristics of the capped Ti/Au samples, their optical absorption was measured so that the absorbed power could be kept constant at 30 mW across all samples investigated. The optical absorption of each film at 488 nm is shown in Figure 7.4. At the lowest capping layer thicknesses (≤1 nm), there is no significant difference in the measured absorption. For capping layer thicknesses >1 nm, however, the results begin to diverge. For the TaOx/TiOx capping layers, the optical absorption steadily increases for increasing thickness. For the Al_2O_3/AlO_x capped samples, the absorption remains constant until the 5 nm Al capping layer, at which point the absorbed power decreases by 13%. This result is quite likely due to an incomplete oxidation of the deposited Al layer. Al will form Al_2O_3 passivation layer of approximately 4 nm thickness under ambient conditions[26], hence there remains ~1 nm of metallic Al affecting the absorption and stability characteristics of the system.

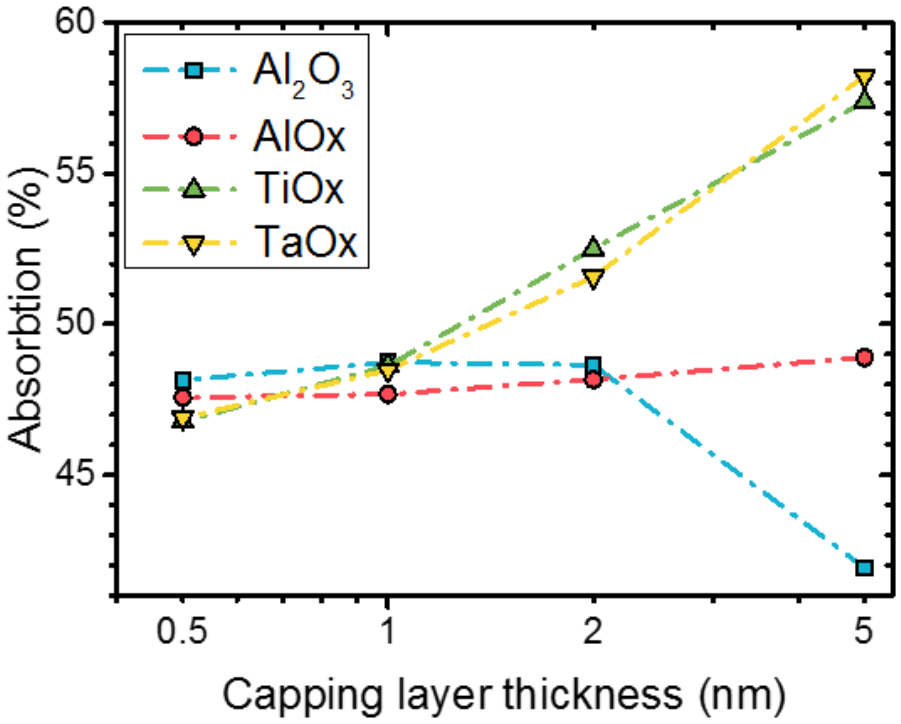

Figure 7.4: optical absorption at 488 nm for each 0.5 nm Ti/50 nm Au/MO_x system investigated, M-different metals. Dashed lines are added to guide the eye.

In Figure 7.5, the degradation curves for 0.5 nm Ti/50 nm Au films with varying thickness of oxidized Al capping layer can be observed. The capping layers appear to follow a similar trend to that of the adhesion layers studied in Chapter 5; thinner layers result in an increase in the dewetting resistance, with 0.5 nm being the optimal thickness. The falloff in stability for the 5 nm capping layer is unexpectedly extreme. This is likely due to incomplete oxidation of the deposited Al as mentioned previously.

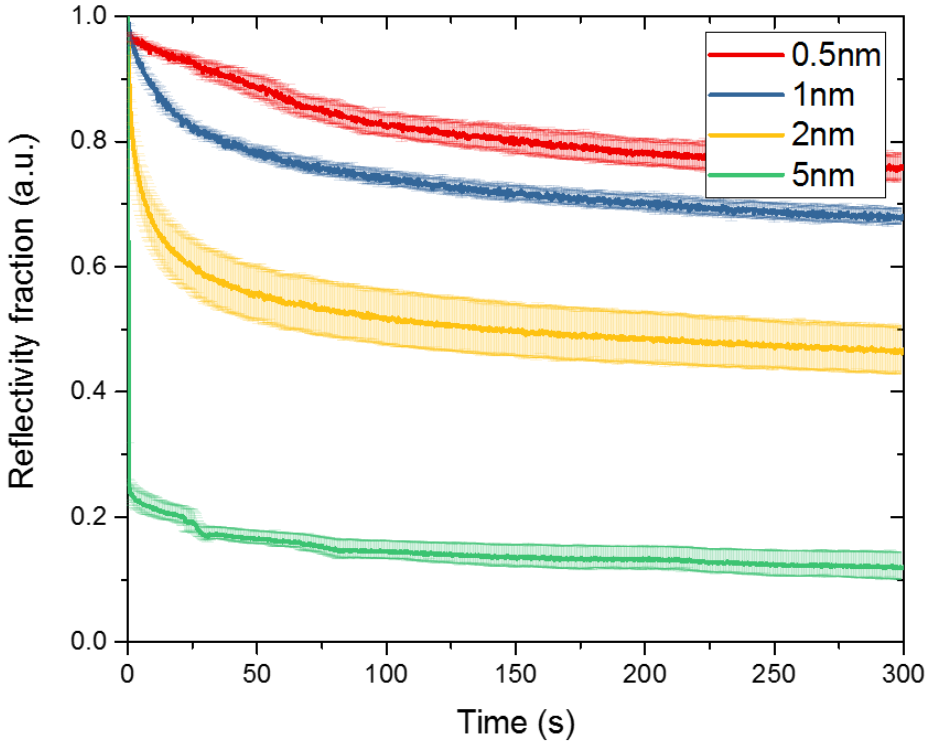

Figure 7.5: degradation curves for 0.5 nm Ti/50 nm Au films with varying thickness of Al deposited as a capping layer.

In order to compare the effectiveness of this deposition technique, capping layers were prepared by directly sputtering from an alumina (AlOx) target. The degradation curves for the AlOx capping layers are shown in Figure 7.6. The first notable difference between the deposition methods is the stability of the 5 nm capping layer. As previously discussed, the 5 nm Al capping layer exhibits exceptionally poor stability, which is most likely due to remnant metallic Al affecting the absorption characteristics. The 5 nm AlOx capping layer, however, exhibits a dewetting behaviour that, while still worse than the other thicknesses investigated, is not as poor as the 5 nm Al capping layer sample. This is due to the deposition of the capping layer as an oxide, hence resulting in there being no remnant

metallic Al within the layer. The degradation curve shows a smooth continuous decrease in film reflectivity, similar to the previous degradation curves that have been obtained.

The optimal thickness measured for the AlOx capping layers was found to be 1 nm. This contrasts with the results from the Al capping layers, where 0.5 nm was found to be the optimal thickness. The reason for this anomaly is likely due to the thickness of the Al capping layer being pre-oxidation: the oxidized thickness is likely much closer to being 1 nm. Note also the increase in relative error for the 0.5 nm AlOx capping layer, suggesting an inconsistent coverage of the Au film.

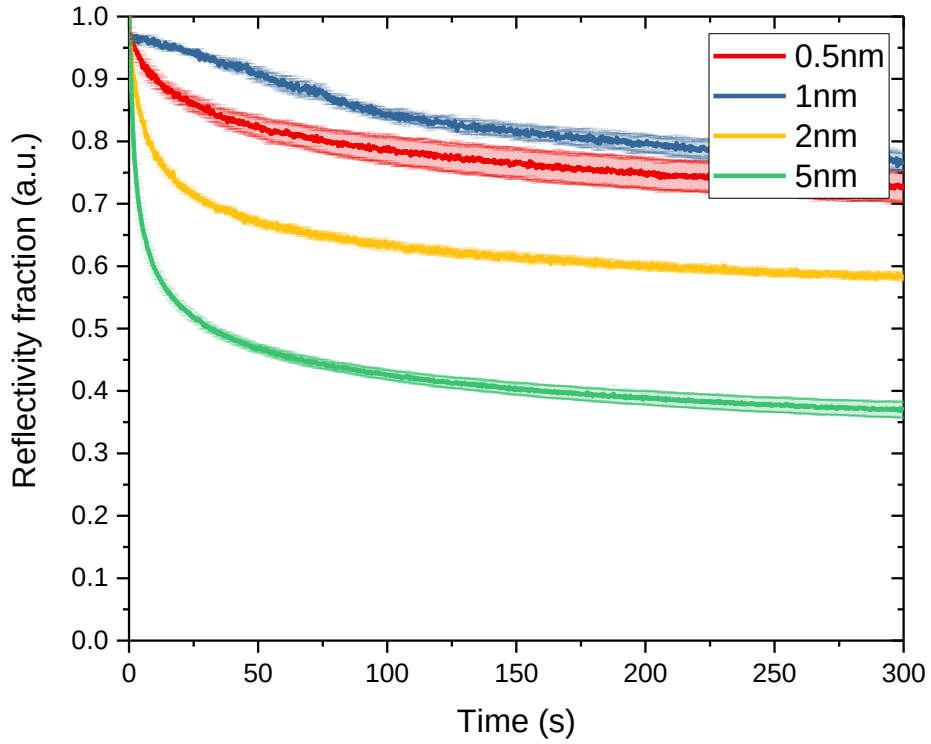

Figure 7.6: degradation curves for 0.5 nm Ti/50 nm Au films with varying thickness of AlOx deposited as a capping layer.

In order to fully confirm the dependence of the capping layer effectiveness on its thickness, degradation curves were obtained for samples capped with Ta (which becomes Ta_2O_5) and Ti (which becomes TiO_2). The degradation curves for Ta_2O_5 and TiO_2 capping layers are shown in Figure 7.7 and Figure 7.8, respectively. Both capping layers exhibit optimal stability at a thickness of 0.5 nm, and the stability decreases upon increasing thickness, which further confirms the thickness dependence on capping layer effectiveness as seen previously.

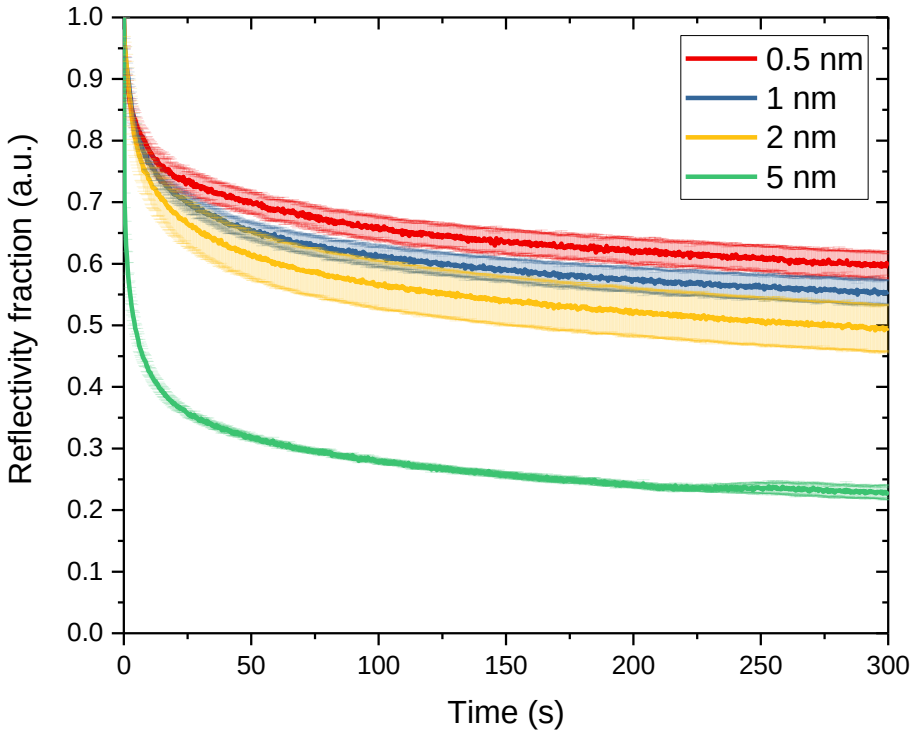

Figure 7.7: degradation curves for 0.5 nm Ti/50 nm Au films with varying thickness of Ta deposited as a capping layer.

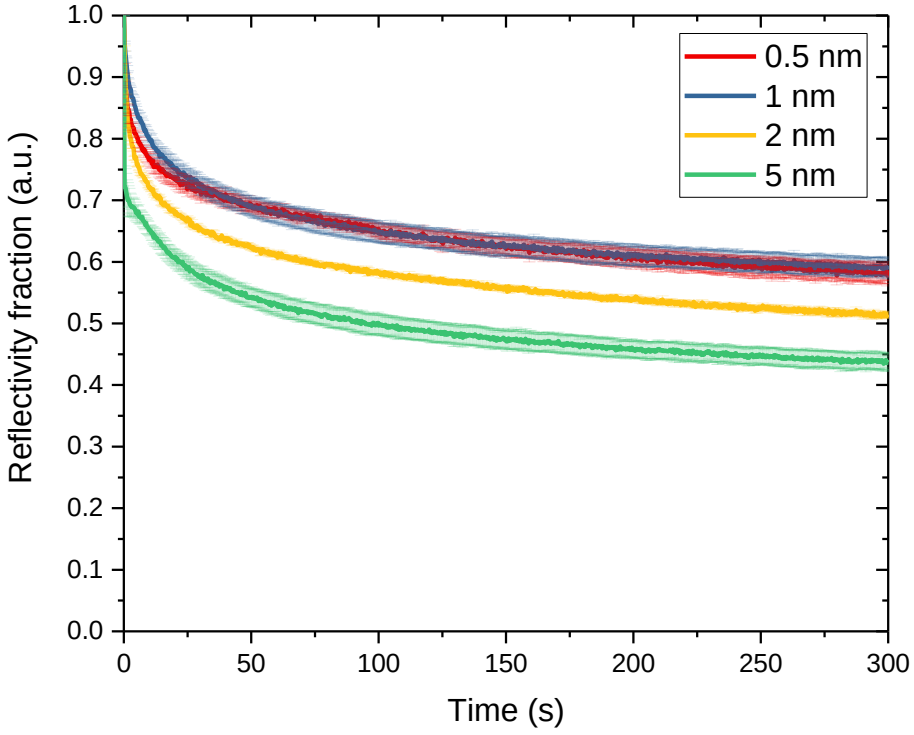

Figure 7.8: degradation curves 0.5 nm Ti/50 nm Au films with varying thickness of Ti deposited as a capping layer.

By extracting the $T_{1/2}$ values from each of the above degradation curves, a quantitative comparison between the capping layers can be made. The $T_{1/2}$ values are displayed as a function of capping layer thickness in Figure 7.9. There is a clear difference in stability between the Al-based, and the Ti- and Ta-based capping layers. Ta_2O_5 and TiO_2 do not show a significant increase in conferred stability on decreasing thickness. The Al capping layer shows a stability trend that is highly similar to that observed with the adhesion layers. The most stable of the capping layers, however, is the 1 nm AlOx capping layer.

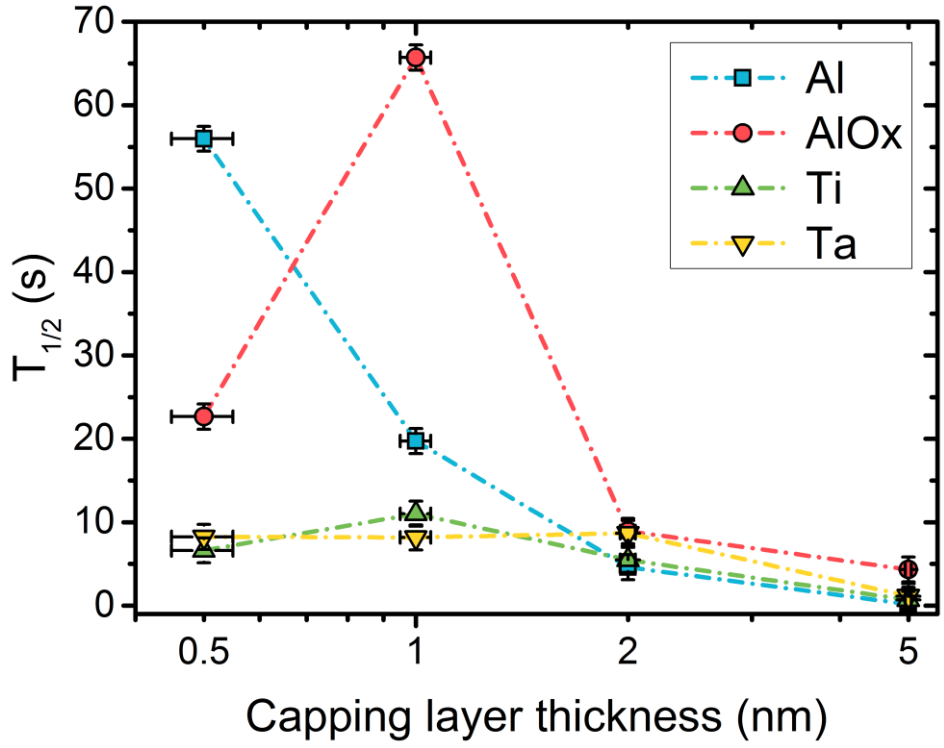

Figure 7.9: $T_{1/2}$ values for each of the capping layers tested, plotted as a function of capping layer thickness. Dashed lines are added to guide the eye.

As a final test to the potential of the Ta_2O_5 and TiO_2 capping layers, the samples were annealed for 10 hrs at 250°C, in order to ensure that the deposited metal had fully oxidized. The thermal stability of the films was measured as before, and the calculated $T_{1/2}$ values were compared with those obtained for the pre-annealed films. The results are shown in Figure 7.10. There is no consistent improvement observed across the different capping layer thicknesses, with some films actually becoming less stable. Notably, none of the films, pre- or post-anneal, are comparable with the best results obtained from the $AlOx/Al_2O_3$ samples. Hence, no further studies were carried out on the Ta_2O_5/TiO_2 samples.

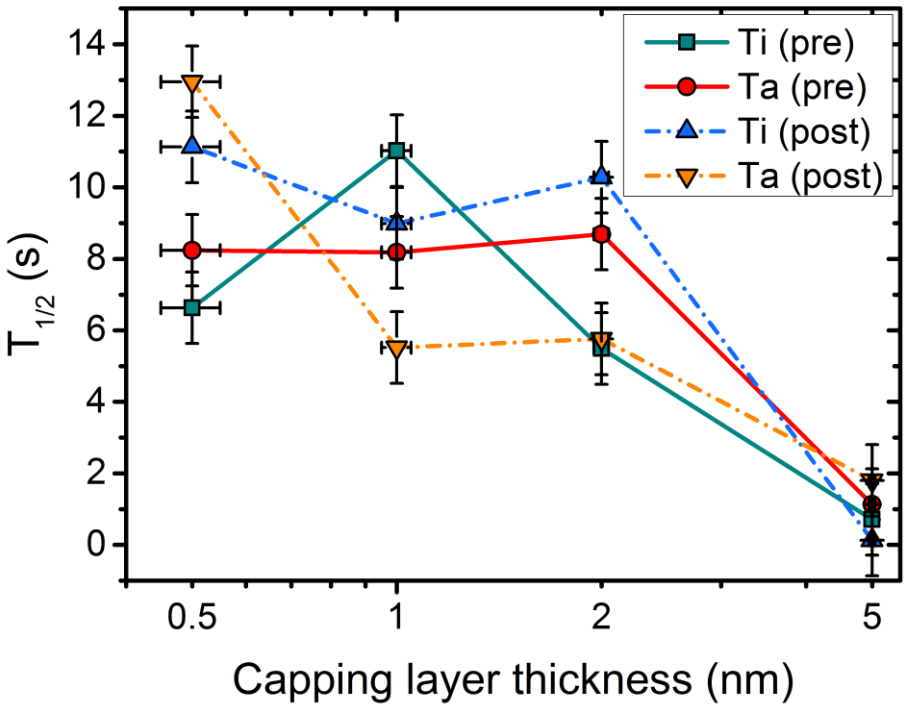

Figure 7.10: $T_{1/2}$ values for 50 nm Au/0.5 nm Ti samples with different thicknesses of Ta_2O_5 and TiO_2 capping layer. Solid lines indicate pre-anneal results, dashed lines indicate post-anneal results. Lines are added to guide the eye.

SEM imaging allows for a visual comparison of the laser-irradiated areas. Images obtained for the Al capping layer are shown in Figure 7.11. Each area (other than the pristine area) was irradiated with 30 mW of absorbed power for 30 s. The stabilizing effect of the 0.5 nm Al_2O_3 capping layer is clearly demonstrated, as it is the only system to not have fully dewetted under the laser irradiation. When all of the areas are considered together, it can be seen that the size of the dewetted area increases as the capping layer thickness increases, confirming the $T_{1/2}$ measurements obtained in Figure 7.9. One notable difference in dewetting characteristics obtained by using capping layers is a complete absence of hillock formation[27]; this is to be expected, as a functional capping layer will be stiff enough to prevent the topography changes induced by hillock formation[3]. This is further proof of the utility of capping layers in thermally stabilizing Au thin films.

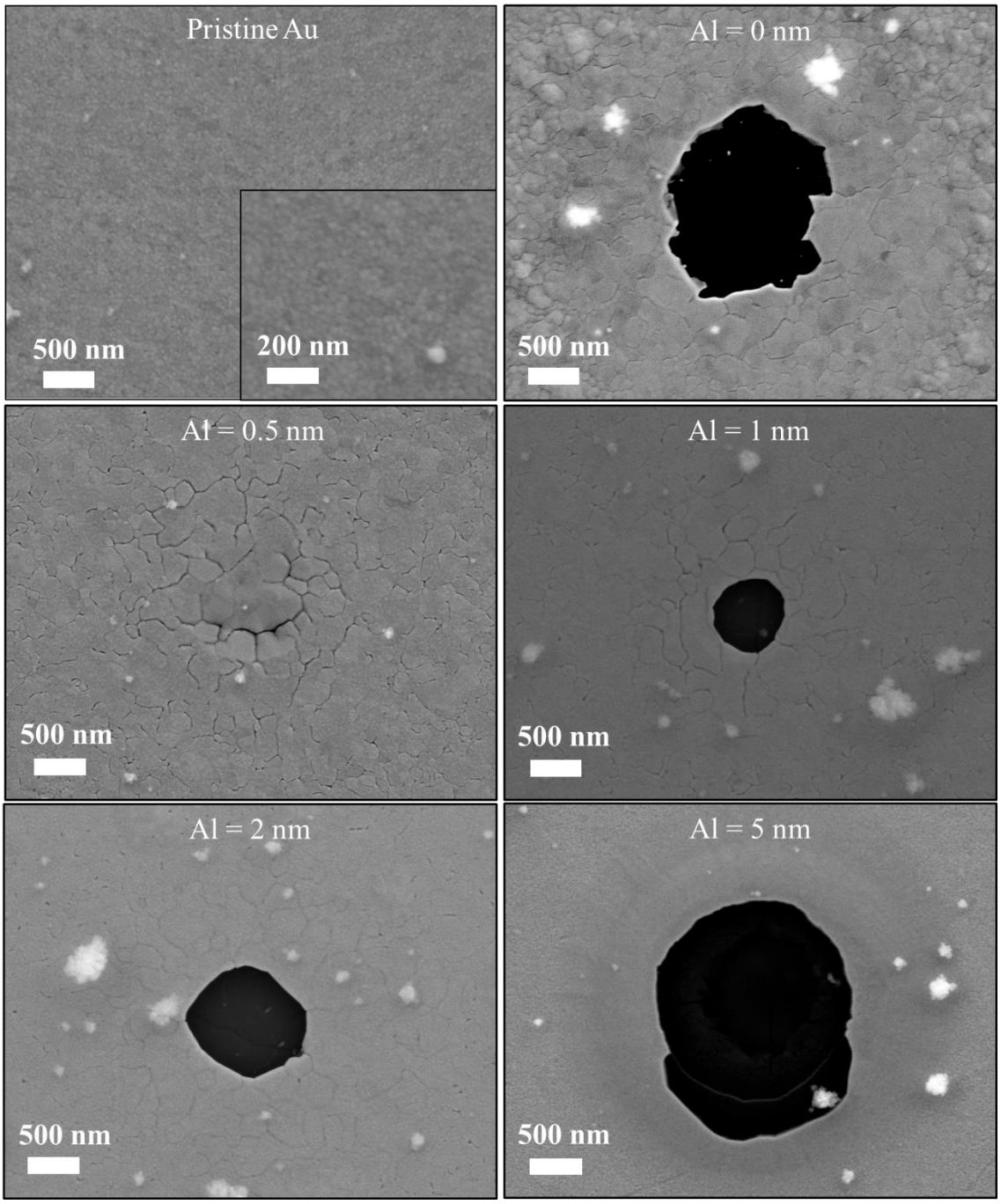

Figure 7.11: SEM images of laser irradiated areas in 0.5 nm Ti/50 nm Au films with varying thickness of Al deposited as a capping layer. Films were irradiated with 30 mW absorbed power for 30 s.

In Figure 7.12, SEM images of laser-irradiated areas for the AlOx capped 0.5 nm Ti/50 nm Au samples are shown. After 30 s of irradiation, the 0.5 nm Ti/50 nm Au/1 nm AlOx has yet to fully exhibit solid-state dewetting, confirming the stability measured in Figure 7.9. In the case of the 5 nm AlOx capping layer, there appears to be some hillock formation within the heat-affected area. This would suggest that either the irradiation is causing a disruption in the capping layer, or that the thicker capping layers possess a lower

Young's Modulus. Nanoindentation can be used to measure the Young's modulus of a material[28]: however it is difficult to measure the Young's modulus of ultra-thin films due to substrate effects[29].

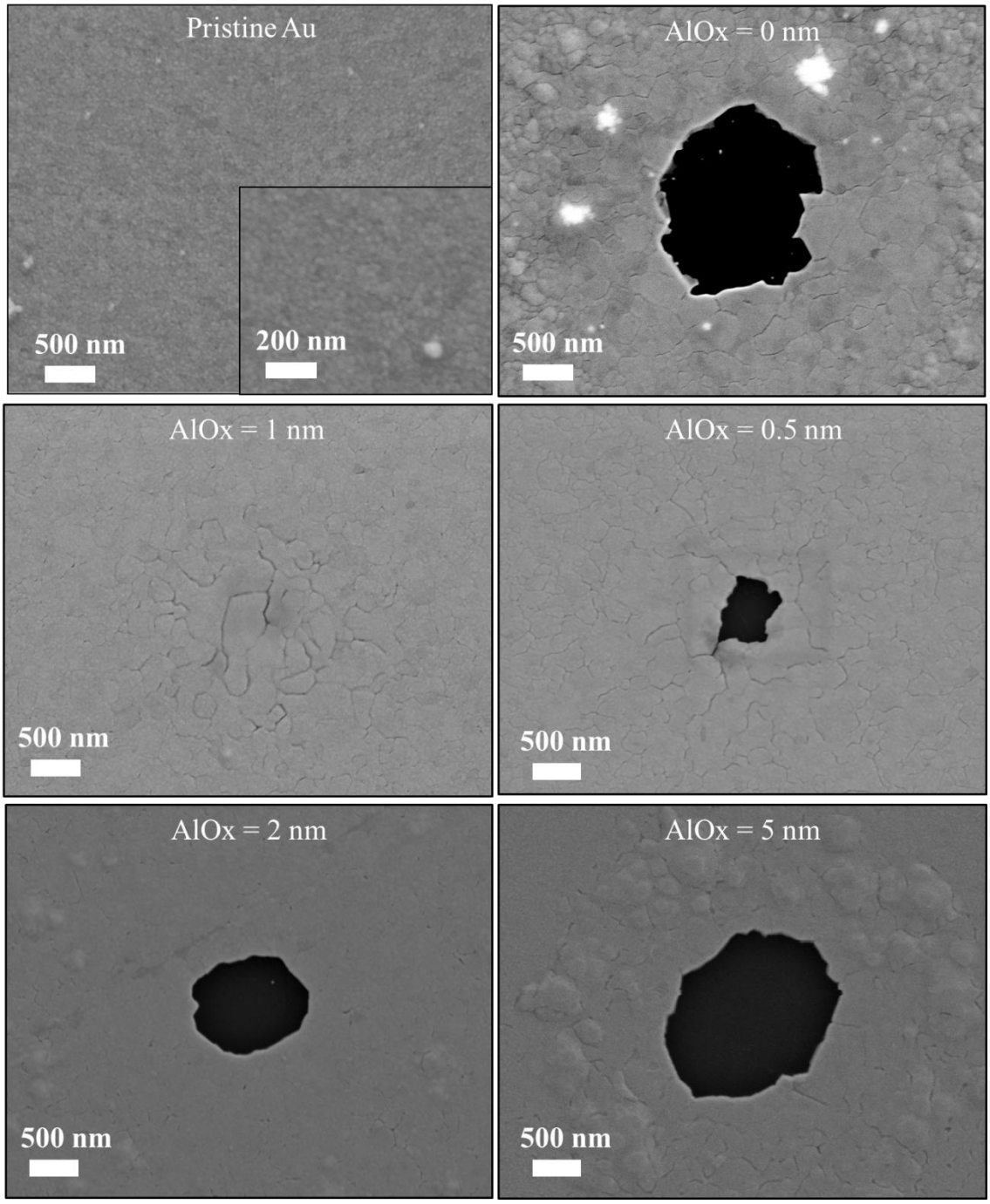

Figure 7.12: SEM images of laser irradiated areas in 0.5 nm Ti/50 nm Au films with varying thickness of AlOx deposited as a capping layer. Films were irradiated with 30 mW absorbed power for 30 s.

AFM was used to characterize the topographical changes of the laser-irradiated 0.5 nm Ti/50 nm Au/5 nm AlOx sample. AFM data is displayed in Figure 7.13. The height profiles show that there is a large increase in the surface roughness, confirming the presence of hillock-like growths as shown in Figure 7.12. The hillock-like growths show a significant increase in height from the original film, with a height measured of 82 nm (Figure 7.13b). Unlike the hillocks described in Chapters 4 and 5, the hillock-like growths for the capped sample do not show a plateau: instead they exhibit a steep, peak-like growth (Figure 7.13c). Previous studies have shown that microscale alumina thin films exhibit a thickness-dependent Young's Modulus, with the value decreasing upon decreasing thickness[30]. If this relationship holds for ultrathin alumina films, it would suggest that their effectiveness as capping layers is not due to possessing a large Young's Modulus.

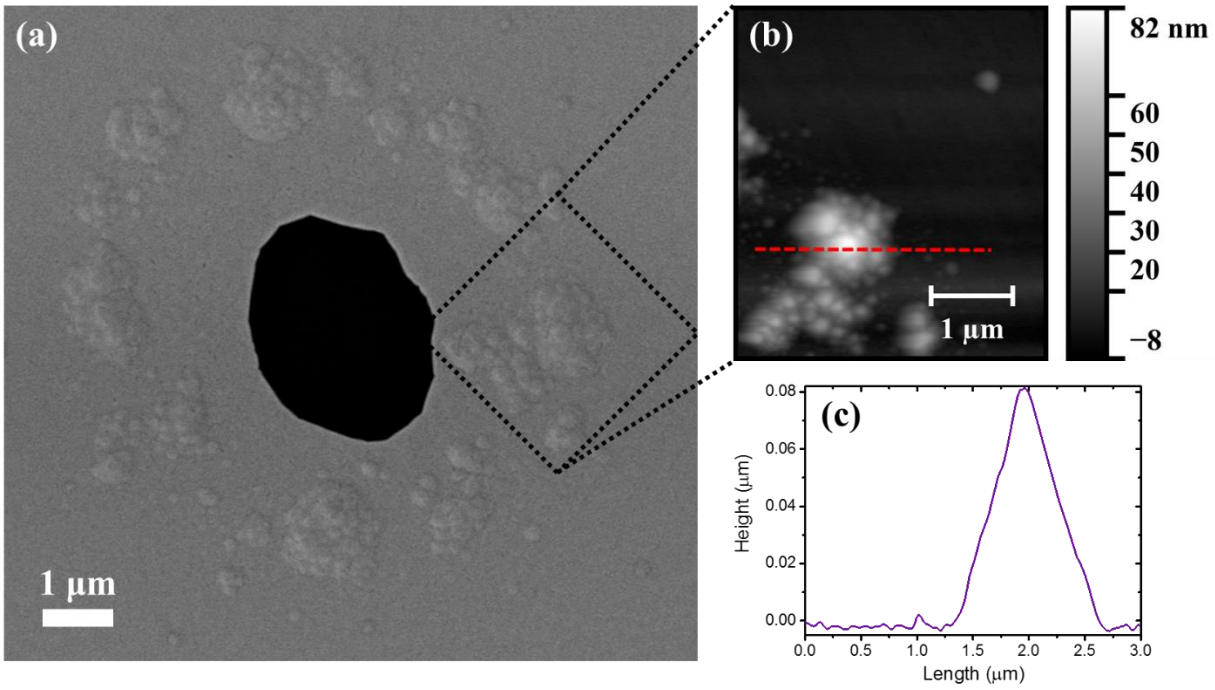

Figure 7.13: AFM measurements on laser irradiated areas in 0.5 nm Ti/50 nm Au/5 nm AlOx film. (a) SEM image showing area of interest, (b) AFM image of hillock region, (c) height profile of hillock region shown in (b).

7.3.2 Plasmonic performance of capped Au films

The plasmonic performance of each capped system was evaluated by measuring the SPP at 633 nm. The results for the Al capping layers are displayed in Figure 7.14. As with the case of the adhesion layers, thinner capping layers will result in less plasmonic damping. The 5 nm capping layer shows a near complete removal of the SPP resonance, which further confirms the hypothesis that the 5 nm layer is not fully oxidized. A noticeable shift in the position of the resonance to higher angles can be seen for samples with a capping layer. This is likely due to the change in local refractive index occurring upon application of the capping layer.

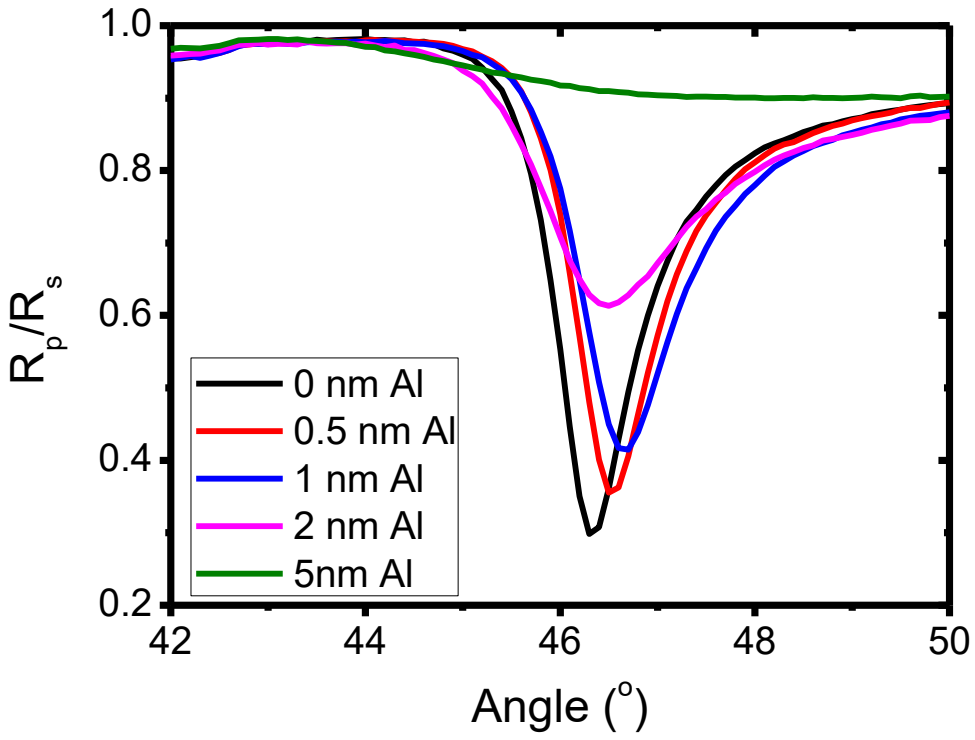

Figure 7.14: SPP measurements for 0.5 nm Ti/50 nm Au films with varying thickness of Al capping layer.

7.3.3 Optimization of the thermal stability of Au thin films

By collating the results obtained in Chapters 4 and 5 with those obtained in this chapter, a final definitive statement on the optimal thickness and materials for adhesion and capping layers can be given. To summarise:

- A 2nm Ti/50 nm Au film is 100 times more resistant to dewetting than a 50 nm Au film with no adhesion layer (Chapter 4).
- A 0.5nm Ti adhesion layer/50nm Au film is 7.29 times more resistant to dewetting than a 2nm Ti adhesion layer/50 nm Au film (Chapter 5).
- A 0.5nm Ti adhesion layer/50nm Au/1nm AlOx capping layer is 10.46 more resistant to dewetting than a 0.5nm Ti adhesion layer/50nm Au film.

If one can assume that the stability enhancement factors are cumulative for each successive optimisation, it can be said that a 0.5nm Ti/50nm Au/1nm AlOx film is 7.3×10^4 times more resistant against dewetting than a 50 nm Au film with no adhesion or capping layer. The use of a 0.5 nm Ta adhesion layer would further improve this stability enhancement.

Hence, it can be stated that the optimal systems for thermo-plasmonic applications are 0.5nm Ta/50nm Au/1nm AlO_x (for when thermal stability is the more critical parameter), and 0.5nm Ta/50nm Au/0.5nm Al_2O_3 (for when plasmonic performance is the more critical parameter).

7.4 Conclusions

In this chapter, the effect of metal oxide capping layers on the dewetting dynamics of 50 nm Au films was studied. It was found that, similar to the case of adhesion layers, thinner capping layers generally result in higher stability against dewetting. Aluminium oxide capping layers outperformed tantalum and titanium oxide layers by a considerable margin, which was expected given the utility of Al_2O_3 as a refractory material. When comparing aluminium oxide capping layers deposited as Al against those deposited as AlOx, the optimal stability enhancement was obtained from the 1 nm AlOx capping layer, followed by the 0.5 nm Al layer. The difference in optimal thicknesses can likely be attributed to the change in film thickness for the Al capping layer after oxidation. Hillock-like growths were shown to be have formed for thicker capping layers, but with a different conformation, suggesting an altered formation mechanism. Measurement of the SPP for

the Al capped samples again showed a superior performance for thinner layers. Finally, by collating the data obtained in previous chapters, it was found that the most thermally stable system is the 0.5nm Ta/50nm Au/1nm AlOx film.

7.5 Bibliography

(1) Manuela Müller, C.; Spolenak, R. Dewetting of Au and AuPt Alloy Films: A Dewetting Zone Model. *J. Appl. Phys.* **2013**, *113* (9), 094301.

(2) Bandyopadhyay, D.; Singh, G.; Becker, M. L.; Karim, A. Capillary Wave Confinement-Induced Stabilization of Polymer Films. *ACS Appl. Mater. Interfaces* **2013**, *5* (10), 4006–4010.

(3) Cao, P.; Bai, P.; Omrani, A. A.; Xiao, Y.; Meaker, K. L.; Tsai, H. Z.; Yan, A.; Jung, H. S.; Khajeh, R.; Rodgers, G. F.; et al. Preventing Thin Film Dewetting via Graphene Capping. *Adv. Mater.* **2017**, *29* (36), 1701536.

(4) Albrecht, G.; Kaiser, S.; Giessen, H.; Hentschel, M. Refractory Plasmonics without Refractory Materials. *Nano Lett.* **2017**, *17* (10), 6402–6408.

(5) Kosinova, A.; Wang, D.; Baradács, E.; Parditka, B.; Kups, T.; Klinger, L.; Erdélyi, Z.; Schaaf, P.; Rabkin, E. Tuning the Nanoscale Morphology and Optical Properties of Porous Gold Nanoparticles by Surface Passivation and Annealing. *Acta Mater.* **2017**, *127*, 108–116.

(6) Gao, L.; Chen, L.; Wei, H.; Xu, H. Lithographically Fabricated Gold Nanowire Waveguides for Plasmonic Routers and Logic Gates. *Nanoscale* **2018**.

(7) Lee, C.; Wei, X.; Kysar, J. W.; Hone, J. Measurement of the Elastic Properties and Intrinsic Strength of Monolayer Graphene. *Science* **2008**, *321* (5887), 385–388.

(8) Finney, E. E.; Ben-Gera, I.; Massie, D. R. An Objective Evaluation of Changes in Firmness of Ripening Bananas Using a Sonic Technique. *J. Food Sci.* **1967**, *32* (6), 642–646.

(9) Jiran, E.; Thompson, C. V. Capillary Instabilities in Thin Films. *J. Electron. Mater.* **1990**, *19* (11), 1153–1160.

(10) Reimanis, I. E.; Dalgleish, B. J.; Brahy, M.; Rühle, M.; Evans, A. G. Effects of Plasticity on the Crack Propagation Resistance of a Metal/Ceramic Interface. *Acta Metall. Mater.* **1990**, *38* (12), 2645–2652.

(11) Xiao, G.; Wang, X.; Zhou, Z. Propagation Properties of Symmetric Surface Plasmon Polaritons Mode in Au/Al_2O_3/Au Waveguide. *IEEE Photonics Technol. Lett.* **2012**, *24* (8), 628–630.

(12) Dua, A. K.; George, V. C.; Agarwala, R. P. Characterization and Microhardness Measurement of Electron-Beam-Evaporated Alumina Coatings. *Thin Solid Films* **1988**, *165* (1), 163–172.

(13) Chou, T. C.; Nieh, T. G.; McAdams, S. D.; Pharr, G. M. Microstructures and Mechanical Properties of Thin Films of Aluminum Oxide. *Scr. Metall. Mater.* **1991**, *25* (10), 2203–2208.

(14) Harrison, W. N.; Moore, D. G.; Richmond, J. C. Ceramic Coatings for High-Temperature Protection of Steel. *J. Res. Natl. Bur. Stand. (1934).* **1947**, *38*, 293.

(15) Lee, E. H.; Poppa, H. Effects of High Temperature and e -beam Irradiation on the Stability of Refractory Thin Films. *J. Vac. Sci. Technol.* **1977**, *14* (1), 223–226.

(16) Cui, J.; Allen, T.; Wan, Y.; Mckeon, J.; Samundsett, C.; Yan, D.; Zhang, X.; Cui, Y.; Chen, Y.; Verlinden, P.; et al. Titanium Oxide: A Re-Emerging Optical and Passivating Material for Silicon Solar Cells. *Sol. Energy Mater. Sol. Cells* **2016**, *158*, 115–121.

(17) Wan, Y.; Bullock, J.; Cuevas, A. Passivation of C-Si Surfaces by ALD Tantalum Oxide Capped with PECVD Silicon Nitride. *Sol. Energy Mater. Sol. Cells* **2015**, *142*, 42–46.

(18) Ottermann, C. R.; Kuschnereit, R.; Anderson, O.; Hess, P.; Bange, K. Young's Modulus and Density of Thin TiO_2 Films Produced by Different Methods. *MRS Proc.* **1996**, *436*, 251.

(19) Siegfried, T.; Ekinci, Y.; Martin, O. J. F.; Sigg, H. Engineering Metal Adhesion Layers That Do Not Deteriorate Plasmon Resonances. *ACS Nano* **2013**, *7* (3), 2751–2757.

(20) Hartzell, D.; Leung, L. K.; Towner, F. J. Cost-Effective, High-Volume Molecular Beam Epitaxy. *JOM* **1998**, *50* (8), 37–39.

(21) Lubitz, M.; Medina, P. A.; Antic, A.; Rosin, J. T.; Fahlman, B. D. Cost-Effective Systems for Atomic Layer Deposition. *J. Chem. Educ.* **2014**, *91* (7), 1022–1027.

(22) Kosinova, A.; Wang, D.; Schaaf, P.; Sharma, A.; Klinger, L.; Rabkin, E. Whiskers Growth in Thin Passivated Au Films. *Acta Mater.* **2018**, *149*, 154–163.

(23) Jeurgens, L. P. H.; Sloof, W. G.; Tichelaar, F. D.; Mittemeijer, E. J. Growth Kinetics and Mechanisms of Aluminum-Oxide Films Formed by Thermal Oxidation of Aluminum. *J. Appl. Phys.* **2002**, *92* (3), 1649–1656.

(24) Reichel, F.; Jeurgens, L. P. H.; Richter, G.; Mittemeijer, E. J. Amorphous versus Crystalline State for Ultrathin Al_2O_3 Overgrowths on Al Substrates. *J. Appl. Phys.* **2008**, *103* (9), 093515.

(25) Gramberg, U.; Renner, M.; Diekmann, H. Tantalum as a Material of Construction for the Chemical Processing Industry - A Critical Survey. *Mater. Corros. und Korrosion* **1995**, *46* (12), 689–700.

(26) Vargel, C.; Jacques, M.; Schmidt, M. P. *Corrosion of Aluminium*; Elsevier, 2004.

(27) Kweon, S. Y.; Yeom, S. J.; Sun, H. J.; Kim, N. K.; Yu, Y. S.; Lee, S. K. Intrinsic Stress Dependence of Pt Hillock Formation and Its Related Electrical Properties of SBT Capacitor. *Integr. Ferroelectr.* **1999**, *25* (1–4), 299–309.

(28) Antunes, J. M.; Fernandes, J. V.; Sakharova, N. A.; Oliveira, M. C.; Menezes, L. F. On the Determination of the Young's Modulus of Thin Films Using Indentation Tests. *Int. J. Solids Struct.* **2007**, *44* (25–26), 8313–8334.

(29) Saha, R.; Nix, W. D. Effects of the Substrate on the Determination of Thin Film Mechanical Properties by Nanoindentation. *Acta Mater.* **2002**, *50* (1), 23–38.

(30) Gong, M. F.; Qiao, S. R.; Mei, F. Determining Young's Modulus and Poisson's Ratio of Thin Hard Films. *Surf. Eng.* **2014**, *30* (8), 589–593.

Chapter 8: Conclusions and Future work

In this chapter, the final conclusions from the work presented in this thesis are stated and discussed. Finally, the future outlook on the work presented is given, and ideas for further study are stated.

8.1 Conclusions

The aims of this thesis were to investigate the changes in film quality that occurred when irradiating Au thin films with a CW-laser, and to propose methods that would help stabilize Au against these changes. For Au thin films deposited on SiO_2 substrates, 3 distinct changes in film quality were observed after irradiation by a CW-laser: namely, solid state dewetting, grain growth, and crystalline texturing. This thesis focused on understanding the solid state dewetting mechanism, which is the dominant effect in thin Au films of interest for HAMR. Before and during the initiation of solid-state dewetting, an irradiated film would undergo non-negligible grain growth. In addition to this, the orientations of individual crystal grains in the film would change, leading to the development of texture in the film.

Three different methods were developed with the aim of preventing or inhibiting the above changes in film quality: metallic adhesion layers, alloying, and dielectric capping layers. The stabilizing effects of each method are summarized in Table 8.1. Adhesion layers are a common method for improving the stability of Au nanomaterials; however, little work has previously been done on optimizing the thickness of the adhesion layer for thermal stabilization. By comparing the stabilization effects of different thicknesses of Ti adhesion layers for a fixed thickness of Au, it was found that sub-nanometer adhesion layers outperformed standard thicknesses (2 – 5 nm) by a large margin, with 0.5 nm being the optimal thickness. The reason for the comparatively poorer performance of standard thicknesses is due to the formation of a fourth change in film quality upon annealing: diffusion of the adhesion layer material through the Au grain boundaries. This analysis was then expanded to include other metallic adhesion layers, and similar findings were

obtained for all metals investigated (Al, Cr, Ta) except for W. For all film systems investigated, sub-nanometer adhesion layers resulted in the least damping on the plasmonic response as expected.

The effect of alloying was investigated through an AuCu alloy. Calculations using measured optical properties showed that the addition of Cu would cause a reduction in the plasmonic performance of the Au, but in certain cases the alloy would still outperform pure Cu. The thermal stability of the alloy, however, was found to be significantly worse than either pure Au or Cu, as the alloy would oxidize and dewet at the same time.

Finally, the effect of capping layers on the thermal stability of Au films was investigated. Similarly to the results obtained for adhesion layers, sub-nanometer capping layers outperformed their thicker counterparts by a large degree. The large stability enhancement was only present when aluminium oxide (either AlO_x or Al_2O_3) was used as a capping layer: capping layers of other oxides (Ta_2O_5 and TiO_2) provided only a marginal stability enhancement. From these results, the optimal capping/adhesion layer system for an Au thin film was proposed: a 1 nm AlO_x capping layer, and a 0.5 nm Ta adhesion layer.

Table 8.1: summary table of results obtained in chapters 4 - 7.

Chapter	Films investigated	Best performing system	Factor of improvement over 50nm Au
4	50nm Au 2nm Ti/50nm Au 2nm Cr/50nm Au	2nm Ti/50nm Au	100
5	Xnm Y/50nm Au (X = 0, 0.1, 0.2, 0.5, 1, 2, 5) (Y = Ta, Ti, W, Al, Cr)	0.5nm Ta/50nm Au	729
6	50nm AuCu alloy	N/A	N/A
7	Xnm Y/50nm Au/0.5nm Ti (X = 0, 0.5, 1, 2, 5) (Y = Al, AlOx, Ti, Ta)	1nm AlOx	7625

8.2 Future outlook

8.2.1 Single crystal Au

The main nucleation point for solid-state dewetting is at grain boundaries and triple points within the film[1], hence it can be expected that a single crystal film will be more resistant to dewetting than polycrystalline films. This has been shown to be the case in previous studies[2]. In the case of a single crystal thin film, dewetting will nucleate at defects within the film, and will exhibit faceted growth (see Figure 8.1).

From a plasmonic perspective, the use of single crystal Au will be highly advantageous: single crystal Au will have a higher plasmonic response due to the absence of scattering from grain boundaries[3–5].

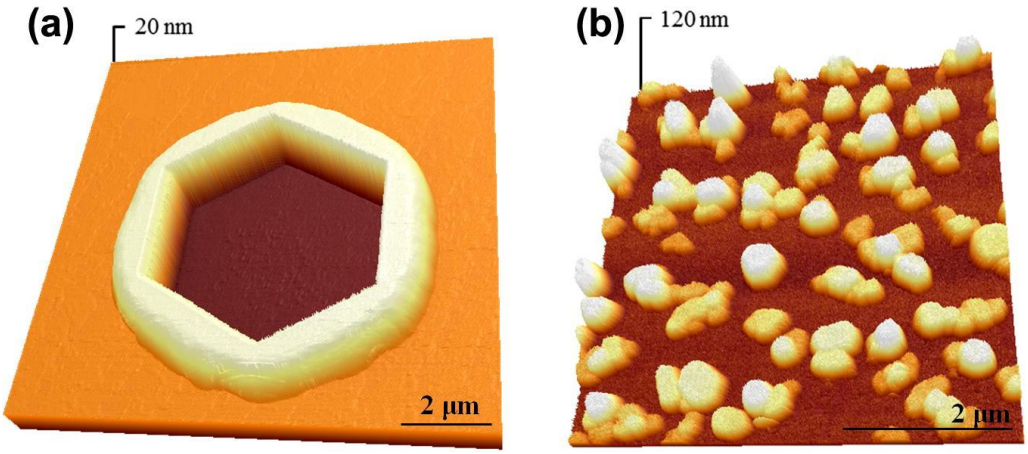

Figure 8.1: comparison of the dewetting process for (a) a single crystal Au-Fe bilayer, and (b) a polycrystalline Au film. Taken from reference[2].

8.2.2 Au alloys and refractory materials for thermo-plasmonics

In Chapter 6, the thermal stability of an AuCu alloy was investigated, but due to the oxidation of the Cu, its potential use in thermo-plasmonic applications is limited. This result does not, however, preclude further investigations on other binary Au alloys. While previous work has shown that AuAg alloys will dewet at similar temperatures to pure Au films[6], alloying Pt with Au will result in significantly more stable films[7] (see Figure 8.2). Extrapolating from this result, it is possible that alloying Au with the other "platinum group" metals (i.e. Ir, Os, Pd, Rh, Ru)[8] will result in other thermally stable alloys. Au-Os is not a suitable candidate, however, due to the solid solubility of Os in Au being negligibly low[9]. The use of Ir, Rh and Ru as an alloying metal is limited by their poor solid solubility in Au (maximum solubility of less than 0.1, 1.6 and 1.9 at. %, respectively[10–12]), although,

based on the stabilizing results of even small amounts of Pt[7], there is still some potential. Additionally, recent results have shown that it is possible to chemically synthesize stable AuIr, AuRh, and AuRu alloyed nanoparticles[13,14]. By way of contrast, the Au-Pd system forms a solid solution, except at specific Au-Pd ratios where it forms an intermetallic alloy[15]. Despite the promise of improved thermal stability, the plasmonic properties of Pd and Pt are poor, and would hence inevitably result in a large dampening of the plasmonic response. Despite this, it has been shown in previous work that a strong near-field enhancement can be observed at Pd tips in AuPd nanoparticles[16]. More recent research has looked at the viability of using refractory materials for plasmonic applications[17–19], and further work must be done to compare both the thermal stability and plasmonic performance of these materials against the stabilization methods investigated in this thesis.

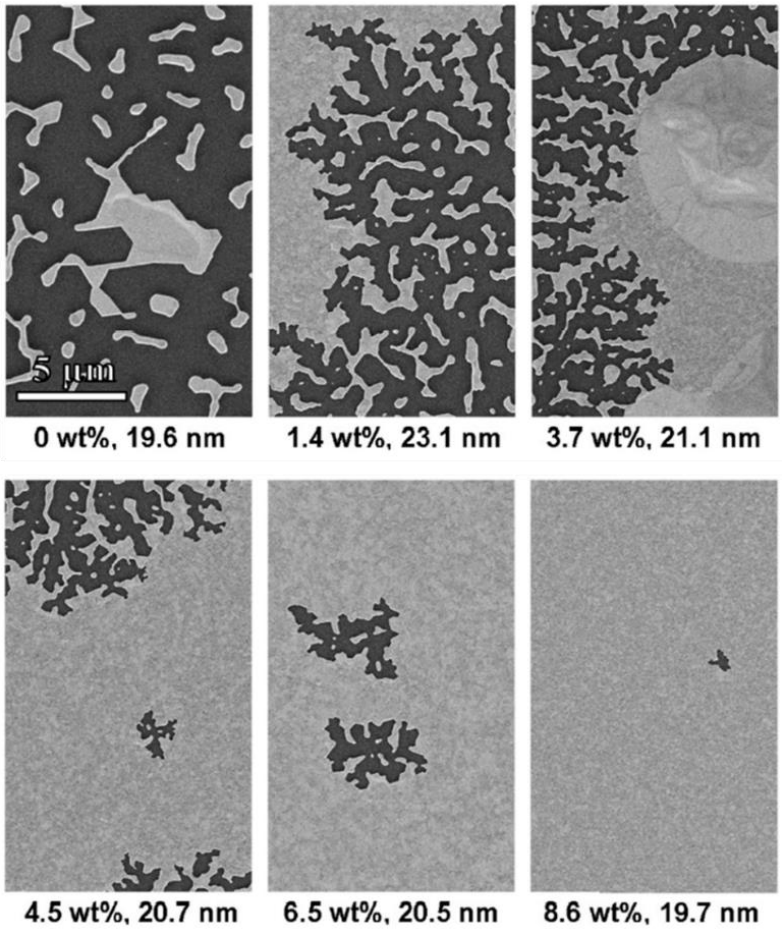

Figure 8.2: demonstration of improved dewetting resistance for AuPt films upon increasing Pt content. Films were annealed for 5 hrs at 500 °C. Adapted from reference[7].

8.2.3 Dewetting characteristics of plasmonic devices

Within this thesis, all measurements were carried out on thin films. The NFTs used in HAMR, however, will be low-dimensional plasmonic focusing elements of various geometries[20–25]. Such devices will potentially be even more susceptible to thermal failure, due to a decrease in their thermal conductivity, and the presence of high surface energy edges and corners, which may act as nucleation points for solid-state dewetting[26] (see Figure 8.3). The stabilization methods presented in this thesis, namely the use of sub-nanometer adhesion and capping layers, could easily be applied to any of the above NFT devices to obtain a significant increase in thermal stability at a small cost of plasmonic efficiency. Previous work on Al_2O_3 capping layers showed that this would be the case[27]; however, these and through the adhesion/capping layer thickness optimization explored in this thesis, it is highly likely that even larger gains in stability could be obtained.

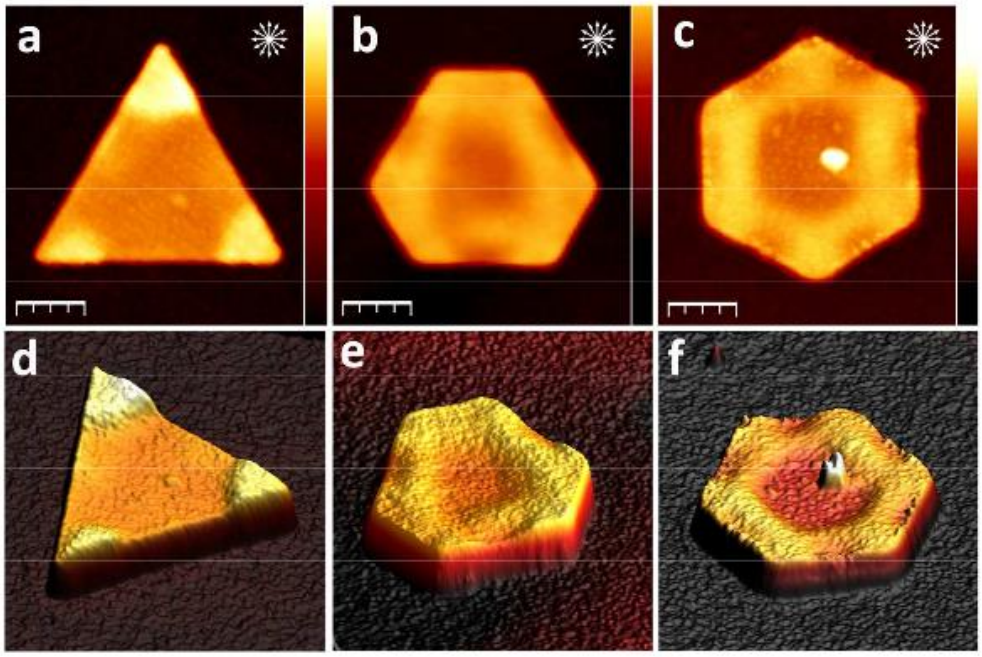

Figure 8.3: changes in topography observed for laser-irradiated Au nanoplatelets. Note that the main changes in topography occur at corners and edges. Scale bars are 200 nm. Taken from reference[26].

The greater susceptibility of Au nanodevices towards thermal failure may lead on to more extreme forms of degradation. Previous studies have shown that high intensity irradiation may lead to nanoparticle explosion[28–30]. It has been observed in studies running parallel to those presented in this thesis, however, that high intensity light is not necessarily required to induce nanoparticle explosion. Au crosses were prepared on quartz via electron beam lithography, which were then irradiated with a 488nm CW-laser (see Figure 8.4). Initial

behaviour was similar to the behaviour of semi-infinite films at high power; a hole is formed in the film through the process of solid-state dewetting, which then slowly expands due to void formation. After a few seconds, the area suddenly explodes. The cause for this explosion is likely due to a combination of void formation and the confined area. The void formation causes a significant decrease in the thermal conductivity of the Au, resulting in a large temperature increase. Due to the confined area and insulating substrate, this leads to thermal runaway, and the explosion of the area. Further work is required in order to confirm this hypothesis on the mechanism behind the nanoparticle explosion, and to explore transition point between particle and semi-infinite film.

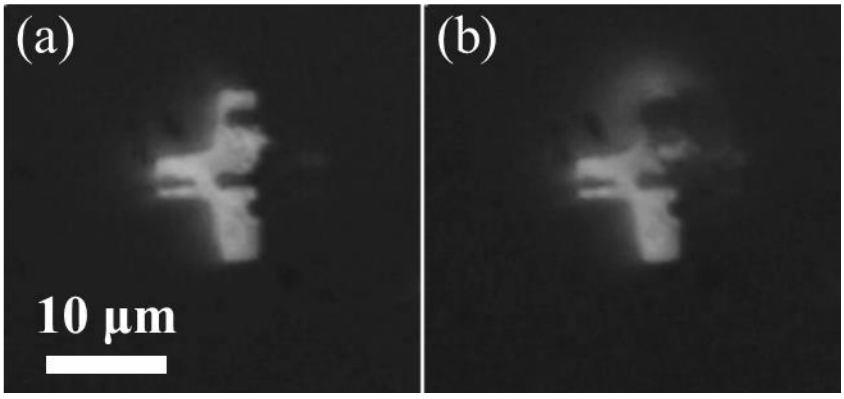

Figure 8.4: Au nanocross irradiated with a 488 nm laser: (a) 0.5 s prior to explosion, (b) 0.5 s after explosion.

8.3 The future of heat-assisted magnetic recording

In light of the work presented in this thesis, and based on encouraging results published by other researchers and companies, there is considerable promise in regards to heat-assisted magnetic recording (HAMR) becoming a viable solution for increasing the storage capacity of magnetic hard-drives. In 2018, Seagate published an update on their blog, detailing how HAMR allowed for the production of a 16 TB 3.5 inch hard-drive[31]. This is the highest capacity hard-drive ever produced, and while not yet available to consumers, it is hard proof of the promise afforded by HAMR. In order for the production of such a hard-drive to be economical, it will be necessary for the NFT to remain functional for much longer than initial prototypes[20]. The work presented in this thesis may help in thermally stabilizing the NFT used in the production cycle, thus allowing HAMR-made magnetic hard-drives to become available to consumers, as opposed to just specialist applications such as data-storage centres. While previous predictions on the availability of

HAMR hard-drives may have been overly optimistic, it would seem that the world is now closer than ever towards having these higher capacity hard-drives in their homes and businesses.

8.4 Bibliography

(1) Jiran, E.; Thompson, C. V. Capillary Instabilities in Thin Films. *J. Electron. Mater.* **1990**, *19* (11), 1153–1160.

(2) Amram, D.; Klinger, L.; Rabkin, E. Anisotropic Hole Growth during Solid-State Dewetting of Single-Crystal Au–Fe Thin Films. *Acta Mater.* **2012**, *60* (6), 3047–3056.

(3) Vesseur, E. J. R.; Polman, A. Plasmonic Whispering Gallery Cavities As Optical Nanoantennas. *Nano Lett.* **2011**, *11* (12), 5524–5530.

(4) Frank, B.; Ruff, A.; Sigle, W.; Fu, L.; Kahl, P.; Ludwigs, S.; van Aken, P.; Osten, W.; Meyer zu Heringdorf, F.-J.; Braun, P. V.; et al. Electrochemical Route to Large-Area Mono-Crystalline Gold Platelets for High-Quality Plasmonic Applications. In *Advanced Photonics*; OSA: Washington, D.C., 2014; p JTu3A.60.

(5) Frank, B.; Kahl, P.; Podbiel, D.; Spektor, G.; Orenstein, M.; Fu, L.; Weiss, T.; Horn-von Hoegen, M.; Davis, T. J.; Meyer zu Heringdorf, F.-J.; et al. Short-Range Surface Plasmonics: Localized Electron Emission Dynamics from a 60-Nm Spot on an Atomically Flat Single-Crystalline Gold Surface. *Sci. Adv.* **2017**, *3* (7), e1700721.

(6) Sugawara, K.; Minamide, Y.; Kawamura, M.; Abe, Y.; Sasaki, K. Agglomeration Behavior of Ag Films Suppressed by Alloying with Some Elements. *Vacuum* **2008**, *83* (3), 610–613.

(7) Manuela Müller, C.; Spolenak, R. Dewetting of Au and AuPt Alloy Films: A Dewetting Zone Model. *J. Appl. Phys.* **2013**, *113* (9), 094301.

(8) Renner, H.; Schlamp, G.; Kleinwächter, I.; Drost, E.; Lüschow, H. M.; Tews, P.; Panster, P.; Diehl, M.; Lang, J.; Kreuzer, T.; et al. Platinum Group Metals and Compounds. In *Ullmann's Encyclopedia of Industrial Chemistry*; Wiley-VCH Verlag GmbH & Co. KGaA: Weinheim, Germany, 2001.

(9) Predel, B. Au-Os (Gold-Osmium). In *Ac-Au – Au-Zr*; Springer-Verlag: Berlin/Heidelberg; pp 1–1.

(10) Predel, B. Au-Ir (Gold-Iridium). In *Ac-Au – Au-Zr*; Springer-Verlag: Berlin/Heidelberg; pp 1–1.

(11) Okamoto, H.; Massalski, T. B. The Au-Rh (Gold-Rhodium) System. *Bull. Alloy Phase Diagrams* **1984**, *5* (4), 384–387.

(12) Okamoto, H.; Massalski, T. B. The Au-Ru (Gold-Ruthenium) System. *Bull. Alloy Phase Diagrams* **1984**, *5* (4), 388–390.

(13) Shubin, Y.; Plyusnin, P.; Sharafutdinov, M.; Makotchenko, E.; Korenev, S. Successful

Synthesis and Thermal Stability of Immiscible Metal Au–Rh, Au–Ir AndAu–Ir–Rh Nanoalloys. *Nanotechnology* **2017**, *28* (20), 205302.

(14) Zhang, Q.; Kusada, K.; Wu, D.; Yamamoto, T.; Toriyama, T.; Matsumura, S.; Kawaguchi, S.; Kubota, Y.; Kitagawa, H. Selective Control of Fcc and Hcp Crystal Structures in Au–Ru Solid-Solution Alloy Nanoparticles. *Nat. Commun.* **2018**, *9* (1), 510.

(15) Predel, B. Au-Pd (Gold-Palladium). In *Ac-Au – Au-Zr*; Springer-Verlag: Berlin/Heidelberg; pp 1–4.

(16) Ringe, E.; Desantis, C. J.; Collins, S. M.; Duchamp, M.; Dunin-Borkowski, R. E.; Skrabalak, S. E.; Midgley, P. A. Resonances of Nanoparticles with Poor Plasmonic Metal Tips. *Sci. Rep.* **2015**, *5* (1), 17431.

(17) Guler, U.; Boltasseva, A.; Shalaev, V. M. Refractory Plasmonics. *Science (80-.).* **2014**, *344* (6181), 263–264.

(18) Lalisse, A.; Tessier, G.; Plain, J.; Baffou, G. Quantifying the Efficiency of Plasmonic Materials for Near-Field Enhancement and Photothermal Conversion. *J. Phys. Chem. C* **2015**, *119* (45), 25518–25528.

(19) Wells, M. P.; Bower, R.; Kilmurray, R.; Zou, B.; Mihai, A. P.; Gobalakrichenane, G.; Alford, N. M.; Oulton, R. F. M.; Cohen, L. F.; Maier, S. A.; et al. Temperature Stability of Thin Film Refractory Plasmonic Materials. *Opt. Express* **2018**, *26* (12), 15726.

(20) Challener, W. A.; Peng, C.; Itagi, A. V.; Karns, D.; Peng, W.; Peng, Y.; Yang, X.; Zhu, X.; Gokemeijer, N. J.; Hsia, Y.-T.; et al. Heat-Assisted Magnetic Recording by a near-Field Transducer with Efficient Optical Energy Transfer. *Nat. Photonics* **2009**, *3* (4), 220–224.

(21) Kong, Y.; Chabalko, M.; Black, E.; Powell, S.; Bain, J. A.; Schlesinger, T. E.; Luo, Y. Evanescent Coupling between Dielectric and Plasmonic Waveguides for HAMR Applications. In *IEEE Transactions on Magnetics*; 2011; Vol. 47, pp 2364–2367.

(22) Bhargava, S.; Yablonovitch, E. Lowering HAMR Near-Field Transducer Temperature via Inverse Electromagnetic Design. *IEEE Trans. Magn.* **2015**, *51* (4), 1–7.

(23) Abadía, N.; Bello, F.; Zhong, C.; Flanigan, P.; McCloskey, D. M.; Wolf, C.; Krichevsky, A.; Wolf, D.; Zong, F.; Samani, A.; et al. Optical and Thermal Analysis of the Light-Heat Conversion Process Employing an Antenna-Based Hybrid Plasmonic Waveguide for HAMR. *Opt. Express* **2018**, *26* (2), 1752–1765.

(24) Zhong, C.; Flanigan, P.; Abadía, N.; Bello, F.; Jennings, B. D.; Atcheson, G.; Li, J.; Zheng, J.-Y.; Wang, J. J.; Hobbs, R.; et al. Effective Heat Dissipation in an Adiabatic Near-Field Transducer for HAMR. *Opt. Express* **2018**, *26* (15), 18842.

(25) Datta, A.; Xu, X. Optical and Thermal Designs of near Field Transducer for Heat Assisted Magnetic Recording. *Jpn. J. Appl. Phys.* **2018**, *57* (9S2), 09TA01.

(26) Viarbitskaya, S.; Cuche, A.; Teulle, A.; Sharma, J.; Girard, C.; Arbouet, A.; Dujardin, E. Plasmonic Hot Printing in Gold Nanoprisms. *ACS Photonics* **2015**, *2* (6), 744–751.

(27) Albrecht, G.; Kaiser, S.; Giessen, H.; Hentschel, M. Refractory Plasmonics without Refractory Materials. *Nano Lett.* **2017**, *17* (10), 6402–6408.

(28) Letfullin, R. R.; Joenathan, C.; George, T. F.; Zharov, V. P. Laser-Induced Explosion of Gold Nanoparticles: Potential Role for Nanophotothermolysis of Cancer. *Nanomedicine (Lond).* **2006**, *1* (4), 473–480.

(29) Last, I.; Jortner, J. Effects of the Nanoplasma on the Energetics of Coulomb Explosion of Molecular Clusters in Ultraintense Laser Fields. *Phys. Rev. A* **2006**, *73* (1), 013202.

(30) Ashiq, M. G. B.; Saeed, M. A.; Tahir, B. A.; Ibrahim, N.; Nadeem, M. Breast Cancer Therapy by Laser-Induced Coulomb Explosion of Gold Nanoparticles. *Chin. J. Cancer Res.* **2013**, *25* (6), 756–761.

(31) Paulsen, J. HAMR Milestone: Seagate Achieves 16TB Capacity on Internal HAMR Test Units | Seagate Blog https://blog.seagate.com/craftsman-ship/hamr-milestone-seagate-achieves-16tb-capacity-on-internal-hamr-test-units/?utm_source=LINKEDIN_COMPANY&utm_medium=social&utm_content=100024808&utm_campaign=Advanced+Technology (accessed Jan 23, 2019).